

Alma Mater Studiorum - Università di Bologna

DOTTORATO DI RICERCA IN

FISICA

Ciclo 36

Settore Concorsuale: 02/A1 - FISICA SPERIMENTALE DELLE INTERAZIONI FONDAMENTALI

Settore Scientifico Disciplinare: FIS/01 - FISICA SPERIMENTALE

SEARCH FOR A DIFFUSE ASTROPHYSICAL NEUTRINO EMISSION FROM THE GALACTIC RIDGE WITH THE FIRST KM3NET/ARCA DATA AND STRATEGIES FOR REAL-TIME FOLLOW-UP SEARCHES OF RAPID TRANSIENT PHENOMENA

Presentata da: Francesco Filippini

Coordinatore Dottorato

Alessandro Gabrielli

Supervisore

Tommaso Chiarusi

Co-supervisore

Annarita Margiotta

Esame finale anno 2024

Guardando la fotografia di una camera a bolle, lo studente vede soltanto linee confuse e interrotte, mentre il fisico vi legge la registrazione di eventi subnucleari a lui familiari. Soltanto quando il suo modo di vedere le cose ha subito trasformazioni di questo genere lo studente entra a far parte del mondo dello scienziato, riesce a vedere le cose che lui vede e a reagire come lui.

—T. Kuhn

Ciò che conta non sono tanto le scalate eclatanti, ma l'umana avventura.

— W. Bonatti

ABSTRACT

Multi-messenger astronomy has allowed a completely and revolutionary new approach to the observation of the Universe. Within this picture, neutrino astrophysics has started in recent years to consolidate the theoretical framework at its basis through the first detection of neutrino sources. However, the complexity of astrophysical environments requires more observational data to fully characterise their internal mechanisms. For this reason, second-generation neutrino telescopes are currently under construction worldwide at different locations. Specifically, KM₃NeT inheriting the experience of the ANTARES telescope is a detector under construction and deployed in the abyssal site of the Mediterranean Sea. Thanks to its design, it is already taking data and will be capable, in the next few years, of complementing the observations conducted up to now and of shedding light on important unanswered questions.

In June 2023 the IceCube Collaboration reported the first observation of astrophysical neutrinos that originated in the centre of our Galaxy. Within the work of this thesis, the first data collected by the KM₃NeT experiment have been analysed, mainly focusing on the search for neutrino emission from this location in the sky. In fact, thanks to the position and to the excellent angular resolution of the KM₃NeT detectors, the Galactic plane is visible for most of the time, representing one of the main physics objectives to address for the experiment. Furthermore, in the observation of fast transient phenomena, neutrino signals could be invaluable precursors of electromagnetic light ejected by sources. For this reason, the last chapter of the thesis is focused on the first correlation studies ever performed with KM₃NeT data with respect to external alerts sent by other observatories.

CONTENTS

INTRODUCTION	1
1 NEUTRINO PHYSICS AND ASTROPHYSICS	3
1.1 Neutrino physics and interactions	4
1.1.1 Neutrino interactions	4
1.1.2 Neutrino oscillations	9
1.1.3 Oscillations over astronomical distances	11
1.2 Cosmic rays	13
1.2.1 Cosmic ray energy spectrum	13
1.2.2 Composition of cosmic rays	15
1.2.3 Galactic cosmic ray acceleration: diffusive shock acceleration	16
1.2.4 Breakthrough discovery: Pevatrons	20
1.2.5 Acceleration mechanisms above the knee	21
1.2.6 GZK cut-off	22
1.2.7 Atmospheric neutrinos	23
1.3 Astrophysical neutrinos	26
1.3.1 Neutrino production mechanisms	26
1.3.2 Neutrino and γ -ray astronomy	28
1.3.3 Neutrino fluxes	30
1.3.4 Neutrinos and Blazars	31
1.3.5 Cosmogenic neutrinos	32
1.3.6 Gravitational wave in the multi-messenger scenario	33
2 NEUTRINO ASTRONOMY	34
2.1 Neutrino telescopes	34
2.1.1 Cherenkov radiation	35
2.1.2 Light propagation	36
2.2 Underwater detectors	37
2.3 Under-ice detectors	39
2.4 Detection principle	41
2.5 Event topologies	42
2.5.1 Environmental background	46
2.5.2 Physics background	47
2.6 Current status and prospects for neutrino astronomy	49
2.6.1 All-sky diffuse neutrino signal	49
2.6.2 Point-source searches	52
2.6.3 Neutrino emission from the direction of the blazar TXS0506+056	54
2.6.4 Neutrino association with tidal disruptive events	55
2.6.5 Neutrino directional association with blazars	55
3 KM3NET DETECTORS	57
3.0.1 The multi-PMT Digital Optical Module	58
3.0.2 Detector layout	59

3.1	Data acquisition system	61
3.2	Trigger	62
3.3	Event reconstruction	63
3.3.1	Track reconstruction	63
3.3.2	Shower reconstruction	64
4	MONTE CARLO SIMULATIONS	66
4.1	Event generation	66
4.2	Particles propagation and light simulation	69
4.3	Trigger simulation	70
4.4	Run-by-run approach	70
5	NEUTRINOS FROM THE MILKY WAY	71
5.1	The Milky Way	71
5.1.1	Galactic Magnetic fields	72
5.1.2	Interstellar medium matter	73
5.1.3	Galactic cosmic rays	75
5.2	Neutrino emission	76
5.3	IceCube observation of a diffuse emission from the Galactic Plane	81
6	DATA SAMPLE AND EVENT SELECTION	84
6.1	Data-taking periods	84
6.2	Stability of the data-acquisition	86
6.3	Dynamic calibrations	87
6.4	Data quality and run selection	88
6.5	Data samples and event selection	89
6.5.1	Neutrino fluxes	89
6.5.2	Effective area	90
6.5.3	Event selection	92
6.6	Peak clustering - KM ₃ NeT/ARCA ₂₁ data set	102
7	GALACTIC RIDGE SEARCH	106
7.1	KM ₃ NeT/ARCA visibility	106
7.1.1	Template fitting and model independent search	107
7.2	Previous searches from the Galactic ridge	108
7.3	Analysis strategy	109
7.4	Optimisation procedure	111
7.4.1	Model rejection factor	111
7.4.2	Optimisation results	112
7.4.3	Angular resolution	115
7.4.4	Merging event selections	116
7.5	Final blinded energy distributions	117
7.5.1	Statistical analysis	118
7.6	Sensitivities	119
7.7	Unblinded results and upper limits	122
7.8	Systematic evaluation	124
8	ONLINE FOLLOW-UP STRATEGY FOR KM ₃ NET	127
8.1	First KM ₃ NeT follow-up: PKS 0735+17	127
8.1.1	Time windows	128

8.1.2	Analysis procedure: ON-OFF method	129
8.1.3	Event selection	130
8.1.4	Results	131
8.1.5	Other IceCube alert follow-ups	133
8.2	GRB221009A follow-up	134
8.2.1	KM ₃ NeT follow-up	134
8.2.2	Event selection	136
8.3	Towards an automatic analysis pipeline	139
8.3.1	Online data reconstruction	139
8.3.2	External trigger receiver	140
8.3.3	Statistics	141
8.3.4	Automatic correlation analysis	141
8.3.5	Optimisation	144
CONCLUSIONS		146
BIBLIOGRAPHY		148

LIST OF FIGURES

Figure 1	Total neutrino per nucleon CC cross section, separated among the different contributions: quasi-elastic scattering (dashed), resonance production (dot-dashed) and deep inelastic scattering (dotted). Figure taken from [10].	6
Figure 2	Feynman diagram of a generic neutrino-nucleon interaction, through NC or CC interaction. In the diagram the interacting particles are represented by their kinematic variables. Figure taken from [11].	6
Figure 3	Neutrino-nucleon CC cross section for DIS. Experimental measurements are reported with points: sub-TeV are obtained from accelerator experiments, few-TeV will be covered by FASERν experiment [12] and TeV-PeV measurements are reported thanks to astrophysical neutrinos detected by IceCube experiment. In the ultrahigh-energy domain (above 10^7 GeV), there are no measurements and predictions for next-generation radio detection experiments are reported. Figure taken from [13].	8
Figure 4	Reconstructed energy distribution for background (blue) and signal+background (green) events, for two building blocks of KM ₃ NeT/ARCA after fifteen years of observation. Figure taken from [17].	10
Figure 5	Neutrino flavour triangle. Points for the three specific scenarios described in the text ($n=0,2,\infty$) are shown with, respectively, triangular, circular and square markers. The flavour ratio in these three scenarios is also shown with the dashed arrows, after oscillation averaging over astrophysical distances. Figure taken from [22].	12
Figure 6	CRs differential energy spectrum, measured from multiple experiments. The spectrum is remarkable for being continuous over the whole energy interval. Figure taken from [24].	14
Figure 7	Relative abundances of Galactic cosmic rays measured at Earth (green), and the elemental abundances within the Solar System (black), normalised to $10^6 \cdot$ Si atoms. Figure taken from [26].	15

Figure 8	Simulated trajectory of CRs in the Galactic magnetic field. The three different energy regimes are chosen to highlight how CRs at energies $\sim 10^{19}$ eV travel along almost straight lines and are not trapped inside the Galaxy.	16
Figure 9	Schematic representation of an acceleration cycle of the DSA mechanism. The particle from the upstream region (interstellar medium) passes through the shock in the downstream region. Figure taken from [27]. . .	17
Figure 10	Schematic representation of CR knee. Figure taken from [29].	20
Figure 11	LHAASO significance map within region $10^\circ \leq l \leq 115^\circ$, $ b \leq 12^\circ$. Top: WCDA ($1 \text{ TeV} < E < 25 \text{ TeV}$) significance map. Middle: KM2A ($E > 25 \text{ TeV}$) significance map. Bottom: KM2A ($E > 100 \text{ TeV}$) significance map (WCDA and KM2A are different sub-detectors within LHAASO). Figure taken from [31]. .	21
Figure 12	Mass composition measurements of primary CR flux performed by Pierre Auger Observatory, through determination of the depth of the maximum development of air shower (X_{max}). Figure taken from [37]. .	23
Figure 13	Measurement of the atmospheric neutrino flux for ν_μ and ν_e reported by various experiments (Frejus, AMANDA, IceCube, Super-Kamiokande and ANTARES). Figure taken from [41].	25
Figure 14	Photon mean free path as a function of the photon energy. Scattering over different contributions of EBL is reported: infrared (blue), CMB (red), and radio (green). Figure taken from [29].	28
Figure 15	Calculation of the γ -ray flux originated from hadronic (left) and photo-pion (right) production, matching the Fermi data, starting from the neutrino flux (black line) measured by IceCube. More details on the theoretical derivation are provided in the text. Figure taken from [44].	29
Figure 16	Expected neutrino flux estimated from different models and atmospheric neutrino background. The black line is the expected atmospheric flux, in which also the <i>prompt</i> component is included. The horizontal green line is the upper bound for the diffuse flux of the astrophysical neutrino derived from the Waxman and Bahcall model (solid) and from the GRB emission (dashed). The blue line instead represents the possible contribution of cosmogenic neutrinos. . .	31

Figure 17	Flux of cosmogenic neutrinos expected at Earth and current IceCube and PAO limits. The different curves represent different assumptions in the cosmological evolution of the source. Left: primary composition of CRs assumed purely from protons. Right: primary mass composition extracted from PAO data, like the one also reported in Figure 12. Figure taken from [47].	32
Figure 18	Schematic representation of Cherenkov light emission, where θ is the characteristic Cherenkov angle. The red arrow marks the propagation of the charged particle in the medium, while the blue arrows represent the propagation of the coherent wavefront of Cherenkov light.	35
Figure 19	Absorption and scattering length as a function of the light wavelength. Figure taken from [58].	36
Figure 20	Schematic representation of IceCube Neutrino Observatory, with particular attention to each of the sub-component: in-ice optical detector, the DeepCore and IceTop.	39
Figure 21	Footprint of the IceCube-Upgrade and IceCube-Gen2, with respect to the already existing optical strings. Figure taken from [64].	40
Figure 22	Illustration of the possible origin of signal and background events inside a neutrino telescope.	41
Figure 23	Comprehensive representation of all the event topologies occurring inside a neutrino telescope. Black dashed lines represent neutrinos, orange solid lines muons, red electromagnetic showers, blue hadronic showers, and green τ leptons. Taken from [62].	43
Figure 24	Parameterisation of the shower transverse profile light emission for an electromagnetic shower. The peak corresponds to the cosine of the Cherenkov angle in water. Figure taken from [58].	45
Figure 25	Vertical muon intensity versus depth (expressed in km of water equivalent) measurements for the NEMO Phase-2 tower (pathfinder detector of KM ₃ NeT/ARCA). For comparison, the results of other experiments and the expected theoretical flux of the Bugaev model [66] are shown. Figure taken from [67].	47
Figure 26	Different contributions to muon background as a function of the cosine of zenith angle at a depth of 2400 m, for two different energy regimes (dashed: $E_\mu > 100$ GeV while solid: $E_\mu > 1$ TeV). Black lines refer to atmospheric muons, while blue lines refer to muon induced by an atmospheric neutrino.	48

Figure 27	Energy and declination distribution of the observed events compared to model predictions by the IceCube detector. Figure taken from [68].	49
Figure 28	Energy distribution of the observed cascade events compared to model predictions by the IceCube detector. Figure taken from [71].	50
Figure 29	Summary of the principal results for the search of the all-sky neutrino emission. Two-dimensional confidence region for the best-fit astrophysical parameters: $\Phi_{@100\text{TeV}}^{\nu_i+\bar{\nu}_i}/10^{-18} \text{ GeV}^{-1} \text{ cm}^{-2} \text{ s}^{-1} \text{ sr}^{-1}$ and spectral index. Figure taken from [74].	52
Figure 30	P-value sky map of the scan of the Northern hemisphere, searching for point-like neutrino emission. Figure taken from [77].	53
Figure 31	Left: comparison of point-source best fitted fluxes with respect to the total diffuse astrophysical neutrino flux measured by IceCube Collaboration [70]. Figure taken from [77]. Right: discovery flux of KM ₃ NeT/ARCA in its final configuration for source NGC1068, assuming the best-fit spectral index $\gamma=3.2$. Figure taken from [78].	54
Figure 32	Time-dependent analysis results. Central time and width are plotted for the most significant cluster of events in time, with the p-value of the result shown by the height of the peak. The orange curves represent the search using a Gaussian-shaped time profile, while the blue curves represent the box-shaped time profile. Figure taken from [79].	54
Figure 33	Light curves from the direction of the blazar J0242+1101 as a function of time observed, respectively from top to bottom, by: ANTARES, OVRO, Fermi-LAT, and IceCube. Figure taken from [82].	56
Figure 34	Left: picture of the KM ₃ NeT digital optical module. Right: schematic representation of the components inside a DOM. Taken from [84].	58
Figure 35	Exploded view of the KM ₃ NeT DOM. Taken from [86].	59
Figure 36	Detector footprint for KM ₃ NeT/ORCA (top) and for KM ₃ NeT/ARCA (bottom) in their final configuration. Taken from [86].	60
Figure 37	Angular resolution for track-like (ν_μ -CC) and shower-like (ν_e -CC) interactions, for KM ₃ NeT/ARCA in its final configuration. For both samples, the selection is at the analysis level, once the atmospheric muon contamination is reduced. Figure taken from [78]. . .	65
Figure 38	Definition of the detector can. Figure taken from [87].	67

Figure 39	Survival probability for neutrinos and anti-neutrinos traversing the Earth in function of the cosine of the zenith (horizon is at 0 and a vertical path traversing all the Earth is at 1). This survival probability is reproduced and taken as a reference by the gSeaGen code. Figure taken from [90].	69
Figure 40	An artist’s impression of the Milky Way galaxy: left a face-on view, right an edge-on view. Figure taken from [93].	72
Figure 41	Top: γ -ray intensity as a function of energy in the window $ b < 5^\circ$ and $25^\circ < l < 100^\circ$. Observational data from TibetAs γ , ARGO-YBJ and LHAASO at high energy are also reported. Bottom: neutrino intensity as a function of energy in the window $ b < 8^\circ$ and $ l < 80^\circ$. For both plots, CRINGE model prediction without (left) and with (right) unresolved source contribution. The shaded bands represent the uncertainties associated with each of the elements taken into account in the modelling. Figures taken from [103].	78
Figure 42	Spectra measured by Fermi-LAT Collaboration from the inner Galaxy, with the associated systematic uncertainty (experimental points reported as black dots, and grey shaded band representing systematic uncertainties). For comparison, also the expected contribution from π^0 -decay (red dashed line), inverse Compton (green dashed line), and bremsstrahlung (cyan dashed line) is reported. Figure taken from [105].	79
Figure 43	γ -ray diffuse spectra from the <i>base</i> and γ - <i>optimized</i> models compared to Tibet As γ , LHAASO, Fermi-LAT and ARGO-YBJ data in the window $ b < 5^\circ$, $25^\circ < l < 100^\circ$. Contribution from unresolved sources is not included. Figure taken from [104].	80
Figure 44	Full sky neutrino emission predicted with the KRA γ in the <i>base</i> and γ - <i>optimized</i> configurations, compared to model independent upper limits obtained from ANTARES Collaboration [108]. The KRA γ^5 expectation is also reported. Figure taken from [104].	80

- Figure 45 Galactic plane emission visible through photons and neutrinos. The γ -ray emission is the integrated flux seen by the Fermi-LAT telescope at energies greater than 1 GeV. The other panels show, respectively, the expected neutrino flux, considering the π^0 template and the template itself convolved with angular uncertainty of the sample analysed ($\approx 7^\circ$). In the last panel, the pre-trial significance is reported from the all-sky scan for point-like sources. Figure taken from [109]. 82
- Figure 46 Energy spectra for the three different tested models. The sky integrated, per-flavour neutrino flux is reported. Dotted lines are the model expectations, while solid ones represent the best fitted normalisation values obtained from the analysis, with the 1σ uncertainty reported through the shaded area. The diffuse all-sky flux measured by IceCube is also reported with a grey band. Figure taken from [109]. 83
- Figure 47 Footprint of the KM₃NeT/ARCA detector with 21 active detection units (circular marks). The different colours refer to different marine sea campaigns (referred to *MOx-year* in the legend) and therefore different detector configurations. The recovered DU (red arrow) is just the DU-18 that no longer collected data during the KM₃NeT/ARCA8 period. The rectangular markers are the junction boxes, specific optical and power split points of the seabed infrastructure. MEOC-1 is instead the 100 km long electro-optical cable, driving data onshore and providing the required power to the detector. 85
- Figure 48 Time integrated number of events acquired with KM₃NeT/ARCA21 detector, in the period 20/08/23 - 27/08/23. The constant and monotonic increase in the events collected, without any plateau, suggests a stable and efficient data taking. The average data taking efficiency for this week was evaluated to be at the 98.3%. 86

Figure 49	<p>Top: angular distance of the directions reconstructed, on the same triggered events, respectively with static and dynamic calibration as a function of time. The median (solid red line) and the 32% quantile (dashed blue line) are shown, calculated over one hour time interval. Points at zero represent time windows with no data available. Bottom: Amplitude of the string displacement, seen here as the angle with respect to the vertical nominal position, as a function of time derived from the acoustic positioning system. The sharp peaked string displacement is highly correlated with the difference in reconstruction that takes advantage of the two different calibrations.</p>	87
Figure 50	<p>Overall uncertainty (black solid line) for atmospheric neutrino flux calculated with Honda model (single error source contribution also shown). Figure taken from [111].</p>	90
Figure 51	<p>Comparison of the effective areas for track-like up-going events of KM₃NeT/ARCA detector, calculated with respectively 6, 8, 19 and 21 active detection units.</p>	91
Figure 52	<p>Data and Monte Carlo comparison for the zenith distribution of KM₃NeT/ARCA8 events. Left: distribution after preliminary selection. Right: distribution after preliminary and anti-noise selection. The discrepancy between data and Monte Carlo observed in the left plot, for zenith values above 120°, is due to environmental background events that are not simulated within the Monte Carlo chain. After applying the anti-noise selection, a satisfactory data/Monte Carlo ratio is recovered.</p>	93
Figure 53	<p>Data and Monte Carlo comparison after upward-going selection for (left:) the angular error estimate β_0, and (right:) the reconstructed track length.</p>	94
Figure 54	<p>Data and Monte Carlo comparison for reconstructed zenith and energy for the KM₃NeT/ARCA6 and KM₃NeT/ARCA8 detector configurations, after the final fixed cut selection.</p>	96
Figure 55	<p>Data and Monte Carlo comparison for reconstructed zenith and energy for the KM₃NeT/ARCA19 and KM₃NeT/ARCA21 detector configurations, after the final fixed cut selection.</p>	97
Figure 56	<p>Distribution for each of the input variables used for the BDT training, directly output of the TMVA package. Background (red) and signal (blue) distributions are separately reported.</p>	100

Figure 57	Left: BDT score distribution evaluated on the training and test sample. The visible agreement between the curves suggests the lack of overfitting during the training. Right: ROC curve, widely used metric to compare and evaluate the performances of ML methods.	101
Figure 58	Data and Monte Carlo comparison for the BDT output score distribution, evaluated on KM ₃ NeT/ARCA6 (left panel) and KM ₃ NeT/ARCA8 (right panel) data sets.	102
Figure 59	Data and Monte Carlo comparison for the BDT output score distribution, evaluated on KM ₃ NeT/ARCA19 (top panel) and KM ₃ NeT/ARCA21 (bottom panel) data sets.	102
Figure 60	Reconstructed zenith distribution from the shower algorithm. The plot was produced after final fixed cut selection, with a further cut on likelihood greater than 75, in order to make more visible the peak in the data distribution.	103
Figure 61	Time residual distribution calculated for triggered hits under the assumption of point-like emission in correspondence of DOM12 DU12. Top: Time residual compatible with the hypothesis, used to flag suspicious events. The further plot presented in the pop-up window shows the time residual distribution on the individual PMTs of DOM13 DU12. As can be seen, most of the hits have been registered for channel-ids > 12, belonging to the lower hemisphere of the DOM. Bottom: time residual distribution of the other events analysed. It is clearly visible that the points are not compatible with the assumption made. The event topology analysed here was presumably caused by a downgoing atmospheric muon.	105
Figure 62	Sky visibility of a neutrino telescope located in the Mediterranean Sea, in Galactic coordinates. The dark (light) blue shaded areas represent the visibility over 75% (25%). Some candidate neutrino sources are also reported. Figure taken from [86].	107
Figure 63	Per flavour neutrino sky map at 10 TeV energy predicted by the γ -optimized Max model, represented in Galactic coordinates. The colour scale is proportional to the logarithm of the flux. Figure taken from [104].	108

Figure 64	Map in Galactic coordinates of the ON (green rectangle) and OFF (viridis rectangles) regions. The OFF region can be seen as the continuous portion of the sky locked up by all the viridis rectangles.	110
Figure 65	Contour plot of the MRF value reported as a function of the three optimised variables. The central plot corresponds to the combination of parameters producing the minimum MRF, marked with a red point. The plots on the left and right show the same distribution for adjacent BDT cuts. The two innermost contours around the minimum represent the relative variation of 1% and 5% with respect to the minimum MRF.	114
Figure 66	Histogram showing the angular resolution (α) of the simulated neutrino sample, weighted with a E^{-2} single power-law, at final fixed cut level and after the BDT and energy cut (top and bottom left panels). For comparison also atmospheric muon angular resolution is reported.	115
Figure 67	Blinded energy distributions for the four different data samples. Shaded blue areas represent the background derived from data in the OFF region, with its relative statistical uncertainty. For comparison but not used in the other steps of the analysis, the background derived from Monte Carlo simulations (dotted blue line) is also reported. The scramble data points falling in the ON region (black triangles) and the expected signal events, weighted with the ANTARES best-fit flux [114], are also drawn (red line).	117
Figure 68	Left: 2D plane showing the posterior distribution as a function of the parameters of interest, Γ and Φ_0 . Red lines mark the 68%, 90% and 99% contours, and the white cross shows the best-fit point, obtained maximising the posterior probability. Right: Profiling of the posterior distribution, fixing the spectral index Γ and deriving the 90% upper limit.	119
Figure 69	Distribution of 90% upper limit obtained for each pseudo-experiment, for a given fixed spectral index, i.e. $\Gamma=3.5$. Sensitivity is extracted taking the median upper limit (marked by the red dashed line).	120
Figure 70	Right: sensitivity reported for the single KM ₃ NeT/ARCA detector configurations as well as final combinations. The best-fit flux by ANTARES is also reported. Right: graphical explanation of the construction of the butterfly contour, summarising, within a single plot, all the different tested spectral indices.	121

Figure 71	KM ₃ NeT combined sensitivity for ARCA6+8 (dark blue dashed line) and the full data set (light blue dashed line). The ANTARES and IceCube best-fit fluxes have been reported. For a fair comparison, the ANTARES and KM ₃ NeT limits have been integrated over the solid angle spanned by Galactic Ridge.	122
Figure 72	Final energy distributions, after unblinding, for the ON and OFF regions, for each different detector configuration.	123
Figure 73	90% confidence level upper limit, for the tested spectral indices, reported in Table 8 and drawn here as butterfly contour. For comparison, ANTARES and IceCube best-fit fluxes are reported. As previously done for the sensitivity plot, ANTARES and KM ₃ NeT limits have been integrated over the solid angle, spanned by the Galactic Ridge.	124
Figure 74	Percentage variation of the modified Monte Carlo simulations with respect to the standard simulation, as a function of the reconstructed energy. Each of the single contribution is visible: PMT quantum efficiency (green solid line), light absorption length (purple dashed line) and the quadrature sum of the two (blue solid line).	125
Figure 75	Percentage variation of the modified Monte Carlo simulations performed with respect to the standard simulation chain, in function of the true neutrino energy.	125
Figure 76	Left: 2D histogram of the Monte Carlo energy (MCE) as a function of the reconstructed energy for ν_{μ} -CC events. With the red points the weighted median distribution is marked. Right: median, 68% and 90% contour distribution for the energy resolution.	126
Figure 77	γ -ray flux of the blazar PKS0735+17 observed by the Fermi-LAT telescope in the period 2009 - 2022 (left) and around the flaring period in December 2021 (right). Figures taken from [134].	128
Figure 78	Schematic representation of the ON and OFF region considered in IceCube-211208A alert follow-up.	129
Figure 79	Sky map for the full month of December 2021, showing KM ₃ NeT/ARCA events falling in a cone with radius of 10°. Reported with shaded areas: the KM ₃ NeT ON region in red (centred on the blazar location detected by the Fermi-LAT telescope), the best-fit IceCube position, and the relative 90% containment error in blue, and the Baikal-GVD shower event with associated uncertainty in green.	131

Figure 80	Reconstructed event rate in KM ₃ NeT/ARCA21 (dominated by the atmospheric muons) as function of UTC time, in time bins of 5 minutes. The T_0 (red), $T_0 \pm 6$ hours (green), and $T_0 \pm 12$ hours (yellow) are also reported with vertical lines.	135
Figure 81	ON and OFF region definition for the GRB2201009A follow-up taking into account the movement of the source in local coordinates (blue points) in the time interval $[T_0 - 50 \text{ s}, T_0 + 5000 \text{ s}]$. OFF zenith band defined as the maximum and minimum zenith values reached by the region of interest in the ON time window (green dashed lines).	136
Figure 82	Top: reconstructed energy distribution of the KM ₃ NeT/ARCA21 data, showing the double peak distribution, also described in the text. Bottom: reconstructed likelihood distribution for the KM ₃ NeT/ARCA21 data set considered in the follow-up, highlighting the distribution before (blue) and after (orange) the cut in energy introduced.	137
Figure 83	Sky map showing a circular region of 15° centred on the FERMI localisation for the GRB2201009A. Highlighted the region of interest (red shaded circle) and possible events found in KM ₃ NeT/ARCA data set (blue dot).	138
Figure 84	Schematic representation of the real-time framework developed within the KM ₃ NeT Collaboration. Figure taken from [149]	140
Figure 85	Left: bar chart showing the number of received (blue bars) and selected (orange bars) external alerts as a function of the four main categories analysed. Right: rate of selected alerts per day, subdivided by category. Both the plots refer to a period ranging from July 1 st 2023 up to October 17 th 2023.	141
Figure 86	Map in equatorial coordinates showing the 90% sky localisation probability for a specific GW event. This contour, sent through GCN notice, is then enlarged by the due angular extension, in order to take into account the angular resolution of the KM ₃ NeT detectors.	143

- Figure 87 **Top:** sky map automatically produced by the analysis pipeline. Left, full-sky distribution of the selected events for background estimation in the Mollweide projection. Right, a zoom around the ON region. **Bottom:** visibility curve for the alert localisation. Displayed also the percentage of time spent below (upgoing sky) and above (downgoing sky) the horizon. In the same plot the bottom panel displays also the energy of events found in the ON region as a function of time. 144

LIST OF TABLES

Table 1	Table summarising events contained in each of the data sets analysed. Numbers reported after each subsequent selection level applied and specified in the text. The cosmic neutrino flux adopted here and for which the numbers refer is $\Phi_0 = 1.2 \cdot 10^{-4} \text{ GeV}^{-1} \text{ m}^{-2} \text{ s}^{-1} \text{ sr}^{-1}$ and $\Gamma=2$	95
Table 2	Reported optimised cut values found after the MRF minimisation over the whole tested parameter space.	112
Table 3	Reported the number of surviving events in the whole sky after the application of the optimised cut on the BDT score and on energy. (*) The data events for ARCA21 reported in the table have been computed after the subtraction of events probably at the cause of the peak observed in the zenith distribution and flagged with the methodology described in Section 6.6. At this stage of the selection, the number of flagged events subtracted from the final sample is 12.	113
Table 4	Energy integrated background estimation derived from data and from Monte Carlo. The Monte Carlo estimate is simply reported as a further check of the data and Monte Carlo comparison. The expected number of signal events is also computed, assuming the ANTARES best-fit flux [114].	117
Table 5	Sensitivities for KM ₃ NeT/ARCA 6, 8, 6+8, 19, 21 and the full combination. Reported in units of $\text{GeV}^{-1} \text{ cm}^{-2} \text{ s}^{-1} \text{ sr}^{-1}$ at a reference energy $E_0=1 \text{ GeV}$	120
Table 6	5% and 95% quantiles for the different detector geometries as a function of the tested spectral index Γ	121
Table 7	Final numbers for the background data estimation from the OFF region, number of events found in the ON region, and expected number of signal events assuming the best-fit flux of ANTARES, specifically for each KM ₃ NeT detector configuration.	122
Table 8	90% C.L. upper limits under a single power-law assumption for a reference energy $E_0 = 1 \text{ GeV}$ and with spectral indices Γ ranging from 2.2 to 2.7 for KM ₃ NeT/ARCA6, KM ₃ NeT/ARCA8, KM ₃ NeT/ARCA19, KM ₃ NeT/ARCA21 and the combined data sets. All results are expressed in units of $\text{GeV}^{-1} \text{ cm}^{-2} \text{ s}^{-1} \text{ sr}^{-1}$ at a reference energy $E_0=1 \text{ GeV}$	123

Table 9	Final number of events in the ON region, once data set has been unblinded. The value "OFF region band" reported the number of events found in the full declination band, whereas the "background" refers to the estimate after the solid angle rescaling. 131
Table 10	Values of the main reconstructed variables for the unique neutrino candidate event found inside the ON region in the full month time window. 132

INTRODUCTION

Neutrino astronomy is a groundbreaking field of multi-messenger astronomy that looks at the Universe through neutrinos, weakly interacting, and nearly massless particles. They can be generated by a wide range of energetic and violent phenomena, such as supernova explosions, inner regions of massive stars, accretion disks around black holes, and even elusive dark matter interactions. Due also to their properties, neutrinos can traverse vast cosmic distances without being absorbed or deflected, providing unique information on the astrophysical sources that generate them and overcoming intrinsic limitations of other messengers like γ -ray or cosmic rays.

Based on the experience gathered with pioneering projects like DUMAND, AMANDA or ANTARES, a second generation of neutrino telescopes is currently under construction. Among the innovative neutrino detectors designed, the KM₃NeT telescope (Cubic Kilometre Neutrino Telescope) is currently taking data and is expected to be completed in the next few years. KM₃NeT, in its final configuration, will comprise a network of detectors that will cover more than one cubic kilometre of deep seawater in the Mediterranean Sea. Its unique concept and position allow to reconstruct, with high precision, the direction of secondary particles emerging from neutrino interactions, tracing them back to the astrophysical source at their origin. Furthermore, being located in the Northern hemisphere, it fully complements the field of view of the IceCube neutrino telescope. This makes KM₃NeT a crucial player in the field of neutrino astronomy, having the opportunity to solve long-standing open questions on the mechanisms steering the evolution of the Universe.

The thesis is organised as follows:

- the first chapter is dedicated to an overview of neutrino properties, to the description of cosmic rays and it tries to deep into the tight link that bounds neutrino to γ -ray and cosmic rays production;
- the second chapter is focused on neutrino astronomy, its principles and the description of the main detectors currently taking data or under construction. In addition, a broad overview of recent results obtained within this field is reported;
- in the third chapter, the KM₃NeT detector is described in more detail, with a large section dedicated to the technical solutions adopted for the construction of the detector;

- the fourth chapter is dedicated to the description of the Monte Carlo simulation chain adopted within the KM₃NeT Collaboration;
- in the fifth chapter a description of the flux of astrophysical neutrinos coming from the centre of our Galaxy is reported, both from the theoretical and experimental point of view. The recent observation by the IceCube Collaboration of an astrophysical flux from the Galactic plane is also described;
- within the sixth chapter, the KM₃NeT data sets analysed for the work of this thesis are presented, together with the event selection techniques adopted;
- in the seventh chapter, the first search with the KM₃NeT/ARCA data for neutrino emission from the Galactic centre is reported. The upper limits and a comparison with the results obtained by other experiments is available;
- In the last chapter, results obtained in the follow-ups of external alerts, sent by other observatories, are reported. Specifically, the first follow-ups ever conducted within the KM₃NeT Collaboration are described in detail.

NEUTRINO PHYSICS AND ASTROPHYSICS

Observation of the Universe has been conducted since ancient times by looking at the sky with the naked eye. The physics and technological knowledge acquired in the meantime allowed significant advancements in sky exploration. Especially during the twentieth century, experimental techniques and new detectors were developed, allowing us to widen the observation with electromagnetic radiation from the optical to the radio, infrared, and X-ray band. There are, however, intrinsic limitations in the study of the Universe through photons, due to their physics properties. In fact, due to the absorption effects of the atmosphere, photons from different energy ranges must be observed in space or with indirect techniques. Furthermore, they can interact with the matter surrounding astrophysical environments or during their propagation towards the Earth, being absorbed and losing the information on the source that generated them. In the last century, new types of messengers have been used to investigate the Universe, such as cosmic rays, neutrinos, and gravitational waves, leading to unprecedented discoveries. Each of these messengers can bring complementary information which, when combined together, allows producing a more complete picture of the astrophysical environment.

In fact, neutrinos because of their properties, as explained ahead in this chapter, can easily escape from dense regions, extending our view within astrophysical sources. Furthermore neutrinos do not interact with the interstellar medium located along their path towards the Earth, neither with Galactic or extra-Galactic magnetic fields. This allows to trace them back and correlate their arrival direction with known sources. Also gravitational waves are not stopped along their travel in the space-time, and their detection with or without neutrinos could strongly constrain the models which describe some of the most relevant astrophysical objects, like the neutron star mergers.

1.1 NEUTRINO PHYSICS AND INTERACTIONS

Neutrinos are fundamental fermions of the Standard Model (SM) of particle physics: they have spin equal to $1/2$ and no electric or colour charge¹. All neutrino flavours are described within the SM, in which they are grouped into three families with their corresponding charged lepton: *electron* (e), *muon* (μ) and the *tau* (τ). An important measurement performed at LEP and SLD constrained to 3 the number of lepton families [5]. In the SM neutrinos are assumed to be massless, but to explain recent observations of neutrino oscillations [6], the existence of a mass for the neutrino field must be postulated. For this reason, neutrinos are also among the most studied particles to discover possible new physics beyond the Standard Model.

1.1.1 Neutrino interactions

Nowadays it has been understood that Fermi's theory is an effective field theory, representing the low-energy limit of electroweak processes well described within the framework of quantum field theory and of the SM. Denoting by l_α the Dirac spinor describing the different fermion families, the weak interaction violates maximally parity [7], making interact only the left-handed components for particles and the right-handed component for the antiparticle. Explicitly writing the left- and right-handed projected spinor fields:

$$l_{\alpha L} = \frac{1 - \gamma_5}{2} l_\alpha, \quad l_{\alpha R} = \frac{1 + \gamma_5}{2} l_\alpha, \quad (1)$$

the leptonic *charged current* (CC) and *neutral current* (NC) terms, respectively associated to the exchange of the W_ρ^\pm and Z_ρ^0 gauge boson fields can be written as follow:

$$j_{W^\pm, L}^\rho = 2 \sum_{\alpha=e, \mu, \tau} \bar{\nu}_{\alpha L} \gamma^\rho l_{\alpha L} = \sum_{\alpha=e, \mu, \tau} \bar{\nu}_\alpha \gamma^\rho (1 - \gamma^5) l_\alpha, \quad (2)$$

$$j_{Z^0, \nu}^\rho = \sum_{\alpha=e, \mu, \tau} \bar{\nu}_{\alpha L} \gamma^\rho \nu_{\alpha L} = \frac{1}{2} \sum_{\alpha=e, \mu, \tau} \bar{\nu}_\alpha \gamma^\rho (1 - \gamma^5) \nu_\alpha. \quad (3)$$

¹ **Historical note:** the existence of this particle was postulated for the first time by W. Pauli in 1930 to explain the continuous spectrum of the electron observed in the β -decay [1]. Soon after, in 1934, E. Fermi formulated a mathematical theory capable of explaining the β -decay. It included the new Dirac's theory on particles and antiparticles and Heisenberg's ideas on symmetry among proton and neutron in strong interactions, renaming neutrino the particle previously introduced by Pauli. Fermi's theory, as outlined in 1934 by Bethe and Peierls, also contained the mechanism to probe the existence of neutrinos: the inverse β -decay. Only twenty years later, Reines and Cowan conceived an experiment capable of detecting the neutrino flux produced by the nuclear plant, near Savannah River, thus confirming the existence of this particle [2]. The experiment also allowed measuring for the first time the cross-section for the reaction, which was in good agreement with the predictions of Fermi's theory. In 1963 Lederman, Shwartz, and Steinberg discovered a second type of neutrino flavour, named muon neutrino [3], and only in 2000 the DONUT experiment observed for the first time the third neutrino flavour, tau neutrino [4].

The interaction term of the electroweak Lagrangian of the Standard Model can therefore be formulated as follow:

$$\mathcal{L}_{L,L}^{CC} + \mathcal{L}_{L,\nu}^{NC} = -\frac{g}{2\sqrt{2}} \left(j_{W,L}^\rho W_\rho + \text{h.c.} \right) - \frac{g}{2\cos\theta_W} j_{Z,\nu}^\rho Z_\rho, \quad (4)$$

with $g = 0.641$ representing the coupling constant of the weak interaction and $\sin^2(\theta_W) = 0.231$ the Weinberg angle. For further details on SM and weak interaction, see [8][9].

1.1.1.1 Neutrino-nucleon interaction

The interaction processes of neutrinos with ordinary matter, as described in Equation 4, are mainly divided into two categories CC and NC, which can be visualised as follows:

$$\nu_l + X \rightarrow l^\pm + Y \quad (\text{CC}), \quad (5)$$

$$\nu_l + X \rightarrow \nu_l + Y \quad (\text{NC}), \quad (6)$$

where X represents the target matter. The charged lepton (l^\pm coming after the CC interaction) and the hadrons Y originated from the interaction can produce an electromagnetic or a hadronic cascade (described in the next chapter). The type of reactions and the resulting outgoing products highly depend on the neutrino energy. Following the schematic representation given in [10], neutrino interactions can be subdivided as follows:

- *threshold-less processes*, $E_\nu \sim 0 - 1$ MeV such as:
 - coherent scattering $\nu + A_N^Z \rightarrow \nu + A_N^{Z,*}$. The coherent condition is satisfied when $R \cdot Q \ll 1$, with R the nucleus radius and Q the transferred momentum;
 - neutrino capture on radioactive nuclei, also know as *enhanced* or *stimulated* beta decay emission.
- *low energy nuclear processes*, $E_\nu \sim 1 - 100$ MeV:
 - inverse beta decay: $\bar{\nu}_e + p \rightarrow e^+ + n$.
- *intermediate energy neutrino interactions*, $E_\nu \sim 0.1 - 20$ GeV:
 - elastic and quasi-elastic scattering of neutrinos over an entire nucleon, liberating a single or multiple nucleons from the target: dominant process for $E_\nu < 2$ GeV;
 - resonance production: neutrinos can excite the target nucleon to a resonance state;
 - Deep Inelastic Scattering (DIS): if the neutrino has enough energy, it can resolve the individual quark constituents of the nucleon, producing an outgoing hadronic shower.

Considering the competition between the above three processes, depicted in Figure 1, the products of neutrino interactions can be of different nature, from nucleons to pions, kaons or multiple mesons.

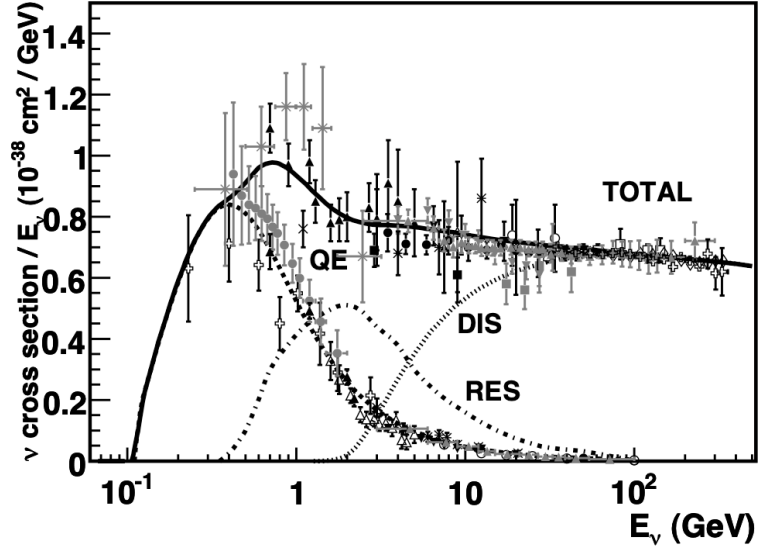


Figure 1: Total neutrino per nucleon CC cross section, separated among the different contributions: quasi-elastic scattering (dashed), resonance production (dot-dashed) and deep inelastic scattering (dotted). Figure taken from [10].

- *ultra high energy neutrino interactions*, $E_\nu \sim 0.5 \text{ TeV} - 1 \text{ EeV}$:
the neutrino cross-section in this energy range can be derived as a simple high energy extension of the parton model used to describe DIS. At these energies, the term from the interaction vertex is no longer dominated by the W-Z gauge boson mass, resulting in an overall suppression with respect to the linear growth experienced in the previous energy regime. For $E_\nu > 10 \text{ PeV}$, the neutrino cross section can roughly be schematised as $\propto (E_\nu/1 \text{ GeV})^\alpha$ with $\alpha \sim 0.363$.

Taking into account the energy regime in which astrophysical neutrinos are produced and detected, a fundamental role is played by DIS processes.

In Figure 2 a generalised Feynman diagram is reported, paying particular attention to the kinematics of the process. The following Lorentz invariants can be derived:

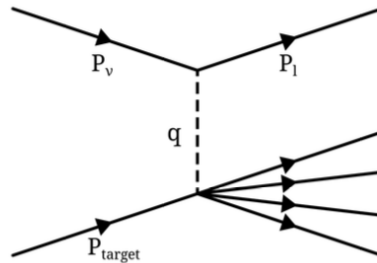


Figure 2: Feynman diagram of a generic neutrino-nucleon interaction, through NC or CC interaction. In the diagram the interacting particles are represented by their kinematic variables. Figure taken from [11].

$$s = (\mathbf{p}_\nu + \mathbf{p}_{\text{target}})^2 \quad (\text{centre of mass energy}), \quad (7)$$

$$Q^2 = -q^2 = -(\mathbf{p}_\nu - \mathbf{p}_l)^2 \quad (\text{four momentum transferred}), \quad (8)$$

$$y = \frac{\mathbf{q} \cdot \mathbf{p}_{\text{target}}}{\mathbf{p}_\nu \cdot \mathbf{p}_{\text{target}}} \quad (\text{inelasticity}), \quad (9)$$

$$x = \frac{Q^2}{2 \cdot \mathbf{p}_{\text{target}} \cdot \mathbf{q}} \quad (\text{Bjorken scaling variable}). \quad (10)$$

In the lab frame, where the target is at rest, the inelasticity or *Bjorken* y can be rewritten as

$$y = \frac{E_\nu - E_l}{E_\nu}, \quad (11)$$

where y represents the fraction of neutrino energy transferred to the target. The neutrino-nucleon inclusive cross section for DIS can be now described as a function of the two Bjorken invariants x and y :

$$\begin{aligned} \frac{d^2\sigma^{\nu,\bar{\nu}}}{dx dy} = & \frac{2G_F^2 m E_\nu}{\pi} \left(\frac{M_{W,Z}^2}{Q^2 + M_{W,Z}^2} \right)^2 \left[\frac{y^2}{2} 2x \cdot F_1(x, Q^2) \right. \\ & \left. + \left(1 - y - \frac{mxy}{2E} \right) \cdot F_2(x, Q^2) \pm y \left(1 - \frac{y}{2} \right) \cdot F_3(x, Q^2) \right], \quad (12) \end{aligned}$$

where m is the target mass, $G_F \sim 1.16 \cdot 10^{-5} \text{ GeV}^{-2}$ is the Fermi coupling constant, and the $+(-)$ sign in the last term refers to neutrino (antineutrino) interactions. Furthermore, $F_i(x, Q^2)$ with $i = 1, 2, 3$ are dimensionless nucleon structure functions. Assuming the nucleon constituted of quarks and gluons, the structure functions can be seen as sum of the probabilities, represented by the product $x \cdot q$ ($x \cdot \bar{q}$), to find a quark carrying a fraction of nucleon's momentum x :

$$F_2(x, Q^2) = 2 \sum [x \cdot q(x, Q^2) + x \cdot \bar{q}(x, Q^2)], \quad (13)$$

$$x \cdot F_3(x, Q^2) = 2 \sum [x \cdot q(x, Q^2) - x \cdot \bar{q}(x, Q^2)], \quad (14)$$

with the sum over all quark species. Trying to derive more quantitative estimates, the cross-section shown in Equation 12 can be integrated, for neutrino energies above 100 GeV, producing the following ratio:

$$\frac{\sigma_{CC}}{\sigma_{CC} + \sigma_{NC}} \approx 0.7. \quad (15)$$

This means that charged current interactions represents around the 70% of all the neutrino-nucleon interactions. Further quantitative estimates can be derived assuming that the four-momentum transferred (Q) is much smaller than the mass of the W^\pm boson and that the centre-of-mass energy s greatly exceeds the mass of the lepton.

Integrating the Bjorken variables out of the Equation 12, under the hypothesis of charged current interactions between neutrino and fermions

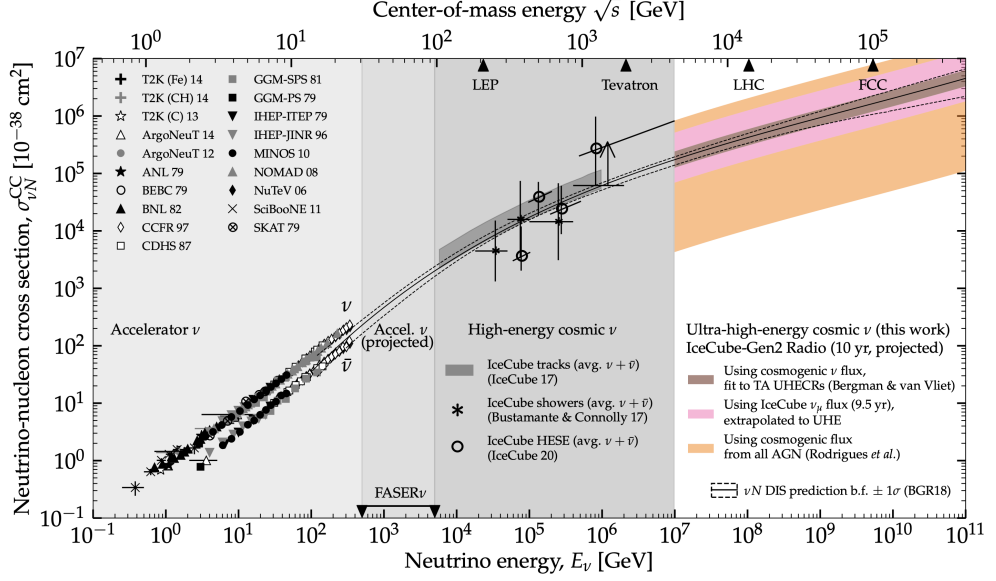


Figure 3: Neutrino-nucleon CC cross section for DIS. Experimental measurements are reported with points: sub-TeV are obtained from accelerator experiments, few-TeV will be covered by FASER ν experiment [12] and TeV-PeV measurements are reported thanks to astrophysical neutrinos detected by IceCube experiment. In the ultrahigh-energy domain (above 10^7 GeV), there are no measurements and predictions for next-generation radio detection experiments are reported. Figure taken from [13].

(equivalent to antineutrino-antifermion interactions), both the differential and total cross-section can be expressed as the following:

$$\frac{d\sigma_{CC}(\nu f)}{d\Omega} = \frac{G_F^2 s}{4\pi^2}, \quad \sigma_{CC}(\nu f) = \frac{G_F^2 s}{\pi}. \quad (16)$$

As explicitly written now in Equation 16, the cross section depends linearly on s . In the rest frame of the target, with mass m , the centre of mass energy can be approximated as $s \simeq 2m(m + E_\nu)$, highlighting the linear increase of the cross section with respect to the neutrino energy (E_ν) and to the mass of the target m . It also does not depend on the neutrino-target scattering angle in the centre of mass frame.

A similar simplification can be made for charged current interactions involving neutrino-antifermion (equivalent to antineutrino-fermion). Due to the properties of weak interaction, the initial state owes a total angular momentum $J = 1$, leading to a preferred direction along the interaction axis for outgoing particles. To take this into account, an additional factor $[1 + \cos(\theta^*)]^2$ is incorporated into the cross-section calculations. As a result, the differential and total cross-sections can now be reformulated in the following manner:

$$\frac{d\sigma_{CC}(\nu \bar{f})}{d\Omega} = \frac{G_F^2 s}{16\pi^2} [1 - \cos(\theta^*)]^2, \quad \sigma_{CC}(\nu \bar{f}) = \frac{G_F^2 s}{3\pi}. \quad (17)$$

Comparing the cross-sections reported in Equation 17 with respect to the one in Equation 16, the process $\bar{\nu} + f$ is suppressed by an overall factor

3 with respect to the process $\nu + f$, simply for helicity considerations. In Figure 3 is shown the behaviour of the total CC cross-section for the neutrino nucleon and the antineutrino nucleon at high energies, in which the dominant process is deep inelastic scattering [14].

1.1.1.2 Neutrino-electron interaction

Neutrinos can scatter on atomic electrons. The process is, however, suppressed over a wide range of energies due to target mass, that is three orders of magnitude smaller in this case with respect to nucleons.

In the energy region $E_\nu = 5.7 \div 7.0$ PeV, electron antineutrinos can resonantly scatter atomic electrons, producing a real W^- boson, following the process: $\bar{\nu}_e + e^- \rightarrow W^- \rightarrow X$ [15]. This process, peaked at 6.32 PeV (value resulting from the ratio $(M_W^2 - m_e^2)/2m_e$), is called *Glashow resonance* and was detected for the first time in 2021 by the IceCube Collaboration [16]².

The Standard Model integrated cross-section for the Glashow resonance process can be written as:

$$\sigma(s) = 24\pi \cdot \Gamma_W^2 \cdot B_{W^- \rightarrow \bar{\nu}_e + e^-} \cdot \frac{s/M_W^2}{(s - M_W^2)^2 + \Gamma_W^2 M_W^2}, \quad (18)$$

where $\Gamma_W = 2.09$ GeV is the W^- decay width and $B_{W^- \rightarrow \bar{\nu}_e + e^-}$ is the branching ratio. This production mechanism offers also a unique opportunity to directly measure the antineutrino fraction of astrophysical fluxes, constraining production mechanisms and the intensity of magnetic fields inside sources (see Section 1.1.3).

Recent studies by the KM3NeT Collaboration, exploiting simulated down-going fully contained shower events (for a detailed explanation of the topology, see Section 2.5), showed what would be the number of events generated by this process for two building blocks of the KM3NeT/ARCA telescope and fifteen years of observation, see Figure 4 [17].

1.1.2 Neutrino oscillations

An important implication for neutrino astrophysics is the phenomenon of neutrino oscillations. In the SM neutrinos are assumed to be massless. Due to evidence collected in the last ~ 30 years demonstrating neutrino oscillations, it is now established that neutrinos have a non-zero mass. To accommodate the small mass of neutrinos within the SM in a natural way, alternative mass production schemes have to be considered. This is also one of the main reasons why neutrinos are considered nowadays to be a privileged probe for physics beyond the SM. The existence of neutrino mass in the SM Lagrangian also opens up the possibility of transition between differ-

The hypothesis of neutrino oscillation was formulated for the first time by Pontecorvo in 1957, and developed few years later by Maki, Nakagawa and Sakata.

² An event of 6.05 ± 0.72 PeV was detected, with a significant probability ($> 5\sigma$ level) of having astrophysical origin. Taking into account the energy resolution of the IceCube detector, the probability that the event is produced off-resonance by deep inelastic scattering processes is at the level of 2.3σ .

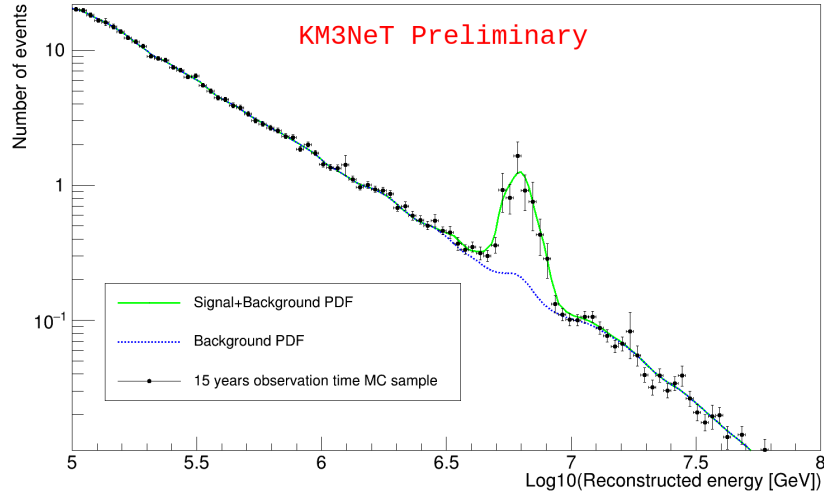


Figure 4: Reconstructed energy distribution for background (blue) and signal+background (green) events, for two building blocks of KM3NeT/ARCA after fifteen years of observation. Figure taken from [17].

ent flavour eigenstates, with the flavour lepton family number no longer conserved.

Specifically, neutrino flavour eigenstates can be written as a coherent superposition of mass eigenstates [18]:

$$|\nu_\alpha\rangle = \sum_k U_{\alpha k}^* |\nu_k\rangle, \quad \alpha = e, \mu, \tau \quad (19)$$

where $|\nu_k\rangle$ are the orthonormal massive neutrino states and $U_{\alpha k}$ is the mixing matrix, also known as *Pontecorvo-Maki-Nakagawa-Sakata* (PMNS) matrix [19][20].

A conventional unitary form for U is:

$$U = \begin{pmatrix} 1 & 0 & 0 \\ 0 & c_{23} & s_{23} \\ 0 & -s_{23} & c_{23} \end{pmatrix} \cdot \begin{pmatrix} c_{13} & 0 & e^{i\delta}s_{13} \\ 0 & 1 & 0 \\ -e^{i\delta}s_{13} & 0 & c_{13} \end{pmatrix} \cdot \begin{pmatrix} c_{12} & s_{12} & 0 \\ -s_{12} & c_{12} & 0 \\ 0 & 0 & 1 \end{pmatrix} \cdot \begin{pmatrix} e^{-i\frac{\alpha_1}{2}} & 0 & 0 \\ 0 & e^{i\frac{\alpha_1}{2}} & 0 \\ 0 & 0 & 1 \end{pmatrix}, \quad (20)$$

parameterised by three mixing angles θ_{ij} , and by three CP-violating phases δ , α_1 and α_2 . α_1 and α_2 are also known as Majorana phases and are nonzero only if neutrinos are Majorana particles: they have no analogue in the quark sector.

In Equation 19 no upper limit has been placed on the number of massive neutrino states. Measurements at LEP have constrained the number of active flavour neutrinos to three [5].

The massive neutrino states are by definition eigenstates of the vacuum Hamiltonian \mathcal{H} , with eigenvalue E_k , and can be written as solutions of the time-dependent Schrödinger equation:

$$i \frac{d}{dt} |\nu_k(t)\rangle = \mathcal{H} |\nu_k(t)\rangle. \quad (21)$$

At this point the time evolution of flavour eigenstates is given by:

$$|\nu_\alpha(t)\rangle = \sum_k U_{\alpha k}^* e^{-iE_k t} |\nu_k(t)\rangle. \quad (22)$$

Taking into account the initial conditions $|\nu_\alpha(t=0)\rangle = |\nu_\alpha\rangle$ and Equation 19, the evolved flavour eigenstate at a generic time t can be written as a function of the initial flavour eigenstate as follow:

$$|\nu_\alpha(t)\rangle = \sum_{\beta=e,\mu,\tau} \left(\sum_k U_{\alpha k}^* e^{-iE_k t} U_{\beta k} \right) |\nu_\beta\rangle. \quad (23)$$

The transition probability $\nu_\alpha \rightarrow \nu_\beta$, as a function of time can be written in the form:

$$\begin{aligned} P_{\nu_\alpha \rightarrow \nu_\beta}(t) &= |A_{\nu_\alpha \rightarrow \nu_\beta}|^2 = |\langle \nu_\beta | \nu_\alpha(t) \rangle|^2 \\ &= \sum_{k,j} U_{\alpha k}^* U_{\beta k} U_{\alpha j} U_{\beta j}^* e^{-i(E_k - E_j)t}. \end{aligned} \quad (24)$$

The neutrino mass enters through energy equation: $E_k = \sqrt{p^2 c^2 + m_k^2 c^4} \sim pc + \frac{m_k^2 c^4}{2E}$. The difference $E_k - E_j$ in Equation 24, can be written in the form $\sim \frac{\Delta m_{kj}^2}{2E}$. Furthermore, replacing the propagation time with the distance between the source and detector L ($t = L$ in natural units) leads to the following:

$$P_{\nu_\alpha \rightarrow \nu_\beta}(L, E) = \sum_{k,j} U_{\alpha k}^* U_{\beta k} U_{\alpha j} U_{\beta j}^* \exp\left(-i \frac{\Delta m_{kj}^2 L}{2E}\right). \quad (25)$$

Note the dependence of the transition probability on the ratio L/E and on the squared mass difference. In other words, neutrino oscillation experiments are sensitive to Δm_{ij}^2 but not to the absolute mass. Furthermore, since $\Delta m_{32}^2 + \Delta m_{21}^2 = \Delta m_{31}^2$, there are only two independent Δm_{ij}^2 , if only three neutrino mass states exist. The problem of figuring out the sequence of massive neutrino states is known as *neutrino mass hierarchy* and is among the main physics goals of many experiments under construction now (DUNE, Hyper-K, JUNO and KM3NeT/ORCA).

1.1.3 Oscillations over astronomical distances

Astrophysical accelerators produce neutrinos that can propagate undisturbed along baselines of the order of kpc-Gpc. Neglecting matter effects, the vac- $1 \text{ pc} = 3.086 \cdot 10^{18} \text{ cm}$

uum oscillation paradigm described in Section 1.1.2 can be applied [21]. Taking the limit for $L \rightarrow \infty$, Equation 24 can be rewritten as $P_{\nu_\alpha \rightarrow \nu_\beta}(L \rightarrow \infty, E) = \sum_k |U_{\alpha k}|^2 |U_{\beta k}|^2$, considering the vanishing of the cosine and sine terms derived from the exponential, once averaged over the limit $L \rightarrow \infty$. Therefore, the cosmic neutrino flux at the detector level can be expressed as a product of a constant matrix P and the neutrino flux at the source, $\phi^0(\nu_i)$, where P can be written as

$$P = \begin{pmatrix} P_{ee} & P_{e\mu} & P_{e\tau} \\ P_{e\mu} & P_{\mu\mu} & P_{\mu\tau} \\ P_{e\tau} & P_{\mu\tau} & P_{\tau\tau} \end{pmatrix} \approx \begin{pmatrix} 0.55 & 0.25 & 0.20 \\ 0.25 & 0.37 & 0.38 \\ 0.20 & 0.38 & 0.42 \end{pmatrix}. \quad (26)$$

The numerical approximation is derived by inserting the most updated values of the mixing angles. The averaging operation over astronomical distances restores the CP-invariance. Taking into account possible different production astrophysical environments, the flux ratio at the source can be written in the form $\nu_e : \nu_\mu : \nu_\tau = 1 : n : 0$, assuming ν_τ production to be very unlikely.

In the "standard" scenario, neutrinos are produced by charged pion decay chain (for more details see Section 1.3.1) and the energy integrated flux ratio produces $n = 2$. There are also scenarios that require extreme astrophysical conditions to be accomplished, in which $n = \infty$, such as thick source environments where muons lose energy before decaying, or $n = 0$ where only ν_e are produced, likely in neutron sources. The flavour composition at the source can be inferred from the measured flavour ratio on Earth simply by inverting the probability matrix P of Equation 26.

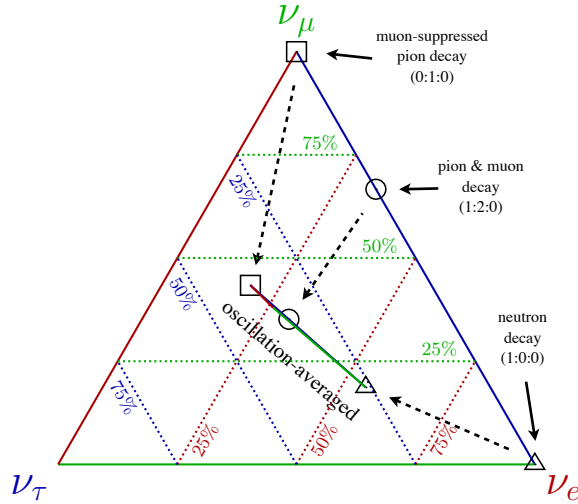


Figure 5: Neutrino flavour triangle. Points for the three specific scenarios described in the text ($n=0,2,\infty$) are shown with, respectively, triangular, circular and square markers. The flavour ratio in these three scenarios is also shown with the dashed arrows, after oscillation averaging over astrophysical distances. Figure taken from [22].

Usually, the flavour ratio is expressed via the *neutrino flavour triangle*, shown in Figure 5. The diagram shows the flavour composition, considering the fraction of each neutrino flavour proportional to the distance from the side of the triangle opposite to the vertex for that flavour. In this scenario the direct observation of astrophysical tau neutrinos is fundamental: the non observation of ν_τ would have consequences on neutrino oscillation paradigm and neutrino astronomy [23]. For more details on the detection principle of tau neutrinos, see Section 2.5.

1.2 COSMIC RAYS

Primary Cosmic Rays (CRs) are stable ionised nuclei that originate in astrophysical environments and hit the upper part of the Earth atmosphere at a rate of about 1000 per square metre per second. They consist mainly of protons and alpha particles, and a smaller fraction of heavy nuclei and electrons. Primary CRs can interact near the source region, producing secondary neutral particles like γ -rays and neutrinos that can arrive at Earth together with primary CRs, and providing important information: both these two messengers are electrically neutral and can travel undeflected by magnetic fields. Antiparticles are also present in cosmic radiation, usually antiprotons and positrons, but in most cases they originate during the propagation of primary CRs and electrons. All secondary particles produced far from the acceleration sites, during propagation or in interaction with the Earth atmosphere, are referred to as *secondary cosmic rays*. Despite advances in the field over the past century, there are still fundamental questions that have to be addressed concerning the sources and origin as well as the possible acceleration mechanisms capable of accelerating particles up to very high energies. ³

1.2.1 Cosmic ray energy spectrum

The principal information that can be collected about cosmic rays are: the relative abundances of the different nuclei, also referred to as CRs composition, the energy distribution of each nuclear species, and their arrival direction. From the comparison of the CR composition measured at Earth with respect to those measured in various astrophysical objects, such as the Sun, the interstellar medium, or neutron stars, important information about the acceleration sites and propagation of CRs can be derived. In Figure 6

³ **Historical note:** the first experiments trying to address the origin of the "mysterious" ionisation measured with electroscopes were conducted in 1909 by T. Wulf on top of the Eiffel Tower and by K. Bergwitz exploiting balloons. The final answer to the question was given in 1912 by V. Hess, whose balloon flights reached an altitude of 5200 metres. The collected observations pointed to an increase in the ionisation with height, supporting the hypothesis that their origin was caused by radiation coming from space. Open questions about the nature of this radiation were still present at that time. Thanks to the idea of B. Rossi, formulated in 1930 of an "East West" modulation of CRs flux, it was possible to confirm that CRs have in average a positive electric charge, excluding the γ -ray hypothesis.

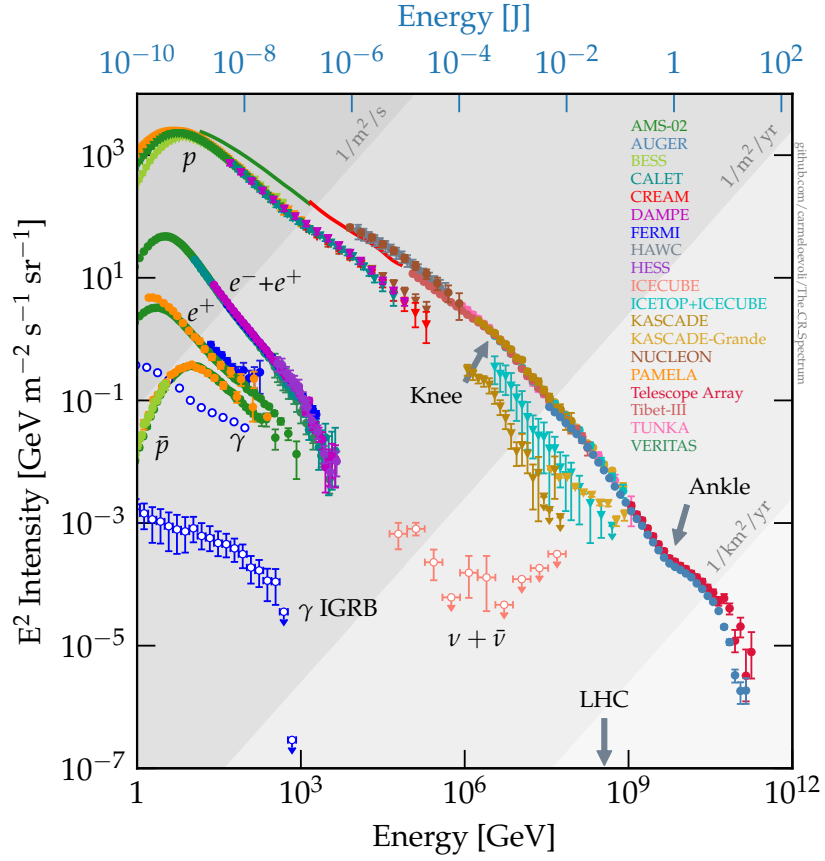


Figure 6: CRs differential energy spectrum, measured from multiple experiments. The spectrum is remarkable for being continuous over the whole energy interval. Figure taken from [24].

the *all-particle* CR energy spectrum is shown. The flux ranges from MeV to 10^{20} eV and is generally modelled by assuming a broken power law of the form [25]:

$$\left[\frac{dN_p}{dE} \right]_{\text{obs}} = K \cdot E^{-\alpha} \quad (\text{GeV}^{-1} \text{cm}^{-2} \text{s}^{-1} \text{sr}^{-1}). \quad (27)$$

Fitting the all-particle spectrum with the power law of Equation 27, four different regions can be identified:

- below 10 GeV the spectrum is modified due to solar modulation;
- from 10 GeV to 1 PeV (10^{15} eV) the spectral index $\alpha=2.7$;
- from 10 PeV to 1 EeV (10^{18} eV) $\alpha=3.1$;
- above 10 EeV the spectrum flattens again to $\alpha \sim 2.6$, with a further cutoff around 10^{20} eV.

The transition regions from one regime to the subsequent one are denominated, respectively: the "knee" (~ 3 PeV) and the "ankle" (~ 3 EeV). These

features in the CR flux have been explained by postulating different populations of CRs: the "knee" is considered to be the end of the spectrum of Galactic cosmic rays, while the "ankle" is associated with the emergence of the extra-Galactic CR population.

1.2.2 Composition of cosmic rays

In the energy range below the knee, the composition of CRs has been measured with high precision directly with balloons or satellite experiments. In Figure 7 the comparison between the CRs and the Solar System abundances is reported. The two samples show an impressive similarity with a differ-

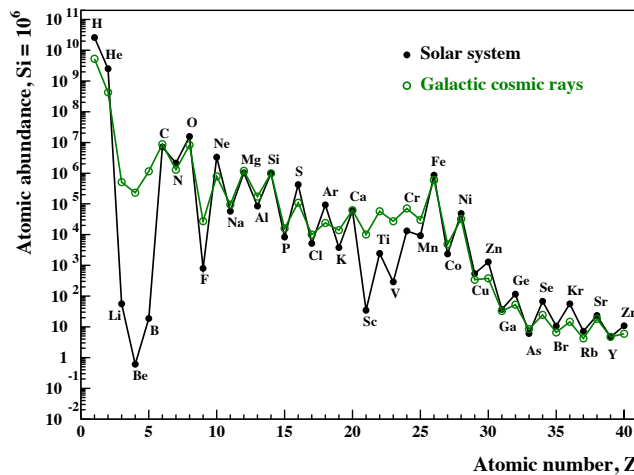


Figure 7: Relative abundances of Galactic cosmic rays measured at Earth (green), and the elemental abundances within the Solar System (black), normalised to $10^6 \cdot \text{Si}$ atoms. Figure taken from [26].

ence lower than 20% in most of the cases. They also show the odd-even effect, reflecting the same trend observed in the nuclear binding energy curve. A simple conclusion that can be derived from Figure 7 is that CRs reaching the Earth are sampled from a region with the same chemical composition as the Solar System.

However, a striking difference is observed between the two groups *Li, Be, B* and *Sc, Ti, V, Cr, Mn*: they are around five orders of magnitude more abundant in CRs than what has been measured in the Solar System. It has been interpreted as the effect of propagation of primary CRs in the Galaxy. These elements are, in fact, almost absent at the end of the life of stellar nucleosynthesis, whereas they can be produced through fragmentation reactions of higher-mass elements, like carbon, nitrogen, oxygen, or iron during their propagation towards the Earth. Exploiting also the knowledge of spallation cross-sections of the relevant nuclei, from fixed target experiments on Earth, important information on CR propagation inside our Galaxy can be derived, like, for example, the amount of matter traversed. Note also for the progress of this chapter that neutrinos, photons, and antiprotons are also produced as secondary products of this fragmentation reaction.

Considering the mean density of matter in the Galactic disk, ~ 1 proton/cm³, the derived estimate of the thickness of the material traversed by CRs is around 1 Mpc, much greater than the half-thickness of the disk of the Galaxy (0.1 kpc). This means that CRs are confined inside the Galaxy in a diffusive process and are trapped for more than $3 \cdot 10^6$ years before they can escape into intergalactic space. The values obtained refer to the bulk of CRs without any specific energy assumption. Since the Larmor radius R_L of a particle with energy E , moving in a magnetic field B is: $R_L \approx \frac{E}{eZB}$, the escape time decreases with the particle energy. Simulations of the trajectories of CRs with different energies inside the Galactic magnetic fields can be seen in Figure 8.

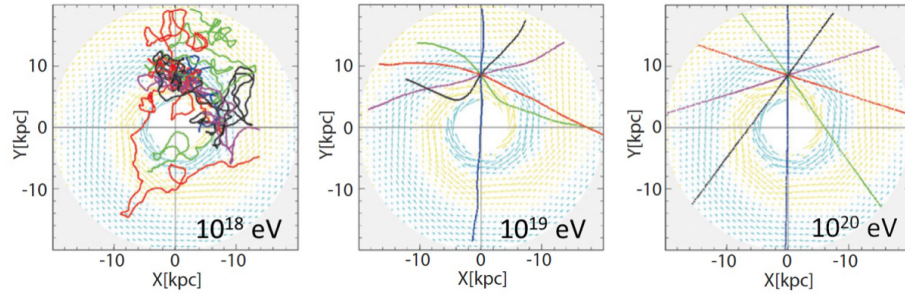


Figure 8: Simulated trajectory of CRs in the Galactic magnetic field. The three different energy regimes are chosen to highlight how CRs at energies $\sim 10^{19}$ eV travel along almost straight lines and are not trapped inside the Galaxy.

Another important consequence of the long time that CRs remain trapped inside our Galaxy is that the spectrum measured at Earth can be factorised into two independent terms: one regarding the acceleration at the source and another one accounting for the propagation inside our Galaxy. Above $\sim 10^{14}$ eV, CR measurements are only accessible from ground detectors, capable of instrumenting a large area and detecting secondary particles contained in the shower, generated by the interaction of primary CRs with nuclei in the atmosphere. The difficulties related to these indirect measurements still cause uncertainty about the precise determination of the chemical composition of CRs. For this reason, in Figure 6 the CR spectrum is summed over all possible mass numbers of primary CRs, resulting in the *all-particle* energy spectrum.

1.2.3 Galactic cosmic ray acceleration: diffusive shock acceleration

The first attempt to describe the mechanism capable of accelerating CRs was proposed by E. Fermi in 1949, pointing to astrophysical environments with strong inhomogeneous magnetic fields. The idea was based on the fact that the interstellar medium is filled with "clouds" of ionised gas, which can in principle reflect charged particles. Considering a relativistic regime, Lorentz transformations have to be applied to go from a reference frame S ,

the one of the observer, to the reference S' , the one where the shock wave or the magnetised cloud is at rest. Applying the transformations iteratively, for each collision, the final energy of the particle in the observer frame can be written in the form:

$$E^* \sim \left(1 + 2 \frac{Uv}{c^2} \cos\theta + 2 \frac{U^2}{c^2} \right) \cdot E, \quad (28)$$

where U is the velocity of the cloud in the S frame. The second term is equal to zero when averaged over all possible directions and the energy gained $\Delta E \propto (U/c)^2$ (*second-order Fermi mechanism*). When considering realistic cases, this kind of mechanism turns out to be inefficient.

Looking more deeply into Equation 28, energy could be efficiently gained when $\cos\theta > 0$, for the so-called *head-on* collisions but lost for *catching* collisions ($\cos\theta < 0$). Assuming an astrophysical environment in which only head-on collisions occur, the quadratic term in U can be neglected, being $U/c \ll 1$, $v \sim c$ being in an ultra-relativistic regime, obtaining an energy gain $\Delta E \propto U/c$.

Astrophysical shocks, existing everywhere in the Universe, are capable to provide such a kind of environment: for this reason, the mechanism is also known as *Diffusive Shock Acceleration (DSA)* or *first-order Fermi mechanism*.

Shocks, which can be defined as regions where the mean plasma velocity changes, have already been demonstrated to be a site of particle acceleration due to the detection of photons, from radio to γ -ray frequencies, generated by electrons of non-thermal origin. The main characteristic of this kind of environment is that astrophysical shock waves are, in most cases, *collisionless*, in the sense that energy dissipation processes do not take place through particle collisions or Coulombian interactions. Considering now

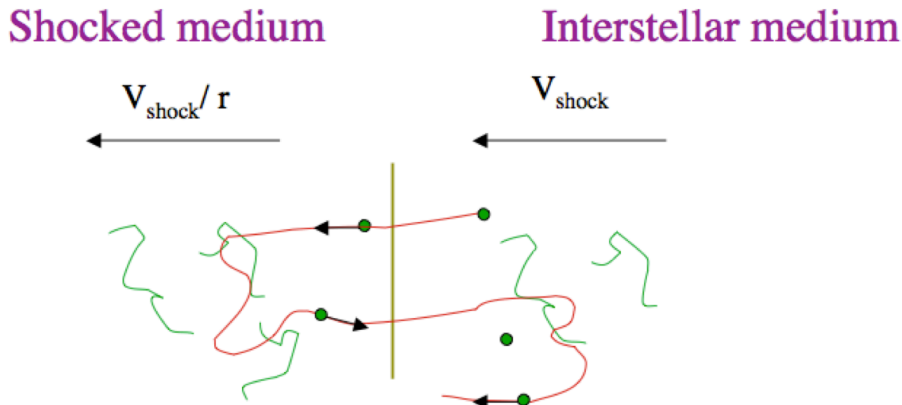


Figure 9: Schematic representation of an acceleration cycle of the DSA mechanism. The particle from the upstream region (interstellar medium) passes through the shock in the downstream region. Figure taken from [27].

a shock wave propagating through the interstellar medium, an upstream (space ahead of the shock that has not yet been shocked) and downstream (space already shocked) regions can be distinguished. The shock itself can

be seen as a discontinuity between upstream and downstream, in which the mass, momentum flux, and energy must be conserved. In the shock frame, the upstream medium approaches the shock with a velocity v_1 equal to the shock velocity v_{sh} . When passing through the shock, the gas slows down and moves away from the shock with a velocity $v_2 = v_1/r = v_{sh}/r$. r is defined as the proportional constant that links the upstream and downstream densities ($\rho_2 = r\rho_1$), and in the case of strong shocks, it can be approximated as $r \approx \frac{\gamma_\alpha + 1}{\gamma_\alpha - 1}$. For a monatomic gas $\gamma_\alpha = 5/3$ and therefore $r = 4$. Assuming that the upstream and downstream media are magnetised, a particle coming from the upstream medium passes through the shock and sees the downstream medium as a "magnetic cloud" approaching it. Taking into account a parallel shock, whose propagation direction is along the magnetic field lines, particles sufficiently energetic are consequently able to pass freely between the upstream and downstream regions several times. The main difference with respect to the configuration originally proposed by Fermi is that now all collisions will be head-on.

The energy threshold for passing through the shock can be considered as the limit where the particle Larmor radius is much larger than the thickness of the shock front.

Now, averaging $\cos\theta$ over the range $[-\pi/2, \pi/2]$, in which only head-on collisions occur, from equation 28 the energy can be written as:

$$\langle E^* \rangle = \left(1 + \frac{4U}{3c}\right) \langle E \rangle \equiv (1+k) \langle E \rangle. \quad (29)$$

The limiting factor to the maximum reachable energy is represented by the number of cycles upstream→downstream→upstream a particle can undergo. In fact, in this scenario, there is the possibility for a particle to escape from the acceleration region, remaining trapped inside the source. In the downstream region, the accelerated particle sees the shock front going away with velocity v_2 . Instead, in the upstream region, assumed in this approximation to be infinite, diffusion over an infinite amount of time will lead the probability of a particle to come back to the shock to be equal to 1. If the mechanism is *efficient*, the escaping probability P_{esc} is small and can be calculated, using diffusion theory, simply as

$$P_{esc} = \frac{\phi_{esc}}{\phi_{ud}}, \quad (30)$$

where ϕ_{esc} is the escaping flux of particles from downstream region, and ϕ_{ud} is the number of particles passing from upstream to downstream region.

The probability that a particle remains inside the acceleration region after n collisions is $(1-P_{esc})^n$, and starting with N_0 particles with initial energy E_0 , after n collisions there will be:

$$N = N_0(1 - P_{esc})^n \quad \text{particles with energy } \geq E = E_0(1+k)^n. \quad (31)$$

Removing the n parameter from previous equation:

$$\frac{\ln(N/N_0)}{\ln(E/E_0)} = \frac{\ln(1 - P_{esc})}{\ln(1+k)}, \quad (32)$$

the power law is obtained:

$$\frac{N(\geq E)}{N_0} = \left(\frac{E}{E_0} \right)^{\ln(1-P_{esc})/\ln(1+k)} \quad (33)$$

Since the shock is non-relativistic, $\beta \ll 1$, $P_{esc} \ll 1$, $k \ll 1$ and Equation 33 can be rewritten as:

$$\frac{N(\geq E)}{N_0} = \left(\frac{E}{E_0} \right)^{-\frac{P_{esc}}{k}} \quad (34)$$

Now, the number of particles $n(E)$, with energy between E and $E + dE$ can be derived:

$$n(E) = \left| \frac{dN(\geq E)}{dE} \right| = (\alpha_{CR} - 1) \frac{N_0}{E_0} \left(\frac{E}{E_0} \right)^{-\alpha_{CR}}, \quad \alpha_{CR} = \frac{r+2}{r-1} \quad (35)$$

Equation 35 shows the required power law, and, in case of monatomic gas and strong shocks ($r=4$, see text above), the spectral index $\alpha_{CR} = 2$ is obtained, function only of the compression ratio r .

The maximum obtainable energy from this kind of mechanism can be derived considering the finite spatial extension and the finite activity duration of the acceleration region. Taking, for example, $B = 100 \mu\text{ G}$ and $L_{source} = 1\text{ pc}$, the maximum energy E_{max}^{size} can be estimated such that the Larmor radius $= L_{source}$. With these parameters, one gets $E_{max}^{size} \approx Z \cdot 10^{17}\text{ eV}$. This is the same argument used by Hillas to derive the famous *Hillas diagram* [28], showing the maximum energy achievable within sources based on their magnetic field and their extension, for CRs with $E > 10^{18}\text{ eV}$. A more precise estimate can be derived, taking into account diffusion in the upstream and downstream regions. It can be shown that the typical distance from the shock, to which a particle can reach, is $L_{diff} \approx \frac{D(E)}{v_{sh}}$. When the value of L_{diff} is on the order of the spatial extension of the magnetised region upstream, the particle escapes from the source. The maximum energy can now be defined as $L_{diff}(E_{max}^{conf}) = L_{up}$. Particles with energy greater than E_{max}^{conf} will escape efficiently upstream rather than recross the shock, and they will propagate through the ISM. They are just the CRs detected on Earth. Assuming the typical parameters for a supernova remnant, a maximum energy of $E_{max}^{conf} \approx Z \cdot 3 \cdot 10^{14}\text{ eV}$ can be derived, much smaller than the estimate derived simply assuming Hillas criteria and just corresponding to the *knee* of the CR spectrum. This also produces a different cutoff for each nuclear species, resulting in a proton-rich spectrum before the knee and iron-rich after, depicted schematically in Figure 10. However, there are still some uncertainties about the nature of the knee in the CR spectrum.

The apparent tension of the result obtained above ($\alpha_{CR} = 2.0$) with respect to the spectral index measured below the knee at Earth ($\alpha = 2.7$) can be solved considering the Galactic diffusion of CRs. For a more complete treatment, see Section 5.1.3. The diffusion effects can be encoded into an energy-dependent diffusion probability P , measured experimentally through the ratio between light isotopes (Li, Be, B); see Figure 7. It was

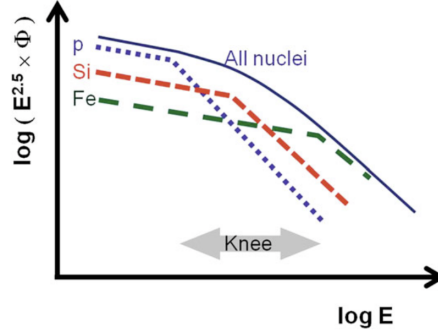


Figure 10: Schematic representation of CR knee. Figure taken from [29].

found $P(E) \propto E^{\alpha_D}$, with $\alpha_D = 0.6$. The final differential flux of CRs at the source can now be estimated to be:

$$\left[\frac{dN_p}{dE} \right]_{\text{source}} \propto \left[\frac{dN_p}{dE} \right]_{\text{obs}} \cdot P(E) \propto E^{-\alpha} \cdot E^{\alpha_D} \propto E^{-\alpha_{CR}}. \quad (36)$$

1.2.4 Breakthrough discovery: Pevatrons

In May 2021 the LHAASO Collaboration announced the first detection of 12 Galactic γ -ray sources well above $E > 100$ TeV with significance $> 7\sigma$ and maximum energy up to 1.4 PeV, therefore called *Pevatrons* [30]. Recently, in May 2023, the LHAASO Collaboration also released the first catalogue, collected with a data set from January 2021 to September 2023, in which 43 sources have been detected with energies greater than 100 TeV, with a significance $> 4\sigma$ [31]. This catalogue complements and expands already detected very high-energy (VHE) sources measured by HAWK in 5 years of observation [32]. The importance of this discovery lies in the fact that ultrahigh-energy (UHE, $E > 100$ TeV) γ -ray photons were considered unquestionable evidence of accelerated Galactic CRs. At these very high energies, the inverse Compton is highly limited by the Klein-Nishina regime, and the only possible mechanism to produce such high-energy photons was believed to be through neutral pion decay, produced in interaction of CRs with the source matter. Another signature of π^0 decay and the subsequent acceleration of CRs is the "pion bump" at about 100 MeV (peak corresponding to the rest mass of the pion itself). Supernova Remnants (SNRs), according to the standard paradigm, are the main contributors to Galactic CRs, and this was confirmed by the Fermi-LAT and AGILE satellite that detected the pion bump [33]. Unfortunately, no association between Pevatrons and known SNRs has been found up to now. This supports the possibility that another source population can accelerate UHECRs. The sources that have been detected producing this high-energy photon flux are Massive Star Clusters (MSCs) with a high star formation rate, Pulsar Wind Nebulae (PWNe), such as the Crab Nebula, with photons $E > 150$ TeV. In particular, PWNe were believed to be leptonic accelerators, but this detection

The inverse Compton scattering losses are dominant for electrons with energies $> \text{GeV}$ s. This approximation is valid in the Thomson regime, when $4E\epsilon/(m_e c^2)^2 \ll 1$, with ϵ the energy of the target photon. A broader formulation for the electron-photon scattering was derived by Klein and Nishina (1929) and valid up to higher energies. The main effect on the IC cross-section, entering in the Klein-Nishina regime, is an overall suppression compared to the Thompson regime.

leaves open the possibility for this kind of source to accelerate hadrons and, consequently, CRs. The DSA theory alone could not explain the energies reached by CRs inside environments such as PWNe. Other mechanisms such as magnetic reconnection or similar alternatives need to take place. Simulations of this second kind of mechanism suggest that it could produce impulsive events (flares), but it is not capable of maintaining stable VHE emission. In this scenario, neutrino detection remains the fundamental channel for disentangle the two different γ -ray emission scenarios.

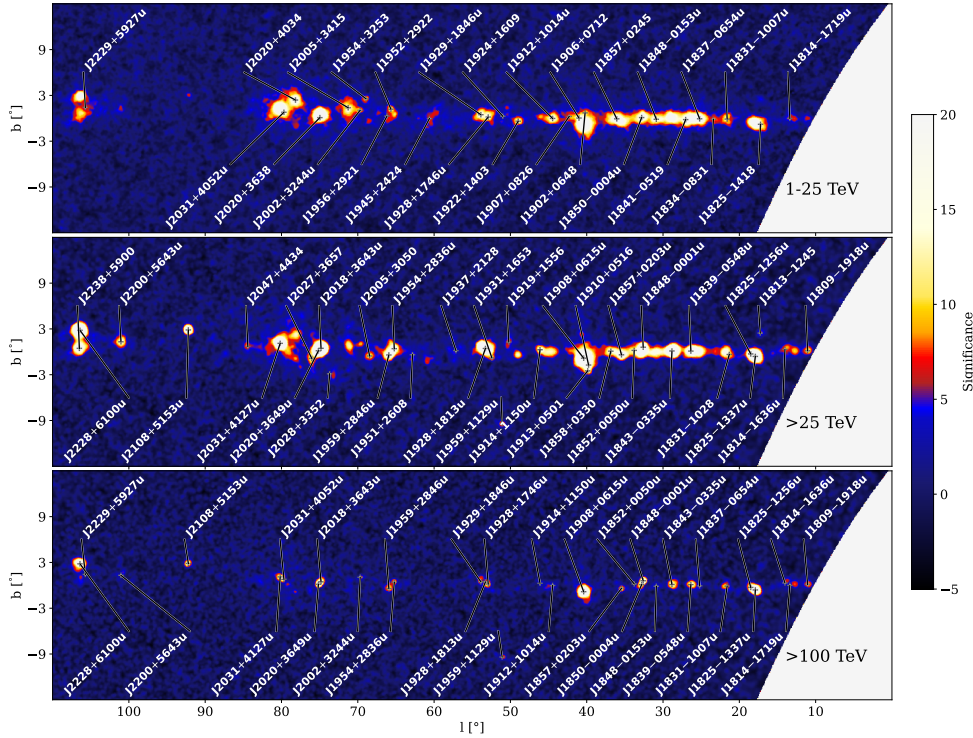


Figure 11: LHAASO significance map within region $10^\circ \leq l \leq 115^\circ$, $|b| \leq 12^\circ$. **Top:** WCDA ($1 \text{ TeV} < E < 25 \text{ TeV}$) significance map. **Middle:** KM2A ($E > 25 \text{ TeV}$) significance map. **Bottom:** KM2A ($E > 100 \text{ TeV}$) significance map (WCDA and KM2A are different sub-detectors within LHAASO). Figure taken from [31].

1.2.5 Acceleration mechanisms above the knee

While there is general agreement on the mechanism that can accelerate CRs up to the knee, the nature and mechanisms responsible for the acceleration of CRs up to 10^{20} eV are still widely debated. In any case, considering the energies at which CRs are accelerated, they exhibit a Larmor radius much larger than the size of our Galaxy. For this reason, it is commonly believed that these CRs are of extra-Galactic origin. The transition between Galactic and extra-Galactic CRs then occurs somewhere between the knee and the ankle, also taking into account the change in the chemical composition of the CRs, responsible for the complex substructure of the knee, as already de-

scribed and shown in Figure 10. Composition studies support this scenario, but heavy nuclei cannot easily account for all CR in the energy range 1-100 PeV, and a further population of protons may be needed. Proton acceleration in the energy range 1-100 PeV is pushing the DSA theory in SNRs to its limits. The idea is therefore focused on the possibility that already accelerated CRs will suffer an additional acceleration, called *one-shot reacceleration*. This occurs when a particle is continuously accelerated by an ordered field. These strong fields can be found in relativistic jets of Active Galactic Nuclei (AGNs) or in neutron stars with strong variable magnetic fields. On the basis of energy budget and luminosity arguments, Gamma-Ray Bursts (GRBs), Tidal Disruption Events (TDEs), and AGNs have been suggested as possible sources of particle acceleration up to 10^{20} eV. For example, from simple dimensional arguments, the maximum energy available from a pulsar can be derived [29]:

$$\frac{\mathcal{E}}{R_{\text{pulsar}}} = \frac{1}{c} \frac{dB}{dt}, \quad (37)$$

$$E^{\text{max}} = \int Ze\mathcal{E}dx = \int Ze \frac{R_{\text{pulsar}}}{c} \frac{dx}{dt} dB = ZeR_{\text{pulsar}}B \frac{\omega_{\text{pulsar}} R_{\text{pulsar}}}{c}. \quad (38)$$

with \mathcal{E} and B respectively the electric and magnetic fields. Replacing the estimated values for the pulsar angular velocity ω_{pulsar} and radius R_{pulsar} :

$$E^{\text{max}} \sim 5 \cdot 10^6 \text{ erg} \sim 3 \cdot 10^{18} \text{ eV}. \quad (39)$$

Even if a small part of the total rotational energy of a single pulsar can be used to generate the power required from the CR flux in the energy range knee - 10^{18} eV, theoretical details on the mechanisms are still not known. Another example of a model that attempts to explain the acceleration of UHECRs through AGNs is the so-called *espresso mechanism* [34]. In this scenario, CR accelerated through the DSA mechanism up to 10^{17} eV within SNRs can then penetrate into a relativistic jet and receive a one-shot boost in energy, proportional to Γ^2 , where Γ is the Lorentz factor of the relativistic flow. With $\Gamma \geq 30$, as observed in some of the most powerful blazars, a single espresso shot may be sufficient to boost CRs to the highest energies. In addition, the energy injection rate required to maintain the flux of UHECRs is consistent with the AGN density observed.

1.2.6 GZK cut-off

With the discovery of the *Cosmic Microwave Background* (CMB) in 1966 independently, G. Zatsepin, V. Kuz'min [35], and K. Greisen [36] hypothesised the suppression of the UHECR flux due to the resonant production of pions in the interaction of protons with the CMB, through the following processes:

$$p^+ + \gamma_{\text{cmb}} \rightarrow \Delta^+ \rightarrow n + \pi^+, \quad (40)$$

$$\Delta^+ \rightarrow p^+ + \pi^0. \quad (41)$$

Pulsar is a rotating neutron star that emits a beam of electromagnetic radiation, typically along its magnetic axis. The typical angular velocity and magnetic field of this object are: $\omega_{\text{pulsar}} = 12500 \text{ rad/s}$, $B_{\text{pulsar}} \sim 10^{12} \text{ G}$. Nowadays more than 2600 pulsars are known.

The neutral pions decay into gammas, whereas the charged pions decay mainly into $\mu^+ + \nu$. The neutron decay in $p + e + \bar{\nu}_e$ producing in all possible final states just a proton with reduced energy compared to the initial one, due to the simultaneous pion production. The final effect is therefore the suppression of the proton flux for energies above $E \sim 5 \cdot 10^{19}$ eV. This suppression is also known as the *GZK cutoff*. The *energy loss length* can be evaluated as $l_{p\gamma} = \langle y \sigma_{p\gamma} n_\gamma \rangle^{-1} = 30$ Mpc, where y is the Bjorken variable. Protons that originated at distances greater than ~ 30 Mpc from Earth are energy suppressed because of this effect. The estimate of the chemical com-

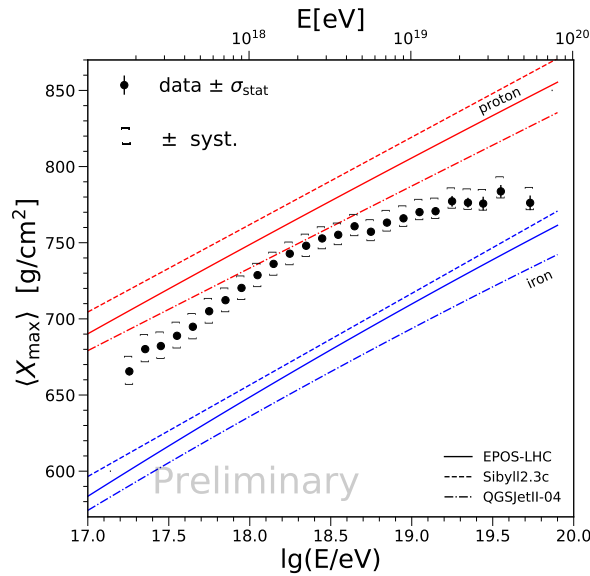


Figure 12: Mass composition measurements of primary CR flux performed by Pierre Auger Observatory, through determination of the depth of the maximum development of air shower (X_{\max}). Figure taken from [37].

position of CRs, even at such high energies, is fundamental to confirm the existence of the GZK cutoff. In fact, for heavy nuclei, with mass number A and energy E , resonance production occurs through the interaction of a nucleon of energy E/A with the CMB. Therefore, the energy threshold for heavier nuclei is a factor A greater than the one for protons, and it cannot explain the features observed in the primary CR spectrum. One experiment, the Pierre Auger Observatory (PAO), has already reported some interesting results [38], capable of partially shedding light on the composition of CRs in the most energetic part of their spectrum, but better resolution and improvements are expected in the near future.

1.2.7 Atmospheric neutrinos

Neutrinos and muons are generated through the interaction of primary cosmic rays with nuclei in the atmosphere. As a result, they are commonly referred to as *atmospheric neutrinos* and *atmospheric muons*. This last component is the most abundant one at sea level because of the small energy

losses of muons and their relatively long lifetime. The complete description of the cascade development, starting from the CR interaction, is done through dedicated Monte Carlo and numerical simulations. Assuming that the primary CR spectrum, impinging on Earth, follows a single power law with spectral index α , the corresponding neutrino spectra roughly can be approximated as:

$$\Phi_{\nu}^{\text{atmo}}(E) \propto E^{-\alpha-1}. \quad (42)$$

High-energy neutrinos are produced together with muons, mainly in the two-body decay of charged pions and kaons generated in hadronic interactions. Neutrinos are also produced in muon decay, a dominant process, especially at low energy. The full decay chain for atmospheric neutrino production can be schematised as follows:

$$p + N \rightarrow \pi^{\pm}(K^{\pm}) + \text{others}, \quad (43)$$

with N generic nucleon. The most important channels and their branching ratios for neutrino productions are:

$$\pi^{\pm} \rightarrow \mu^{\pm} + \nu_{\mu}(\bar{\nu}_{\mu})(\sim 100\%), \quad (44)$$

$$K^{\pm} \rightarrow \mu^{\pm} + \nu_{\mu}(\bar{\nu}_{\mu})(\sim 63.5\%). \quad (45)$$

In turn, the muon, with a lifetime of $\sim 2.2 \cdot 10^{-6}$ s, decays:

$$\mu^{\pm} \rightarrow e^{\pm} + \bar{\nu}_{\mu}(\nu_{\mu}) + \nu_e(\bar{\nu}_e). \quad (46)$$

The kinematics of the processes is such that, roughly, each neutrino in the chain carries the same energy. In this "standard" scenario, the production rate follows the ratio $\nu_e : \nu_{\mu} : \nu_{\tau} = 1 : 2 : 0$. Complications to this scheme arise when the muon decay length becomes larger than the typical production height in the atmosphere (~ 15 km), occurring for E_{μ} more than 2.5 GeV. The ν_e/ν_{μ} ratio rapidly decrease with energy, such that at high energy the only channel contributing to atmospheric ν_e production is the K_L^0 and K^{\pm} decay ($K_L^0 \rightarrow \pi + e + \nu_e$ and $K^{\pm} \rightarrow \pi^0 + e + \nu_e$). Following kinematical considerations for 2-body decay, limits on the lab energies of the secondary particles can be derived:

$$\frac{m_{\mu}^2}{M^2} \cdot E \leq E_{\mu} \leq E \quad \text{and} \quad 0 \leq E_{\nu} \leq \left(1 - \frac{m_{\mu}^2}{M^2}\right), \quad (47)$$

for respectively atmospheric muons and neutrinos, with E corresponding to the lab energy of the decaying meson and M its mass. Numerically

$$\langle E_{\mu} \rangle / E_{\pi} = 0.79 \quad \text{and} \quad \langle E_{\nu} \rangle / E_{\pi} = 0.21, \quad (48)$$

while for kaon decay the numbers are respectively 0.52 and 0.48. The numbers suggest that the contribution of charged pions to neutrinos is suppressed at high energy with respect to their contribution to muon fluxes.

The importance of kaon decay and the details of its production are of great importance for precise flux calculations, especially for atmospheric ν_e .

At sufficiently high energies, another production mechanism is possible. The so-called prompt emission of atmospheric neutrinos is taking place in semi-leptonic decays of charmed mesons, like D^\pm , D^0 and baryons. Taking into account the very short lifetime of charmed particles ($\sim 10^{-12}$ s), muons and neutrinos are produced before the parent meson loses energy in collisions. For this reason, the prompt flux at high energy follows the same power law of the primary CR flux, therefore being harder than the *conventional* flux (see Equation 42). The prompt flux has not yet been measured (only upper limits have been placed by the IceCube Collaboration [39]), but it is expected to contribute significantly over 100 TeV. An additional source of uncertainty, to be added on top of the already existing one for conventional atmospheric neutrino production, concerns the charm production cross-sections. A review of the importance of the measurement of prompt component for a better characterisation of the all-sky diffuse signal observed by IceCube is given in [40].

Furthermore, the effect of neutrino oscillations causes a modification of the neutrino flavour ratio within a relatively small energy range, compared to the one spanned by conventional and prompt atmospheric neutrinos. In fact, above ~ 100 GeV, it can be neglected for terrestrial baselines ($\mathcal{O}(10^4)$ km). A precise measurement of the atmospheric neutrino flux is available and is shown in Figure 13. Above some TeVs, only neutrino telescopes have the sufficient effective area to detect, with high statistics, the flux of atmospheric neutrinos.

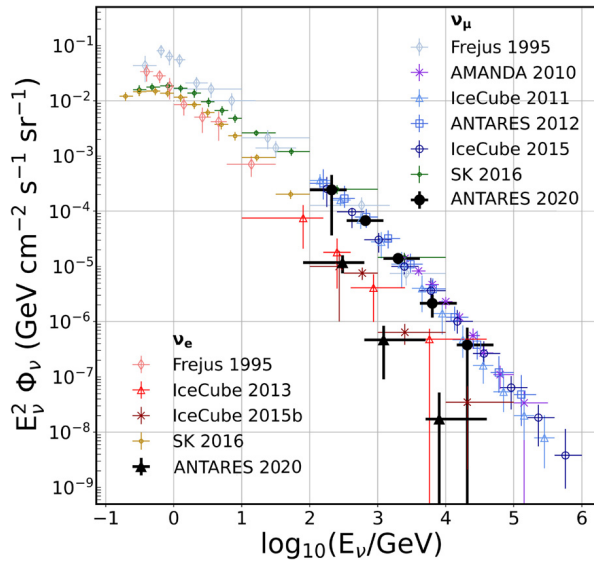


Figure 13: Measurement of the atmospheric neutrino flux for ν_μ and ν_e reported by various experiments (Frejus, AMANDA, IceCube, Super-Kamiokande and ANTARES). Figure taken from [41].

1.3 ASTROPHYSICAL NEUTRINOS

High-energy neutrinos, produced inside astrophysical sources, travel through the Universe unmodified, except for redshift energy losses and flavour oscillations. They are electrically neutral and, therefore, do not interact with magnetic fields or with interstellar medium matter, pointing back directly to the source that generated them. In this section, the main mechanisms responsible for the production of astrophysical neutrinos will be treated, even if some of the reaction chains have already been exposed in Equations 44 - 46. The main difference resides in the target on which accelerated protons impinge, being atmospheric nuclei or the astrophysical source matter itself. For a complete review of the arguments treated in the following sections, see [42].

1.3.1 Neutrino production mechanisms

In the standard production mechanism, CRs are at the beginning of both the neutrino and the γ -ray production chains. Neutral and charged pions can be produced in the interaction with ambient matter within the astrophysical source. The theoretical formulation of this section has been mainly inspired by [43]. In pion photo-production,

$$p + \gamma \rightarrow p + \pi^0, \quad p + \gamma \rightarrow n + \pi^+, \quad (49)$$

charged and neutral pions are produced via Δ^+ resonance, with probability respectively $2/3$ and $1/3$ and non resonantly with probability $1/2$ and $1/2$. The fraction of energy released to the secondary particles, with respect to the total energy, can be defined through the *inelasticity* parameter k_i . Specifically, from Equation 49 k_π for pions is ≈ 0.2 . In hadronic collisions

$$p + p \rightarrow \pi + X, \quad (50)$$

the three pions are produced with equal probabilities and the inelasticity is $k_\pi \approx 0.5$. In turn, pions decay through the process

$$\pi^\pm \rightarrow \mu^\pm + \nu_\mu \text{ and } \mu^\pm \rightarrow e^\pm + \nu_e + \nu_\mu, \quad (51)$$

with neutrino energy approximated as $\sim 25\%$ of pion energy (using the same notation above $k_\nu \approx 0.25$). In neutral pion decay

$$\pi^0 \rightarrow \gamma + \gamma, \quad (52)$$

the energy of each photon is half of the pion energy, $k_\gamma \approx 0.5$. Defining the ratio $K_\pi = N_{\pi^\pm}/N_{\pi^0} = 1(2)$ for photo-production (hadron production), the relation between charged and neutral pions and their production probabilities can be written in the form:

$$N_{\pi^\pm} = K_\pi N_{\pi^0}, \quad (53)$$

$$P_{\pi^\pm} = \frac{K_\pi}{1 + K_\pi}. \quad (54)$$

Moreover, since in photo-pion production $k_\pi \approx 0.2$ and $k_\nu \approx 0.25$, the final neutrino energy is $\sim 5\%$ of the energy of the original proton. Considering a CR proton with energy at Earth of $E_p = E_{p,17} \cdot 10^{17}$, the neutrino energy detected at Earth will be:

$$E_\nu \approx 0.05 \cdot E_p \approx 5 \text{ PeV} \cdot E_{p,17} \approx 5 \text{ PeV} \cdot \frac{\epsilon_{p,17}}{1+z}, \quad (55)$$

where the redshift energy loss of the proton, from the neutrino production point ($\epsilon_{p,17} = (1+z) E_{p,17}$) should be taken into account. This relation suggests that PeV neutrinos can be produced by photo-pion production of protons with energies just above the knee.

Taking into account the relative inelasticities involved in the γ -ray production chain, they have 10% of the energy of the original proton.

Using Equation 54, the pion rate, considered here as the number of charged pions per unit of energy and time (with typical units $\text{GeV}^{-1}\text{s}^{-1}$), results proportional to the corresponding CR rate:

$$Q_\pi^\pm(E_\pi) = \frac{dN_{\pi^\pm}}{dt dE} = \frac{K_\pi}{1+K_\pi} [Q_N(E_N)]_{E_N=E_\pi/k_\pi}. \quad (56)$$

Since Equation 49 has, among its final products, also protons with lower energies, in efficient CR acceleration sources this mechanism should be suppressed.

Connecting now pion production rates to photon and neutrino ones, the number of charged pions with energy between E_1 and E_2 can be written in the form:

$$N_\pi^\pm = \frac{1}{2} \int_{k_\nu E_1}^{k_\nu E_2} \frac{dN_{\nu_\mu}}{dE_\nu} dE_\nu. \quad (57)$$

A similar equation can be written for γ -rays, simply replacing the due inelasticities. From Equations 56 and 57, the following relations for the production rates can be obtained:

$$Q_{\nu_\mu}(E_\nu) = \frac{2}{k_\nu} Q_{\pi^\pm} \left(\frac{E_\nu}{k_\nu} \right) \approx 8 Q_{\pi^\pm}(4E_\nu), \quad (58)$$

$$Q_{\nu_e}(E_\nu) = \frac{1}{k_\nu} Q_{\pi^\pm} \left(\frac{E_\nu}{k_\nu} \right) \approx 4 Q_{\pi^\pm}(4E_\nu), \quad (59)$$

$$Q_\gamma(E_\gamma) = \frac{2}{k_\gamma} Q_{\pi^0} \left(\frac{E_\gamma}{k_\gamma} \right) \approx 4 Q_{\pi^0}(2E_\gamma). \quad (60)$$

Assuming a flavour ratio of 1 : 1 : 1 due to neutrino oscillations, the neutrino and γ -ray production rates can be related to pion ones as follow:

$$\sum_\alpha E_\nu Q_{\nu_\alpha} \approx 3 [E_\pi Q_{\pi^\pm}(E_\pi)]_{E_\pi \approx 4E_\nu}, \quad (61)$$

$$E_\gamma Q_\gamma(E_\gamma) \approx 2 [E_\pi Q_{\pi^0}(E_\pi)]_{E_\pi \approx 2E_\gamma}. \quad (62)$$

Lastly, using the relation $Q_{\pi^\pm}(E_\pi) = K_\pi Q_{\pi^0}(E_\pi)$, the direct relation between γ -ray and neutrino production rates can be derived:

$$\frac{1}{3} \sum_\alpha E_\nu^2 Q_{\nu_\alpha}(E_\nu) \approx \frac{K_\pi}{4} [E_\gamma^2 Q_\gamma(E_\gamma)]_{E_\gamma=2E_\nu}, \quad (63)$$

with the factor $1/4$ accounting for the two γ -rays produced with each twice the energy of the accompanying neutrino. In addition, the relative production rate of γ -rays and neutrinos depends only on the ratio of charged-to-neutral pions, without any reference to the CR spectrum that generates them. This is a direct consequence of the fact that pion production conserves only isospin. Before comparing neutrino and γ -ray fluxes measured at Earth, one should also consider the fact that the Universe is not transparent to PeV γ -rays.

1.3.2 Neutrino and γ -ray astronomy

As explained in the previous section, the production in astrophysical environments of neutral secondary particles, such as neutrinos and photons, is strictly connected. Therefore, recent studies and results obtained by γ -ray astronomy can put severe constraints on the neutrino flux expected at Earth coming from specific sources. However, differences of neutrinos with respect to photons should be taken into account. First, the origin of at least part of the emitted photons could be due to leptonic processes that do not produce neutrinos in the final states. Furthermore, γ -rays can be absorbed by the source, if thick, and during propagation with the following reaction:

$$\gamma + \gamma_{\text{bkg}} \rightarrow e^+ + e^-, \quad (64)$$

with γ_{bkg} represented by the extra-Galactic background light (EBL). This process attenuates the photon flux, starting from energies of the incident photon of hundreds of TeV, if the infrared background light emitted from stars is considered. The photon mean free path is shown in Figure 14.

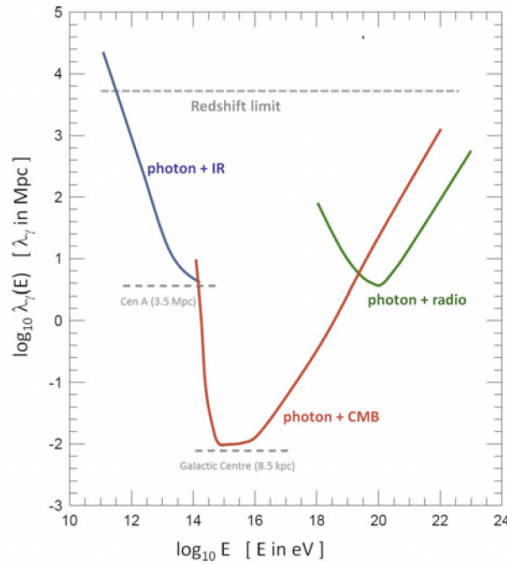


Figure 14: Photon mean free path as a function of the photon energy. Scattering over different contributions of EBL is reported: infrared (blue), CMB (red), and radio (green). Figure taken from [29].

At high energies, therefore, the connection between neutrinos and γ -rays is not so intuitive, and detailed numerical simulations are needed.

Moreover, if the source itself is opaque, the high-energy part of the γ -ray flux will lose energy even before escaping from it. Efficient neutrino factories require a dense environment: this will make the source opaque to high-energy γ -rays. Therefore, the energy of photons, associated with cosmic neutrinos, may thus emerge below the threshold of current γ -ray instruments, making these sources γ -obscure.

To fully understand the interplay and the power of multi-messenger astronomy, it has been calculated [44] and reported here the γ -ray flux accompanying the diffuse cosmic neutrino flux observed by IceCube, described by a single power law with a spectral index of -2.15. The results are shown in Figure 15, assuming a hadronic production mechanism ($K_\pi=2$), transparent sources and equal multiplicities of all three pion charges.

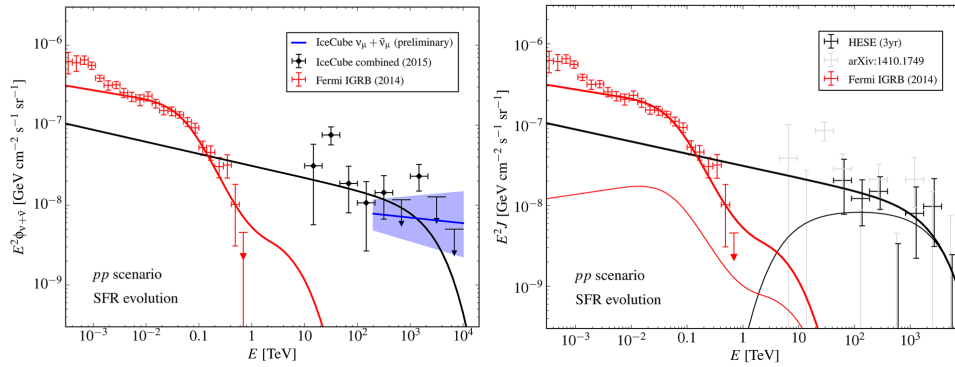


Figure 15: Calculation of the γ -ray flux originated from hadronic (left) and photo-pion (right) production, matching the Fermi data, starting from the neutrino flux (black line) measured by IceCube. More details on the theoretical derivation are provided in the text. Figure taken from [44].

The γ -ray energy flux, resulting from neutral pion decay, matches the extra-Galactic γ -ray energy flux measured by Fermi-LAT. This suggests that IceCube observes the same Universe as Fermi. In the calculations above, the overall normalisation of the neutrino spectrum has been adjusted to not exceed the isotropic extra-Galactic γ -ray background observed by the Fermi satellite. Adjusting the spectral index for the fit of the IceCube data, closer to the current observations (see Section 2.6.1), i.e. -2.5, results in a photon flux at energies below 100 TeV, exceeding Fermi measurements. This could be explained by the fact that sources are opaque to photons that lose energy even before the propagation through EBL, and reaching Earth, with energies that are too low to be detected by the Fermi satellite, in the MeV range or lower. Alternatively, neutrino could be produced through photo-pion reactions: this changes the value of K_π ($=1$) and the shape of the energy spectrum, which peaks near the PeV energies, as shown in Figure 15. However, even in this scenario, the neutrino spectrum below 100 TeV is difficult to reconcile with the assumptions made. Interestingly, the common

energy density of photons and neutrinos is also comparable to that of the ultrahigh-energy extra-Galactic cosmic rays.

1.3.3 Neutrino fluxes

Some more generic considerations can be made about neutrino production in sources, starting from the description of some bounds that can be derived on neutrino fluxes.

1.3.3.1 Bound on neutrino flux

CRs can be attenuated by interaction with background photons: this means that the observed CRs come from the local (200 Mpc, $z < 1$) Universe. Starting from the measurement of their flux, one can go back to the CR production rate. On the basis of the relations written above on the neutrino and CRs production rates (i.e. Equation 61), it is possible to derive bounds, like the Waxman-Bachall bound (WB) [45]:

$$[E^2 \Phi_{\nu_\mu}(E)]_{\max} \approx 0.9 \cdot 10^{-8} \frac{\text{GeV}}{\text{cm}^2 \text{ s sr}}. \quad (65)$$

It was obtained under the following assumptions:

- UHECRs are protons from optically thin sources with Fermi acceleration spectrum ($\alpha = -2$) normalised to the measured UHECR flux above EeV energies, $E^2 dN_p / (dt dE) \sim 10^{44} \text{ erg} / (\text{Mpc}^3 \text{ yr})$;
- the whole proton energy is transferred to pions inside sources;
- no magnetic fields are considered.

Another bound can be derived, based on the fact that IceCube has failed to identify extra-Galactic sources, which should therefore contribute to the diffuse neutrino flux. If these sources, each of them with a production rate $Q_{\nu_\alpha}(E_\nu)$ for a given flavour, are distributed with a redshift density $\rho(z)$, then the sources between z and $z + dz$, in the solid angle element $d\Omega$, contribute to the neutrino flux at Earth $\phi_{\nu_\alpha}(E_\nu)$. Then the flux per unit solid angle of a given neutrino flavour is:

$$\phi_{\nu_\alpha}(E_\nu) = \frac{1}{4\pi} \int_0^\infty \frac{dz}{H(z)} \rho(z) Q_{\nu_\alpha}((1+z)E_\nu). \quad (66)$$

This expression corresponds to the integral of individual point sources, distributed with density $\rho(z)$ and flux given by

$$\phi_{\nu_\alpha}^{\text{PS}}(E_\nu) = \frac{(1+z)^2}{4\pi d_L^2(z)} Q_{\nu_\alpha}((1+z)E_\nu), \quad (67)$$

thanks to the definition of the luminosity distance $d_L = (1+z)r$.

Using the diffuse flux measured by IceCube, $E^2 \sum_\alpha \phi_{\nu_\alpha} \approx 10^{-8} \text{ GeV cm}^{-2} \text{ s}^{-1} \text{ sr}^{-1}$ for energies in excess of 100 TeV, bounds on the production rate of single sources can be inferred.

SUMMARY In Figure 16 different contributions exposed in the previous sections are summarised. The atmospheric neutrino flux (only ν_μ and $\bar{\nu}_\mu$), including the *prompt* component, contributes significantly for energies below ~ 100 TeV. It is distributed according to a power law as in Equation 42, with spectral index $\alpha \sim 3.7$. In the PeV region, the Waxman-Bachall upper bound for an extra-Galactic diffuse neutrino flux is depicted [45].

Taking into account the upper bound for all flavours ($\nu_e + \nu_\mu + \nu_\tau$), this is three times larger than Equation 65. In the same energy region, the expected neutrino flux from the single GRB component is reported, with the green dashed line. Also in this case, it is possible to estimate the maximum neutrino flux [45]:

$$[E^2 \Phi_{\nu_\mu}(E)]_{\max}^{\text{GRB}} \approx 3 \cdot 10^{-9} \frac{\text{GeV}}{\text{cm}^2 \text{ s sr}}. \quad (68)$$

Astrophysical neutrinos can therefore be selected with respect to the background, outlining an excess of events in a given direction (point-like search) or as an excess of high-energy events (diffuse search), considering that starting from ~ 100 TeV the diffuse astrophysical neutrino flux exceed the atmospheric one.

In the fireball model, one of the most accredited model for GRB production, shock waves emerge in the relativistic outflow of material, producing the characteristic burst of electromagnetic radiation. In the same region, also protons can be accelerated, possibly producing high-energy neutrinos, accompanying the electromagnetic burst.

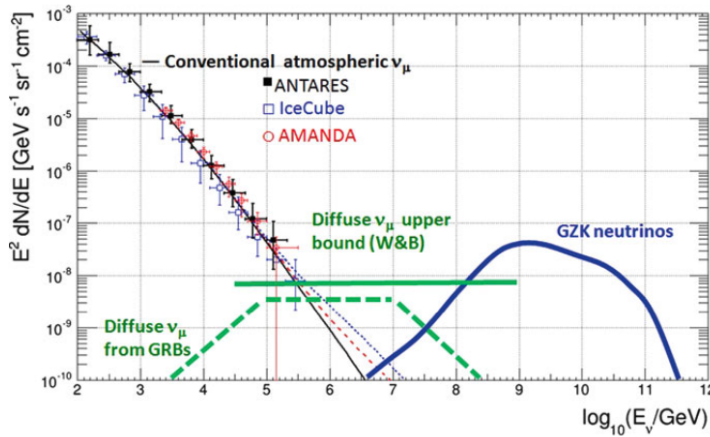


Figure 16: Expected neutrino flux estimated from different models and atmospheric neutrino background. The black line is the expected atmospheric flux, in which also the *prompt* component is included. The horizontal green line is the upper bound for the diffuse flux of the astrophysical neutrino derived from the Waxman and Bachall model (solid) and from the GRB emission (dashed). The blue line instead represents the possible contribution of cosmogenic neutrinos.

1.3.4 Neutrinos and Blazars

Several types of astrophysical sources have been suggested to be responsible for the production of astrophysical neutrinos: in particular, blazars, known to be efficient cosmic accelerators. Blazars are the most powerful sources of non-thermal radiation in the Universe. They are a special and

rare type of AGN with unique characteristics, such as the emission of highly variable radiation over the entire electromagnetic spectrum, from radio to the very high-energy γ -ray band, which originates within a relativistic jet that moves away from the central supermassive black hole and oriented in the direction of the Earth. The central black hole is usually surrounded by an optically thick accretion disk. The emission from the disk can be obscured by a surrounding torus of molecular dust. Today, a few thousand blazars are known, and they all emit across the entire electromagnetic spectrum with a Spectral Emission Distribution (SED) displaying two broad bumps: one attributed to synchrotron radiation that peaks in between infrared and X-ray bands, and the second, more energetic one, due to inverse Compton or other mechanisms (i.e. neutral pion decay), which peaks in the low- or high-energy γ -ray band. Recently, statistically significant associations have become possible thanks to data accumulated, mostly from IceCube observatory. Investigations of this type have been conducted largely by comparing neutrino arrival directions with lists of bright radio or γ -ray sources or with catalogues of well-known blazars and other types of AGN [46]. In this phase of multi-messenger astronomy, associations would benefit from the detection of high-energy neutrinos together with a flaring activity in some parts of the electromagnetic spectrum.

1.3.5 Cosmogenic neutrinos

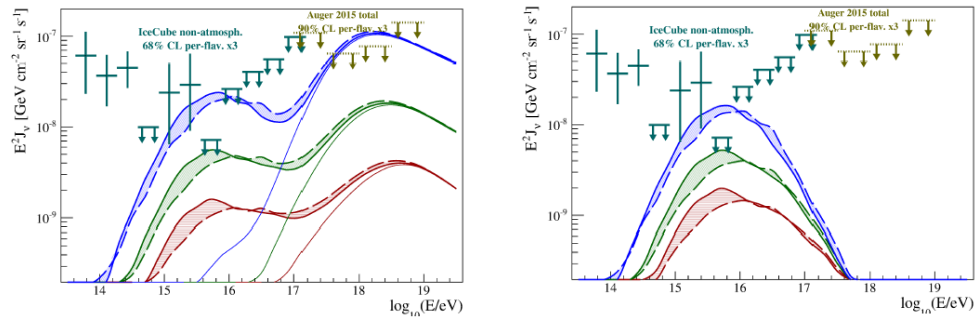


Figure 17: Flux of cosmogenic neutrinos expected at Earth and current IceCube and PAO limits. The different curves represent different assumptions in the cosmological evolution of the source. **Left:** primary composition of CRs assumed purely from protons. **Right:** primary mass composition extracted from PAO data, like the one also reported in Figure 12. Figure taken from [47].

Cosmogenic neutrinos are produced from secondary pions and neutrons originated as result of GZK suppression, discussed in Section 1.2.6. To accurately calculate their flux, a detailed simulation of the propagation of CRs is needed. This flux adds to the fluxes produced by standard sources. Their energies have a maximum of the order of EeV, based on the assumed redshift evolution of the source and on the primary CR mass composition. The authors in [47] assumed a pure proton composition: this results in a total

neutrino flux in excess with respect to the current limits set by the PAO and IceCube Collaboration, as shown in the left panel of Figure 17. If instead the primary mass composition measured by PAO is assumed, shown also in Figure 12, this results in a Universe with no observable neutrinos at high energy. In this scenario, in fact, the cutoff observed in the CR spectrum is more likely due to a rigidity-dependent acceleration mechanism at the source, with $E_{\text{max}}(Z) = Z E_p$, where E_p is the maximum acceleration energy for protons. For iron nuclei, for example, the maximum acceleration energy obtainable is $E_{\text{max}} \sim 100\text{-}300 \text{ EeV}$, which implies too small energies for nucleons, no longer capable of satisfying the threshold of the GZK effect. Therefore, no cosmogenic neutrinos could be produced by protons on CMB, even if neutrinos of lower energies would come from the interaction of protons with EBL. The detection of an EeV neutrino would also shed light on different primary mass composition scenarios.

1.3.6 Gravitational wave in the multi-messenger scenario

With the first detection of the Gravitational Wave (GW) by the Ligo Collaboration in September 2015 [48], a new window on the Universe was opened. Since then, many other GWs have been detected, but probably one of the most important ones was revealed in October 2017 by the VIRGO/Ligo Collaboration [49]. It was in fact announced the first coincidence signal of a GW and its electromagnetic counterpart. The astrophysical event that generated it was the coalescence of two neutron stars, 40 Mpc away from Earth. From the study of the electromagnetic *follow-up* in the next days, the signatures of synthesised materials, like gold and platinum was revealed, resolving a long lasting mystery on the nature of the heaviest elements of the periodic table. Furthermore, the neutrino signal counterpart was searched by the IceCube, ANTARES and PAO Collaborations, but no statistically significant excess was found [50]. In any case, since the merger of a Binary Black Hole (BBH) could be very slow, surrounding matter is not expected at the time of the coalescence. In fact, there is no theory of neutrino generation associated with BBH merger, even if neutrinos could be emitted from the black hole accretion disk. A more interesting situation, from the point of view of multi-messenger astronomy, is represented by neutron star mergers, as in the case of GW170817. Even in this kind of system, the acceleration of particles by compact objects is still not well understood, and observation of neutrinos could be striking evidence for hadronic processes. Just to mention, many efforts have been made not only on the experimental side, trying to detect these coincident signals, but also on the theoretical one. Many works, for example, have studied the modification of neutrino oscillations in the presence of a static gravitational field. Some of them have also tried to infer the impact of the interaction with a time-dependent gravitational field, as the one produced by a GW, on astrophysical neutrino mixing [51].

NEUTRINO ASTRONOMY

2.1 NEUTRINO TELESCOPES

Neutrinos are weakly interacting particles, therefore being able to escape thick astrophysical environments. However, the same trait makes it difficult to detect them. Taking into account the smallness of neutrino cross-section ($\sigma \sim 10^{-38} \cdot E_\nu/\text{GeV}$), in order to increase the detection probability, large transparent instrumented volumes are needed. Theoretical expectations on neutrino fluxes and neutrino cross-section suggest that a detection area of the order of 1 km^2 is necessary in order to have a rate of $\sim \mathcal{O}(10)$ events/year from a source ¹. Neutrino telescopes register the Cherenkov light produced by secondary particles emerging from the interaction of neutrinos with the matter inside or surrounding the detector with a large 3D array of photo-sensors. Furthermore, they can operate as a telescope if the neutrino arrival direction is reconstructed with good angular precision ($<1^\circ$), correlating the direction of flight of the particle with possible sources.

Moreover, neutrino telescopes are generally optimised to detect TeV-PeV neutrinos, where the background of atmospheric particles is reduced, and much above the energy regime relevant for the determination of the neutrino mass hierarchy, in which many neutrino experiments on Earth are operating.

¹ **Historical note:** the first idea of a telescope, based on the detection of secondary particles produced in neutrino interactions, was formulated by Markov and Zheleznykh in 1960 [52]. In the mid-1970s the DUMAND Collaboration started a pioneering project to deploy a neutrino telescope offshore Hawaii Island [53]. Unfortunately, the technology was not yet mature and the tentative was abandoned. This marked the starting point for a series of other projects. AMANDA at the South Pole [54], which was the precursor of the currently large detector IceCube [55]; Baikal under the water of the Baikal Lake, which is currently expanding towards a km^3 structure, named GVD [56]. In the Mediterranean Sea, the ANTARES experiment [57], located offshore the Southern French coast, is the precursor of the KM₃NeT/ARCA and ORCA detectors.

2.1.1 Cherenkov radiation

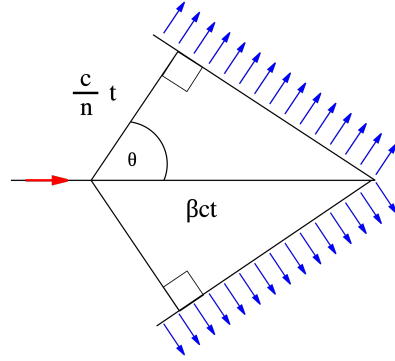


Figure 18: Schematic representation of Cherenkov light emission, where θ is the characteristic Cherenkov angle. The red arrow marks the propagation of the charged particle in the medium, while the blue arrows represent the propagation of the coherent wavefront of Cherenkov light.

Cherenkov radiation is produced when a charged particle propagates in a medium, with refractive index n , faster than the speed of light in the medium itself ($v=c/n$, with c speed of light in vacuum). In such cases, an electromagnetic shock wave is created, recalling the Mach cone of aircraft moving faster than the speed of sound. This is due to charged particles that polarise the molecules of the medium along the trajectory. Only when the electrons return to their ground state, this coherent radiation is produced. The peculiar conical shape is emitted at a precise angle:

$$\cos(\theta_c) = \frac{c/n(\omega)}{\beta c} = \frac{1}{\beta n(\omega)}, \quad (69)$$

with respect to the trajectory of the particle. This angle is dependent on the speed of the particle and on the frequency of the radiation emitted. In water $n \simeq 1.35$, giving a Cherenkov angle for relativistic particles ($\beta \sim 1$) of $\theta_c \simeq 42^\circ$ and independent of the particle's energy. The number of photons emitted per unit path length dl and unit wavelength interval $d\lambda$, is given by the Frank-Tamm formula as follows:

$$\frac{d^2N}{dl d\lambda} = \frac{2\pi\alpha Z^2}{\lambda^2} \left(1 - \frac{1}{\beta^2 n(\omega)^2}\right), \quad (70)$$

where α is the fine structure constant and Z is the electric charge of the particle. In the wavelength range from 300 to 600 nanometres, in which the water is transparent, the number of photons per particle path length is approximately:

$$\left. \frac{dN}{dl} \right|_{\text{water}} = 340 \text{ cm}^{-1}. \quad (71)$$

At the same time, the energy loss per unit path length of the charged particle emitting Cherenkov radiation can be written in the form:

$$-\frac{dE}{dl} = Z^2 \frac{\alpha \hbar}{c} \int \omega d\omega \sin^2 \theta_c. \quad (72)$$

Even at relativistic energies this loss is of the order of $\approx 10^{-3} \text{ MeV cm}^2 \text{ g}^{-1}$, almost negligible compared to other energy losses.

For the future development of this chapter it is also important to consider the geometrical constraint of the Cherenkov light emission. In fact the number of detectable photons per unit wavelength and per unit area at a distance R from the particle trajectory can be formulated as:

$$\Phi_0(R, \lambda) = \frac{d^2 N}{d\lambda d\lambda} \frac{1}{2\pi R \sin\theta_c}. \quad (73)$$

2.1.2 Light propagation

During the propagation of light from the emission point, along the particle track, until the detection point on photosensors, light suffers mainly from two processes: absorption and scattering. Absorption affects the amount of light and can be taken into account by introducing an extra term in the Equation 73 of the form:

$$\Phi' = \Phi_0 \cdot e^{-d/\lambda_{\text{abs}}}, \quad (74)$$

with λ_{abs} referring to the absorption length and d is the distance travelled by light. The absorption length is a function of the wavelength itself, as shown in Figure 19. Scattering instead affects the path travelled by the light,

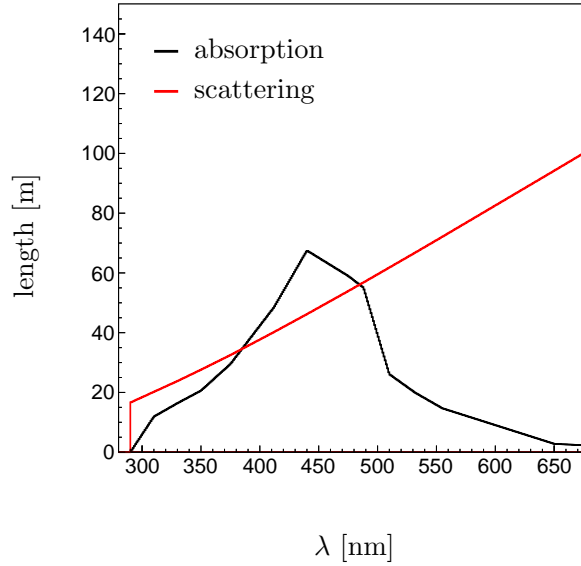


Figure 19: Absorption and scattering length as a function of the light wavelength. Figure taken from [58].

and its consequent arrival time on the photosensors: for this reason the photon path is not uniquely defined. There are several models that describe the scattering of light. Since it is an effect symmetric under rotation, it depends only on the angle between the direction of light before and after the scattering, here called θ_s . One of the models, adopted, for example, within the KM3NeT Collaboration, is called p0.0075 and is based on a combination of

Rayleigh and Mie scattering. Rayleigh scattering is the elastic scattering of light by particles that are typically much smaller than the wavelength of the light. The resulting angular distribution is ad hoc modelled, in order to take into account the anisotropy of water molecules, with the term:

$$g(a, b; \cos\theta_s) = a \cdot (1 + b \cdot \cos\theta_s), \quad (75)$$

where $a = 0.06225$ and $b = 0.835$. The effect of Mie scattering, over large particles, is obtained from in-situ measurements. For water, the average cosine of the scattering angle has been measured and found to be 0.924. Therefore, the probability density function can be defined as follows:

$$\frac{dP_s}{d\Omega_s} = p \times g(\cos\theta_s) + (1 - p) \times f(c; \cos\theta_s), \quad (76)$$

where $c = 0.924$ and $p = 0.17$, where p can be seen as the contribution of the Rayleigh scattering. This process can be taken into account by introducing another extra term in Equation 73, of the form:

$$\Phi' = \Phi \cdot e^{-d/\lambda_s}, \quad (77)$$

with d always referring to the path travelled by light. An overall effective attenuation length can be derived, in the form:

$$\frac{1}{\lambda_{att}} = \frac{1}{\lambda_{abs}} + \frac{w}{\lambda_s}, \quad (78)$$

with $w=1$ for direct light, and $w=1-\langle\cos\theta_s\rangle$ for indirect light. Optically pure seawater shows the highest transparency for photon wavelength of ~ 400 nm, where typical values of $\lambda_{abs} \approx 60$ m and of $\lambda_s \approx 55$ m are reached.

In general, ice is more transparent than water, i.e. its light absorption length is up to three times larger than that of water. On the other hand, the dust and air bubbles, trapped into the ice, produce a stronger scattering. Additionally, while water is a homogeneous medium, the Antarctic ice shell was formed after snow accumulation over an extremely long period of time, with differences in dust concentration over time.

2.2 UNDERWATER DETECTORS

One way to exploit a large amount of transparent natural medium is to place neutrino telescopes underwater. The main advantage is the huge availability of the medium and the reduced scattering length, resulting in a better angular resolution for particle direction reconstruction. Disadvantages, with respect to other mediums, such as ice, are that the detector moves under the effect of sea current, the difficulty in modelling the environmental background surrounding the detector, and the corrosion due to the salinity of seawater. A couple of experiments have been or are currently in operation in underwater locations:

- the pioneering DUMAND project, started in 1976 offshore the Hawaii Island at a depth of 4800 m. It didn't reach its planned final configuration due to technical and financial problems, but all the subsequent projects took huge advantage of the experience gathered with it [53];
- the lake Baikal, Russia, at a depth of 1800 m hosts the Baikal/GVD neutrino telescope. Actually, the Gigaton Volume Detector (GVD) is under construction and has reached an instrumented volume of 0.5 km^3 , with respect to cascade-like neutrino-induced events. The effective target volume of 1 km^3 is expected to be reached by 2030. A thick ice shell is present on the lake during winter, allowing easy deployment of instruments in the water. A lower optical background rate is expected in fresh water than in seawater, but lake Baikal is less transparent than seawater or ice, limiting the reconstruction performance. The optical modules (OM) are grouped into vertical strings, with 36 modules each at a distance of 15 m. The OMs are located at a depth between 750 and 1275 m below the surface. Eight strings, organised in an approximately regular heptagon shape (one string per edge and one at the centre), form the so-called *cluster*. At the end of 2022, 11 clusters were deployed [59];
- the first successful attempt to construct and operate a neutrino telescope in the Mediterranean Sea was the ANTARES detector. It was completed in 2008 and has been fully operational up to February 2022. It was located 40 km offshore of Toulon, France, at a depth of 2500 m. It fully demonstrated the feasibility of measuring neutrinos with a large-volume Cherenkov detector in the deep sea. From the experience gathered from the first-generation neutrino telescope, like ANTARES, KM₃NeT detectors have been designed and are actually under construction. KM₃NeT is a multi-site deep sea infrastructure that will host a second-generation neutrino telescope and Earth and sea science instrumentation. A more detailed explanation of KM₃NeT detectors, subject of this work, will be given in Chapter 3.
- the Pacific Ocean Neutrino Experiment (P-ONE) is a planned multi-cubic-kilometre neutrino telescope at a depth of 2660 metres in the Northeast Pacific Ocean, offshore of Vancouver Island, British Columbia. P-ONE will be connected to an already existing deep sea infrastructure. Following the successful deployment of two pathfinder missions, deployed in 2018 and 2020, respectively, and recovered in 2023, to characterise the deployment location, the P-ONE Collaboration is working towards the realisation of the first P-ONE detector line, called P-ONE1. The final geometry is being optimised to maximise the discovery potential and will be adjusted based on the experience of the first lines deployed [60];
- TRopical DEep-sea Neutrino Telescope (TRIDENT) is a next generation neutrino observatory that will be located in the South China Sea,

at a depth of ~ 3500 m. The location is about 180 km from the nearest island, where detector's power supply and data storage are located. TRIDENT will exploit a unique position near the equator and the usage of advanced hybrid digital optical modules (hDOMs), which contain multiple small photomultiplier tubes and silicon photomultipliers. The preliminary design of TRIDENT comprises 1211 strings, each containing 20 hDOMs separated vertically by 30 m, resulting in an instrumented volume of ~ 7.5 km³. In September 2021, the TRIDENT pathfinder experiment was successfully completed at the selected site in the South China Sea [61].

2.3 UNDER-ICE DETECTORS

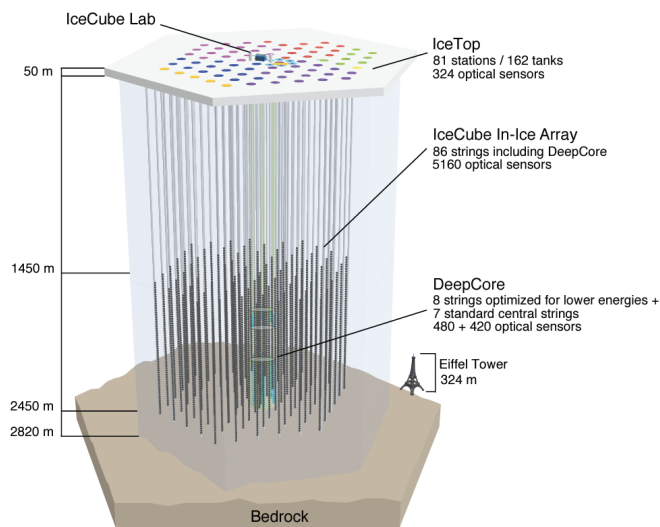


Figure 20: Schematic representation of IceCube Neutrino Observatory, with particular attention to each of the sub-component: in-ice optical detector, the DeepCore and IceTop.

AMANDA experiment was the first attempt to exploit Antarctic ice to deploy and operate a neutrino telescope. In 2005, after nine years, it became officially part of its successor project, the IceCube Neutrino Observatory. Currently, the biggest neutrino detector in the world, IceCube is located at the geographic South Pole, at the permanent Amundsen-Scott Pole station, which offers the logistic support required for the construction and operation of the observatory. The IceCube Neutrino Observatory consists of a subsurface array of DOMs, including the more densely instrumented DeepCore sub-array and the IceTop surface array. The entire detector uses the same DOM design and associated surface readout. A schematic layout of the observatory is shown in Figure 20. The current detector configuration consists of 5160 DOMs deployed between 1450 m and 2450 m below the surface of the ice on 86 vertical strings. Each string consists of 60 DOMs deployed along a single cable, and the primary in-ice array consists of 78

strings with a vertical separation of the DOMs of 17 m and with 125 m horizontal spacing, instrumenting a volume of one cubic kilometre of ice. A subset of in-ice DOMs is deployed, forming a denser instrumented volume called DeepCore. It consists of eight specialised and closely spaced strings of sensors in the centre of the array, with a DOM-to-DOM spacing of 7 m for the bottom 50 DOMs. The remaining 10 DOMs are deployed at depths shallower than 2000 m with a spacing of 10 m to form a veto cap. Depths from 2000 to 2100 m are not instrumented, as optical scattering and absorption increase significantly in this region of the ice due to the high presence of dust: the *dust layer*. Cherenkov tanks are placed on the surface, forming the so-called IceTop detector, capable of detecting cosmic rays and characterising also the background coming from downward-going atmospheric events. The angular resolution for muon tracks and hence the incident neutrino direction is typically 0.6° [62].

PLANNED AND FUTURE ICECUBE UPGRADES There are mainly two expansions of IceCube detector planned and under development. The first, called IceCube Upgrade [63], consists of seven new columns of photosensors, densely embedded near the DeepCore. The upgrade strings will also include new calibration devices, designed to deepen the understanding of the optical properties of glacial ice and the detector response. This will be used to improve the quality of the reconstruction, through more precise calibrations, extendable also to the already available 10-year IceCube data set. Its goal is to provide world-leading sensitivity to neutrino oscillations and will enable IceCube to take unique measurements of tau neutrino appearance.

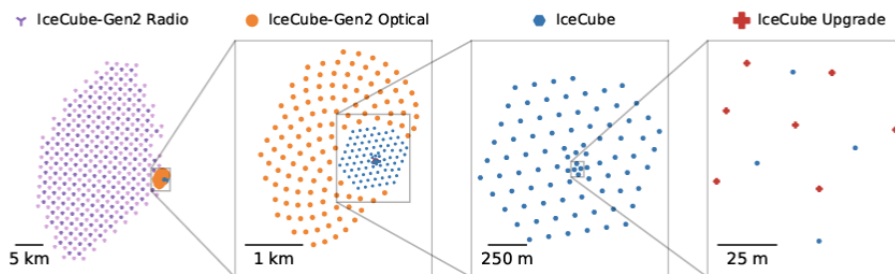


Figure 21: Footprint of the IceCube-Upgrade and IceCube-Gen2, with respect to the already existing optical strings. Figure taken from [64].

The other planned upgrade for the IceCube detector is called IceCube-Gen2 [64]. Currently under development, it will consist of three essential components: an array of about 10,000 DOMs, expanding the volume of the optical array from 1 km^3 to $\sim 8 \text{ km}^3$, with an expected sensitivity five times greater than the current one. IceCube-Gen2 digital optical modules will include a multi-PMT installation within an elongated glass vessel, resulting in an improved photon detection efficiency of a factor ~ 4 . The other two components of the upgrade will focus on the surface array with the installa-

tion of scintillation panels targeting air showers, and buried radio antennas distributed over an area of more than 400 square kilometres to detect neutrinos beyond EeV. In Figure 21 a schematic representation of the footprint is presented.

2.4 DETECTION PRINCIPLE

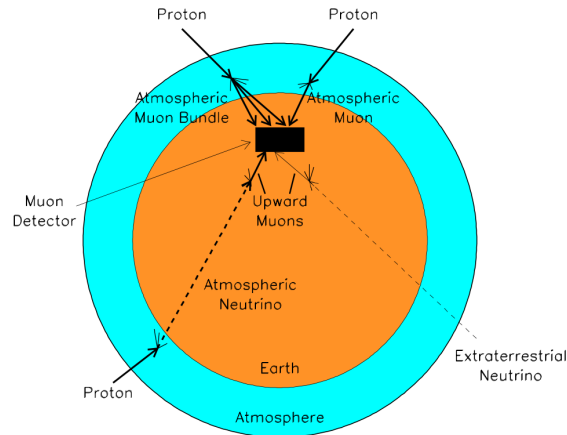


Figure 22: Illustration of the possible origin of signal and background events inside a neutrino telescope.

Despite the different geographical locations and the medium characteristics exploited by neutrino telescopes currently in operation, they are all based on the same detection principle. As already anticipated in Section 2.1, it is based on the detection of Cherenkov optical photons, generated by secondary particles, emerging from neutrino interaction with the rock at the base of the telescope or in the material surrounding it. The light pattern left inside the detector is different depending on the type of neutrino interaction channel. In fact, ν_{μ} -CC interactions generate an emerging muon that can travel undisturbed for several kilometres in seawater or ice. In this case, the muon direction can be reconstructed with high precision, representing the *gold channel* for neutrino telescopes. The drawback is that the energy determination is not well constrained, since part of the light produced can be deposited outside the sensible volume. Other neutrino flavours, such as ν_e or ν_{τ} , instead, produce a completely different light deposit inside the detector, identifiable through the particle shower initiated by charged leptons or hadrons. The search for astrophysical neutrino fluxes is very challenging considering the signal-to-noise ratio that these experiments usually have to deal with. In fact, while an astrophysical neutrino source produces $\mathcal{O}(10)$ events per year in a km^3 scale detector, the greatest number of recorded events comes from atmospheric muons, generated from the interaction of CRs in the atmosphere above the detector. At sea level, the atmospheric muon flux is about 10^{11} times larger than the atmospheric neutrino flux.

For this reason, the detector is placed under thousands of metres of water or ice, which act as a shield. Even in this case the shielding is not enough to stop all the flux of atmospheric muons, which at the detector level is still $\sim 10^6$ times larger than the neutrino flux. Therefore, further selection techniques need to be applied. Taking into account the incoming direction of the particles involved, atmospheric muons generate events that have a top-bottom development. They are called for this reason *downgoing events*. In fact, atmospheric muons cannot propagate through the Earth's diameter (~ 13000 km) and are absorbed before reaching the detector. Neutrinos instead, considering the low cross-section, barely interact with Earth, and can be detected over the full sky. For this reason, bottom-top signals, called *upgoing events*, can be selected based on the reconstructed zenith and are therefore capable of exploiting the Earth as a shield. Considering the error in the zenith determination of reconstruction algorithms, upgoing events still suffer from atmospheric muon background contamination due to misreconstructed events. Another technique, instead, tries to select neutrino-induced cascades in the detector, using the external layer of optical modules as a veto, and selecting in this way only neutrino events that interact inside the instrumented volume. For these contained events, no particular zenith direction is required. Shower events, despite the difficulty in the precise determination of the direction of the incoming neutrino, allow better energy determination due to the containment of most of the light deposit. At the same time, they suffer a lower background level generated by atmospheric neutrinos (in some energy ranges, the atmospheric neutrino flux ratio can reach $\phi_{\nu_\mu}/\phi_{\nu_e} \sim 20:1$).

For underwater detectors, another source of background is represented by the decay of radioactive elements dissolved in seawater, especially ^{40}K , or by light generated by bio-organisms (*bioluminescence*). In this case, the light signature left inside the detector has a random pattern over different optical modules, and this source of background can simply be rejected asking for spatial and time correlation of hits.

2.5 EVENT TOPOLOGIES

The event signatures in a water/ice Cherenkov neutrino telescope are split into two main categories: a track-like event, originating from the ν_μ -CC interaction and producing a muon that can propagate in water for several kilometres; shower events, originating from ν_e -CC, ν_τ -CC and ν_l -NC interactions that give rise to particles that propagate only for tens of metres. A schematic representation of the different topologies that occur in the detector is shown in Figure 23.

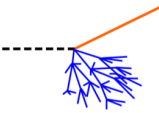
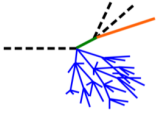
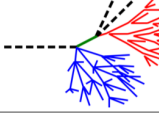
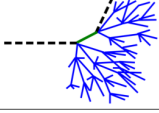
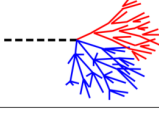
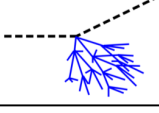
Interaction	Particle signature	Detector signature
$\bar{\nu}_\mu$ CC		hadronic shower and μ track
		track-like
		hadronic shower and μ track ($\tau^\pm \rightarrow \mu^\pm \bar{\nu}_\mu \bar{\nu}_\tau$, $\sim 17\%$ BR)
$\bar{\nu}_\tau$ CC		hadronic and EM shower ($\tau^\pm \rightarrow e^\pm \bar{\nu}_e \bar{\nu}_\tau$, $\sim 18\%$ BR)
		hadronic showers ($\tau^\pm \rightarrow \text{hadrons}$, $\sim 65\%$ BR)
		point-like or shower-like
$\bar{\nu}_e$ CC		hadronic and EM shower
$\bar{\nu}$ NC		hadronic shower

Figure 23: Comprehensive representation of all the event topologies occurring inside a neutrino telescope. Black dashed lines represent neutrinos, orange solid lines muons, red electromagnetic showers, blue hadronic showers, and green τ leptons. Taken from [62]

MUON TRACK The direction of high-energy muons produced in ν_μ -CC interactions is highly correlated with the direction of the incident neutrino and can be expressed through the angle $\theta_{\nu\mu}$:

$$\theta_{\nu\mu} \simeq \frac{0.6^\circ}{\sqrt{E_\nu(\text{TeV})}}. \quad (79)$$

The precise reconstruction of the muon trajectory allows consequently to know the direction of the incident neutrino. Looking at the kinematic contribution of Equation 79, the angular resolution above few TeVs is dominated by the error of the track reconstruction algorithms. The total energy loss for muons with energies greater than 1 TeV can be expressed as:

$$\left\langle \frac{dE}{dX} \right\rangle = -\alpha(E) - \beta(E) \cdot E, \quad (80)$$

where X is the thickness of crossed material expressed in g cm^{-2} , α refers to ionisation and β to radiative losses like bremsstrahlung, pair production and photonuclear interactions. Energy loss due to the emission of Cherenkov radiation (see Equation 72) is almost negligible. Both parameters α and β slowly vary with energy, especially in the regime where radiative contributions dominate (below 100 GeV, $\beta(E) \times E$ is less than 1% of

α), and are dependent on the chemical composition of the medium in the form: $\alpha \propto Z/A$ and $\beta \propto Z^2/A$. At very high energies, where α and β can be considered constant, the muon range can be approximated as:

$$R = \frac{1}{\beta} \ln \left(1 + \frac{E_\mu \beta}{\alpha} \right). \quad (81)$$

The ratio α/β is the muon critical energy, defined as the energy at which the radiative losses are equal to the ionisation ones (≈ 500 GeV). The formula in Equation 81, derived from the so-called *Continuous Slowing Down Approximation*, is of limited usefulness due to the effects of large fluctuations at high energies. Above 100 GeV, range straggling starts to become considerable because of stochastic muon interaction processes with large energy transfers, like bremsstrahlung. These radiative energy losses are visible as electromagnetic showers along the muon track, producing clustered light deposition on top of the track signature. Most of the track reconstruction algorithms, based on a maximum likelihood approach, assume a continuous energy loss pattern for muons. Recently, a newly developed approach, which also exploits the energy released inside the detector through stochastic losses, has been developed by the IceCube Collaboration, producing an improvement in track reconstruction of the 20% for through-going tracks and up to a factor 2 for starting tracks [65]. Furthermore, considering, for example, a 10 TeV muon travelling 4 km in water, it can reach the detector with still 1 TeV energy. The event will be detected and reconstructed, even if the neutrino interaction vertex is far away from the sensible volume, increasing the effective size of the detector. After slowing down, the muon eventually decays at rest into two neutrinos and an electron that causes an electromagnetic shower.

ELECTROMAGNETIC AND HADRONIC SHOWERS Neutrino events due to NC and ν_e and ν_τ -CC interactions, within or close to the instrumented volume, generate a hadronic and an electromagnetic (EM) shower, often referred to as a *shower-like* or *cascade* event. In ν_e -CC interactions, for example, an EM shower is initiated by the high-energy electron resulting from the neutrino interaction. Charged particles produced in the cascade can then emit light as long as they are above the Cherenkov threshold. The detectable signal is, in fact, mainly due to Cherenkov light produced by charged particles in the shower. Considering the radiation length of electrons in water ($X_0 \sim 36$ cm), the shower light emission appears point-like compared to the typical distances between photosensors in neutrino telescopes. In water the hadronic interaction length (~ 83 cm) is very similar to the radiation length, and therefore the light emission from EM and hadronic showers can be treated in the same way. The transversal distribution of light yield for EM showers is almost energy independent and can be parameterised by the following formula, shown also in Figure 24:

$$\frac{d^2P}{d\cos\theta_0 d\phi_0} = c e^{b|\cos\theta_0 - \cos\theta_c|^a}, \quad (82)$$

where $a = 0.35$, $b = -5.40$. The constant c is defined such that P is normalised to unity for the full solid angle.

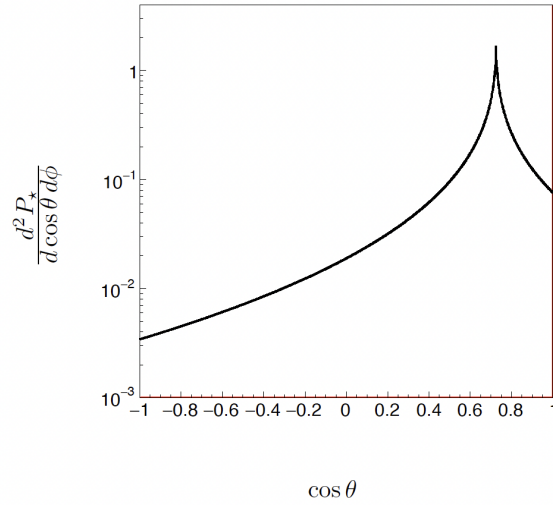


Figure 24: Parameterisation of the shower transverse profile light emission for an electromagnetic shower. The peak corresponds to the cosine of the Cherenkov angle in water. Figure taken from [58].

The longitudinal profile instead can be parameterised reasonably well by the formula:

$$\frac{dP}{dz} = z^{a-1} \frac{e^{-z/b}}{b^a \Gamma(a)}, \quad (83)$$

where $z = x/X_0$ is the number of radiation lengths, $a = 1.85 + 0.62 \cdot \log \frac{E}{\text{GeV}}$ and $b = 0.54$, determined specifically for water from simulations. The maximum, in the longitudinal profile, is $z_{\text{max}} = (a - 1)/b$ and is equivalent to the brightest point in Cherenkov light emission, located ~ 1 m beyond the starting point of the shower for energies around some GeVs. The total Cherenkov light yield produced in EM showers is proportional to the initial neutrino energy with fluctuations smaller than 1%, allowing a very precise energy measurement. Hadronic showers, with the same initial energy as an EM one, produce less Cherenkov light because of the heavier masses of secondary products. Moreover, hadronic showers show larger event-to-event fluctuations in the total light yield.

TAU NEUTRINO A third event signature occurring in neutrino telescopes is the so called *double pulse* or *double bang* [23], depending on the distance of the two reconstructed vertices, and as depicted in the third cartoon from above in Figure 23. It occurs when ν_τ interacts through charged current interaction, producing a first hadronic shower and an exiting τ lepton. The τ can propagate for several metres, producing a track of length:

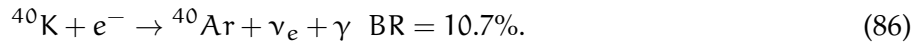
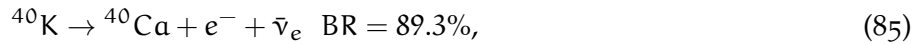
$$L_\tau \approx 49 \text{ m} \cdot \frac{E_\tau}{\text{PeV}}, \quad (84)$$

before decaying (τ lifetime is $2.9 \cdot 10^{-13}$ s). τ can decay through hadronic ($\tau \rightarrow \nu_\tau +$ pions and kaons, BR=64.8%) or through leptonic processes ($\tau \rightarrow e + \nu_e + \nu_\tau$, BR=17.8% or $\tau \rightarrow \mu + \nu_\mu + \nu_\tau$, BR=17.4%) producing a second electromagnetic or hadronic shower. Variants of this double bang signature can occur when one of the two showers occurs outside the detector or when the τ energy is not enough to separate the two showers and make them distinct. In the final states, ν_τ is generated with a lower energy than the starting neutrino. In turn, it can again give rise to the same reactions producing a so-called τ *regeneration*. This is a phenomenon of particular importance for the propagation of neutrinos inside the Earth.

2.5.1 Environmental background

In underwater neutrino telescopes, an optical continuous background rate is also present. This is mainly due to the decay of radioactive isotopes dissolved in seawater, that is, ^{40}K , and due to bioluminescence. ^{40}K contribution is constant and is essentially dependent on the working conditions of PMTs. For example, on a 10-inch PMT (such as for ANTARES) with a threshold set at 0.25 photo-electrons the mean ^{40}K background rate is within the range 45-50 kHz. Bioluminescence bursts could enhance the measured hit rate up to 10 MHz. The entity of light production by bioluminescence is related to the depth of the submarine site which hosts the telescope. The deeper the site, the less contribution of bioluminescence. In the case of one KM₃NeT 3-inch PMT, the related optical background rate can be obtained from the measured one at the ANTARES site, simply considering a conversion factor of 0.1, given by the ratio of the PMT areas. This implies that for a 3-inch PMT the ^{40}K background continuous rate is ~ 5 kHz.

RADIOACTIVITY Seawater contains a small amount ($\sim 0.04\%$) of radioactive isotopes, such as Potassium-40 (^{40}K), that has two main decays channels:



The electrons produced in the first process can achieve a maximal energy of 1.33 MeV and can produce Cherenkov light. Furthermore, the photon produced in the second reaction has an energy of 1.46 MeV, which can generate, through Compton scattering, an electron over the Cherenkov threshold. Radioactive decays may produce photons in a time window of 1 ns, giving rise to coincidences on neighbouring PMTs.

DARK CURRENT RATE This type of background is the rate measured by photosensors without external light sources. It is usually generated by thermal noise inside the PMT or by radioactive decays in the glass sphere or in the optical gel.

BIOLUMINESCENCE Almost 90% of the organisms that inhabit the deep ocean are capable of emitting a burst of light through the chemical process of bioluminescence. The measurements performed at the KM₃NeT/ARCA site (at 3500 m below sea level), after more than one year of data taking, showed a stable average rate at ~ 5 kHz, which comes from a quasi-pure ^{40}K contribution. The fraction of times the rates were above 100 kHz was less than 0.5%. In the French site of the KM₃NeT experiment, which is shallower than the Italian site, bioluminescence measurements show higher rates, with an average of ~ 9.5 kHz for the 31 3-inch PMTs of the DOM.

2.5.2 Physics background

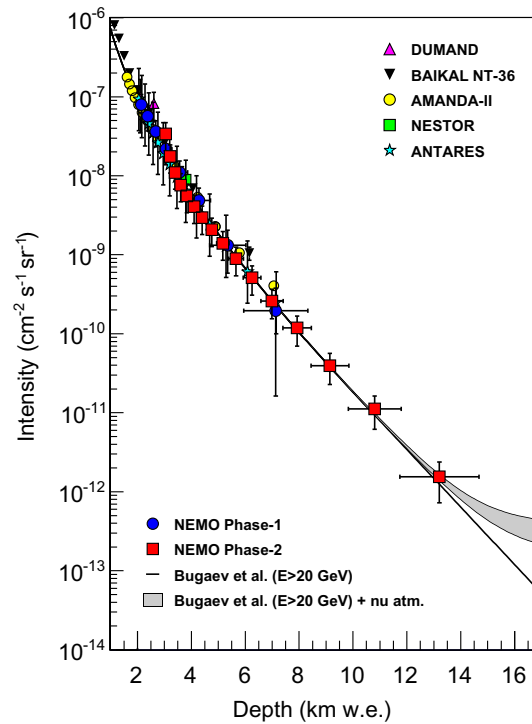


Figure 25: Vertical muon intensity versus depth (expressed in km of water equivalent) measurements for the NEMO Phase-2 tower (pathfinder detector of KM₃NeT/ARCA). For comparison, the results of other experiments and the expected theoretical flux of the Bugaev model [66] are shown. Figure taken from [67].

As already reported in previous sections, atmospheric muons represent, in underwater and under-ice experiments, the bulk of events registered. These highly penetrating particles can reach the detector even if they are located below several kilometres of water or rock.

There is a formula that relates the intensity of muons in the vertical direction as a function of depth, called *Depth Intensity Relation* (DIR). As the underground detectors are at a fixed depth, in principle only one point can be measured. However, when measuring the muon intensity at different zenith angles θ , the amount of material changes. Therefore, DIR $I_\mu(h, \theta)$

can be expressed as a function of a given direction θ , corresponding to a slant depth h , and is shown in Figure 25. Assuming that the muon spectrum at sea level is approximated by a power law $I_\mu(> E_\mu) = A \cdot E_\mu^{-\gamma}$, and using Equation 81, relating the muon range (R) with its energy, the DIR can be written in the following form:

$$I_\mu(> E_\mu, R) = A \left[\frac{\alpha}{\beta} (e^{\beta R} - 1) \right]^{-\gamma}. \quad (87)$$

In Figure 26 instead the intensity of the flux of atmospheric muons is shown at a fixed depth of 2400 m. It is a factor $\sim 10^6$ times higher than the flux of atmospheric neutrinos interacting inside or near the detector. For this reason, in order to remove this huge background, a geometrical

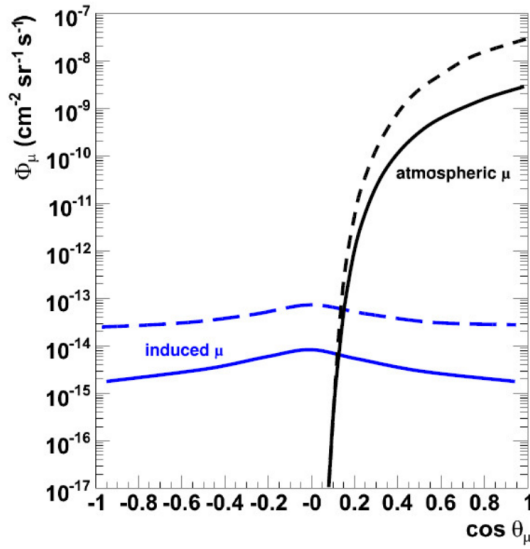


Figure 26: Different contributions to muon background as a function of the cosine of zenith angle at a depth of 2400 m, for two different energy regimes (dashed: $E_\mu > 100$ GeV while solid: $E_\mu > 1$ TeV). Black lines refer to atmospheric muons, while blue lines refer to muon induced by an atmospheric neutrino.

selection is applied. Atmospheric muons can only generate downward-going tracks, while upward-going tracks can only be produced by neutrino-induced muons that interact in the proximity of the detector. Nevertheless, atmospheric muons can leave an event signature in the detector that can be mis-reconstructed as upward-going particles. The methods to further reject this source of background highly depend on the reconstruction algorithm capability, and it is different in every neutrino telescope. At the same time, events induced by atmospheric neutrinos represent a small but irreducible background present in the detector (blue line in Figure 26 and uniformly distributed in $\cos \theta_{zenith}$ between -1 and +1).

2.6 CURRENT STATUS AND PROSPECTS FOR NEUTRINO ASTRONOMY

In recent years, neutrino astronomy has evolved rapidly consolidating its practices and analysis methodologies. Some recent breakthrough discoveries have demonstrated, once for all, the performances and capabilities of this field, highlighting its importance in the context of multi-messenger astronomy. IceCube detector, with its 1 km^3 of active volume and more than 12 years of livetime in this configuration geometry, is the leading experiment in the field. Nevertheless, more and more neutrino telescopes are taking data or are under construction (a comprehensive list was produced in previous sections), reaching their final configuration ($\sim 1 \text{ km}^3$) in a couple of years from now. This will improve and complement the field of view of the IceCube detector, pushing further current limits and boosting discoveries. In this section, a brief recap of the status of this field is given.

2.6.1 All-sky diffuse neutrino signal

The first evidence of the existence of astrophysical neutrinos was provided by the IceCube Collaboration in 2013, detecting an excess of events coming from all the sky at high energy with respect to the expected atmospheric background. Since then, the diffuse all-sky flux has been studied through different neutrino detection channels and topologies. The following is a tentative list of the most updated analyses and consequent results:

- the first measurement of the all-sky diffuse neutrino flux was performed with events with energies ranging between 30 TeV and 1200 TeV: 28 events were observed, against a background expectation of 10, statistically significant at a level higher than 4σ , see Figure 27 [68].

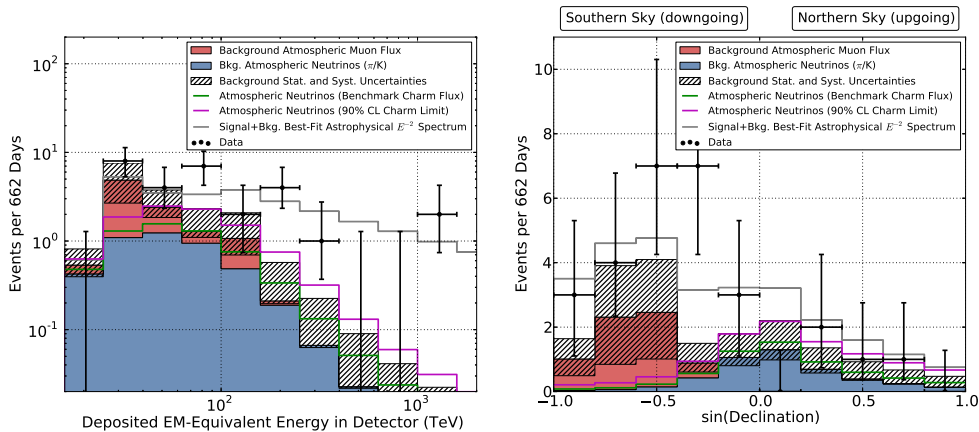


Figure 27: Energy and declination distribution of the observed events compared to model predictions by the IceCube detector. Figure taken from [68].

The event selection exploited was based on the search for neutrinos with vertices well contained within the detector volume and at high energies. This event sample is, in fact, also known as *High Energy*

Starting Events (HESE). The search methodology is sensitive to neutrinos of all flavours and from all directions and is capable to reduce the background, not only from atmospheric muons, but also from atmospheric neutrinos. An improvement of this result was obtained, including an additional 4.5 years of data, newer glacial ice models, and improved systematic treatment. From this sample, an astrophysical neutrino flux was measured and characterised to follow a single power law with a spectral index of 2.87, rejecting the background hypothesis over 5σ [69].

- a second sample used to address the diffuse astrophysical neutrino flux is the so-called *Northern Sky tracks*. This data set consists of a high purity sample of neutrino-induced muon tracks from the Northern celestial hemisphere, for a total livetime of 9.5 years. The best-fit parameters, under a single power law assumption, result in a per-flavour normalisation $\Phi_{@100\text{TeV}}^{\nu_i+\bar{\nu}_i} = 1.44 \cdot 10^{-18} \text{ GeV}^{-1} \text{ cm}^{-2} \text{ s}^{-1} \text{ sr}^{-1}$ and a spectral index of 2.37, constrained in the energy range from 15 TeV to 5 PeV [70];
- a third sample, for a total lifetime of 6 years, is the one exploiting cascades. Assuming standard neutrino oscillations, this cascade sample is dominated for the $\sim 90\%$ by electron and tau neutrinos. The sensitive energy regime is from 16 TeV to 2.6 PeV, consistent with a single power law model. The best-fit parameters are flux normalisation $\Phi_{@100\text{TeV}}^{\nu_i+\bar{\nu}_i} = 1.66 \cdot 10^{-18} \text{ GeV}^{-1} \text{ cm}^{-2} \text{ s}^{-1} \text{ sr}^{-1}$ and the spectral index of 2.53 [71]. The energy distribution for this data set is reported in Figure 28;

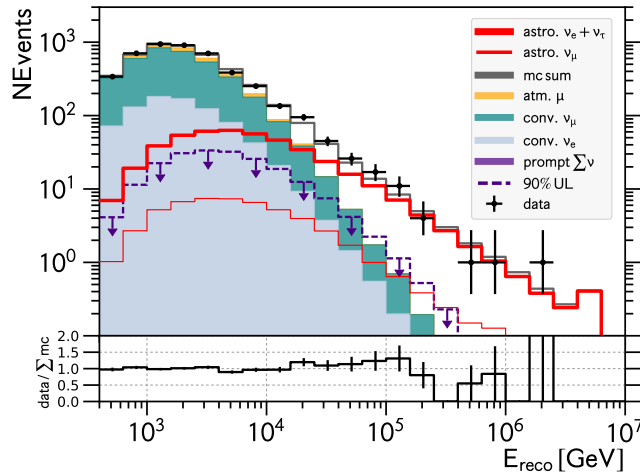


Figure 28: Energy distribution of the observed cascade events compared to model predictions by the IceCube detector. Figure taken from [71].

- a fourth sample, presented for the first time in 2023, comprising 10.3 years of IceCube data, is composed of starting track events. It combines an excellent angular and energy resolution [72]. Veto techniques, similar to those employed for HESE data sample, allow an efficient

reduction of the atmospheric neutrino rate from the Southern sky, accessing the astrophysical neutrino flux well below 100 TeV. In total, 1/3 of the events included in this sample come from the Southern sky. This sample is also known as *Enhanced Starting Track Event Selection (ESTES)*. The best-fit parameters found, under the single power law assumption, are normalisation $\Phi_{@100\text{TeV}}^{\nu_i+\bar{\nu}_i} = 1.68 \cdot 10^{-18} \text{ GeV}^{-1} \text{ cm}^{-2} \text{ s}^{-1} \text{ sr}^{-1}$ and a spectral index of 2.58, with the 90% sensitive energy range between 3 and 550 TeV. With this data set, the search for a specific emission from the Galactic plane was also performed, not finding any significant excess.

Other data samples have been exploited by IceCube Collaboration during the years trying to address and characterise the diffuse astrophysical neutrino flux, although the ones listed above are the main results obtained up to now. Furthermore, for the first time, a general combination of IceCube data sets was produced, taking advantage of coherent signal and background modelling, as well as detector response and systematic uncertainties [73]. The best-fit value for the combination has been found to be, under the single power law assumption, $\Phi_{@100\text{TeV}}^{\nu_i+\bar{\nu}_i} = 1.8 \cdot 10^{-18} \text{ GeV}^{-1} \text{ cm}^{-2} \text{ s}^{-1} \text{ sr}^{-1}$ and a spectral index of 2.52.

In addition, other neutrino telescopes observed the all-sky diffuse flux. Baikal-GVD reported the observation of high-energy neutrinos using cascade-like events with data collected from 2018 to 2021 [74]. An excess of events was found with respect to the expected atmospheric background at a level of 3.05σ . Assuming a single power law model, with identical contribution from all flavours, the best-fit parameters found were $\Phi_{@100\text{TeV}}^{\nu_i+\bar{\nu}_i} = 3.04 \cdot 10^{-18} \text{ GeV}^{-1} \text{ cm}^{-2} \text{ s}^{-1} \text{ sr}^{-1}$ and a spectral index of 2.58.

The ANTARES neutrino telescope also observed a mild excess of events at high energies, with a combined data set containing both tracks and cascades. The resulting best-fit parameters found are $\Phi_{@100\text{TeV}}^{\nu_i+\bar{\nu}_i} = 1.5 \cdot 10^{-18} \text{ GeV}^{-1} \text{ cm}^{-2} \text{ s}^{-1} \text{ sr}^{-1}$ and a spectral index of 2.3. The significance of this excess over the background-only hypothesis is 1.8σ .

The single power law, isotropically distributed assumption made to model the diffuse all-sky neutrino flux is generally accepted by the community. It minimises the number of free parameters and the starting hypothesis for the modelling. Furthermore hints for substructures in the spectrum seen in independent measurements are so far not statistically significant. A critical discussion of the single power law assumption is available here [75].

A graphical summary of the results presented above is also available in Figure 29. The first evidence, once they are compared, is that the data sets are not fully compatible with the same power law spectrum. IceCube Collaboration reported a discrepancy greater than 3σ between HESE and Northern Sky Tracks, known also as *spectral anomaly*. This could suggest that a multi-component spectrum has been observed, specifically a Galactic contribution on top of the extra-Galactic one. The recent discovery of a diffuse neutrino emission from the Galactic plane (see Section 5.3), and other hints, like the excess of events coming from the Southern sky larger

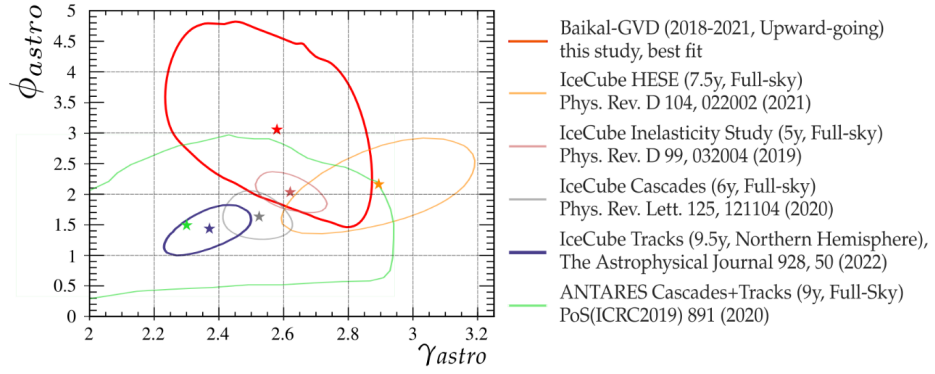


Figure 29: Summary of the principal results for the search of the all-sky neutrino emission. Two-dimensional confidence region for the best-fit astrophysical parameters: $\Phi_{@100\text{TeV}}^{\nu_i+\bar{\nu}_i}/10^{-18} \text{ GeV}^{-1} \text{ cm}^{-2} \text{ s}^{-1} \text{ sr}^{-1}$ and spectral index. Figure taken from [74].

than what is expected assuming isotropy are supporting this hypothesis. A preliminary estimate of the Galactic contribution to the all-sky diffuse flux was also evaluated at the level of $\sim 6\text{-}13\%$ at 30 TeV. However, its relative contribution is still very difficult to address, worsened by different spectral assumptions and tested energy ranges. A critical revision on the IceCube spectral anomaly and on the possible Galactic contribution is available here [76].

Furthermore, to definitively solve this puzzle, a careful evaluation of the prompt atmospheric contribution should be made. As described in [40], shower-like events are the most promising channel to address this measurement, specifically in the energy range between 1-200 TeV, since the conventional atmospheric component is a factor ~ 30 less important for electron than for muon neutrinos. In this energy range, the number of prompt and cosmic neutrinos for the cascade channel are indeed very similar to each other, requiring great care in the handling of the data set and trying to disentangle these two components.

2.6.2 Point-source searches

Another breakthrough discovery, recently reported by the IceCube Collaboration, is the first evidence of neutrino emission from the nearby active galaxy NGC1068 [77]. Data collected from May 2011 to May 2020 were analysed, searching for point-like neutrino sources in the Northern sky, where IceCube is more sensitive to astrophysical sources. A probability skymap of the Northern hemisphere is shown in Figure 30.

The quoted angular resolution is 1.2° at 1 TeV, 0.4° at 100 TeV, and 0.3° at 1 PeV. In this specific work, 110 sources have been selected on the basis of their γ -ray flux, and tested for a possible neutrino emission. Above all, NGC1068 was the most significant, with 79 signal events detected and a local post-trial p-value corresponding to a significance of 4.2σ . The best-fit

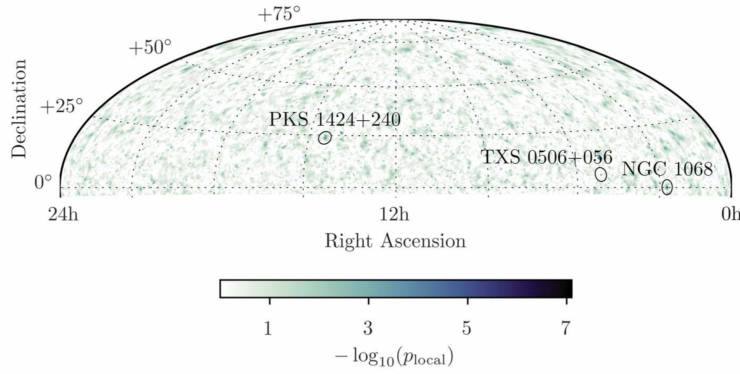


Figure 30: P-value sky map of the scan of the Northern hemisphere, searching for point-like neutrino emission. Figure taken from [77].

values obtained, under a single power law assumption, were a spectral index equal to 3.2 and a normalisation at 1 TeV of $\Phi_{@1\text{TeV}}^{\nu_i+\bar{\nu}_i} = 5.0 \cdot 10^{-11} \text{ TeV}^{-1} \text{ cm}^{-2} \text{ s}^{-1}$. The main contribution to the excess comes from energies ranging from 1.5 to 15 TeV. Assuming an isotropic emission for this source, and a distance of 14.4 Mpc, this leads to a neutrino luminosity $L_\nu = (2.9 \pm 1.1) \cdot 10^{42} \text{ erg s}^{-1}$, an order of magnitude higher than the equivalent γ -ray luminosity observed in the energy range between 100 MeV - 100 GeV. The source was detected by the Fermi-LAT satellite in the energy range $\sim 0.1\text{-}30 \text{ GeV}$, but the MAGIC telescope did not observe any higher-energy γ -ray. This no-observation can be explained assuming NGC1068 as a γ -obscure source (see Section 1.3.2). Some theoretical models predict the neutrino and γ -ray emission to originate from the obscured environment around the AGN of NGC1068. In these models, the supermassive black hole in the AGN is the right acceleration site, producing also strong X-ray emission from the hot plasma above the accretion disk, called *corona*. Future MeV-scale observations of NGC1068 would provide a powerful probe of the physics nature of this source.

The other two sources with the highest significance observed were TXS0506+056 (3.5σ) and PKS1424+240 (3.7σ). The significance related to TXS0506 is the time-integrated over the entire data set, while previous analyses found evidence of transient emission from this source (see Section 2.6.3).

Another important connection, with the arguments already treated above, is the contribution of these sources to the all-sky diffuse flux. NGC1068 and TXS0506 can contribute up to $\sim 1\%$ to the diffuse flux, even if the energy range of the spectrum, measured for NGC1068, does not strongly overlap with that of the diffuse flux, and the fitted spectral index is much softer than the 2.53 measured, as shown in Figure 31.

The discovery potential for NGC1068 for the KM₃NeT/ARCA detector, in its final configuration, is reported in Figure 31. Assuming the best-fit spectral index of 3.2, a 5σ discovery can be claimed after 3 years of operation.

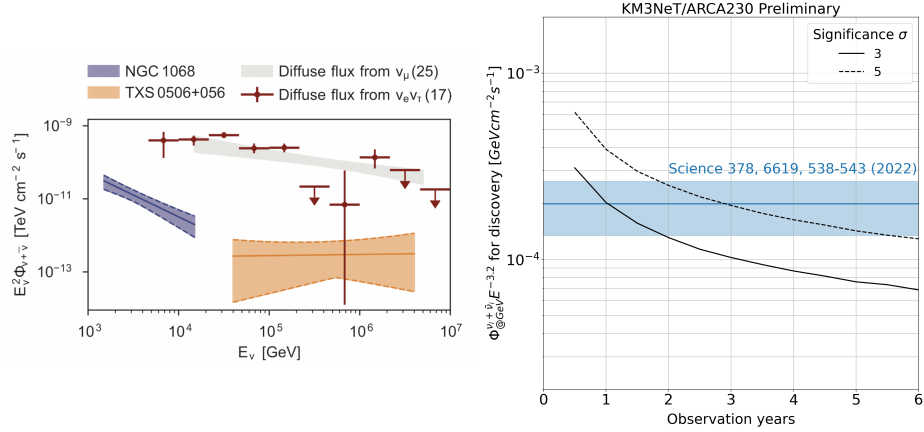


Figure 31: **Left:** comparison of point-source best fitted fluxes with respect to the total diffuse astrophysical neutrino flux measured by IceCube Collaboration [70]. Figure taken from [77]. **Right:** discovery flux of KM₃NeT/ARCA in its final configuration for source NGC1068, assuming the best-fit spectral index $\gamma=3.2$. Figure taken from [78].

2.6.3 Neutrino emission from the direction of the blazar TXS0506+056

One of the first breakthrough discoveries in neutrino astronomy occurred in September 2017 [79]. For the first time, a neutrino event was detected in spatial and time coincidence with a γ -ray flaring source, named TXS0506+056, with the most probable energy of 290 TeV. The association with the position of the source TXS0506+056 was performed shortly thereafter, thanks to the observations conducted by the Fermi-LAT detector. Also, the MAGIC telescope followed up the alert by detecting photons from the source up to 400 GeV. The significance of spatial and temporal coincidence was estimated to be greater than 3σ . Other specific analyses have been carried out by searching, within the registered data, for other significant clusters in time of events in coincidence with the source, as shown in Figure 32. A second

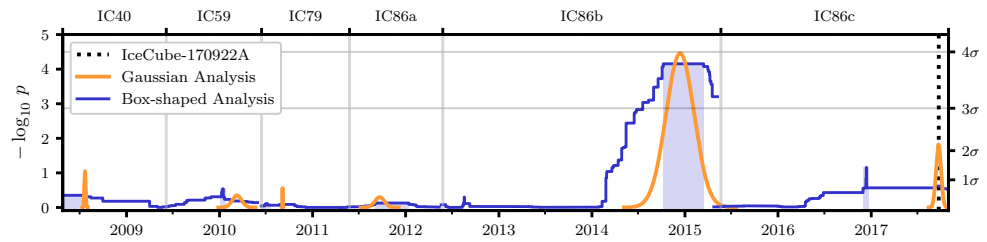


Figure 32: Time-dependent analysis results. Central time and width are plotted for the most significant cluster of events in time, with the p-value of the result shown by the height of the peak. The orange curves represent the search using a Gaussian-shaped time profile, while the blue curves represent the box-shaped time profile. Figure taken from [79].

excess of events was found, dated December 13th 2014, see Figure 32. The observed significance for the cluster of events was 3.5σ or 3.7σ , depending

on the time profile assumed to model the emission and on the energies of the events and their proximity to the source.

2.6.4 *Neutrino association with tidal disruptive events*

The observation of point sources emitting neutrinos, discussed in Section 2.6.2 and the Galactic neutrino contribution, have still left open the question of which kind of extra-Galactic sources are responsible for the diffuse astrophysical neutrino flux. Another population found in association with neutrino emission was Tidal Disruptive Events (TDEs). These are rare astrophysical events that occur when a star passes close to a supermassive black hole, sitting at the centre of a galaxy. The star, subjected to the intense gravitational field, can disintegrate leaving its material orbiting around the black hole itself. On October 1st 2019, IceCube reported the detection of a high-energy neutrino candidate event, with an estimated energy of ~ 0.2 PeV. The event has been associated in time and space by the Zwicky Transient Facility (ZTF) with the radio-emitting TDE AT2019dsg. Another coincident observation occurs in May 2020, with the TDE AT2019fdr discovered by ZTF one year earlier. During this time window, AT2019fdr was not observed in any of the X-ray observations by the Swift-XRT telescope or in the γ -ray surveys conducted by the Fermi-LAT telescope. Theoretical models have suggested that TDEs can be high-energy neutrino sources and, in particular, those showing relativistic jets. A further work [80] identified a third event in coincidence with a high-energy neutrino alert and a 3.7σ correlation between a wider set of similar TDE-like flares and IceCube alerts.

2.6.5 *Neutrino directional association with blazars*

In the recent years several analyses have shown statistically significant coincidences between high-energy neutrinos and blazars. A first association was made by selecting IceCube track-like neutrino events above some TeVs in coincidence with radio-bright blazars [81]. Radio observations were carried out through Very Long Baseline Interferometry (VLBI), and capable of resolving the central part of AGN. Moreover, on average these potential neutrino sources exhibited radio flares at the time of the neutrino arrival. TXS0506+056 is, for example, a typical bright blazar both in radio and in γ -ray. The coincidence of neutrinos with a subset of radio-bright blazars is found to be statistically significant at the level of 4.1σ : 70 blazars were found in association with neutrinos. The consequent estimate of the neutrino fluence implies that blazars, hosting radio-bright jets, could explain at least $1/4$ of the entire all-sky diffuse neutrino flux, without requiring any extreme conditions in the source environment.

A similar tentative association has been performed with data collected by the ANTARES neutrino telescope [82]. The association has been tested by means of a neutrino-blazar pair-counting analysis, by a time-integrated likelihood approach, and also by a time-dependent likelihood scan. The

first counting analysis, conducted on the same blazar catalogue used in the IceCube search, produced 469 associations compared to the 410 expected (excess of 2.2σ). Even the other two likelihood searches produced similar results in terms of statistical significance. As a follow-up study, the most significant sources, associated to the highest p-value in the likelihood scan, have been compared to radio light curves, extracted from Owens Valley Radio Observatory (OVRO). An intriguing overlap has been observed in coincidence with the source J0242+1101 and its largest radio flare, as reported in Figure 33. Additionally, Fermi-LAT and IceCube public data related to the source have been investigated. In both cases, the most noticeable flare seen in the last decades was in coincidence for all the four spectra. The chance of the triple coincide between the observed flares by Fermi, OVRO, and ANTARES has been studied and found to be at the level of 2.9σ . This is an estimate that confirms the strong connection between variable neutrino and electromagnetic emissions and motivates further studies with more observational data in the future.

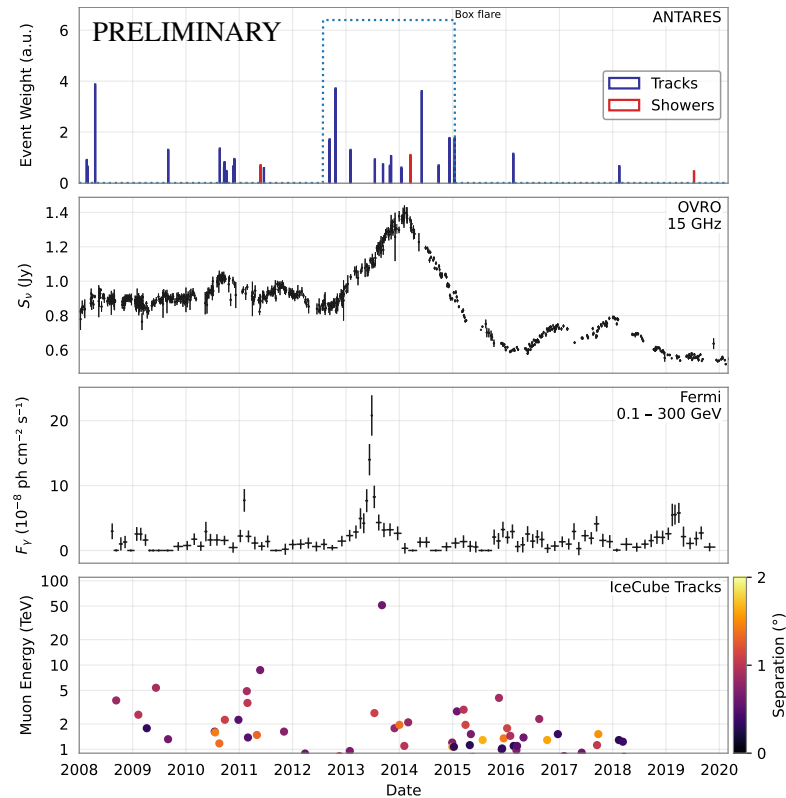


Figure 33: Light curves from the direction of the blazar J0242+1101 as a function of time observed, respectively from top to bottom, by: ANTARES, OVRO, Fermi-LAT, and IceCube. Figure taken from [82].

KM₃NeT DETECTORS

KM₃NeT is a European research infrastructure building second-generation multi-km³ neutrino telescopes. It will host a network of Cherenkov detectors, located at the bottom of the Mediterranean Sea: it, in fact, represents a favourable environment for the construction and operation of neutrino telescopes in its abyssal sites. The KM₃NeT (acronym for Cubic Kilometre Neutrino Telescope) design was built under the return of experience gathered with the first-generation neutrino telescope built in the Mediterranean Sea, ANTARES [83], in operation for more than fifteen years and dismantled in February 2022. This was the first experiment that demonstrated the feasibility of measuring neutrinos in the deep sea with Cherenkov detectors. KM₃NeT comprises mainly two sites, related, respectively, to the two main physics goals of the experiment:

KM₃NeT/ARCA stands for ‘Astroparticle Research with Cosmics in the Abyss’. It is located ~ 100 km offshore the Sicily coasts at a depth of 3500 metres, and aims to detect and characterise sources responsible for the production of astrophysical neutrinos. In its final configuration, it will instrument more than one cubic kilometre of seawater.

KM₃NeT/ORCA stands for ‘Oscillation Research with Cosmics in the Abyss’. It is located ~ 40 km offshore the Southern French coasts at a depth of 2500 metres, ~ 10 km far from the ANTARES deployment site, and will address the question of neutrino mass hierarchy through the detection of atmospheric neutrinos, instrumenting in its final configuration ~ 7 Mton of seawater.

The two detectors exploit the same construction technology, namely a 3D array of photosensors and the same detection principle. The main difference lies in the spacing between the modules itself, optimised for the detection of the abundant flux of atmospheric neutrinos in the few-GeV (KM₃NeT/ORCA) or for the rarer astrophysical neutrino fluxes in the TeV-PeV range (KM₃NeT/ARCA).

3.0.1 The multi-PMT Digital Optical Module



Figure 34: **Left:** picture of the KM₃NeT digital optical module. **Right:** schematic representation of the components inside a DOM. Taken from [84].

The Digital Optical Module (DOM) developed by the KM₃NeT Collaboration is an innovative multi-PMT solution enclosed in a single pressure-resistant glass sphere of 0.44 m diameter [85]. It contains 31 3-inch photomultiplier tubes (PMTs), all electronics for the power and data acquisition system, and all calibration devices. The innovative design was proposed for the first time in 2003 and the first prototype was qualified, in deep water, in 2013. With respect to other solutions used previously by other neutrino telescopes, like the 10-inch photomultiplier tubes adopted in ANTARES or in IceCube, the segmentation of the KM₃NeT DOM has three times the photocathode area and also better photon-counting performances and better position and timing calibrations. Coupled with the required nanosecond timing accuracy, it also allows defining local triggers (implemented onshore) to easily reject the environmental background (see Section 2.5.1). Furthermore, considering the inaccessibility of the site, the impact of a failing PMT on the overall detector performance is reduced since the module can still be operated efficiently. For what concern the technical implementation, PMTs have a convex bialkali photocathode with an 80 mm diameter and a 10-stage dynode structure. A polished metal ring surrounds the head of each PMT, placed at an angle of 45° and providing a 92% reflectance for optical photons, with the main goal of increasing photon acceptance by 20-40%. The PMTs are placed in rings, evenly spaced by 60° in azimuth: 19 PMTs are arranged in the lower hemisphere of the optical module and 12 in the upper one. Even the displacement of PMTs has been optimised considering the event topologies of signal events (mainly upgoing events) and considering that sedimentation will affect primarily the top hemisphere of the module, reducing the view efficiency of those PMTs. For this reason, electronics and mechanical supports are placed in the top part of the DOM. A portion of the top surface of the DOM is occupied by a mushroom-shaped aluminium structure, specifically designed to dissipate heat generated inside the module, transferring it to the sea. The DOM is optically and electrically connected to the network of the telescope via a hole, in the upper glass sphere, and equipped with an hermetic pressure resistant penetrator for

copper wires and optical fibres. In turn, each module is enclosed in a titanium collar with polyethylene bollards to anchor it to the Dyneema® ropes of the Detection Unit (see Section 3.0.2). The geometry of the full detector is affected by the sea current and the position of the modules varies. At the same time, the reconstruction precision needed for targeting neutrino sources requires a position resolution of the optical modules on the order of 10 cm. For this reason, each module is equipped with calibration devices that provide tilt, pitch, and yaw to continuously measure its position and orientation. In addition, an acoustic positioning system is used, comprising a long baseline of acoustic emitters anchored at the seabed, hydrophones at the base of the detection unit, and piezoelectric acoustic sensors in each module. For timing calibrations, instead, each module is equipped with a 470 nm LED pulser, called *nanobeacon*, producing fast light pulses for timing calibration of neighbouring DOMs. Nanobeacons are operated only during dedicated calibration runs.

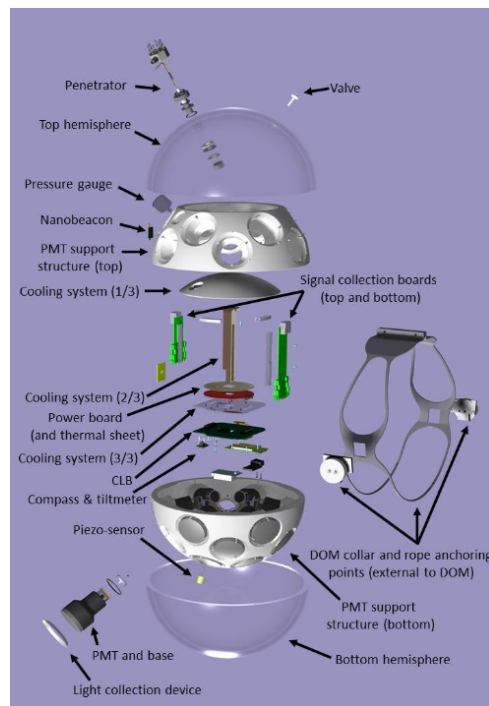


Figure 35: Exploded view of the KM₃NeT DOM. Taken from [86].

3.0.2 Detector layout

A collection of 18 optical modules are connected together in a vertical structure called Detection Unit (DU) or string. Each DU is anchored on the seafloor and is taught by buoyancy at the top to reduce the horizontal displacement of the top relative to the base, in case of large sea currents. For power supply and optical data transmission, each DU also comprises an electro-optical cable, connected to the base module at the bottom of the string. Each DU is connected in turns to a complex submarine network of

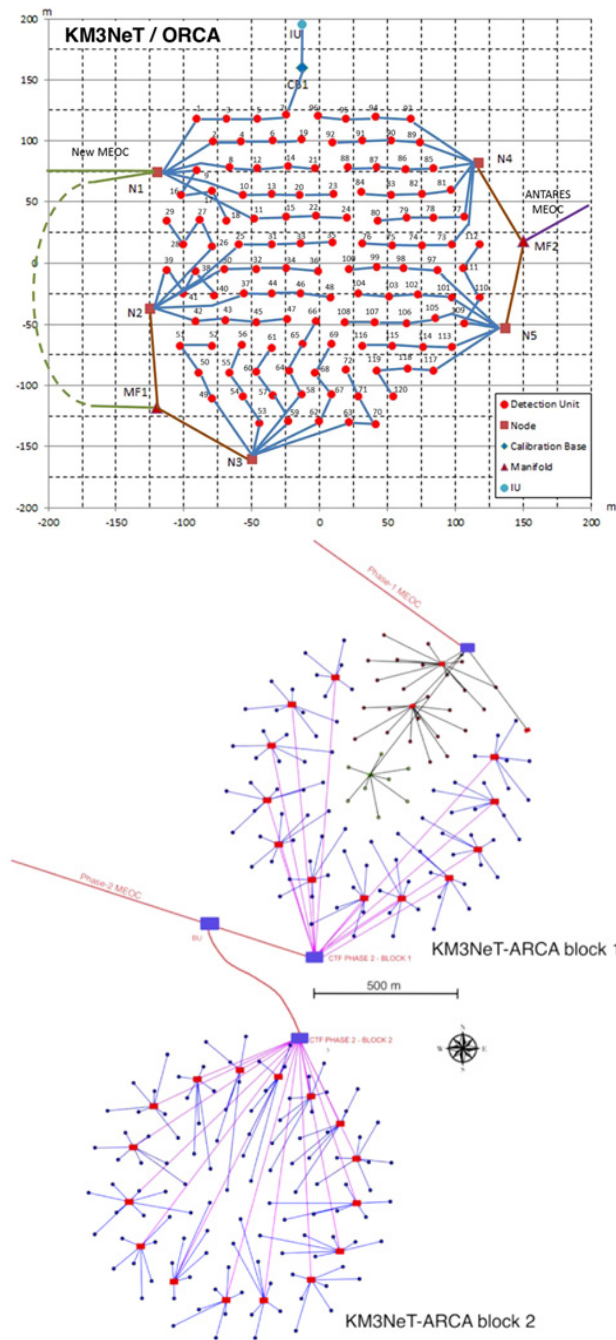


Figure 36: Detector footprint for KM3NeT/ORCA (top) and for KM3NeT/ARCA (bottom) in their final configuration. Taken from [86].

cables and junction boxes, specifically designed and deployed. The whole detector is connected to the shore station via several main electro-optical cables containing a limited number of optical fibres, but capable of guaranteeing the required bandwidth.

In their final configurations, the KM3NeT detectors will be organised in Building Blocks (BB) of 115 strings each, 1 BB for KM3NeT/ORCA and 2

BB for KM₃NeT/ARCA. The footprint of the detectors is shown in Figure 36.

The detector layout is therefore defined by the inter-DOM distance within a DU and by the distance between DUs. As already mentioned in the previous section, in order to target the specific goal for which KM₃NeT detectors are designed, KM₃NeT/ARCA has an inter-DOM distance of 36 metres, and the distance between neighbouring DUs is ~ 100 m, trying to instrument the largest volume of seawater, preserving the ability to reconstruct high-energy particles. DOMs in KM₃NeT/ORCA are 9 metres away and the DUs are spaced by 20 metres, creating a denser environment.

3.1 DATA ACQUISITION SYSTEM

In order to reduce the complexity of the hardware inside the optical modules, the "all data to shore" concept is adopted: all the photon hits are sent to shore via a computer network which comprehends both the shore-station and the detector. In the final configuration, the expected data throughput from both sites is up to 500 Gbps. This implies that most of the detected photons come from the environmental background (⁴⁰K decay) at a rate of 5 kHz per PMT. This must be compared with the signal event rate: astrophysical neutrinos ~ 3 events/day in ARCA and atmospheric neutrinos $\sim 50,000$ events/year reconstructed in ORCA, having a signal-to-noise ratio of about 1 in a million. For this reason, the performance required are: nanosecond timing accuracy on the photon arrival time, effective and fast onshore on-line trigger algorithms searching for correlations between all the photon hits sent from the detector, rejecting environmental background. Concerning the technical implementation, DOMs and base modules are submarine nodes of the global networking infrastructure, together with the computing resources of the shore station. The largest part of the data stream sent from the detector to shore contains digitised signals from the PMTs, samplings of the acoustic waveform for detector positioning, and a continuous stream of summary information sent by each DOM. The traffic required to the slow-control section and from other instruments is negligible, while each DOM is linked to the onshore network infrastructure with a dedicated 1 Gbps connection. Therefore, the main characteristic of the network is its asymmetry, which originates after the so-called *optical broadcast* architecture adopted for the global optical infrastructure. It consists of few downstream optical links that broadcast slow control commands to the DOMs, while the upstream links (one per DOM) transport the collected data to the shore station. Exploiting these connections, a White Rabbit Switch fabric is used to achieve the required sub-nanosecond synchronisation among the DOMs. The data stream that arrives at the shore station is handled by a complex, specifically designed architecture of queuing and filtering software. The filtered data is then routed to a process that writes them to a ROOT-based file on local storage.

The signal received from PMTs is digitised as photon hit, defined as integrated electric charge of the PMT signal over a certain threshold, the crossing time and the duration of that Time over the Threshold (ToT).

3.2 TRIGGER

Trigger algorithms are the very first step in selecting physical events and reducing environmental background. However, an optimised balance is required among looser and stricter conditions, considering also the available resources in terms of computing and data storage. Within the KM3NeT experiment, trigger algorithms are based on the requirement of space-time correlations between the registered photon hits. The following filter steps are applied consequently to the data onshore, a part the first one, which is applied offshore:

- the level-zero filter (L0) is a threshold for the analogue pulses of the PMT. The threshold value can be modified online and is typically set at 0.3 photoelectrons;
- the level-one (L1) asks for a coincidence of two or more L0 hits from different PMTs in the same optical module, within a fixed time window, ΔT . The spread of this window is determined by possible delays occurring during photon propagation in water, due to, for example, scattering, setting typically values of $\Delta T = 10$ ns. The estimated L1 rate per optical module is about 1000 Hz, of which about 600 Hz from ^{40}K decays (in KM3NeT/ARCA environment). The rate of L1 coincidences depends on the assumed threshold set for the L0 filtering step;
- the level-two filter (L2) asks for coincidences on PMTs too, but with a further constraint on the angle between PMT orientation inside the DOM itself, further reducing the data rate by a factor two;
- SuperNova (SN) trigger is a specific trigger implemented for super-nova detection and is based on L1 hits with additional constraints on the number of hit PMTs.

At this point, other aggregation steps are performed, searching for and forming local clusters of hits that respect the following relation:

$$|\Delta t| < |\Delta r|/c_{\text{water}} + T_{\text{extra}}, \quad (88)$$

where Δt and Δr is the time difference and the distance between two hits within a possible cluster, c_{water} the group velocity of photons in water, i.e. c/n , and T_{extra} is the additional time window, accounted for timing uncertainties on photon propagation. After this step, all other hits that satisfy the following conditions are connected to the already clustered ones:

- hits are causally connected to at least 75% of the cluster hits;
- hits are closer than 50 m to at least 40 % of the cluster hits.

Then, optimised algorithms for different event topologies, track-like or shower-like, are applied in parallel to data: in fact *muon trigger* and *shower trigger* are defined.

MUON TRIGGER Under some approximations, i.e. ignoring the string movement due to sea current effects, point-like geometry for DOMs and straight line for muon tracks, the point of closest approach, called *hot spot*, of the muon track to the detector line can be determined. The hot spot represents the seed for finding other casually connected hit clusters. DOMs belonging to a single string are consecutively numbered along the z axis, and for a given DOM in position i , the adjacent and next-to-adjacent are those on the floor $i \pm j$ with $j = 1, 2$. To correlate hits between these DOMs, the arrival time of the photons must be within the interval:

$$\Delta t < j \cdot \Delta z \frac{n}{c} + t_s, \quad (89)$$

where Δz is the vertical distance between adjacent DOMs, n the refractive index of the medium and t_s the additional time delay.

SHOWER TRIGGER For shower events, the trigger is simpler, since the maximal 3D distance between PMTs can be applied without specific requirements on the direction of the shower. A maximum distance travelled by the light can be assumed, safely set to a few times the absorption length, without a significant loss of the signal. This reduces the number of PMTs to be considered and the time window that follows from causality.

3.3 EVENT RECONSTRUCTION

Various reconstruction algorithms have been developed, according to the specific event topology occurring in the detector. Since no selection is performed a priori, each event is reconstructed with all the algorithms.

3.3.1 Track reconstruction

The main goal of this reconstruction is the precise determination of the direction and energy of ultra-relativistic muons.

DIRECTION RECONSTRUCTION The 3-dimensional muon trajectory, assumed as a straight line, can be parameterised through five independent parameters: its direction angles, time, and position along the trajectory. The main issue is given by the non linearity of the problem, overtaken by the use of pre-fits to provide a meaningful set of starting values. Assuming a muon direction, a coordinate system can be defined with the z axis aligned with the trajectory. The trajectory traverses the point $z = 0$ at time t_0 and position x_0 and y_0 . In absence of scattering and dispersion, direct Cherenkov light is expected to be detected by PMTs at the time:

$$\hat{t}_i = t_0 + \frac{z_i}{c} + \tan(\theta_C) \frac{\rho_i}{c}, \quad (90)$$

$$\rho_i = \sqrt{(x_i - x_0)^2 + (y_i - y_0)^2}, \quad (91)$$

where ρ_i is the minimum distance, on the horizontal plane, of the muon trajectory to the PMT, the vector (x_i, y_i, z_i) represents the PMT position and θ_c is the Cherenkov angle. The linear pre-fit is sensible to outliers caused by environmental background, and by delayed scattered Cherenkov photons. In order to exclude these, a cluster of causally related hits is selected from the data (see Trigger section above). Possible outliers can also be subsequently removed based on their effect on the total χ^2 . The procedure is repeated for a scan of the assumed track directions with a typical grid angle of one degree. A set of n pre-fit directions provides a suitable start value for the subsequent fit stage. n is a parameter that the user can decide and adjust, now set to 50 for KM3NeT/ARCA.

Starting from the n pre-fits, the maximisation of the likelihood is performed, fitting simultaneously all the five independent parameters. In the likelihood function, the detector and physics effects are encoded thanks to probability density functions:

$$\mathcal{L} = \prod_{\text{hit PMTs}} \left[\frac{\partial \mathcal{P}}{\partial t}(\rho_i, \theta_i, \phi_i, \Delta t) \right], \quad (92)$$

where θ_i and ϕ_i are the orientations of the PMTs, and Δt is the time residual of the expected arrival time of Cherenkov photons with respect to the measured one. An example of the PDF describing photon scattering and muon energy losses is described in Section 2.5.

ENERGY RECONSTRUCTION The energy reconstruction of track-like events is carried out once the trajectory has been determined. Information concerning the spatial distribution of hit and non-hit PMTs is used. All PMTs within a predefined width (typically 200 m) around the muon trajectory are used to compute the hit probability.

3.3.2 Shower reconstruction

The shower reconstruction algorithm follows a two-step procedure: the fit of the vertex, based on hit times, and the estimation of direction and energy, using the probability of hit PMTs.

VERTEX FIT The fit of the shower vertex starts from a small sample of hits, which occurred to be in coincidence within 20 ns on the same DOM. Possible contamination coming from environmental background is reduced by exploiting an M-estimator score function, comparing the expected arrival time of photon hits, propagating on a spherical wavefront, with respect to the measured one. In this way, the best-fit shower position and the starting time are found, minimising the M-estimator.

DIRECTION AND ENERGY SHOWER FIT The fitted vertex position is used as a starting point for the direction and energy estimation of the

shower. The parameters are found starting from isotropic directions and minimising a likelihood function based on the hit/non-hit probability.

From preliminary estimates, once KM3NeT will be completed, the direction and energy of the shower can be reconstructed with a median angular resolution of 1.5 degrees and an error of approximately 5% in the energy estimate, as shown in Figure 37.

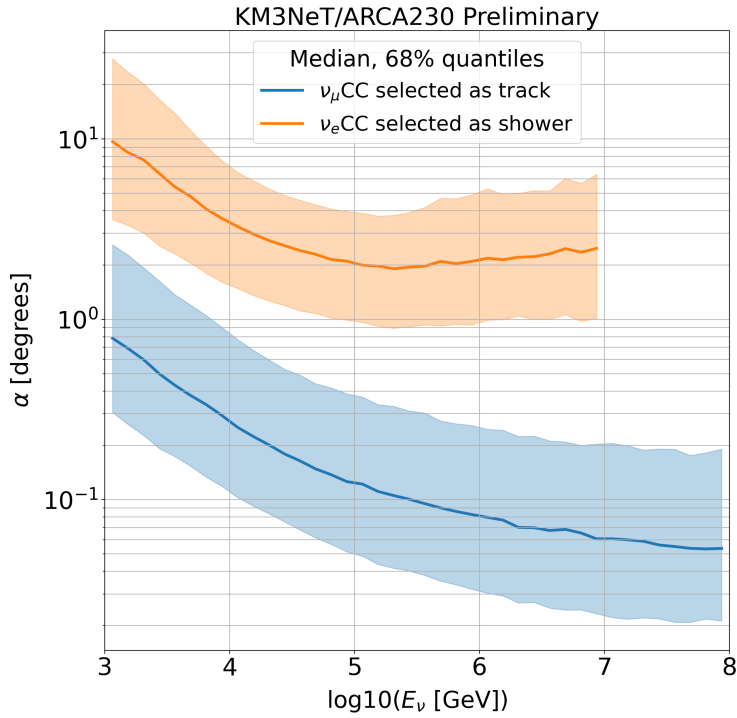


Figure 37: Angular resolution for track-like (ν_{μ} -CC) and shower-like (ν_e -CC) interactions, for KM3NeT/ARCA in its final configuration. For both samples, the selection is at the analysis level, once the atmospheric muon contamination is reduced. Figure taken from [78].

MONTE CARLO SIMULATIONS

Monte Carlo simulations are a key ingredient to interpret data recorded by the detector and to understand systematic effects. Inside the simulation package, the state of the art concerning theoretical knowledge on neutrino interaction processes and a deep understanding of the performances and characteristics of all detector elements are encoded. In the context of neutrino telescopes, Monte Carlo (MC) simulations can be subdivided into three main consecutive steps: event generation, containing the physical properties of particles, generated in the proximity of the detector; particle and light propagation up to the optical modules; detector response in terms of PMT behaviour, electronic response, data acquisition chain, and trigger algorithms. The software packages used within the KM₃NeT Collaboration have been partially developed within the ANTARES Collaboration and have been updated to km³ scale detectors.

4.1 EVENT GENERATION

The complete simulation of neutrino interactions and of atmospheric muon bundles reaching the detector could be computationally intensive. For this reason, particles are generated in the proximity of the detector. The instrumented volume can be seen as a cylinder that contains all the DOMs. At the same time, particles that interact in its proximity can generate Cherenkov light that reaches the optical modules. For this reason, the active volume is defined as a cylinder, called *can*, having the bottom bounded by the seabed and surrounding the instrumented volume, see Figure 38. The extension of the can is defined by its radius, equal to n absorption lengths ($R_{can} = n \times \lambda_{abs}$) and by Z_{can}^{max} . All the events that produce, directly or through secondary products, Cherenkov radiation inside the can are stored in the output file.

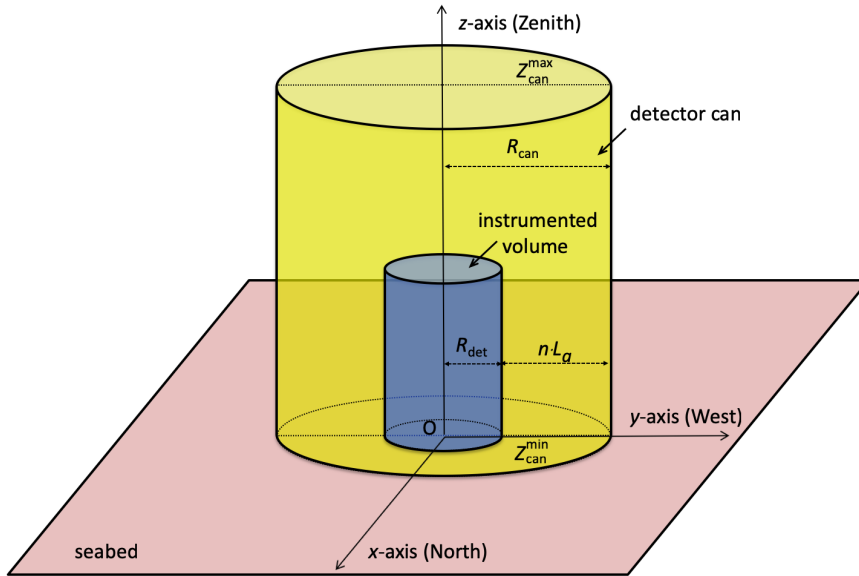


Figure 38: Definition of the detector can. Figure taken from [87].

NEUTRINO EVENTS The software used to simulate neutrino interactions inside the detector, developed within the KM₃NeT Collaboration, is gSeaGen [87]. It is a GENIE based code capable of simulating neutrino interactions induced by all flavours (muon, electron, and tau neutrinos, interacting via neutral or charged current) with energies up to several PeV. Neutrino fluxes can be simulated isotropically in the sky or coming from a specific localisation. An important concept is also the *interaction volume*. It is defined as the volume surrounding the detector in which a neutrino interaction can produce detectable particles. Even in this case, it is defined as a cylinder around the can made of seawater or rock. The size of the interaction volume is defined by the type of neutrino event: for shower-like events, specifically ν_e -CC and all NC interactions, the interaction volume coincides with the can. For track-like events, instead, muons produced in neutrino interactions can propagate for several kilometres reaching the can, even if the vertex is outside it. In this case, the interaction volume is computed taking into account the muon range in water or rock. When the ν_τ -CC interaction occurs, a muon can be produced as a result of τ decay. Even in this case, the interaction volume is defined by the muon range. The muon propagation code used in the context of the gSeaGen library is the internal PropaMuon or an external one, such as MUSIC [88] or PROPOSAL [89]. The neutrino energy is always simulated according to a power law spectrum. The code then provides a proper weight for each event that can be used to re-weight the generated events according to a specific atmospheric or astrophysical flux.

The weight of each event can be seen as $w_{\text{evt}} = w_{\text{gen}} \cdot \Phi(E, \theta, \phi)$, with $\Phi(E, \theta, \phi)$ representing the neutrino flux and the generation weight given by:

$$w_{\text{gen}} = \frac{I_E \cdot I_\theta \cdot T_{\text{gen}} \cdot A_{\text{gen}} \cdot N_\nu \cdot E^X \cdot P_{\text{scale}} \cdot P_{\text{Earth}}(E; \cos\theta)}{N_{\text{Tot}}} \quad (93)$$

with:

- I_E is the energy phase space. It is the integral of the generation spectrum $\propto E^{-X}$, in the energy range $(E_{\text{min}}, E_{\text{max}})$. If $X=1$, $I_E = \ln(E_{\text{max}} - E_{\text{min}})$ otherwise $I_E = (E_{\text{max}}^{1-X} - E_{\text{min}}^{1-X})/(1-X)$;
- I_θ (sr) is the angular phase space, depending on the type of neutrino emission simulated: diffuse $I_\theta = 2\pi \cdot (\cos\theta_{\text{max}} - \cos\theta_{\text{min}})$ or point-like emission $I_\theta = 1$, dimensionless;
- T_{gen} is the simulated lifetime;
- A_{gen} is the area of the generation surface;
- N_ν is the number of generated neutrino types;
- E^X is the inverse of the generation spectrum, evaluated at the neutrino energy;
- N_{Tot} is the number of simulated incoming neutrinos;
- P_{scale} is the GENIE interaction probability scale;
- P_{Earth} is the survival probability through Earth evaluated as:

$$P_{\text{Earth}}(E, \cos\theta) = e^{-N_A \cdot \sigma(E_\nu) \cdot \rho_l(\theta)} \quad (94)$$

where $\sigma(E_\nu)$ is the total CC cross-section per nucleon. The Earth composition, entering through the column depth along the neutrino path $\rho_l(\theta)$, is schematised assuming several consecutive layers of varying density, encoded in the Preliminary Earth Model (PREM). This probability ignores NC interactions, where the neutrino energy decreases but is not absorbed. The same applies to τ regeneration. The survival probability as a function of the cosine of the zenith angle is reported in Figure 39.

ATMOSPHERIC MUONS Atmospheric muons represent the majority of events recorded in a neutrino telescope, reaching the detector despite thousands of metres of shielding material above it. They can also be used for detector checks and calibration. Two main strategies have been developed within the community to reproduce the flux of muon bundles reaching the detector. The first is to take advantage of a complete simulation of air showers, as done in CORSIKA [91]. The starting point for this approach is the

Multiple atmospheric muons can reach simultaneously the detector in bundle, with multiplicity spanning from one up to hundreds and with a radial spacing of several metres.

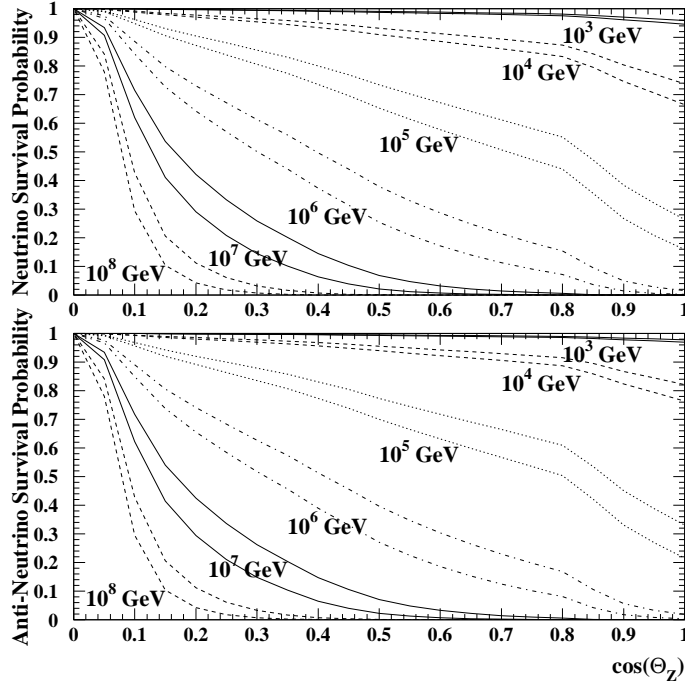


Figure 39: Survival probability for neutrinos and anti-neutrinos traversing the Earth in function of the cosine of the zenith (horizon is at 0 and a vertical path traversing all the Earth is at 1). This survival probability is reproduced and taken as a reference by the gSeaGen code. Figure taken from [90].

simulation of the interaction of primary CRs with the atmosphere, developing and propagating the entire shower particle content down to sea level. Lastly, muons are propagated up to the detector level. Despite the precision obtained, the main drawback is the extremely high computational cost. In addition, large uncertainties are still present on the interaction models and on the primary composition of CRs. For these reasons, within the KM₃NeT Collaboration, MUPAGE software is adopted [92]. It is based on a parameterisation of the angular and energy distribution of atmospheric muons underwater, as a function of the multiplicity and the radial distance to the bundle axis. The parameterisation was derived from complete simulations and measurements made at the MACRO experiment and extrapolated under the sea. It has the advantage of producing extremely high statistics in a reasonable amount of time, even if only a fixed atmospheric flux can be simulated. Atmospheric muons are generated on the can surface, see Figure 38, between 0° and 85° in zenith angle, between 1 and 200 in multiplicity, and up to 500 TeV.

4.2 PARTICLES PROPAGATION AND LIGHT SIMULATION

Long-lived particles that are saved in the generation step are then propagated through the volume of the can. The water composition and density is adjusted for each KM₃NeT experimental site. However, the overall homo-

generality of seawater allows the usage of pre-compiled tables containing the probability to detect a photon as a function of time, distance to the source of Cherenkov light, energy of the particle, and incident angle of the light. In under-ice detector, instead, the optical properties show an important dependence on the ice stratification, requiring a single-photon simulation, highly time and resource consuming. Tables are computed taking into account light production mechanisms (ionisation, δ -rays and Bremsstrahlung), light transmission, and detection of light by PMTs. Tabulated values include only direct light and single-scattered light.

4.3 TRIGGER SIMULATION

After light generation, the detector response is simulated. Random photon hits can be added, according to a Poisson distribution, with a mean rate extracted from real-data measurements. This procedure is capable of simulating not only the environmental background, caused by decay of radioactive salt in seawater, but also biological activity (bioluminescence) and any kind of temporary problem related with the detector electronics. At this point, the trigger and reconstruction steps are the same applied to data (see Section 3.2 and Section 3.3).

4.4 RUN-BY-RUN APPROACH

The deep sea environmental conditions have a significant impact on data acquisition and the rate of recorded events. Biological and physics phenomena show a seasonal evolving trend, even though, they are quite hard to model and to predict. Also some elements of such big detectors can temporarily or permanently be excluded by the data taking. The variation in the event rate due to the optical background is extracted directly from the data and used as input for trigger simulation. At the same time, the programme is connected to a database where all the information concerning the status of the detector elements is stored for each data taking run. To correctly reproduce all these effects as reliably as possible, a run-by-run approach is adopted. It consists of the extraction of specific parameters from the registered data to be used as input for the simulation. In this way, each physics data taking run is associated with a specific simulated run.

5

NEUTRINOS FROM THE MILKY WAY

Several theoretical models predict and describe, in detail, the properties of part of the diffuse neutrino flux originating from the interaction of Galactic CRs with interstellar medium matter located at the centre of our Galaxy. The common production mechanism of neutrinos and γ -rays, through pion decay, allows constraining the expected neutrino flux thanks to γ -ray measurements. The neutrino flux is therefore expected to be of the same order of magnitude as the one measured by Fermi-LAT close to the Galactic plane. Recently, the ANTARES Collaboration reported an excess of events coming from the centre of the Galaxy over 2σ , and the IceCube Collaboration reported the observation, for the first time, of neutrinos coming from the Galactic plane at the level of 4.5σ . Despite the location of IceCube detector that can look at the Southern sky only through downgoing events, dealing with the overwhelming background represented by atmospheric muons, new machine learning techniques and vetoing approach have been exploited, leading to this breakthrough discovery. The computation of the expected neutrino flux from the Galactic plane requires a broad knowledge of several different aspects of our Galaxy, like the Galactic CR source population and its distribution, gas and matter density distribution, Galactic magnetic fields, and much more. In the following section, a brief overview of the topic will be given.

5.1 THE MILKY WAY

The Milky Way is the galaxy hosting the Solar System and the Earth. The astronomical measurements of the properties of the Galaxy, with standard optical photons, have been difficult, in the past, due to the position of the Solar System within the Galaxy. Actual images show that the Milky Way is basically a disk with a central bulge surrounded by a globular cluster halo and can be classified as a *barred spiral galaxy*. Geometrically, it can be divided mainly into two components: a spheroidal and a disk structure, populated respectively by a different stellar population and by materials

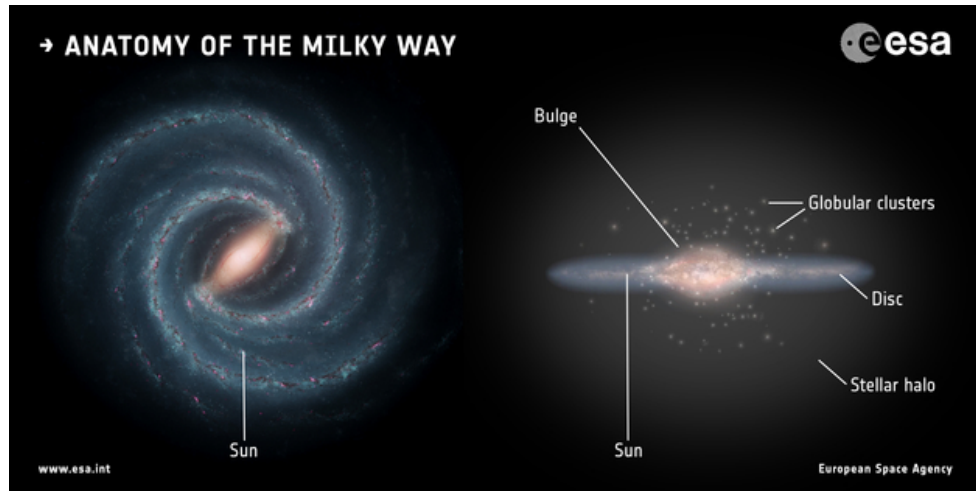


Figure 40: An artist's impression of the Milky Way galaxy: **left** a face-on view, **right** an edge-on view. Figure taken from [93].

The mass of the supermassive black hole at the centre of our Galaxy, Sagittarius A, is $\sim 2 \cdot 10^6 M_{\odot}$.

with different characteristics. The spheroidal structure has three concentric substructures: a very massive nucleus of around 3 pc of radius with a massive black hole at its centre, the bulge with a radius of ~ 3 kpc, and the extended halo of about 30 kpc. The disk instead is 200-300 pc thick and has a radius of 15 kpc. However, the precise determination of the disk radius is quite difficult: the gas and atomic hydrogen disk extend up to 25 kpc, even if the density decreases suddenly after 15 kpc. The sun is located in the disk at 8.5 kpc from the centre. The spheroidal component is populated by metal-poor stars and globular clusters, with a low density of gas and dust. The disk, instead, has a high density of dust and gas, also known as Interstellar Medium (ISM), and a high density of metal-rich stars. Complementary information can be derived by looking at the Galaxy through the radio emission at low frequency, generated by non-thermal synchrotron emission of relativistic electrons moving into the Galactic magnetic field. It shows a disk emission within Galactic latitude $|b| < 5^{\circ}$ and an ellipsoidal halo.

5.1.1 Galactic Magnetic fields

The Faraday rotation affects linearly polarised electromagnetic waves, whose polarisation plane rotate when they propagate in the presence of a magnetic field B , in a medium with electron density n_e . The rotation angle depends on the parallel component of the magnetic field.

Galactic Magnetic Fields (GMFs) play a primary role in driving Galactic CRs, in star formation, and in many other physics processes. Knowledge of its 3D structure is still limited, mainly due to the difficulties of studying an object in which we are embedded. At the same time, it offers a unique opportunity to study the magnetic field structure at much smaller scales than the one measured from nearby galaxies. Precise information on GMFs can be derived from radio astronomy, measuring several observable like Zeeman spectral splitting lines, polarised thermal emission, total intensity and polarisation of Galactic synchrotron emission, Faraday rotation of polarised sources, and UHECRs. Polarisation measurements tell us about the direction of the Galactic magnetic field. The strength of the magnetic field, in-

stead, can be inferred from the Zeeman splitting lines effect and the Faraday rotation of light from pulsars [94]. GMFs, on the basis of the actual knowledge, can be modelled as a combination of: a large kiloparsec-scale coherent component; a random component on a small scale (1-100 parsec); and an intermediate-scale component that is ordered overall, but with small-scale field direction reversals. The coherent component, observed, for example, in the spiral arms, confines CRs. The similarity of field line patterns with the ionised gas distribution supports the hypothesis that Galactic magnetic fields affect the formation of spiral arms and the general evolution of the Galaxy. The random component, caused by turbulence, supernovae, and shocks, plays a role in the formation of molecular clouds and stars. The intermediate-ordered component plays a role in the transport, heat, and angular momentum of the Milky Way. Large-scale GMFs have a field strength of the order of $\sim 2\text{-}10 \mu\text{G}$, $\approx 2\mu\text{G}$ at the Sun position and with an increasing trend towards the Galactic centre. The field is orientated mainly parallel to the Galactic disk, with a small vertical component along the z-axis. Another component of the GMF is the halo. Its geometrical structure is not yet well understood, with a magnetic field strength one order of magnitude weaker than that in the disk. The halo magnetic field is of great importance for the propagation of Galactic cosmic rays. Moreover, GMFs have important implications in the deflection of extra-Galactic UHECRs. In fact, it may be difficult to correlate the direction of UHECRs with astrophysical sources, even if their charge and energy are accurately known, until GMFs are better understood [95].

5.1.2 *Interstellar medium matter*

The Interstellar Medium (ISM) is the matter and radiation located in the space between star systems within a galaxy. It is made of gas in ionised, atomic, and molecular form and of dust. The gas distribution is traced by the detection of emission or absorption lines, both in optical and in radio. Dust instead is observed as large clouds obscuring the light of stars, as nebulae reflecting the light of a nearby star, or through their infrared emission in the vicinity of hot stars. At the level of our Galaxy, the ISM is located mainly in the proximity of the Galactic centre and in the spiral arms. The estimated mass is $10^{10} M_{\odot}$, 98% of which is made up of hydrogen and helium, the remaining 2% made up of heavier elements such as carbon, oxygen, and other metals. Most of these atoms are in the form of gas, but half of the heavier elements form dust. Going into more detail:

- *Neutral atomic gas*: it is mainly composed by atomic hydrogen (HI). The gas could be in thermal equilibrium at relatively low temperatures, $T \sim 100$ K and located in dense clouds with a density of $20\text{-}50 \text{ cm}^{-3}$ or at a temperature less than 10^4 K with a density of 0.3 cm^{-3} . These two states could coexist in pressure equilibrium, so that the neutral atomic gas can be considered to be a two-phase medium. The HI density, in the vicinity of the Sun, is lower than the values quoted

Considering the volume of the Galaxy and the volume of a star, only a small portion of the Galaxy is occupied by stars.

above, suggesting that our Solar System is located inside a HI cavity, called Local Bubble [96]. The bubble is filled with ionised hydrogen with a very low density ($\sim 0.005 \text{ cm}^{-3}$) and was generated by several past supernova explosions. It can be modelled as a cylindrical structure with a radius of 100-175 pc, with missing ends toward the north and south Galactic poles. Studies have shown that the magnetic field strength generated by the ionised gas in the wall of the Local Bubble, perpendicular to the cylinder, is $B_{\perp}=8\mu\text{G}$. This could have important consequences on the propagation of CRs and neutrino emission [97]. For higher energies ($E_p \geq 10^{17} \text{ eV}$), the bubble is transparent, since the Larmor radius ($R_L \sim 100 \text{ pc}$) of such protons is larger compared to the thickness of the bubble wall. For energies below 1 PeV instead particles can be trapped in the wall and the flux measured inside the bubble, suppressed;

- *Ionized hydrogen* (indicated as HII): near hot stars, neutral atomic gas can be ionised through UV emission. When electrons and protons recombine, the photon emission is shifted toward lower frequencies, with a typical wavelength of 656.3 nm, emitting Balmer lines. The neutral hydrogen can be re-ionised, and the cycle continues. These regions are associated with active star formation. In the end, when supernova explosions and strong stellar winds occur, they disperse the gases of HII, leaving a cluster of stars. Usually, ionised hydrogen regions are concentrated in the spiral arms;
- *molecular gas*: it is expected in high density and low temperature regions, necessary for HI to bind in form of H₂. These conditions are met in cold dense clouds, called therefore molecular clouds. The most common component of these clouds is in fact molecular hydrogen (H₂). Other molecules include carbon monoxide (CO), with its $J = 1 \rightarrow 0$ line, which astronomers often use to trace molecular cloud structure. In fact, H₂ has no permanent electric dipole moment and small moment of inertia, unable to produce emission/absorption through vibrational or rotational motions. The H₂ distribution is then derived through CO measurements;
- *dust*: it is typically in the form of ice grains of various species, such as graphite, silicates, and perhaps metals. The size varies from 0.1 to 1 μm . Thousands of tons of cosmic dust are estimated to reach the Earth's surface every year, and the density of the dust cloud, through which the Earth is travelling, is approximately $10^{-6} \text{ dust grains/m}^3$. Cosmic dust can also contain complex organic compounds.

Balmer lines describe a series of spectral line emissions of the hydrogen atom, and were calculated through an empirical formula. It corresponds to the transitions from $n \geq 3$ to $n=2$ [98].

5.1.3 Galactic cosmic rays

The measured spectrum of Cosmic Rays (CRs) at Earth is the result of the convolution of two basic processes: the acceleration in astrophysical sources (see Section 1.2.3) and the propagation into ISM and GMF.

CR PROPAGATION The majority of the information concerning CR propagation comes from the comparison of *light elements* (Li, Be, B) abundances in CR and in the Solar System. In Section 1.2.2, a more complete explanation can be found. A proton embedded in the Galactic magnetic field ($\approx 3\mu\text{G}$) of energy 10^6 GeV has a Larmor radius of 0.36 pc, much smaller than the dimensions of the Milky Way. For energies up to 10^8 GeV, where the Larmor radius starts to be comparable with the dimension of the Galaxy, CRs can be considered confined in the Milky Way. Galactic magnetic fields are the main factor that affects CR motion. If a constant magnetic field is present, the particle energy cannot change and the CR would propagate undisturbed. The diffusive regime is reached by introducing perturbations to magnetic fields, in the form of fluctuations of the fields itself, or induction of instabilities, self-generated by the stream of charged particles [99]. It is also important to note that the diffusion process is (quasi)resonant. This implies that the component of the CR momentum, along the regular field, changes if the particle finds a fluctuation in the magnetic field whose wavelength matches the Larmor radius of the CR itself. Therefore, CRs can lose complete memory of their initial direction with respect to the regular magnetic field over a few gyroperiods. This is a very short timescale compared to astrophysical times and also to collisional timescale, for a typical ISM density of 1 cm^{-3} . All these elements suggest that the CR movement is essentially diffusive and *collisionless*, since CRs do not scatter on other particles but on inhomogeneities of the magnetic field. The equation, describing the CR propagation, is called *diffusion-loss* equation: it contains energy losses and absorption resulting from the interaction of CRs with the ISM and a source term, responsible for the injection of freshly accelerated CRs. Therefore, the diffusion-loss equation can be formulated in the general form as follows [100]:

$$\begin{aligned} \nabla \cdot (\vec{J} - v_w \vec{N}_i) + \frac{\partial}{\partial p} \left[p^2 D_{pp} \frac{\partial}{\partial p} \left(\frac{N_i}{p^2} \right) \right] - \frac{\partial}{\partial p} \left[\frac{\partial p}{\partial t} N_i - \frac{p}{3} (\vec{\nabla} \cdot \vec{v}_w) N_i \right] = \\ (95) \\ Q + \sum_{i < j} \left(c \beta n_{\text{gas}} \sigma_{j \rightarrow i} + \frac{1}{\gamma \tau_{j \rightarrow i}} \right) N_j - \left(c \beta n_{\text{gas}} \sigma_i + \frac{1}{\gamma \tau_i} \right) N_i, \end{aligned}$$

where N_i is the density of particles per total momentum p for each CR species i , $D_{pp}(\vec{r}, p)$ is the momentum diffusion coefficient, $Q(\vec{r}, p)$ encodes the source and energy distribution. $\vec{v}_w(\vec{r})$ is the Galactic wind velocity responsible for the advection of CR. In any case, for typical values of $\vec{v}_w \sim 10$ km/s, its effect is relevant at 1 GeV and decreases at higher energies. The time derivative of the momentum p accounts for momentum losses. The

High speed particle wind blowing between 300-3000 km/s towards the halo, generated by the SMBH at the centre of the Milky Way.

parameter τ_i is the time scale for radioactive decay at rest, while σ_i is the spallation cross-section with interstellar gas. The macroscopic current of CR $\vec{J}(\vec{r}, p)$ is determined through the spatial diffusion tensor D_{ij} as $J_i = -D_{ij} \nabla_j N$. The presence of a large-scale Galactic magnetic field could break the isotropy assumption, introducing a preferred direction. To solve the transport equation numerically, it is necessary to discretise the equation, i.e., writing it on a discrete grid and transform the derivative operators into finite differences [100].

5.2 NEUTRINO EMISSION

In previous sections, the ingredients necessary for the calculation of the Galactic neutrino diffuse flux have been introduced.

However, different models [75, 76, 101] based purely on IceCube all-sky diffuse flux measurements have been formulated trying to solve the *spectral anomaly* observed (see Section 2.6.1) postulating a Galactic diffuse neutrino emission. They are based on minimal assumptions and on a very limited number of free parameters, however showing common features and similar predictive results with models exposed in the next section. Nonetheless a coupled measurement of diffuse γ -ray and neutrino flux offers invaluable information on the spatial and spectral distribution of Galactic CRs. Furthermore, the diffuse neutrino flux will provide a clear and unique window into the mechanisms responsible for Galactic CR acceleration and propagation. The two common approaches in this case are to solve the problem analytically, simplifying the CR transport equations, or numerically. The numerical approach has been developed mainly based on codes such as GALPROP [102] or DRAGON2 [100]. In the following sections, some of the most up-to-date models will be briefly exposed.

CRINGE MODEL CRINGE is a recently published model [103]. It has been derived by fitting the CR spectrum from newly collected data from AMS-02, DAMPE, IceTop and KASCADE. One of the main innovations of this model is the accurate treatment of systematic uncertainties associated with each component considered. A general formulation for the neutrino or hadronic γ -ray flux, given by the line-of-sight integral (s) of the volume emissivity as a function of Galactic latitude (l) and longitude (b) and as a function of energy (E) can be written as:

Volume emissivity is the energy per unit time per unit volume per steradian. These units are the same as intensity, except that they are per unit volume instead of per unit area.

$$J(l, b, E) = \frac{1}{4\pi} \sum_{m,n} \int_0^\infty ds \int_E^\infty dE' \frac{d\sigma_{m,n}}{dE}(E', E) \cdot J_m(\mathbf{r}, E') \cdot n_{gas,n}(\mathbf{r}) \Big|_{\mathbf{r}=\mathbf{r}(l,b,s)}, \quad (96)$$

where J_m is the Galactic CR intensity, and $(d\sigma_{m,n}/dE)$ is the differential cross-section for γ -ray or neutrino production from CRs of species m and energy E' on a gas species n . The variable $n_{gas,n}(\mathbf{r})$ is the 3D distribution of ISM in the Galaxy.

In the specific:

- the Galactic CR (GCR) distribution is derived by solving numerically Equation 95 through DRAGON code. The assumptions made are the isotropy of the diffusion process. The diffusion coefficient then depends only on the rigidity of the particles. No advection nor particle re-acceleration has been considered here. The source term in the diffusion equation has been considered as $Q(\mathbf{r}, p) = S(\mathbf{r}, z) \cdot g(p)$, where the momentum and spatial dependencies have been factored into two separate components. The spatial distribution of the source $S(\mathbf{r}, z)$ has a significant impact on the morphology of the diffuse emission signal. The assumed parameterisation is based on population studies of SNRs and pulsars in the Milky Way. The injected spectrum $g_i(p)$ for all nuclear species i is assumed to follow a single power law;
- the 3D map of ISM can be obtained from surveys of emission and absorption lines. Assuming a different velocity between the gas and the observer and a velocity model for the Galaxy, 2D surveys can be moved into a 3D map;
- another source of uncertainty is represented by unresolved sources. These are point-like sources with an emitted flux smaller than a certain threshold, linked to the sensitivity of current experiments. These sources, however, collectively contribute to the diffuse flux, even though the emission comes from specific astrophysical objects in the sky and not from GCR interaction with the ISM and GMFs. For this specific model, following Fermi-LAT observations in γ -ray, the source population, composing the major part of unresolved sources, has been attributed to pulsar;
- the flux of γ -ray above few TeV is subject to absorption in the interaction with the Galactic CMB and EBL. This should also be included when the flux of γ -rays is evaluated at Earth. It is incorporated by calculating the survival probability $\propto \exp(-\tau(E, s(l, b)))$, where $\tau(E, s(l, b))$ is the optical depth evaluated along the line of sight. The overall effect of absorption depends on the assumed CR and gas distribution, even if the dominant effect is the interaction with CMB.

All the parameters left free in the model are fitted simultaneously to the available observational data. The best-fit model reproduced the GCR data with a relatively good χ^2 .

In Figure 41 the predicted flux of γ -rays is reported in the window $|b| < 5^\circ$ and $25^\circ < l < 100^\circ$, for which observational data are available. Without the inclusion of unresolved sources, the single power law emission of γ -rays is $\propto E^{-2.7}$ for an energy range between GeV and tens of TeV. Above this limit, the power law assumption is no more valid due to the knee in the CR spectrum. The theoretical flux derived cannot explain the measurements by LHAASO and Tibet AS γ . The inclusion of unresolved sources significantly

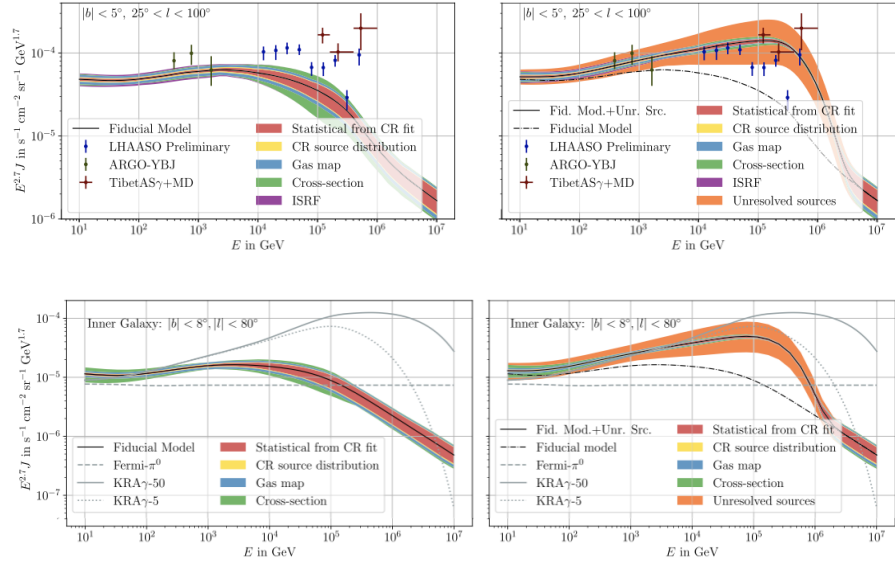


Figure 41: **Top:** γ -ray intensity as a function of energy in the window $|b| < 5^\circ$ and $25^\circ < l < 100^\circ$. Observational data from TibetAs γ , ARGO-YBJ and LHAASO at high energy are also reported. **Bottom:** neutrino intensity as a function of energy in the window $|b| < 8^\circ$ and $|l| < 80^\circ$. For both plots, CRINGE model prediction without (left) and with (right) unresolved source contribution. The shaded bands represent the uncertainties associated with each of the elements taken into account in the modelling. Figures taken from [103].

increases the emission above a few tens of TeV, leading to a harder spectral index, $E^{-2.3}$. However, in the high-energy part, the uncertainties associated with unresolved sources dominate the total uncertainty. The single-flavour neutrino intensity for the inner Galaxy region ($|b| < 8^\circ$ and $|l| < 80^\circ$) is represented in Figure 41, compared to other models such as Fermi- π^0 , KRA γ^5 and KRA γ^{50} . Even in this case, the inclusion of unresolved sources in the inner Galaxy window produces an enhancement in the intensity above 10 TeV. The prediction is close to the KRA γ^5 model, even if the origin of the hardening is of completely different nature. The predicted Galactic neutrino flux from the CRINGE model, integrated between 10 GeV and 10 PeV, can account for $\sim 3\%$ of the all-sky diffuse emission.

KRA γ MODEL A complementary approach, with respect to CRINGE model, is the one adopted for the formulation of the KRA γ model [104]. It aims to reproduce γ -ray observations in different regions of the Galaxy, with particular attention to the explanation of the hardening of the spectrum in the inner Galaxy, observed by Fermi-LAT [105] (shown in Figure 42). Furthermore, LHAASO [106] and Tibet As γ [107] experiments have recently reported the first evidences of a diffuse γ -ray emission from the Galactic plane up to PeV energies. This should be originated by ≈ 10 PeV CRs injected into the Galaxy, produced in the so-called *PeVatrons* (see Section

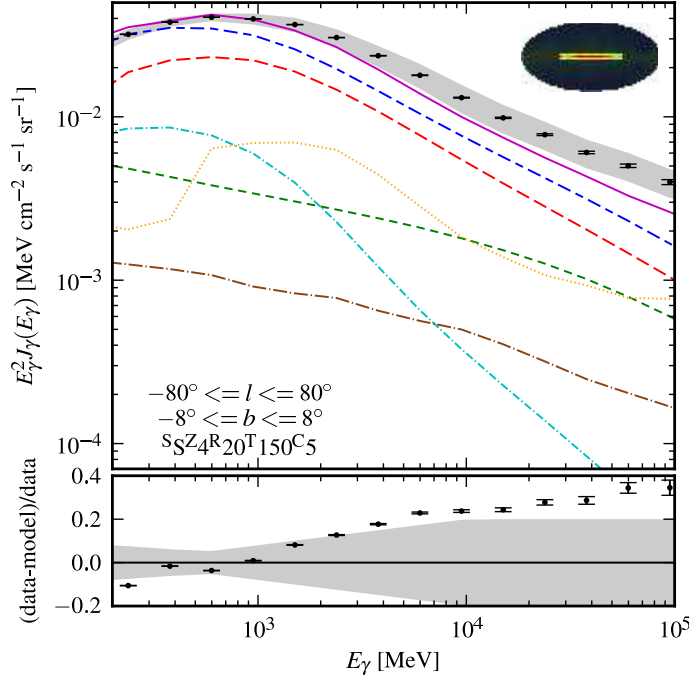


Figure 42: Spectra measured by Fermi-LAT Collaboration from the inner Galaxy, with the associated systematic uncertainty (experimental points reported as black dots, and grey shaded band representing systematic uncertainties). For comparison, also the expected contribution from π^0 -decay (red dashed line), inverse Compton (green dashed line), and bremsstrahlung (cyan dashed line) is reported. Figure taken from [105].

1.2.4), allowing to study directly the *knee* region of the CR spectrum. Even in this case, the starting point is the numerical solution of the diffusion-loss equation using the DRAGON2 code. The current model is based on the assumption of an inhomogeneous diffusion of CRs in the Galaxy, taken into account specifically to explain the hardening of the γ -ray flux.

The diffusion coefficient can be written therefore as:

$$D = D_0 \cdot \left(\frac{\mathcal{R}}{\mathcal{R}_\odot} \right)^{\delta(\mathcal{R})}. \quad (97)$$

Based on Equation 97 two scenarios have been postulated: a γ -optimized model where the spectral index of the diffusion coefficient $\delta(\mathcal{R})$ depends on the galactocentric distance (\mathcal{R}); and the *base* model where the diffusion coefficient is spatially constant and tuned on CR measurements. Specifically for the base model $\delta=0.5$ is assumed, while for the γ -optimized one it has been parameterised as follow:

$$\delta(\mathcal{R}) = 0.04(\text{kpc}^{-1}) \cdot \mathcal{R}(\text{kpc}) + 0.17 \quad (\text{for } \mathcal{R} < \mathcal{R}_\odot = 8.5 \text{ kpc}), \quad (98)$$

$$\delta(\mathcal{R}) = 0.5 \quad (\text{for } \mathcal{R} > \mathcal{R}_\odot). \quad (99)$$

In both scenarios, the normalisation of the diffusion coefficient D_0 has been chosen to reproduce the boron-to-carbon ratio. Taking into account

also the large discrepancies observed in the CR spectrum measured by different experiments, two hypotheses have been chosen, which have been called *Min* and *Max* configurations. The comparison of the derived γ -ray flux obtained through the *base* and the γ -ray *optimized* scenario, with respect to the observational data, is shown in Figure 43, in the window $|b| < 5^\circ$, $25^\circ < l < 100^\circ$.

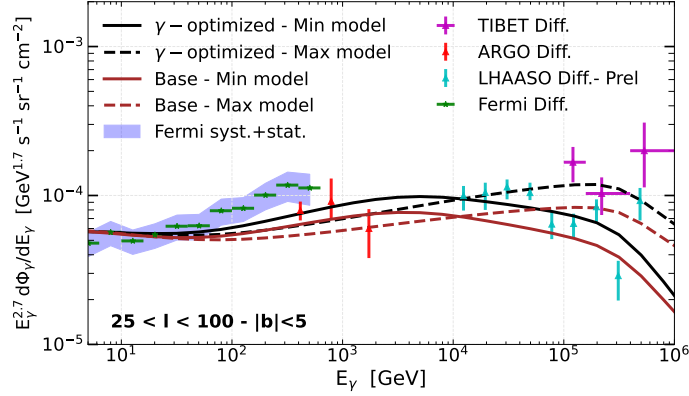


Figure 43: γ -ray diffuse spectra from the *base* and γ -*optimized* models compared to Tibet Asy, LHAASO, Fermi-LAT and ARGO-YBJ data in the window $|b| < 5^\circ$, $25^\circ < l < 100^\circ$. Contribution from unresolved sources is not included. Figure taken from [104].

The main consequence of this model is that hadronic emission dominates the γ -ray flux at very high energies and in the innermost region of the Galactic plane. The consequent neutrino emission is expected to overcome possible point-like sources sitting on the Galactic plane region and also inheriting features of the initial CR spectrum. In Figure 44 the expected neutrino emission is reported, together with the upper limits placed by ANTARES [108] and together with the all-sky IceCube astrophysical neutrino flux.

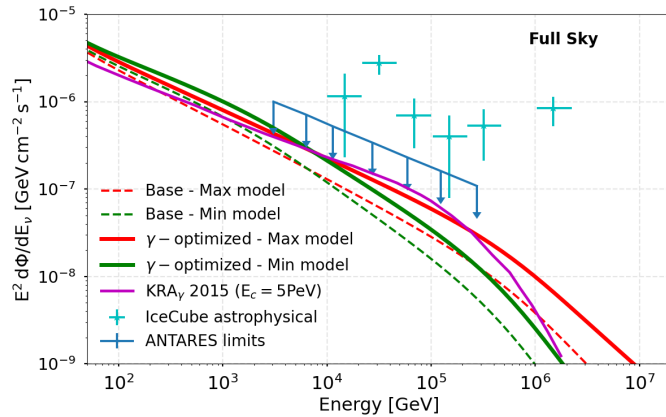


Figure 44: Full sky neutrino emission predicted with the KRA_γ in the *base* and γ -*optimized* configurations, compared to model independent upper limits obtained from ANTARES Collaboration [108]. The KRA_γ^5 expectation is also reported. Figure taken from [104].

An earlier version of the model, known as KRA_γ^5 , has been widely used in the past and also in the recent IceCube template fitting analysis. This model is based on the same assumptions as the one exposed above, with the additional introduction of an exponential cutoff in the CR spectrum. The apex 5 just refers to the value of the cutoff energy.

FERMI- π^0 MODEL A simple extrapolation of the neutrino diffuse emission can be obtained using the γ -ray flux measured by the Fermi-LAT satellite. As usual, the γ -ray flux is a superposition of a leptonic and hadronic contribution. Therefore, the main assumption to be made here is the percentage of γ -ray flux originating from π^0 decay. An estimate of the diffuse photon flux, produced inside the Galaxy, was derived from the Fermi-LAT Collaboration, subtracting all the detected point sources. The data collected, above 3.4 GeV, can be described very well by a single power law where the flux normalisation and spectral index are fitted from the data. The spectral index obtained in the inner Galactic plane ($|b| < 4^\circ$ and $||l| < 40^\circ$) is found to be slightly softer, between 2.5 and 2.6, relative to the rest of the sky. In the inner part of the Galactic plane, the π^0 contribution is found to be around 70% at 10 GeV, and extrapolating at higher energies shows that it is at the level of 45% at 1 PeV. The photon attenuation plays an important role for photon energies above 10 TeV, for Galactic distances, but here it is not taken into account. From the measured diffuse γ -ray flux, the π^0 flux can be derived. Lastly, neutrino emission can thus be obtained in a similar formulation, thanks to the relation between the π^\pm and π^0 flux. Assuming a single power law for neutrino emission, the fitted spectral index varies from about 2.6 to 2.7, depending on the primary CR spectral index chosen to reproduce γ -ray measurements and depending on the particular region of the sky.

5.3 ICECUBE OBSERVATION OF A DIFFUSE EMISSION FROM THE GALACTIC PLANE

At the end of June 2023, the IceCube Collaboration reported the observation, for the first time, of neutrino emission coming from the direction of the Galactic plane, at a significance level of 4.5σ [109]. As shown in Figure 45, it was possible to obtain a neutrino map of the Galactic plane, paired with those obtained through other optical and γ -ray observations.

The Galactic Centre and the bulk of the expected neutrino fluence is located in the Southern sky. IceCube neutrino observatory, located at the South Pole, has perfect visibility for the Northern sky through upgoing track-like events that use the Earth as a shield against the background of atmospheric muons. To observe the Southern sky, the analysis of IceCube data focused on events whose reconstructed interaction vertex was located inside the instrumented volume. Also, vetoing techniques can be exploited to reduce the background represented by atmospheric neutrinos. In fact, at high energies, a fraction of atmospheric neutrinos can be tagged and

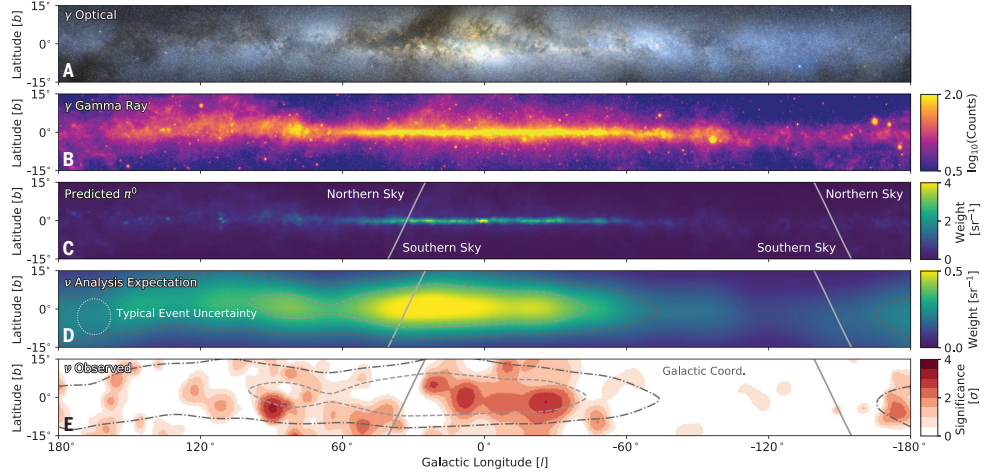


Figure 45: Galactic plane emission visible through photons and neutrinos. The γ -ray emission is the integrated flux seen by the Fermi-LAT telescope at energies greater than 1 GeV. The other panels show, respectively, the expected neutrino flux, considering the π^0 template and the template itself convolved with angular uncertainty of the sample analysed ($\approx 7^\circ$). In the last panel, the pre-trial significance is reported from the all-sky scan for point-like sources. Figure taken from [109].

excluded eliminating those events that contain also a simultaneous atmospheric muon, originated within the same CR air shower. The flux of atmospheric ν_e , which generates cascade-like events inside the detector, is also an order of magnitude smaller than the corresponding atmospheric ν_μ flux at the TeV scale (see Section 1.2.7). Focusing on cascade events allows reducing atmospheric muon contamination and lowering the energy threshold for the search for astrophysical neutrinos. The main disadvantage is the low angular resolution, but in the case of extended regions, like the Galactic plane, this can be compensated for. The discovery has been made possible thanks to the application of innovative machine learning techniques that have produced an increase in the statistics of the 10 year IceCube data set, producing more than 20 times as many events as previous analysis, and an improvement in the angular resolution by a factor 2 at TeV energies. Atmospheric muon contamination obtained, with the developed event selection, is on the order of 6%, and the contribution of astrophysical neutrino events is at the level of 7%, with the remaining percentage represented by atmospheric neutrinos. Three models have been tested for Galactic diffuse emission: Fermi π^0 , KRA_γ^5 and KRA_γ^{50} . The expected neutrino emission from the models has been converted into a spatial template, convolved with detector acceptance and angular resolution of the data set. The π^0 model assumes a single power law spectrum, with spectral index equal to 2.7, which can be extrapolated up to TeV-PeV energies. The KRA_γ model assumes a more complex energy dependence, based on the specific spatial region. No assumption on absolute model normalisation has been made, considering the uncertainties related to the distribution of unresolved sources. The background-only hypothesis has been rejected at the level of 4.71σ for the

π^0 , 4.37σ for the KRA_γ^5 and 3.96σ for the KRA_γ^{50} model. The fitted flux normalisation obtained for the π^0 model at 100 TeV is $21.8 \cdot 10^{-12} \text{ TeV cm}^{-2} \text{ s}^{-1}$. For the KRA_γ models, since it has a more complex spectral dependence, flux normalisation has been reported as a multiple of the predicted flux, corresponding to 0.55 and 0.37 for the KRA_γ^5 and KRA_γ^{50} , respectively. The predicted energy spectra for the three tested models are shown in Figure 46, together with their best-fit flux normalisation.

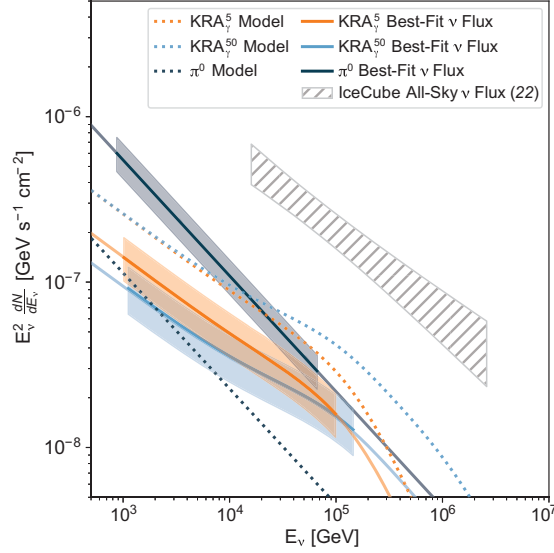


Figure 46: Energy spectra for the three different tested models. The sky integrated, per-flavour neutrino flux is reported. Dotted lines are the model expectations, while solid ones represent the best fitted normalisation values obtained from the analysis, with the 1σ uncertainty reported through the shaded area. The diffuse all-sky flux measured by IceCube is also reported with a grey band. Figure taken from [109].

The Galactic diffuse neutrino emission contributes also to the all-sky astrophysical diffuse flux. Its contribution varies according to each different model, ranging from 6 to 13% at 30 TeV. However, these comparisons are quite difficult considering the different spectral shapes tested, the different energy ranges, and the event topologies exploited for the different analysis. Interesting consequences of this observation can already be derived [110].

DATA SAMPLE AND EVENT SELECTION

KM₃NeT detectors, thanks to their modular design, are capable of acquiring data even in the construction phase and with an incomplete detector. During each of the sea campaigns conducted by the KM₃NeT Collaboration in the last three years, new DUs have been deployed, producing a great enlargement of the effective area of the KM₃NeT/ARCA detector. After the recent deployment, in September 2023, the KM₃NeT/ARCA detector comprises 28 fully working DUs. The data analysed within the context of this thesis were among the first collected by the Collaboration in its multi-DU configuration. A lot of work has also been done in the tuning and testing of the several components taking an active role in the data analysis, i.e., Monte Carlo simulation parameters, reconstruction algorithms, calibrations, and more. Within this chapter, the analysed data set will be presented, with particular attention to data quality and the strategies adopted to filter and analyse data. The number following the name KM₃NeT/ARCA (i.e. KM₃NeT/ARCA6, KM₃NeT/ARCA8) refers to the number of active DUs that were taking data actively in a specific period.

6.1 DATA-TAKING PERIODS

The data included in the analyses reported within this thesis were collected by the KM₃NeT Collaboration starting from May 2021 up to the end of 2022. During this period, four main detector configurations, and subsequent data sets, have been made available to the analysers, for an overall livetime of 432 days, after data quality selection.

In the specific:

- KM₃NeT/ARCA6 was in operation from May 2021 up to September 2021, for a livetime of 102 days. In Figure 47, the footprint of KM₃NeT/ARCA6 can be derived considering the light blue and grey points plus the DU in the red circle, marked as "recovery". Within this period, a further split of the data set must be taken into account. A first period, extending up to July 22nd, accounts for 60.2 days of live-

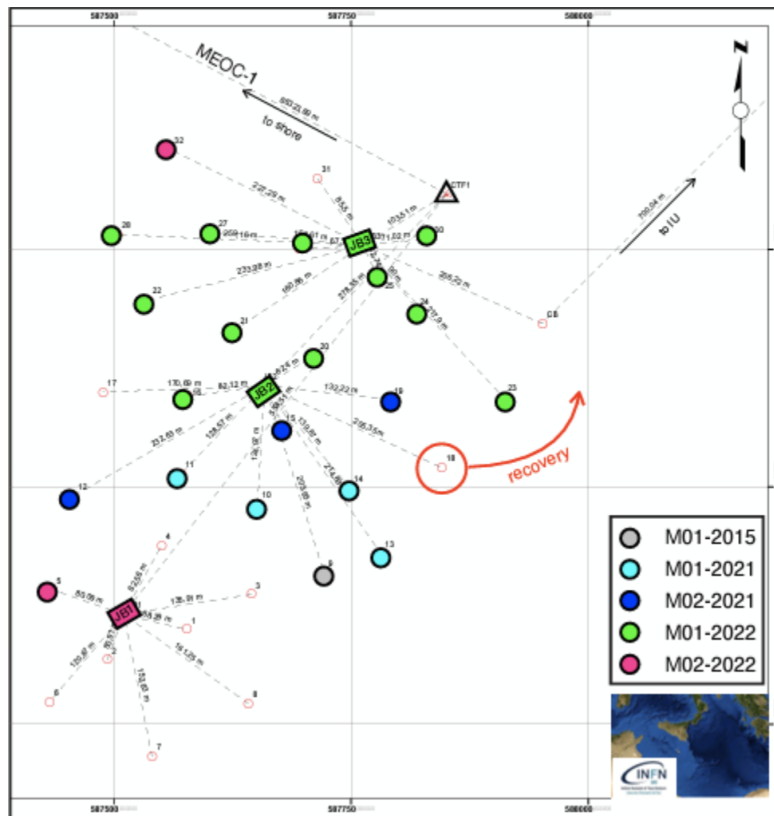


Figure 47: Footprint of the KM₃NeT/ARCA detector with 21 active detection units (circular marks). The different colours refer to different marine sea campaigns (referred to *MOx-year* in the legend) and therefore different detector configurations. The recovered DU (red arrow) is just the DU-18 that no longer collected data during the KM₃NeT/ARCA8 period. The rectangular markers are the junction boxes, specific optical and power split points of the seabed infrastructure. MEOC-1 is instead the 100 km long electro-optical cable, driving data onshore and providing the required power to the detector.

time over the full KM₃NeT/ARCA6 period. A second period from July 22nd up to September 10th was subjected to a special treatment in the simulation, as erroneous time calibrations were assumed in the acquisition of the data at trigger level. This erroneous calibration has an overall impact quantifiable in a loss of 32% in the number of signal events (number evaluated after a set of preliminary cuts). A special treatment of the Monte Carlo allowed obtaining good agreement with data and also to fully exploit this second part of the data set;

- KM₃NeT/ARCA8 was operational from the end of September 2021 until the end of May 2022, for a total livetime of 212 days. During this period, in December 2022, one of the DUs stopped working (DU-18), leaving the detector, since then, with seven working DUs up to the end of this period. From Figure 47, the KM₃NeT/ARCA8 footprint can be derived by adding, with respect to the previous configuration, the dark blue points. Unfortunately, DU-19 was connected, but did

not take data during this period due to a connector failure within the junction box;

- KM₃NeT/ARCA₁₉ was acquiring data from June up to September 2022, for a total livetime of 50.6 days. The footprint of this geometry configuration can be obtained considering the additional green points.
- KM₃NeT/ARCA₂₁ was in operation from September 2021 until September 2022. Within the work of this thesis, for practical reasons, data up to the end of 2022 were included, analysing an overall livetime of 67.4 days. The rest of the data, concerning this configuration geometry, are currently under analysis by the Collaboration. The footprint in this case is obtained by adding the purple points.

Although the final geometry of the building block will be symmetric under rotations, these partial configurations are not. This could introduce some azimuth dependence in the distribution of the reconstructed events.

6.2 STABILITY OF THE DATA-ACQUISITION

KM₃NeT detectors acquire data continuously throughout the day, with an up-time of more than 95%. Thanks to the full-sky field of view and no particular environmental constraints, the detector can always look at the whole sky. The data acquisition is split into runs ranging from 3 to 6 hours. Weekly, the "physics" data taking is interrupted, and some runs, scheduled in advance, are devoted to calibration of the detector. A part from these specific time periods, other dead times could be due to expert intervention to fix specific problems. Usually, the stability of the event rate is used as an estimator of the good quality of the acquired data, as shown in Figure 48.

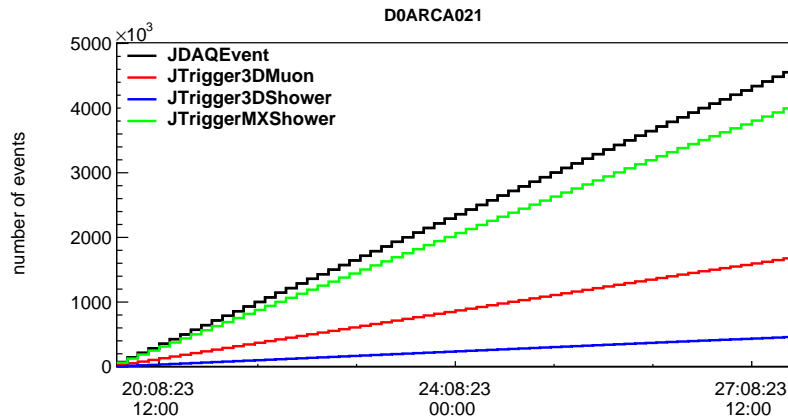


Figure 48: Time integrated number of events acquired with KM₃NeT/ ARCA₂₁ detector, in the period 20/08/23 - 27/08/23. The constant and monotonic increase in the events collected, without any plateau, suggests a stable and efficient data taking. The average data taking efficiency for this week was evaluated to be at the 98.3%.

6.3 DYNAMIC CALIBRATIONS

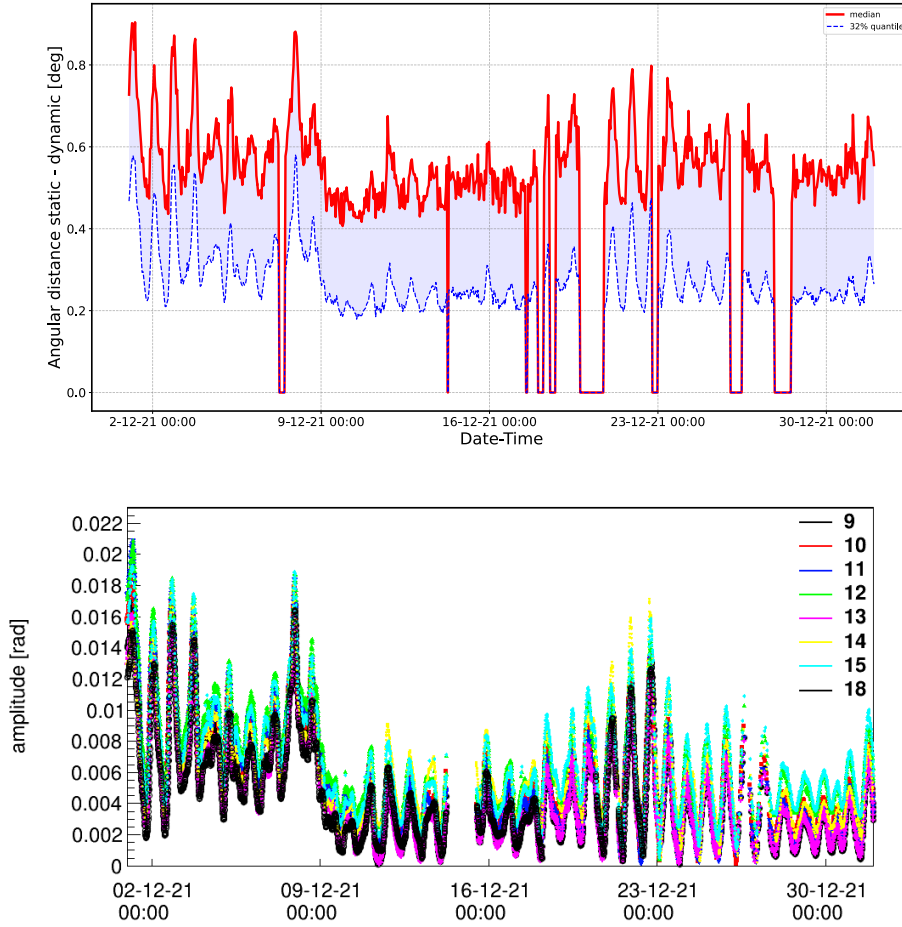


Figure 49: **Top:** angular distance of the directions reconstructed, on the same triggered events, respectively with static and dynamic calibration as a function of time. The median (solid red line) and the 32% quantile (dashed blue line) are shown, calculated over one hour time interval. Points at zero represent time windows with no data available. **Bottom:** Amplitude of the string displacement, seen here as the angle with respect to the vertical nominal position, as a function of time derived from the acoustic positioning system. The sharp peaked string displacement is highly correlated with the difference in reconstruction that takes advantage of the two different calibrations.

All the data collected are filtered through specific trigger algorithms (see Section 3.2) and then stored in ROOT-based files. The next step, before performing high-level analyses, is to apply calibrations and reconstruction software. A system of dynamic calibrations allows reaching very good angular resolutions. Strings of the KM₃NeT detector are moving under the effect of the sea current. In both Monte Carlo simulations and data at the trigger level, for simplicity, the detector is assumed to be at its nominal position. The acoustic positioning system, together with gyroscopes and other sensors within the DOM, allows to know, with high precision (less than

~ 10 cm), the position of each active element of the detector as a function of time. This time-dependent position calibration, together with refined mechanical models of the string, allows fully reconstructing the movement of the string. In Figure 49, the angular displacement of the string with respect to the nominal vertical position as a function of time, measured through the acoustic system, is shown in the bottom panel. To compare the impact of dynamic calibrations with respect to a "static" calibration system, the same events were reconstructed with the two different calibration approaches. In the top panel of Figure 49, the angular distance between the reconstructed directions of the same events is shown, assuming, respectively, a static and dynamic calibration. This difference is binned in time and the 32% and 50% quantiles are reported. The correlation between peaks in the string displacement and in the median angular difference, once dynamic positioning is taken into account, is quite striking. This improvement in calibration, witnessed by inspecting the time residuals of the reconstructed tracks and the likelihood distribution, has been made available starting from the KM3NeT/ARCA8 data set.

6.4 DATA QUALITY AND RUN SELECTION

The KM3NeT detectors will produce a huge amount of data in more than 10 years of activity. For this reason, a wide spectrum of parameters and observables must be considered in order to ensure a good quality of the data analysed. More specifically, each factor that could change data permanently or temporarily should be taken into account and its impact quantified. More or less stringent criteria for data quality could also affect the data/Monte Carlo agreement. Therefore, this is also another important parameter that is constantly evaluated and considered. All the runs registered by the detector are classified as *silver*, *gold* and *platinum* runs, having more and more stringent requirements for the quality of the data. The *gold* selection level already represents a good set of candidate runs through which robust scientific results are extracted. The *platinum* selection was designed for specific searches for rare events that require high purity. In the analysis presented in this thesis, the *gold* run selection has been used to produce the results exposed. The main selection criteria that runs need to satisfy are:

- lifetime of the run between 1200 and 61200 seconds. The lower limit is derived from the possibility to minimise errors occurring at run change, while the upper limit is a constraint in order to have a reasonable file size;
- lower limit on the efficiency of the data-taking evaluated here as the $(UTC_{\max} - UTC_{\min}) / \text{lifetime}$;
- upper and lower limit on the trigger rate, appropriately tuned based on each specific detector geometry;

- fraction of High Rate Veto (HRV) over the whole run. HRV is a veto condition embedded in the firmware of the central logic board related to the bioluminescence activity, and is tuned for each abyssal site of the KM₃NeT experiment;
- upper and lower limit on the mean and on the root mean squared rate of PMTs, in order to avoid any issue related to malfunctioning PMTs and in order to limit the bioluminescence activity;
- good and stable conditions for the electronic and time synchronisation of the active elements in the detector.

The application of the run selection exposed above, once all calibration runs and those scheduled for specific maintenance or upgrade are excluded, selected the $\sim 90\%$ of the runs collected throughout all the different detector geometries.

6.5 DATA SAMPLES AND EVENT SELECTION

In the following section, a general overview of the analysed data samples will be provided, specifically for each detector configuration. Before going into details and evaluating the numbers, some details must be specified.

6.5.1 Neutrino fluxes

As already anticipated in Section 4.1, neutrino events are generated in Monte Carlo according to a specific power law and are stored in files along with a generation weight w_{gen} . To obtain the proper weight for each event, w_{gen} should only be multiplied by a specific neutrino flux. In this work, the conventional atmospheric neutrino flux adopted to weight events is that provided by Honda [111]. The flux ϕ is available in tables as a function of the neutrino energy and of the incoming zenith direction. Unfortunately, tables are available up to 10 TeV. Therefore, an extrapolation has been performed by the Collaboration to derive the flux parameters at higher energies. The extrapolation was extended over the PeV energy range; therefore corrections for the CR knee have to be taken into account, specifically assuming a primary mass composition for the CR spectrum given by the Gaisser-H3a model [112]. For the prompt flux component, the calculations made in the ERS model [113] have been adopted. In this case, the flux is available for all energies of interest. Only a corrective factor for the CR knee (similar to that used for conventional flux) has been adopted. For the subsequent development of this chapter, the uncertainty associated with the atmospheric fluxes used is also important. As shown in Figure 50, the relative error associated with the Honda flux is reported as a function of the neutrino energy. The computation is available up to 1 TeV and is then extrapolated to higher energies. For simplicity, it is generally assumed to be a constant contribution of the order of 20-30%. For what concerns the

ERS model, also here the error has been provided directly from the authors, coming mainly from the uncertainty on the primary CR mass composition and slightly on the cross-section of charmed particles. It is assumed to be about 40%.

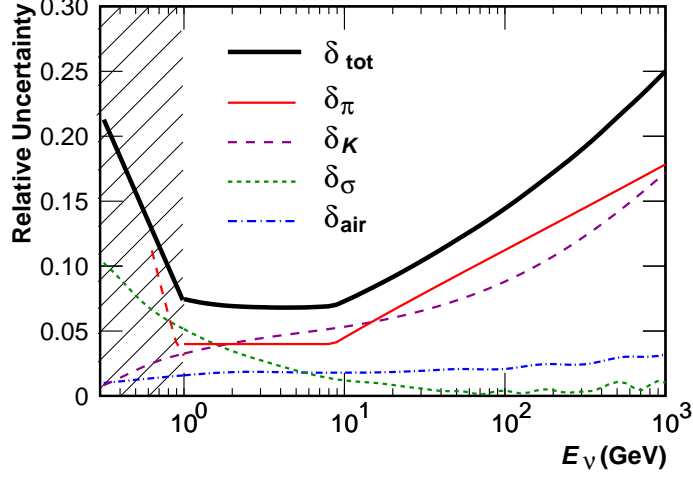


Figure 50: Overall uncertainty (black solid line) for atmospheric neutrino flux calculated with Honda model (single error source contribution also shown). Figure taken from [111].

For what concern astrophysical neutrino fluxes a simple power law per each individual neutrino flavour is generally assumed, of the form:

$$\Phi_{\nu}^{\text{astro}}(E_{\nu}) = \Phi_0 \cdot \left(\frac{E_{\nu}}{E_0}\right)^{-\Gamma} \text{ GeV}^{-1} \text{ m}^{-2} \text{ s}^{-1} \text{ sr}^{-1}. \quad (100)$$

Some standard fluxes have been considered in this work. Specifically, an all-sky diffuse flux of the form $\Phi_0=1.2 \cdot 10^{-4} \text{ GeV}^{-1} \text{ m}^{-2} \text{ s}^{-1} \text{ sr}^{-1}$ and $\Gamma=2$, used also in [86], and the best fit flux obtained in a recent work from the ANTARES Collaboration for neutrino emission from the Galactic Ridge of the form $\Phi_0=7.6 \cdot 10^{-5} \text{ GeV}^{-1} \text{ m}^{-2} \text{ s}^{-1} \text{ sr}^{-1}$ and $\Gamma=2.45$ [114].

6.5.2 Effective area

The number of detected events for a given neutrino flux can be obtained through what is called *effective area*, following the formula:

$$N_{\nu} = \int \Phi(E_{\nu}) \cdot dE_{\nu} \cdot A_{\nu}^{\text{eff}} \cdot T \quad (101)$$

where T is the livetime considered. The effective area can, in turn, be defined as follows [29]:

$$A_{\nu}^{\text{eff}}(E_{\nu}) = A \cdot P_{\nu\mu}(E_{\nu}, E_{\text{thr}}^{\mu}) \cdot \epsilon \cdot e^{-\sigma(E_{\nu}) \cdot \rho N_A Z(\theta)} \quad (102)$$

with A the geometrical detector area, $P_{\nu\mu}$ the probability, for a neutrino with energy E_{ν} , to produce a muon with sufficient energy to reach the detector and ϵ relates to the overall efficiency, including possible trigger, reconstruction, and analysis selection cut efficiencies. The term encoded in the

exponential instead is the Earth survival probability, also shown in Figure 39. More refined calculations can be obtained directly from the Monte Carlo simulation. In fact, the effective area information is implicitly encoded into the generation weight with the following relation:

$$A_{\nu}^{\text{eff}}(E_{\nu}) = \frac{N_x(E_{\nu})}{N_{\text{tot}}(E_{\text{max}}^{1-X} - E_{\text{min}}^{1-X})} \cdot \frac{w_{\text{gen}} \cdot (1-X)}{F \cdot I_{\theta} \cdot E^X} \quad (103)$$

with $N_x(E_{\nu})$ number of events in a given energy bin, X the generation spectrum (usually equal to 1.4 in KM3NeT simulations), E_{max} and E_{min} are the maximum and minimum generated neutrino energies and N_{tot} is the number of generated events. The effective area is also a parameter through which the performances and construction status of neutrino telescopes can be evaluated. In Figure 51, a comparison of the effective areas of KM3NeT/ARCA for upgoing track-like events is reported, specifically evaluated for each different detector geometry. Also, the effective area of ANTARES is reported, although it is not a completely fair comparison, considering the different muon contamination present in the data samples and, therefore, the different analysis selection efficiency.

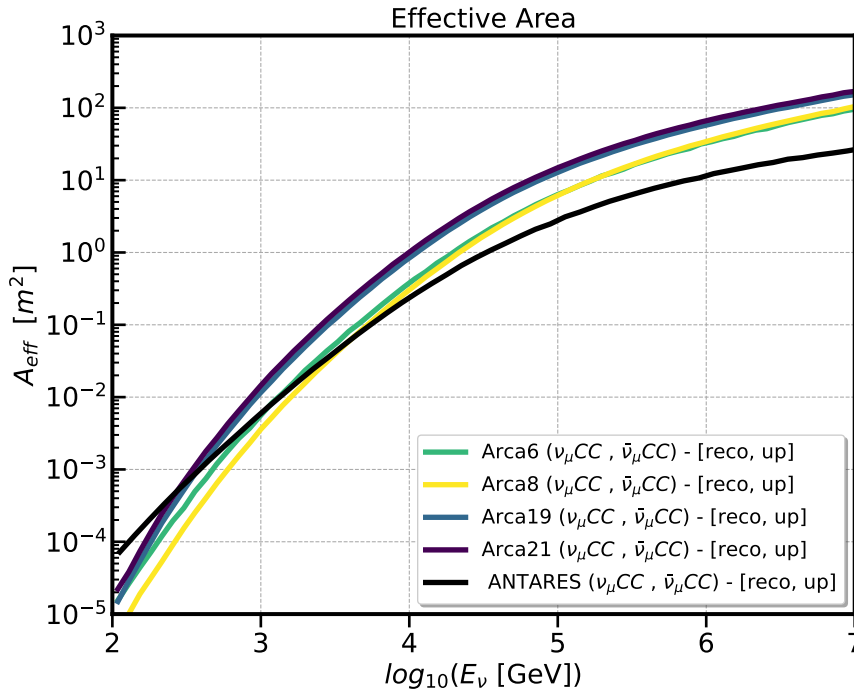


Figure 51: Comparison of the effective areas for track-like upgoing events of KM3NeT/ARCA detector, calculated with respectively 6, 8, 19 and 21 active detection units.

6.5.3 Event selection

The primary issue of all analyses developed within the KM3NeT Collaboration is to reduce the background represented by atmospheric muons and generated within the environment surrounding the detector itself. Most of the environmental background is reduced at the trigger level, asking for photon-hit clusters, in between different DOMs, to be casually connected. What still survives from this first filtering step can be rejected with some simple cuts on reconstruction variables like likelihood or number of hits. The atmospheric muon background rejection is more difficult. The topology of these events, being downward-going particles (see Section 2.4), can be exploited to reduce this component by using the Earth as a shield. Therefore, a cut is applied to the reconstructed zenith. The surviving atmospheric muons are those that have been wrongly reconstructed as upward-going particles. The rejection of this component change according to the analysis, depending on several aspects, i.e., signal efficiency required, purity, source extension, methodology of the search, and more. In the context of the analysis presented in this thesis, the signal is represented by astrophysical neutrinos that produce track-like events within the detector. Taking into account also the extension of the source in the sky, a further requirement of well-reconstructed tracks can help in obtaining a better overall background rejection. The event selection developed is mainly organised into two steps. Firstly, a set of fixed cuts on reconstruction variables, common also to other offline analyses developed by the Collaboration, has been applied in order to get rid of the environmental and part of the atmospheric muon background. A second step was also developed, using Boosted Decision Trees (BDT), capable of classifying the surviving part of atmospheric muons and rejecting the majority of them. More details are provided in the following sections.

6.5.3.1 Fixed cut selection

The fixed cut selection has been developed by the Collaboration for the first time and has been slightly modified during several expansions of the detector. It consists of a series of consecutive cuts on reconstruction variables, as explained more in detail in the following:

- *Preliminary selection*: a first set of preliminary cuts have been applied in order to select all the events that have been successfully reconstructed by the track algorithm. Furthermore, this selection level contains the requirement that the variables of interest (likelihood, see Equation 92, estimate of the angular error called β_0 , the reconstructed track length, and energy) are within a physics range, specifically greater than zero;
- *Anti-noise selection*: random coincidences in the detector, produced by environmental background, are generally reconstructed as track-like candidate events with a low likelihood value. These events are also usually reconstructed as up-going particles. For this reason, a cut in

likelihood is adopted. In particular, in Figure 52, the zenith distribution for data and Monte Carlo of the KM₃NeT/ARCA8 detector is reported before (left) and after (right) the application of anti-noise selection (likelihood cut at 40). The discrepancy observed at zenith values above 120° is due to the environmental background, which is not simulated in Monte Carlo. During the enlargement of the detector geometry, the trigger conditions have been changed and appropriately tuned. Despite this, the specified likelihood cut has always been verified to efficiently remove the surviving environmental background;

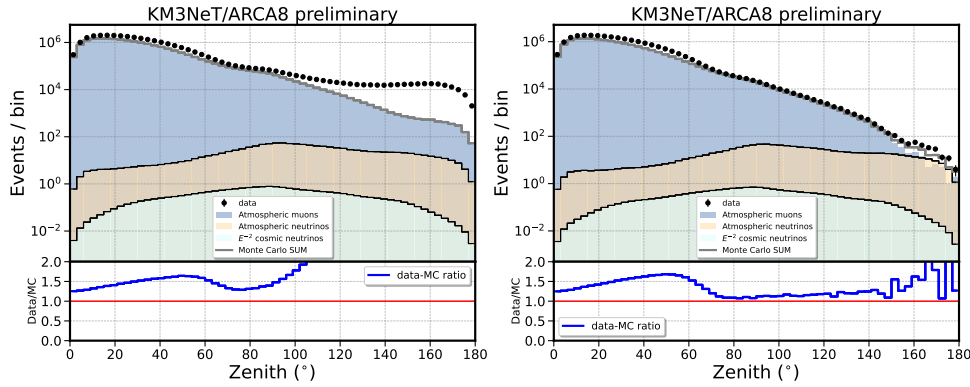


Figure 52: Data and Monte Carlo comparison for the zenith distribution of KM₃NeT/ARCA8 events. **Left:** distribution after preliminary selection. **Right:** distribution after preliminary and anti-noise selection. The discrepancy between data and Monte Carlo observed in the left plot, for zenith values above 120°, is due to environmental background events that are not simulated within the Monte Carlo chain. After applying the anti-noise selection, a satisfactory data/Monte Carlo ratio is recovered.

- *Upward-going selection:* a cut is applied to the reconstructed zenith of the events to reduce the number of downward-going atmospheric muons. Looking at the distributions of the reconstructed zenith (see Figure 52), for each single component simulated in Monte Carlo, the curve representing atmospheric muons is steeply decreasing with the increase of the zenith angle. Neutrinos instead are almost flat, evenly distributed in zenith, except for a mild peak at the horizon. Despite the fact that a stricter cut on the zenith would have allowed rejecting more atmospheric muons, at this stage of the selection the priority was also to keep the larger number of signal events as possible. For this reason, the zenith cut, after several optimisations, has been chosen to be set at $\cos(\theta_{\text{zenith}}) < 0.1$ (equivalent to $\theta_{\text{zenith}} > 85^\circ$);
- *Final fixed cut selection:* other two cuts on reconstruction variables have been applied. The first is performed on the parameter referred to as β_0 . It is an output of the track reconstruction algorithm and should be a proxy of the angular error associated with the track direction. It

is defined as $\sqrt{\sigma_x^2 + \sigma_y^2}$, where σ_x and σ_y are the errors along the x and y axes of the transverse plane with respect to the direction of the incident particle. Considering the aforementioned cut on the reconstructed zenith, the surviving muons are only those that have been wrongly reconstructed as upward-going particles, having therefore a large angular error. However, the β_0 variable did not show a high correlation with the angular resolution, evaluated on the Monte Carlo sample. When inspecting the distribution, a cut in $\log_{10}(\beta_0) < -1.5$ helped in the rejection of the remaining atmospheric muons. The second cut was applied to the reconstructed track length. As shown in the right panel of Figure 53, most of the atmospheric muons show a track length shorter than 200 m. This could be mainly due to the convolution of the detector geometry and the incoming particle direction.

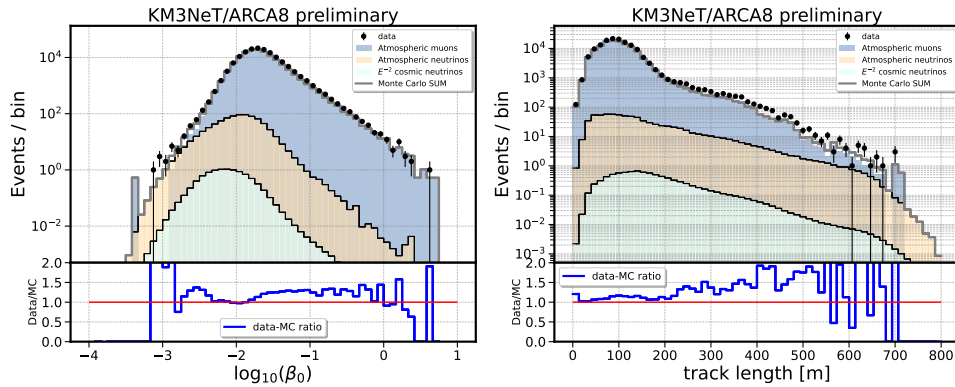


Figure 53: Data and Monte Carlo comparison after upward-going selection for **(left:)** the angular error estimate β_0 , and **(right:)** the reconstructed track length.

TUNING AND VERSIONING For each new detector configuration, the data and Monte Carlo have been processed with the most up-to-date software versions at that specific moment. Multiple tests have been conducted to try to reduce the data/Monte Carlo mismatch, especially in some specific zenith and energy ranges. However, these changes produced a significant modification in the overall data/Monte Carlo ratio, as can be seen from Table 1. In any case, regular updates to Monte Carlo, reconstruction software, and other points of the processing chain, coupled with enlargement of the detector, have significantly improved overall performance. One of the most important updates, whose effects are visible also in the change of the data-Monte Carlo ratio trend, is the tuning of the MUPAGE parameterisation on the data. In fact, starting from the KM₃NeT/ARCA8 data set, a tuning of the parameters used to simulate the flux of atmospheric muons has been conducted, thanks also to the parallel work done on the KM₃NeT/ORCA detector. In Table 1, a detailed description of the numbers related to the different data sets is reported at different levels of selection.

Selection level	Atmo μ	Conv atmo ν	Prompt atmo ν	cosmic ν	DATA	DATA/MC
KM₃NeT/ARCA6 - first period						
Preliminary	8.0×10^6	429	3.1	5.91	8.8×10^6	1.11
Anti-noise	5.8×10^6	313	2.0	4.2	5.7×10^6	0.98
Upward-going	4.9×10^4	231	1.7	2.33	3.48×10^4	0.71
Final fixed cut	3.3×10^4	191	1.4	2.0	2.4×10^4	0.70
KM₃NeT/ARCA6 - second period						
Preliminary	9.5×10^5	237	1.8	3.16	8.5×10^5	0.89
Anti-noise	7.9×10^5	188	1.6	3.12	5.6×10^5	0.70
Upward-going	2.3×10^4	152	1.1	1.6	1.6×10^4	0.71
Final fixed cut	1.7×10^4	128	1.0	1.4	1.2×10^4	0.70
KM₃NeT/ARCA8						
Preliminary	1.8×10^7	1231	11	18.78	2.6×10^7	1.46
Anti-noise	1.6×10^7	1049	9.8	16.63	2.3×10^7	1.45
Upward-going	1.3×10^5	779	6.4	9.21	1.5×10^5	1.13
Final fixed cut	4.5×10^4	422	3.7	6.7	5.1×10^7	1.13
KM₃NeT/ARCA19						
Preliminary	1.4×10^7	940	6.8	9.31	1.9×10^7	1.4
Anti-noise	1.3×10^7	829	6.3	8.61	1.8×10^7	1.38
Upward-going	6.1×10^4	599	4.0	4.8	7.4×10^4	1.21
Final fixed cut	2.5×10^4	445	2.9	4.05	3.2×10^4	1.24
KM₃NeT/ARCA21						
Preliminary	2.4×10^7	1534	10.6	14.21	3.0×10^7	1.26
Anti-noise	2.1×10^7	1346	9.8	13.13	2.6×10^7	1.24
Upward-going	1.1×10^5	977	6.3	7.33	1.2×10^5	1.07
Final fixed cut	4.7×10^4	733	4.6	6.1	5.1×10^4	1.06

Table 1: Table summarising events contained in each of the data sets analysed. Numbers reported after each subsequent selection level applied and specified in the text. The cosmic neutrino flux adopted here and for which the numbers refer is $\Phi_0 = 1.2 \cdot 10^{-4} \text{ GeV}^{-1} \text{ m}^{-2} \text{ s}^{-1} \text{ sr}^{-1}$ and $\Gamma=2$.

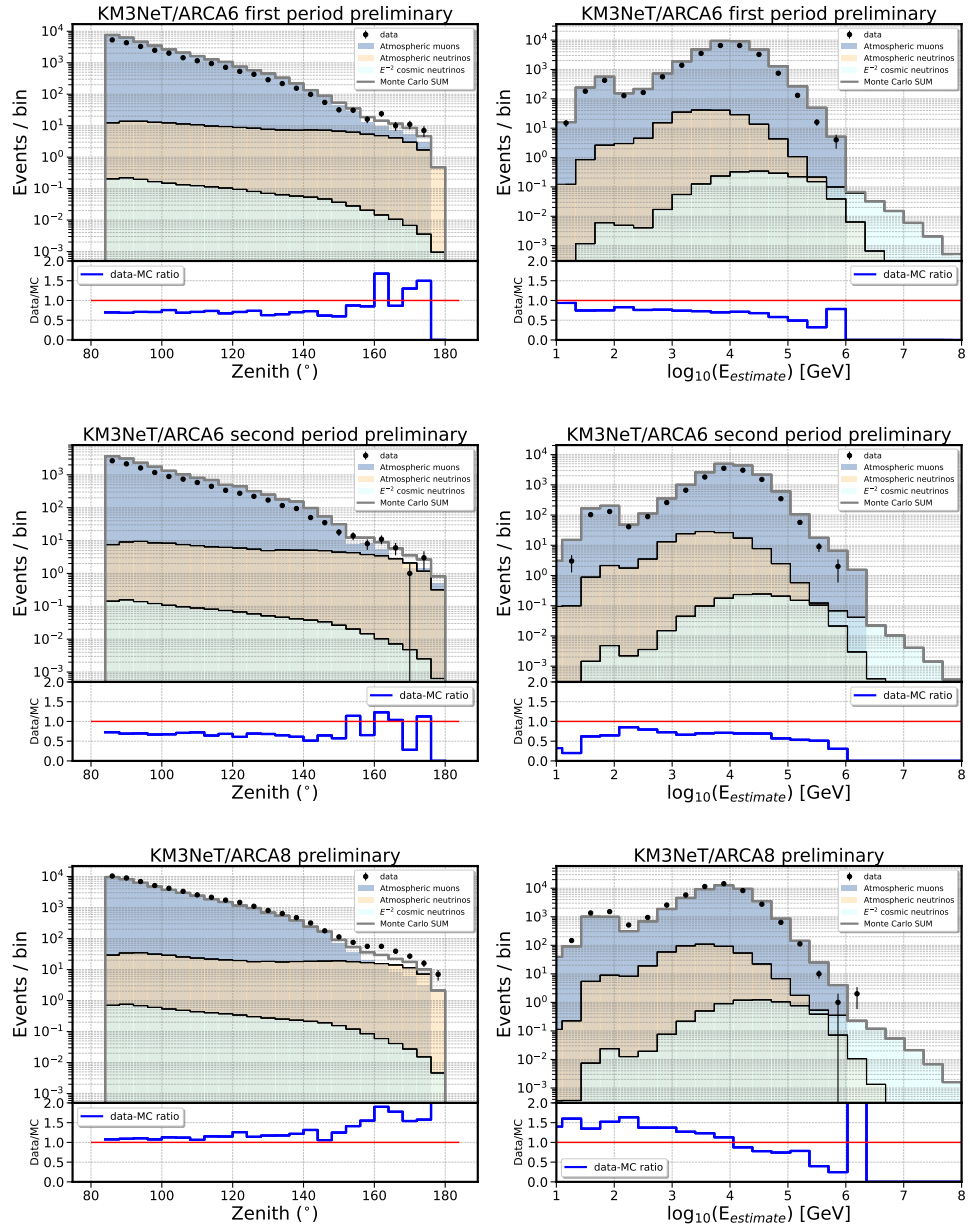


Figure 54: Data and Monte Carlo comparison for reconstructed zenith and energy for the KM₃NeT/ARCA6 and KM₃NeT /ARCA8 detector configurations, after the final fixed cut selection.

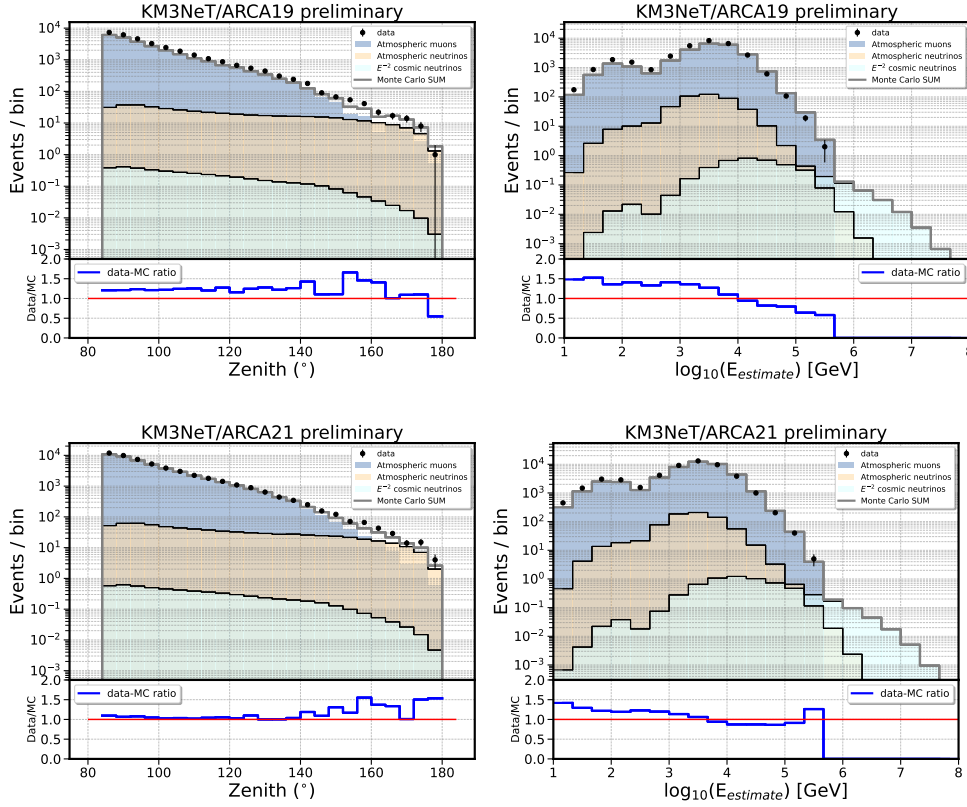


Figure 55: Data and Monte Carlo comparison for reconstructed zenith and energy for the KM₃NeT / ARCA₁₉ and KM₃NeT / ARCA₂₁ detector configurations, after the final fixed cut selection.

6.5.3.2 Boosted Decision trees

Even after the application of the final fixed cut selection, the background represented by atmospheric muons is still larger than the neutrino sample. For this reason, it was decided to train a Machine Learning (ML) algorithm, specifically a Boosted Decision Tree (BDT), in order to classify and reject atmospheric muons.

A decision tree is a binary tree classifier in which repeated decisions are made (yes/no), on a single variable at a time, until a stopping criterion is found. The boosting part, for this ML method, refers to the possibility to aggregate more binary trees (forest) and to combine each output at the end into a single classifier, assigning to each of the trees a specific weight.

The different detector geometries included in the whole data set do not allow to produce a coherent classification, exploiting one single trained model. For this reason, two separate models were trained, respectively, on KM₃NeT / ARCA₈ and on KM₃NeT / ARCA₂₁ Monte Carlo. The KM₃NeT / ARCA₈ model was then used to also predict the output score on the KM₃NeT / ARCA₆ data set, after a careful evaluation of the score distribution. Instead, the model trained on KM₃NeT / ARCA₂₁ was used to predict the output score also on the KM₃NeT / ARCA₁₉ data set.

Specifically for the KM₃NeT/ARCA8 training, 10% of the simulated lifetime within the Monte Carlo production is taken as a train sample and is not used in the later steps of the analysis. At the analysis level, the entire data lifetime is used, simply by rescaling Monte Carlo with the missing 10%. For KM₃NeT/ARCA21 instead a specific ML production has been made available by the Collaboration, and therefore the trained model has been applied to all the data and Monte Carlo standard production. The BDT was trained with unweighted events in Monte Carlo. Taking into account the simulated statistics for each neutrino flavour and for atmospheric muons, the resulting training data set was unbalanced. The signal, labelled as 1, was considered to be all neutrino flavours with an angular resolution lower than 5 degrees. The background, labelled as -1, was all events reconstructed with an angular resolution greater than 10 degrees. This choice was made since after the upward-going selection step, the training data set is mainly composed by wrongly reconstructed atmospheric muons, having a median angular resolution much greater than 10 degrees. Finally, considering also the limited portion of the sky in which we are interested in the analysis, a signal event with an angular resolution greater than some degrees would not be detected.

The features used to train the BDT were variables produced as output from the reconstruction algorithm.

FEATURE SELECTION Among all the available variables, a subset of 15 was selected, based on their separation power, and chosen to be as less correlated as possible. The feature selection has the main advantage of reducing overfitting, improving overall accuracy, and reducing training times. The selection was based on the possibility of ordering each input variable based on a specific scoring function. The function adopted was ANOVA, acronym for Analysis of Variance, a commonly used statistical method to check whether the mean of two groups is significantly different and to evaluate their distance. The 15 variables selected with this method are:

- *track length*;
- $\log_{10}(\beta_0)$: the logarithm in base 10 of β_0 variable;
- *likelihood*: the likelihood resulting from the track reconstruction algorithm;
- *zenith angle* reconstructed by the shower algorithm. A good capability for the shower algorithm to reconstruct the zenith direction of track-like candidate events was observed. This variable therefore enhances the already applied cut within the upward-going selection step;
- *ratio₁₁₀* defined as the ratio of early time photon hits with respect to all hits used in reconstruction;
- *ratio lower hits* defined as the total number of triggered hits on the lower hemisphere of the DOM with respect to the total number of triggered hits;

- *reconstructed zenith* produced by the track reconstruction algorithm;
- *number of Cherenkov DOMs* defined as the number of DOMs which registered a photon hit time compatible with the direct Cherenkov light emission;
- *minimum zenith solution*: each track-like candidate event was reconstructed exploiting 50 pre-fits, each of them reconstructing a different zenith direction for the event. This variable is the minimum reconstructed zenith among the 50 pre-fits produced for each event;
- *normalised likelihood* defined as the difference between the maximum and minimum likelihood among the 50 values available from the pre-fit step normalised to the value of the best likelihood;
- *maximum triggered ToT* representing the maximum registered Time over Threshold (ToT) for the triggered hits within each event;
- *number of good solutions* defined as the number of pre-fits whose angular distance with respect to the best-fitted track direction is below one degree;
- *maximum difference solution* defined as the maximum angular distance of the pre-fit solutions with respect to the best-fit track;
- *number of triggered lines* is the number of DUs containing at least one DOM that registered a triggered hit;
- *downgoing solutions* is the number of solutions among all the available pre-fits, that produced a downgoing track-like candidate.

The order of the variables reported in the above list is also representative of their importance in the classification step for the trained model. In Figure 56, the unweighted distributions of the signal and background sample are reported, for each of the selected variables.

MODEL OPTIMISATION The tuning of the hyperparameters of the chosen model is another step required to produce an efficient and accurate classifier. This can be done with already built-in methods in common ML libraries, like the Grid Search method. It allows to scan and test all the possible combinations of hyperparameters, within pre-defined values. Each of the models, resulting from a specific combination of hyperparameters, can then be ordered on the basis of selected metrics. Specifically, for each model tested during optimisation, a set of predefined cuts was also applied to the resulting BDT score, linearly spanning the whole range (within -1 and +1). Therefore, the chosen metrics to order and categorise the models were: cosmic neutrino efficiency, atmospheric neutrino and muon contamination, and the overall data/Monte Carlo ratio. More than 2500 combinations of hyperparameters were tested. The tuned hyperparameters optimised were:

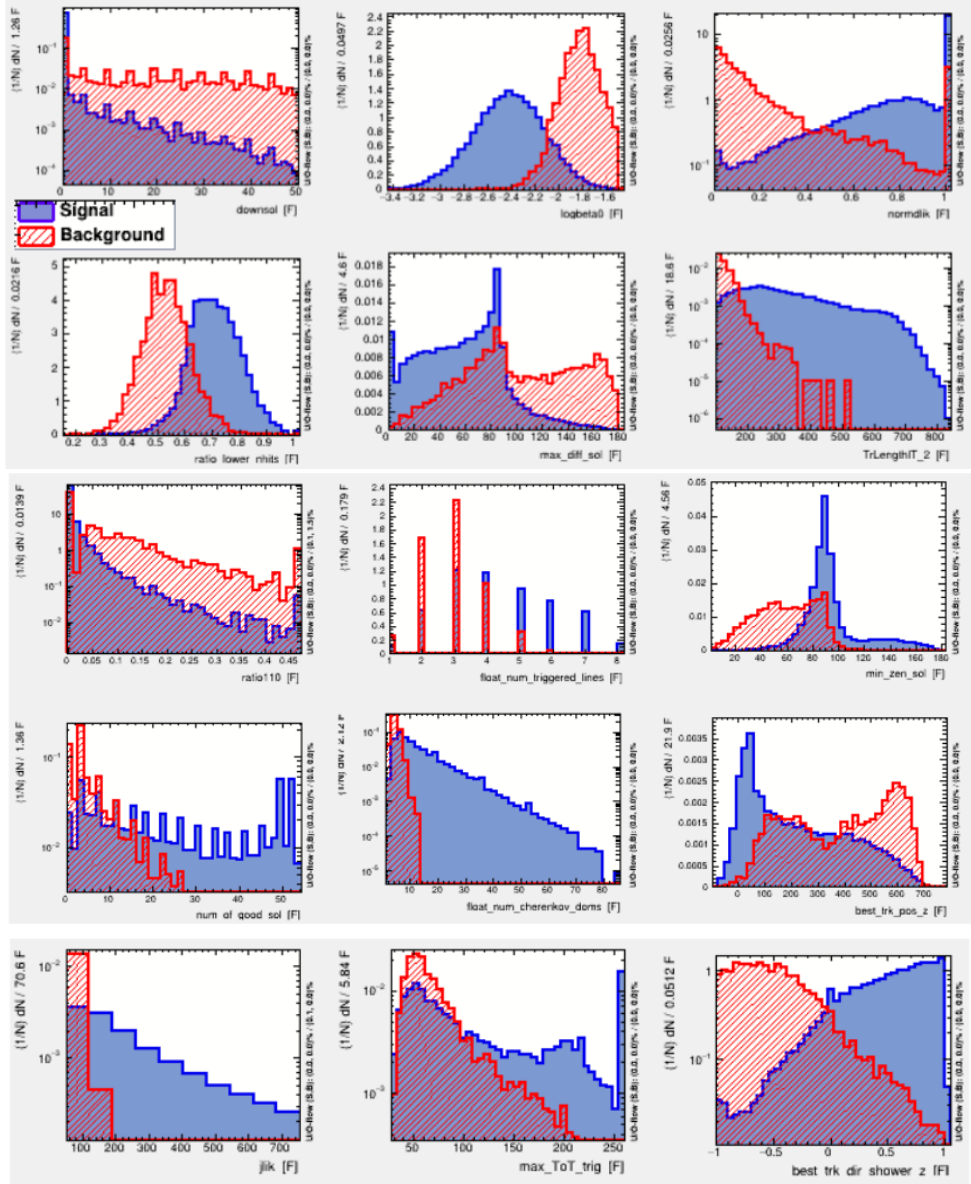


Figure 56: Distribution for each of the input variables used for the BDT training, directly output of the TMVA package. Background (red) and signal (blue) distributions are separately reported.

- *NTrees*: number of trees in the forest. Within the best model, it was set to 1200;
- *MinNodeSize*: minimum percentage of training events required in a leaf node. Within the best model, it was set to 1;
- *NCuts*: number of grid points in a variable range used to find optimal cut in node splitting. Within the best model, it was set to 14;
- *MaxDepth*: maximum depth of the decision tree allowed. Within the best model, it was set to 6;

- *AdaBoostBeta*: learning rate for AdaBoost algorithm. Within the best model, it was set to 0.02.

The boosting technique used here is the well-known Adaptive Boost (or AdaBoost shortly). It consists in a re-weighting of the incorrectly classified instances such that the subsequent classifiers focus more on difficult cases. The boost weight is defined, starting from the misclassification rate err of the previous tree, as:

$$\alpha = \frac{1 - \text{err}}{\text{err}}. \quad (104)$$

Within this framework, the learning rate is represented by the parameter β that influences the variation of the boost weight $\alpha \rightarrow \alpha^\beta$. A "slow learning" can, in fact, improve the performance of the algorithm. For more details, see [115].

OUTPUT SCORE DISTRIBUTIONS In the left panel of Figure 57, the final unweighted distribution of the BDT score is shown, evaluated, respectively, on training and test samples. In the right part of Figure 57, the receiver operating characteristic curve, or the ROC curve, is reported instead. The *ROC-integ* value, also reported in the figure, is the integral of the ROC curve. This value is also known as AUC (area under the ROC curve) and represents a scalar metric of the efficiency of all possible cuts in the classification score.

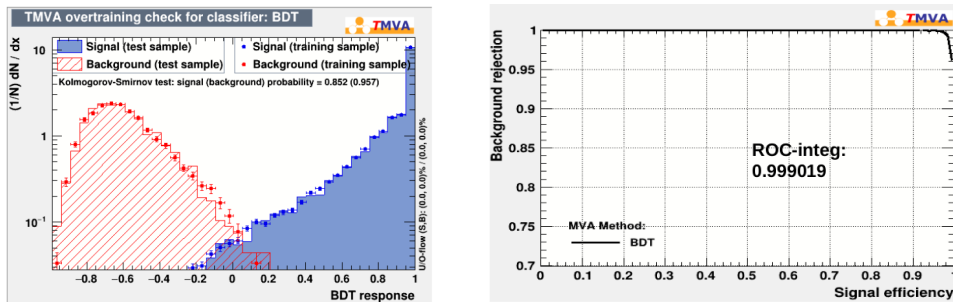


Figure 57: **Left:** BDT score distribution evaluated on the training and test sample. The visible agreement between the curves suggests the lack of overfitting during the training. **Right:** ROC curve, widely used metric to compare and evaluate the performances of ML methods.

An important step, in order to assess the robustness of the trained model, is to check and verify the agreement between the BDT score distribution evaluated both on data and Monte Carlo. Here in the following, the weighted BDT score distributions on Monte Carlo and on data for the different detector geometries are reported. Taking into account the region of interest for the development of the analysis (generally above 0.4), a satisfactory agreement is reached ¹.

¹ Event selection developed in tight collaboration with V. Tsourapis: tsourapis@inp.demokritos.gr.

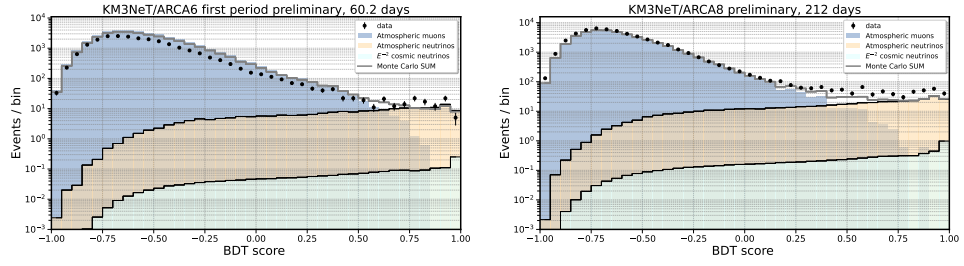


Figure 58: Data and Monte Carlo comparison for the BDT output score distribution, evaluated on KM₃NeT/ARCA6 (left panel) and KM₃NeT/ARCA8 (right panel) data sets.

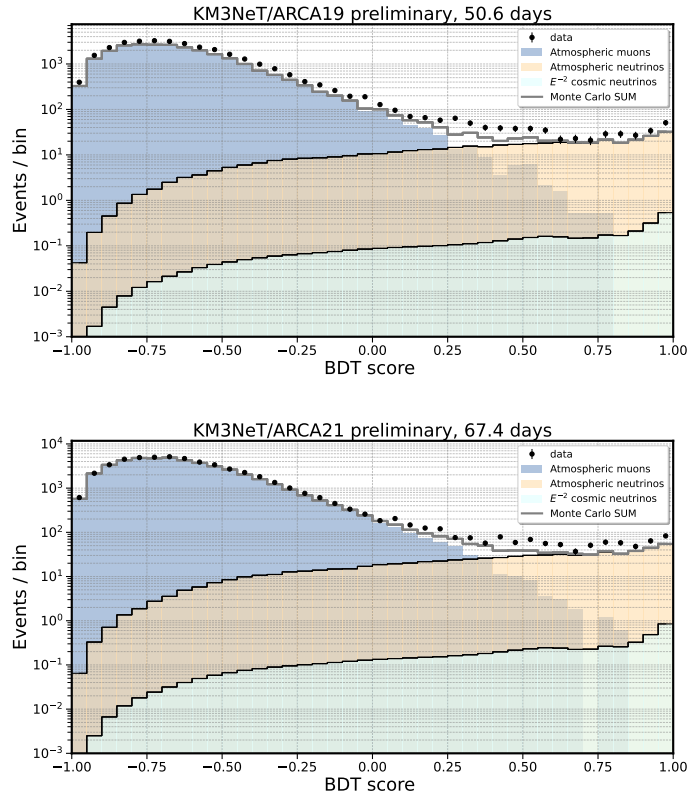


Figure 59: Data and Monte Carlo comparison for the BDT output score distribution, evaluated on KM₃NeT/ARCA19 (top panel) and KM₃NeT/ARCA21 (bottom panel) data sets.

6.6 PEAK CLUSTERING - KM₃NET/ARCA21 DATA SET

During preliminary data and Monte Carlo comparisons conducted on the KM₃NeT/ARCA₂₁ data set, a peak has been observed in the reconstructed zenith distribution of the data, which is not present in Monte Carlo. The peak, as shown in Figure 60, is suspiciously located at a distance of $\sim 42^\circ$ from the vertical position, equivalent to the Cherenkov angle for ultrarelativistic particles propagating in water. After a more detailed study, it was

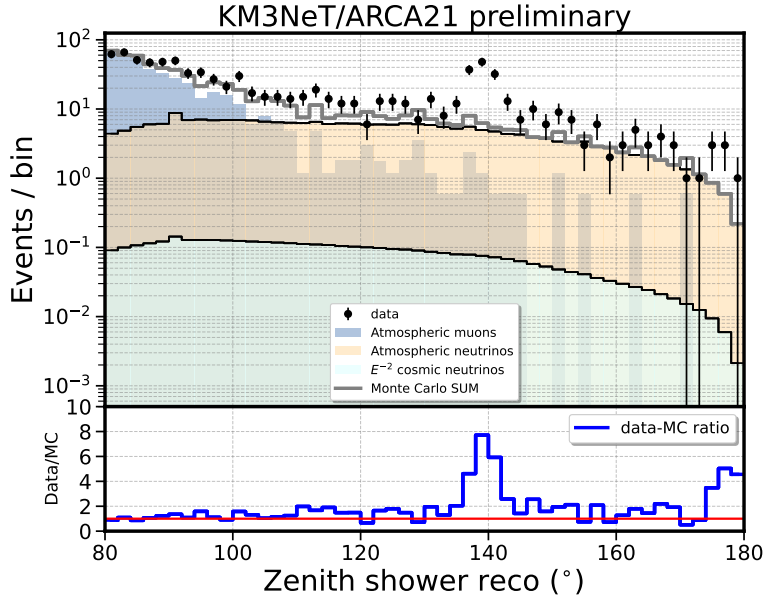


Figure 60: Reconstructed zenith distribution from the shower algorithm. The plot was produced after final fixed cut selection, with a further cut on likelihood greater than 75, in order to make more visible the peak in the data distribution.

possible to reconstruct the shower vertex position of those events and correlate it with the nearest DOMs. All events that make up the observed peak are compatible with a possible light emission in correspondence with DOM 12 on DU 12. Unfortunately, this is a DOM that lost communication with onshore more than a year ago, and was not possible to check its status nor re-configure and disable the instruments on-board. To try to assess and isolate this kind of events, a detailed analysis at the triggered hit level was performed. The main idea is to try to cluster events, based on a common topology or signature of the light pattern left inside the detector. The first thing noticed was a high number of hits with long ToT durations in the upper DOMs within DU12, i.e. DOM13 DU 12, and specifically on the PMTs located in the lower hemisphere. Furthermore, also looking at the footprint of the KM3NeT/ARCA21 detector (see Figure 47), DU12 was quite isolated from the other DUs. The nearest DUs that could have also seen some light were DU5 and DU11. Taking into account this, it was possible to test and compute the time residuals of the registered triggered photon hits with respect to the expected arrival time. The expected arrival time was calculated by assuming a point-like emission of light produced in correspondence with DOM12 DU12, even if the exact cause of this light emission is still a mystery. The script developed was therefore launched on each single event in each of the 561 runs that were forming the KM3NeT/ARCA21 data set. Among all events analysed, it was possible to identify and isolate some, as can be seen in Figure 61, that showed a time residual on the upper

DOMs of DU12 and the DOMs of DU5 consistent with the hypothesis made. Additionally, all events selected based on their time residuals also showed a common topology of photon hits registered by DOM13 DU12. They were quite uniformly distributed on all PMTs contained within the lower hemisphere of DOM13 and also showed a very long ToT duration. Thanks to this analysis, it was possible to compile a list and exclude the majority of these suspicious events, allowing to restore a satisfactory data/Monte Carlo ratio and to safely analyse the KM₃NeT/ARCA21 data set. Further investigations are, however, still ongoing by the Collaboration. The same kinds of checks have also been performed on the other KM₃NeT/ARCA data sets, included in the analysis, but they do not show any of the characteristics of the distributions observed in the KM₃NeT/ARCA21 data set.

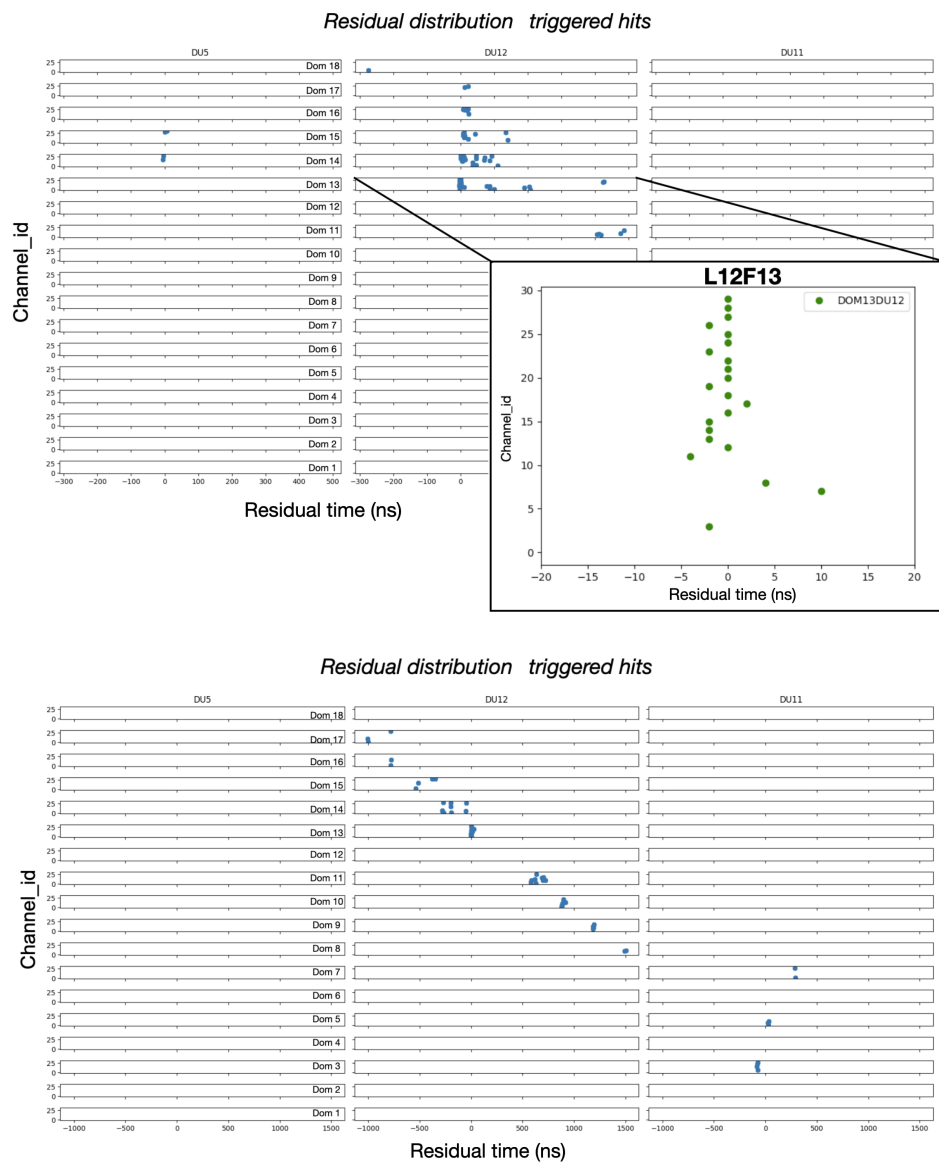


Figure 61: Time residual distribution calculated for triggered hits under the assumption of point-like emission in correspondence of DOM12 DU12. **Top:** Time residual compatible with the hypothesis, used to flag suspicious events. The further plot presented in the pop-up window shows the time residual distribution on the individual PMTs of DOM13 DU12. As can be seen, most of the hits have been registered for channel-ids > 12, belonging to the lower hemisphere of the DOM. **Bottom:** time residual distribution of the other events analysed. It is clearly visible that the points are not compatible with the assumption made. The event topology analysed here was presumably caused by a downgoing atmospheric muon.

GALACTIC RIDGE SEARCH

The Galactic plane is the most evident source in the sky in all the electromagnetic wavelengths. According to the hadronic production mechanism, the predicted neutrino flux is expected to be of the same order as the γ -ray flux, and in the innermost part of the Galactic plane, defined here $|l| < 30^\circ$ and $|b| < 2^\circ$, namely the Galactic Ridge, the CRs spectrum should be described by a spectral index harder than that measured locally at Earth. The ANTARES Collaboration recently reported an excess of events coming from the Galactic Ridge that was incompatible with the background expectation at the $\sim 96\%$ confidence level. The IceCube Collaboration has reported the first observation of high-energy neutrinos from the Galactic plane, with a statistical significance of 4.5σ (see Section 5.3). In this context, the analysis performed and described in this Chapter, searching for a neutrino emission from the Galactic Ridge, was the first ever done with data collected by the KM3NeT experiments.

7.1 KM3NET/ARCA VISIBILITY

KM3NeT detectors are located in the Northern hemisphere. Taking also into account track-like events and the accuracy in their reconstruction, these events represent the *golden channel* for searches of astrophysical neutrino sources. As explained in Section 2.4, in order to reduce the overwhelming background represented by atmospheric muons, the Earth is used as a shield and upgoing events are selected. Specifically, the KM3NeT visibility, through track-like upward-going events, covers, for most of the time, the Southern sky, where the Galactic Centre is located. A visibility map for a neutrino telescope located in the Mediterranean Sea is shown in Figure 62, where the largest part of the Galactic plane is visible for more than 75% of the time. At the contrary, neutrino observatories located in the Southern hemisphere, like IceCube, are more sensible to astrophysical neutrino sources located in the Northern celestial hemisphere. However, thanks to cascade and veto techniques, they were also able to observe this portion of

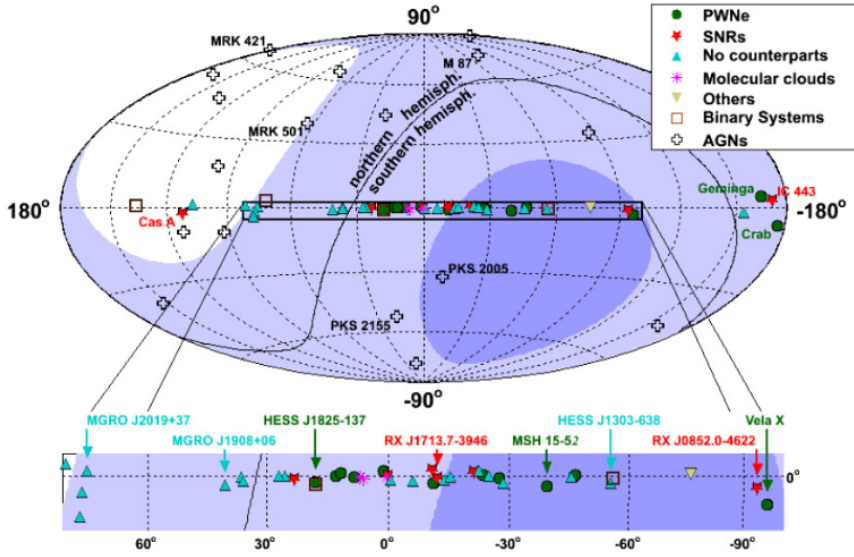


Figure 62: Sky visibility of a neutrino telescope located in the Mediterranean Sea, in Galactic coordinates. The dark (light) blue shaded areas represent the visibility over 75% (25%). Some candidate neutrino sources are also reported. Figure taken from [86].

the sky, but with an overall angular accuracy of $\sim 7^\circ$ [109]. In Chapter 5, it was also shown how the expected neutrino flux is highly influenced by unresolved sources. For this reason, the good angular accuracy of track-like upward-going events detected by KM3NeT and other neutrino telescopes in the Northern hemisphere will be fundamental in the precise characterisation of the neutrino flux coming from the Galactic plane.

7.1.1 Template fitting and model independent search

Up to now, two different methodologies have been used for the study of the neutrino emission from the Galactic plane. One is based on a template fitting, like the one used recently by IceCube Collaboration and previously also by ANTARES [116]. Models like the ones presented in Chapter 5, i.e. KRA_γ , CRINGE, Fermi- π^0 are capable of producing a detailed pixelised map of the neutrino emission from each portion of the sky. Furthermore, the fluence and spectral shape can vary as one moves from one pixel to another on the map. An example of the neutrino sky map predicted by the KRA_γ model can be seen in Figure 63. The analysis is then carried out through an unbinned likelihood method, testing the signal hypothesis (H1) with respect to the background only hypothesis (H0). The number of signal events is then incorporated in the likelihood for the H1 hypothesis as $\mu_s = r \cdot \mu_{\text{model}}$, extracting the parameter r directly from the fit of the data. This method has the advantage of constraining each model and the subsequent starting hypothesis with high precision and fully exploiting the statistical power of a likelihood method. On the contrary, it is highly depen-

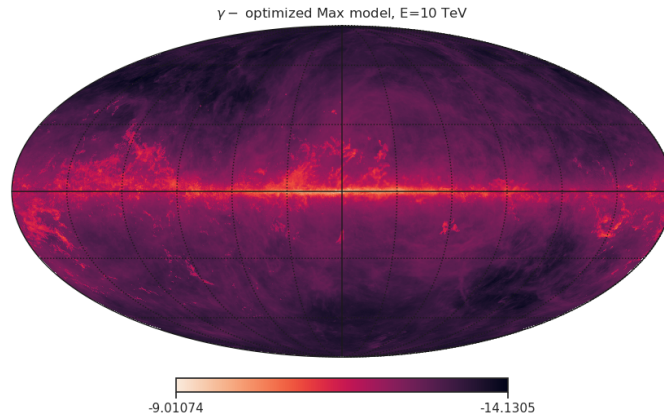


Figure 63: Per flavour neutrino sky map at 10 TeV energy predicted by the γ -optimized Max model, represented in Galactic coordinates. The colour scale is proportional to the logarithm of the flux. Figure taken from [104].

dent on the theoretical model considered, with all the uncertainty related to it, as has also been shown in Chapter 5. Another technique exploited by ANTARES and then by the KM₃NeT Collaboration is a model-independent search, capable of putting more general limits on the neutrino flux, without relying on any specific model assumption. This technique is based on a cut-and-count approach, comparing the number of events and the energy distributions observed from the region of interest, called the ON region, with respect to a background estimation derived from regions in which no signal is expected and therefore defined as OFF regions. In this second methodology, background estimation is a crucial part. For observatories like KM₃NeT, located at mid-latitude, the Earth rotation allows observing different portions of the sky, but with the same exposure and the same coverage for the detector, simply at different times within the day. For IceCube, located at the South Pole, the Earth rotation does not produce the same effect, leaving the Galactic plane in almost the same location of the sky. Also for this specific reason, KM₃NeT detectors are privileged observatories in the search for neutrino emission from the Galactic plane, being capable of exploiting both the two analysis methodologies exposed above. Taking into account all the uncertainties related to a new detector, currently under construction, such as KM₃NeT, and the possible bias in the energy and direction reconstructions, the second methodology has been chosen, being more reliable and less error prone. In fact, at its final stage, it simply relies on a data-to-data comparison of the obtained energy distributions.

7.2 PREVIOUS SEARCHES FROM THE GALACTIC RIDGE

The ON-OFF technique exposed above was already used in other searches carried out within the ANTARES Collaboration. An attempt was carried out in 2016 [117], taking advantage of the first six years of data, but already

able to put constraints on the theoretical models available up to that time. A second search was recently performed, increasing the size of the data set and also including the shower sample [114]. This search, in which I participated in developing and producing shower selection, observed an excess of events from the ON region incompatible with the background expectation at the level of 2.2σ . Under the single power law assumption, as follows:

$$\Phi(E_\nu) = \Phi_0 \cdot \left(\frac{E_\nu}{E_0}\right)^{-\Gamma}, \quad (105)$$

it was possible to fit and derive the per-flavor neutrino flux parameters:

$$\begin{aligned} \Phi(1\text{GeV}) &= 7.6_{-3.9}^{+5.0} \cdot 10^{-5} \text{ GeV}^{-1} \text{ cm}^{-2} \text{ s}^{-1} \text{ sr}^{-1}, \\ \Gamma &= 2.45. \end{aligned} \quad (106)$$

7.3 ANALYSIS STRATEGY

The overall strategy adopted within the work of this thesis is the ON-OFF technique exposed also in the previous section. The simple idea is to compare the energy distributions obtained from, respectively, the ON and OFF regions, searching for a possible excess originated by the signal we are searching for. The Galactic Ridge is the region in which our searches focus and can be defined as $|b| < 2^\circ$ and $|l| < 30^\circ$ in Galactic coordinates. The choice of this definition for the Galactic Ridge extension was motivated mainly by the fact that it contains the Galactic bar and the innermost part of the spiral arms. These are responsible for the highest star formation rate inside our Galaxy. Furthermore, with respect to previous searches, where the Galactic Ridge was defined as $|b| < 3^\circ$ and $|l| < 40^\circ$ [117], the smaller region adopted here allows easier comparison with respect to the observed γ -ray fluxes exposed in [118], and with respect to the recent results obtained by the ANTARES Collaboration [114]. Also, reducing the extension of the observed sky region from which we are expecting the signal to come from has the advantage of reducing the signal dilution into the background, which originates from atmospheric muons and neutrinos reconstructed in the same portion of the sky.

An important effect to consider in the search is also the angular resolution of the events. In fact, even if the Galactic Ridge is defined as $|b| < 2^\circ$ and $|l| < 30^\circ$, some part of the signal originated inside this region could be reconstructed outside. For this reason, to take this effect into account, the ON region has been dynamically defined as $|b| < |b_{\text{reco}}|$ and $|l| < |l_{\text{reco}}|$. To mimic the effect of angular resolution on the simulated signal, only events whose true Monte Carlo direction falls in the region $|b| < 2^\circ$ and $|l| < 30^\circ$ are taken into account. Furthermore, a second requirement is also applied, which asks the reconstructed direction to come from the region $|b| < |b_{\text{reco}}|$ and $|l| < |l_{\text{reco}}|$. The two dimensions ($b_{\text{reco}}, l_{\text{reco}}$) will be chosen on the basis of an optimisation procedure (see Section 7.4.2).

The events selected in this way are then weighted according to a proper astrophysical flux, i.e. the best fit found by ANTARES.

The OFF region is defined as the same region in the sky as the ON region, with therefore the same sky-coverage, but shifted in right ascension. Taking into account a movement of $\sim 15^\circ/\text{hour}$ in right ascension, the shift can be translated into a shift in time. A schematic representation of the shift in right ascension and the subsequent definition of the OFF region is given in Figure 64. The map, in Galactic coordinates, shows the ON-region (green rectangle) and the OFF-region, obtained by shifting the ON-region by a given time. Each rectangle refers to a precise time shift. Therefore, the OFF region can be defined continuously, applying a random shift in time between the two extremes $[t_0, t_1]$. The exact values of t_0 and t_1 are chosen based on the optimised amplitude of the ON region and with the unique constraint to avoid an overlap of the OFF region with the Fermi Bubbles. On the map reported in Figure 64, the two extremes were $[4.5\text{h}, 17.5\text{h}]$. The exclusion of the Fermi Bubbles from the OFF region was done to avoid possible bias in the background determination. This in fact is a region whose γ -ray emission was detected by the Fermi-LAT telescope and in which the nature of the γ -ray production is not yet understood, possibly being leptonic or hadronic. Therefore, from this region a flux of astrophysical neutrinos could originate. Past searches for neutrinos coming from Fermi Bubbles have also been conducted by the ANTARES Collaboration [119].

To reduce the statistical error associated with the background estimation, each event that does not fall either in the ON or within the Fermi Bubble region is shifted multiple times. After each shift, if the event falls into the ON region, then it is selected and used for the background estimation. Thus, for each event, a weight w_i is assigned proportional to the number of times the event has been selected.

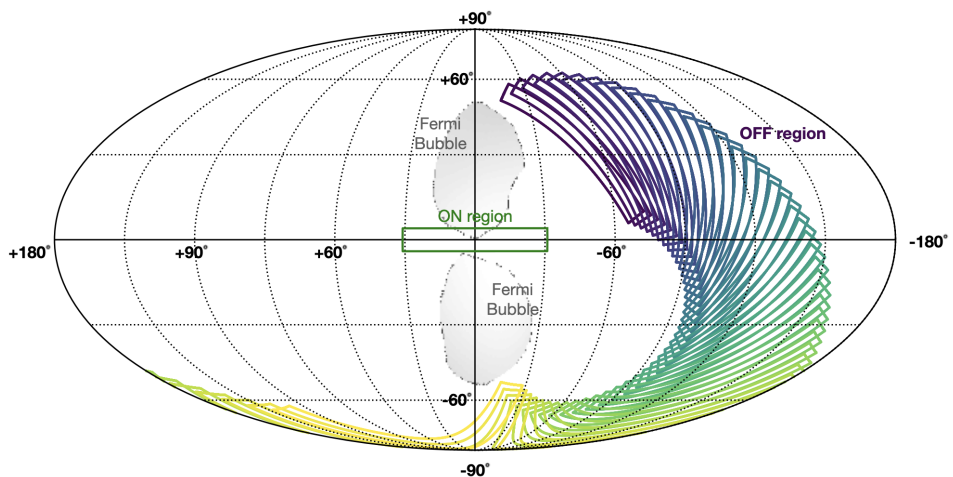


Figure 64: Map in Galactic coordinates of the ON (green rectangle) and OFF (viridis rectangles) regions. The OFF region can be seen as the continuous portion of the sky locked up by all the viridis rectangles.

7.4 OPTIMISATION PROCEDURE

Putting together all the different parts exposed in the previous sections, the final selection is chosen based on an optimisation procedure. After the final fixed cut selection (see Section 6.5.3), the remaining cuts that still need to be determined are the following:

- a cut on the BDT score: this is strictly connected to the atmospheric muon contamination. Furthermore, it has been trained to recognise events with angular resolution below 5° , therefore it has an impact also on the final resolution of the sample considered;
- the extension of the ON region (b_{reco}, l_{reco}). The optimal point reflects the angular resolution of the data set and also represents the right balance between the inclusion of as much signal as possible, avoiding to include too much background;
- another variable scanned in the optimisation is the reconstructed energy of the events. The range of values scanned for this variable is, however, limited since precise knowledge of the signal shape is not available, and the excess of ANTARES starts to be visible around 10 TeV.

7.4.1 Model rejection factor

The Model Rejection Factor (MRF) is a method to optimise experimental cuts in order to place the strongest constraints on theoretical models [120]. All optimisation procedures, which were developed within the blinding policy of the KM3NeT Collaboration, were performed only on Monte Carlo simulations. The definition of MRF is based on the concept introduced by Feldman and Cousins of the average upper limit. This limit calculation can be seen as the limit that would be observed, after hypothetical repetitions of the experiment, with an expected background n_b and no true signal. The average upper limit can therefore be defined in the following manner:

$$\bar{\mu}_{90}(n_b) = \sum_{n_{obs}=0}^{\infty} \mu_{90}(n_{obs}, n_b) \frac{(n_b)^{n_{obs}}}{(n_{obs})!} \exp(-n_b), \quad (107)$$

with n_b the number of expected background events and μ_{90} the expected upper limit. Over the set of hypothetical experiments, the strongest constraint is given by the set of cuts that minimise the quantity:

$$\text{MRF} = \frac{\bar{\mu}_{90}(n_b)}{n_s}, \quad (108)$$

where n_s is the number of signal events. Both n_b and n_s can be derived from the Monte Carlo simulation. From the value of the MRF itself it is also possible to derive an estimate of the sensitivity as follows:

$$\bar{\Phi}(E, \theta)_{90} = \Phi(E, \theta) \cdot \text{MRF}. \quad (109)$$

7.4.2 Optimisation results

An optimisation procedure was performed, based on the minimisation of the MRF, on each individual data set. A critical point could be raised considering that the optimal set of cuts for the whole merged data set does not coincide with the optimal points found for each single data set. As it will be shown in the following section, all the minima found are quite wide in the parameter space, and for data sets referring to a similar detector configuration, i.e. ARCA6 and ARCA8 or ARCA19 and ARCA21, the individual optimal selections often coincide. Furthermore, the BDT models have been trained on different configuration detectors, leading to slightly different final score distributions. Lastly, considering the rapid growth of KM₃NeT detectors and the increase in the number of different data sets to handle, it will be easier and faster in the future to combine results at the statistical level, with respect to handling a common optimisation each time.

For each of the variables taken into account in the optimisation, different cut values have been considered, linearly spanning a pre-defined range of values. Therefore, the MRF value is calculated for each possible combination of cut values. The number of signal events considered here are weighted with a single power law spectrum with a spectral index $\Gamma=2.4$, similar to the best fit found by ANTARES [114]. The optimal point does not depend on the spectrum normalisation assumed, but only on the specified spectral index. In Table 2, the optimised selections for each detector configuration are reported, with particular attention also to other checks performed.

b_{reco}	l_{reco}	BDT score	Γ	n_s	n_b	Energy cut [GeV]	MRF
ARCA6							
7	33	0.6	2.4	$1.0 \cdot 10^{-4}$	6.1	500	$5.33 \cdot 10^4$
ARCA8							
5	31	0.6	2.4	$2.10 \cdot 10^{-4}$	6.4	No cut	$2.68 \cdot 10^4$
5	31	0.6	2.4	$2.05 \cdot 10^{-4}$	5.4	500	$2.59 \cdot 10^4$
5	32	0.6	2.4	$1.95 \cdot 10^{-4}$	4.4	1000	$2.55 \cdot 10^4$
6	32	0.6	2.4	$1.35 \cdot 10^{-4}$	1.45	5000	$2.66 \cdot 10^4$
5	33	0.6	2.0	$1.65 \cdot 10^{-2}$	6.8	No cut	$3.47 \cdot 10^2$
5	31	0.6	2.7	$1.2 \cdot 10^{-5}$	6.38	No cut	$4.56 \cdot 10^5$
ARCA19							
4	31	0.4	2.4	$1.65 \cdot 10^{-4}$	3.9	500	$2.90 \cdot 10^4$
ARCA21							
4	31	0.5	2.4	$2.44 \cdot 10^{-4}$	5.6	500	$2.20 \cdot 10^4$

Table 2: Reported optimised cut values found after the MRF minimisation over the whole tested parameter space.

In Figure 65, the contour plots of the MRF are reported as a function of the three optimised variables.

Specifically, for the KM₃NeT/ARCA8 data set, more entries have been reported. In each of them, a different starting value for the optimisation procedure was chosen, i.e. a change of the assumed signal spectral index or an increasing energy cut, to check possible differences with respect to the selection adopted. The amplitude of the ON region and the BDT cut are quite stable for all different parameters tested. Concerning the energy cut, the best value would result in a cut at 1 TeV. Despite this, considering also the energy resolution of the detector still to be improved, a conservative approach has been adopted. Therefore, a cut at 500 GeV was adopted. In fact, moving the energy cut to a value of 500 GeV produces a degradation of the MRF value of the order of $\sim 2\%$.

To estimate the efficiencies obtained after the final optimised selection and to easily compare the numbers with those reported in Table 1, the number of events for the full sky is reported in Table 3, after the application of the optimal BDT and the energy cut found. The signal efficiency and

Detector	BDT cut	Atmo μ	Atmo ν	Cosmic ν	DATA	ϵ_{signal}	μ_{cont}
ARCA6 - 1 st period	0.6	18	76.92	0.91	108	46%	$\sim 20\%$
ARCA6 - 2 nd period	0.6	13	53.23	0.67	77	48%	$\sim 20\%$
ARCA8	0.6	9	193.13	3.37	308	47%	$\sim 5\%$
ARCA19	0.4	7	193	2.2	289	54%	$\sim 5\%$
ARCA21	0.5	12	330	3.3	510(*)	54%	$\sim 5\%$

Table 3: Reported the number of surviving events in the whole sky after the application of the optimised cut on the BDT score and on energy.

(*) The data events for ARCA21 reported in the table have been computed after the subtraction of events probably at the cause of the peak observed in the zenith distribution and flagged with the methodology described in Section 6.6. At this stage of the selection, the number of flagged events subtracted from the final sample is 12.

muon contamination reported in Table 3 are computed respectively as:

$$\epsilon_{\text{signal}} = \frac{\text{number of selected cosmic signal events}}{\text{number of cosmic signal events at previous selection level}}$$

$$\mu_{\text{cont}} = \frac{\text{number of atmo muon surviving the selection}}{\text{sum of all events passing the selection level}}$$

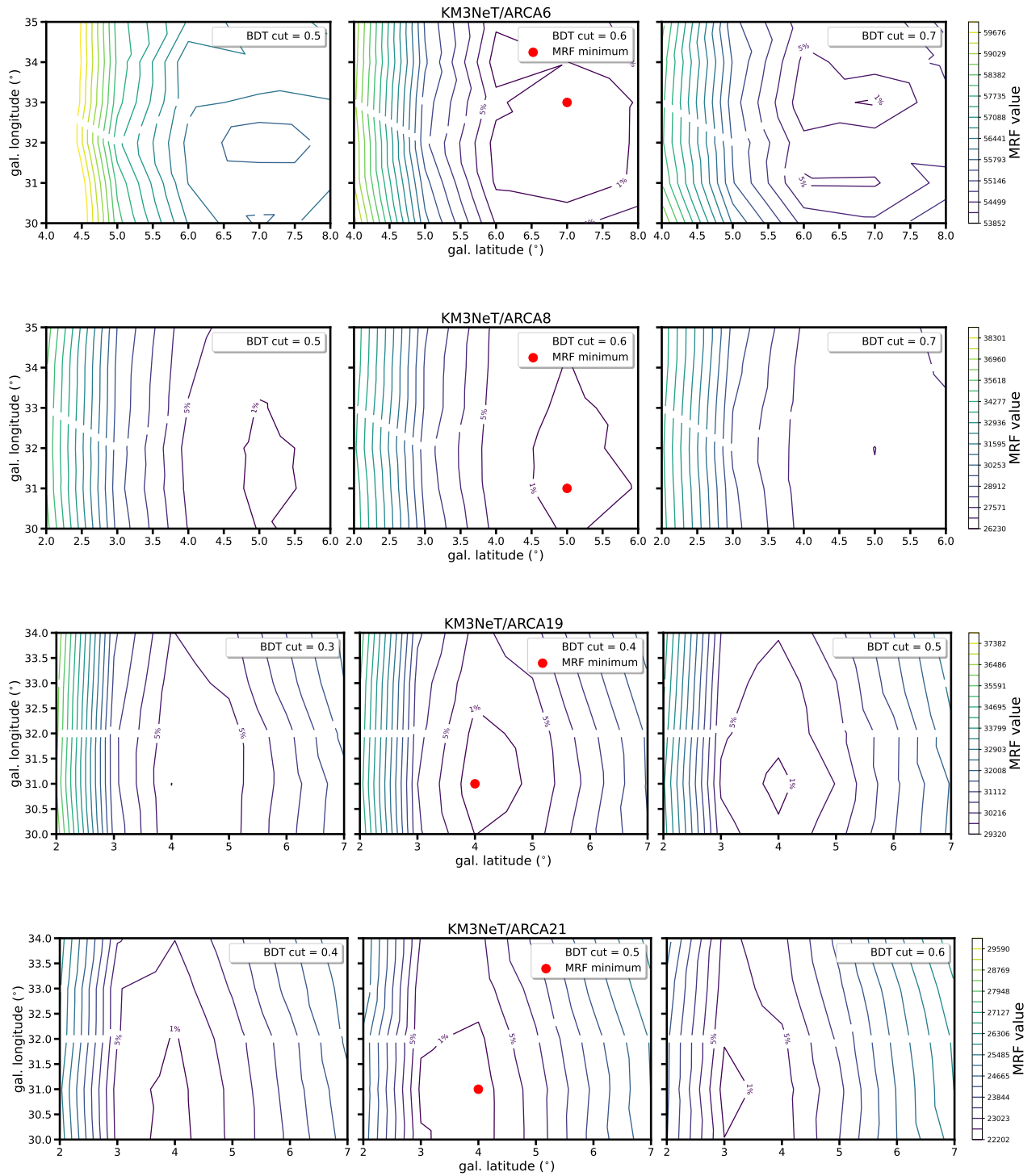


Figure 65: Contour plot of the MRF value reported as a function of the three optimised variables. The central plot corresponds to the combination of parameters producing the minimum MRF, marked with a red point. The plots on the left and right show the same distribution for adjacent BDT cuts. The two innermost contours around the minimum represent the relative variation of 1% and 5% with respect to the minimum MRF.

7.4.3 Angular resolution

The final optimised cut on the BDT dramatically reduced the number of atmospheric muons in the final sample. At the same time, the signal efficiency suggests that almost 50% of the overall signal (containing track-like and shower-like events) is lost with the introduction of this final cut level. Looking more deeply into the numbers, and in the methodology of the analysis, the events we are more interested in are those with a good angular resolution. For this reason, the plots of the angular resolution are reported in Figure 66. The parameter α has been computed considering the angular distance between the true neutrino direction and the reconstructed direction of the outgoing muon.

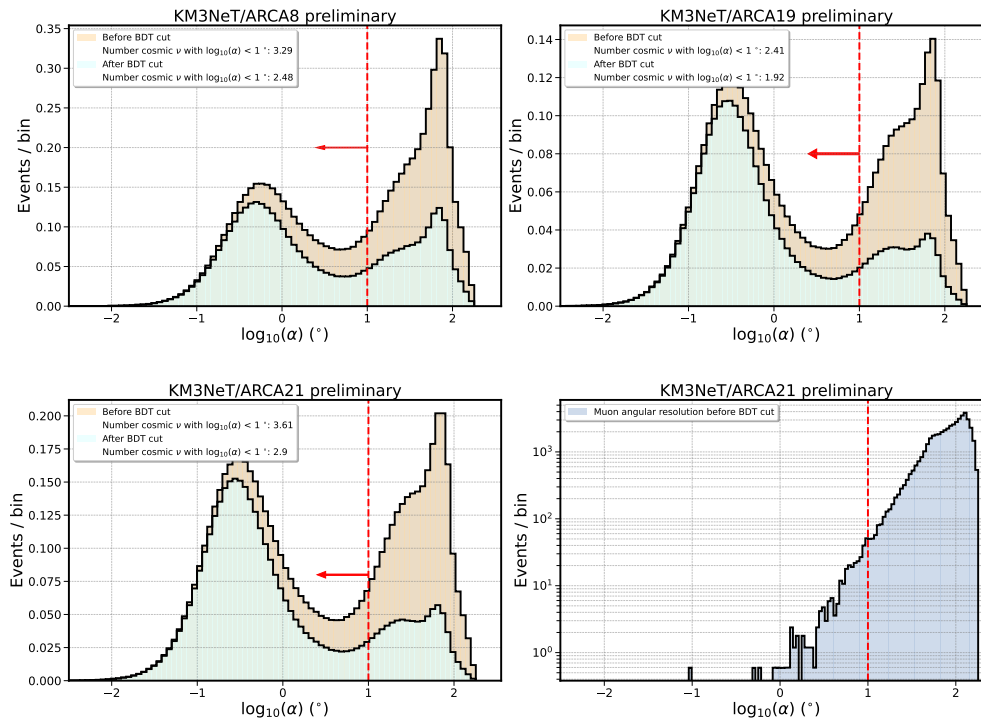


Figure 66: Histogram showing the angular resolution (α) of the simulated neutrino sample, weighted with a E^{-2} single power-law, at final fixed cut level and after the BDT and energy cut (top and bottom left panels). For comparison also atmospheric muon angular resolution is reported.

In the legend of the plots in Figure 66, the integral number of signal events with an angular resolution below 10° , before and after the introduction of the BDT cut is also reported. The value of 10° is taken as a reference, also considering the typical optimised angular amplitude of the ON region. If the signal efficiency is now recomputed considering only the subset of events with a good angular resolution (below 10°), a general value of $\sim 80\%$ is obtained. For completeness, the angular resolution of muons at the final fixed cut selection is also reported. In fact, considering the cut on the reconstructed zenith, most of the muons are badly reconstructed as upgoing

and, therefore, showing a high angular resolution. A peak around $\log_{10}(\alpha) \sim 1.9$ is visible for both neutrinos and muons. A possible explanation could be given considering those events interacting outside the detector and producing photon hits that impinge on multiple DOMs at the same time. With this specific topology, the reconstruction algorithm can mis-reconstruct the direction of the particles shifting the direction by a value equal to double the Cherenkov angle.

7.4.4 Merging event selections

In order to simplify and get comparable results, further studies have been performed to try to merge the different event selections for the smaller detector, i.e. KM₃NeT/ARCA6 and 8 and the larger detector geometries, i.e. KM₃NeT /ARCA19 and 21.

Inspecting the optimal selection found for KM₃NeT/ARCA6 and for KM₃NeT/ARCA8 the only difference is in the amplitude of the ON region. For this reason, the sensitivities, only for KM₃NeT/ARCA6, have been calculated assuming a smaller ON region, namely $|b| < 5^\circ$ and $|l| < 31^\circ$ like the one found for the KM₃NeT/ARCA8 detector. This produces a degradation in the final sensitivity of KM₃NeT/ARCA6 of the order $\sim 4\%$ with respect to optimal selection. Considering the impact of this detector geometry on the final combined sensitivity, the final selection adopted for both KM₃NeT/ARCA6 and KM₃NeT/ARCA8 is:

$$\begin{aligned} \text{Final fixed cut selection} + \text{BDT score} > 0.6 + \text{Energy} > 500 \text{ GeV}, \\ |l_{\text{reco}}| < 31^\circ, |b_{\text{reco}}| < 5^\circ \end{aligned}$$

The same treatment has been applied for the KM₃NeT/ARCA19 and 21 data sets. In fact, the only difference there is the value of the cut in the BDT score. Even in this case the sensitivities for KM₃NeT/ARCA19-only have been computed with a stricter cut on the BDT score > 0.5 . This has an impact quantifiable in a sensitivity degradation of the order of $\sim 3\%$. Also in this case the two event selections have been merged into a common one, as follows:

$$\begin{aligned} \text{Final fixed cut selection} + \text{BDT score} > 0.5 + \text{Energy} > 500 \text{ GeV}, \\ |l_{\text{reco}}| < 31^\circ, |b_{\text{reco}}| < 4^\circ \end{aligned}$$

The numbers reported in following sections will refer to this two selections.

7.5 FINAL BLINDED ENERGY DISTRIBUTIONS

Once the final selection is implemented in the different data sets, the ON and OFF energy distributions can be derived selecting the events falling in the ON and OFF regions, as described in the previous sections. For blinding policy, the energy distribution from the ON region was blinded, scrambling the right ascension of the events considered. Blinded energy distributions are reported in Figure 67.

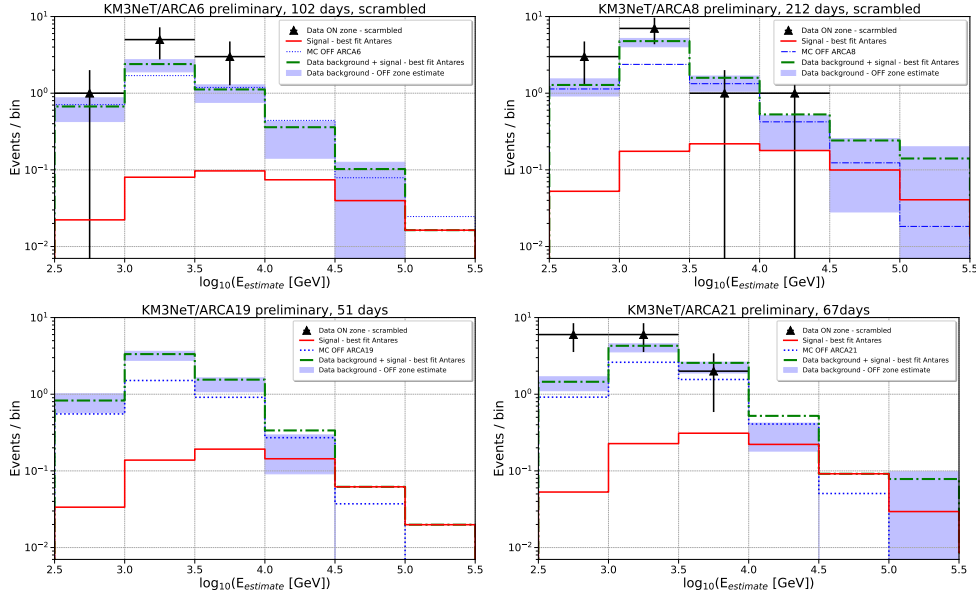


Figure 67: Blinded energy distributions for the four different data samples. Shaded blue areas represent the background derived from data in the OFF region, with its relative statistical uncertainty. For comparison but not used in the other steps of the analysis, the background derived from Monte Carlo simulations (dotted blue line) is also reported. The scramble data points falling in the ON region (black triangles) and the expected signal events, weighted with the ANTARES best-fit flux [114], are also drawn (red line).

In Table 4, the integrated energy numbers obtained from the distributions of Figure 67 are reported.

Detector	MC bkg estimate	Data bkg estimate	Signal events
ARCA6	4.1	4.8	0.34
ARCA8	5.4	7.6	0.8
ARCA19	3.2	4.9	0.59
ARCA21	5.5	8.03	0.93

Table 4: Energy integrated background estimation derived from data and from Monte Carlo. The Monte Carlo estimate is simply reported as a further check of the data and Monte Carlo comparison. The expected number of signal events is also computed, assuming the ANTARES best-fit flux [114].

7.5.1 Statistical analysis

To derive limits and fitting parameters of interest, the following statistical approach have been used. It allows also to handle easily possible combination with other detectors, i.e. ANTARES, and a proper treatment of systematic uncertainties. The statistical treatment starts from the binned energy distributions in the ON and OFF regions. From the content of each bin, the following binned likelihood method can be applied, considering Poisson statistics:

$$\mathcal{L}(N_i, S_i(\Gamma), B_i, \epsilon) = \prod_i \text{Poisson}(N_i, B_i + \epsilon \cdot S_i(\Phi_0, \Gamma)) \quad (110)$$

where:

- $S_i(\Gamma)$ is the expected number of signal events in each i -th bin, according to a specific signal flux. In the context of this work, only single power law (Φ_0, Γ) was assumed to shape the signal;
- B_i is the expected background derived from data in the OFF region;
- N_i is the number of ON events;
- ϵ accounts for systematic on the signal acceptance. Further details are given in Section 7.8.

To easily treat systematic and statistical uncertainties, a Bayesian approach has been used. This offers the main advantage of integrating out the nuisance parameters, thanks to the marginalisation of the posterior probability. In the frequentist approach, the profiling of the likelihood is very intensive from a computational point of view, and it greatly increases with the number of nuisance parameters to be profiled. To build the posterior distribution, some assumptions have to be made, incorporated in the prior terms as follows:

$$\text{Background prior, } \pi(B_i; B_i^0, e_B^i) = \prod_i \text{Gaussian}(B_i, \mu = B_i^0, \sigma = e_B^i) \quad (111)$$

$$\text{signal systematic, } \pi(\epsilon; e_z) = \text{Gaussian}(\epsilon, \mu = 1, \sigma = e_z) \quad (112)$$

$$\text{signal prior, } \pi(\Phi_0, \Gamma) = \text{flat} \quad (113)$$

As the background is derived directly from data, only statistical uncertainties e_B^i have been taken into account. The systematic on signal acceptance e_z has been incorporated after detailed calculations (exposed in Section 7.8) accounting for an overall 20% uncertainty. The prior on the signal has been taken flat, $\propto 1$. Putting together previous Equations 110-113, the posterior probability can be obtained as a product of the priors with the likelihood function. Again, due to posterior marginalisation, nuisance parameters are integrated out, and the posterior distribution can be written as a function

only of the parameters of interest, specifically Φ_0 and Γ . Further information from the posterior distribution can be obtained as best-fit points, 68% 90% and 99% credible interval contours, upper limits, the best-fit normalisation for each tested spectral index, and sensitivities drawing pseudo-experiments. An example of the statistical procedure, through some images, is reported in Figure 68.

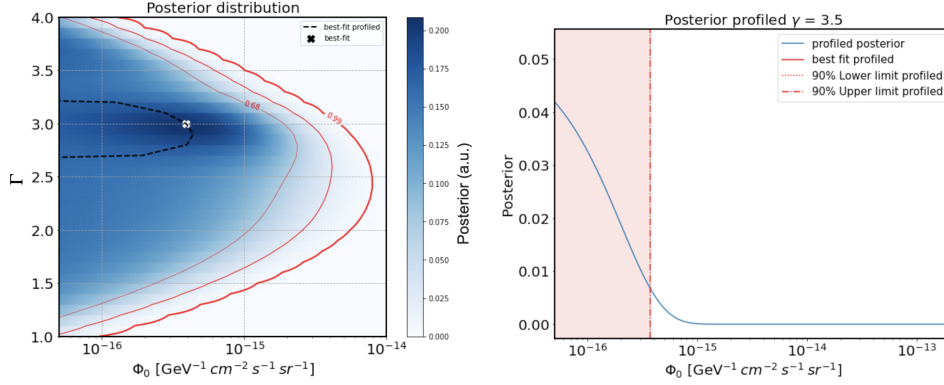


Figure 68: **Left:** 2D plane showing the posterior distribution as a function of the parameters of interest, Γ and Φ_0 . Red lines mark the 68%, 90% and 99% contours, and the white cross shows the best-fit point, obtained maximising the posterior probability. **Right:** Profiling of the posterior distribution, fixing the spectral index Γ and deriving the 90% upper limit.

7.6 SENSITIVITIES

Sensitivities can be obtained from the same scheme exposed above, thanks to pseudo-experiments. The number of observed events in each energy bin N_i is extracted as follows:

$$N_i \sim \text{Poisson}(B_i^0), \quad (114)$$

compatible with the background only hypothesis. For each pseudo-experiment, consisting of the extraction of the n values N_i , with n the number of energy bins, the 90% upper limit can be calculated, producing the distribution shown in Figure 69. Therefore, the sensitivity is calculated as the median upper limit. This calculation can be repeated in parallel for all spectral indices tested, allowing to put specific constraints as a function of the spectral index itself.

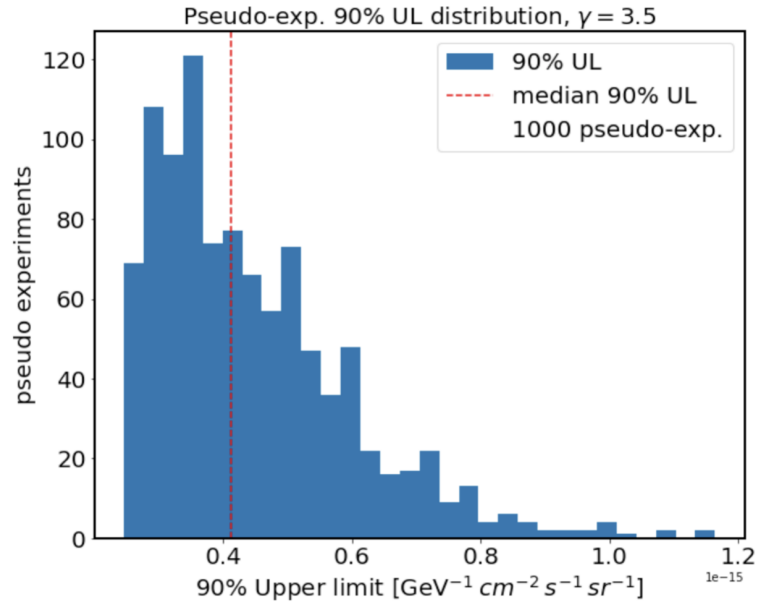


Figure 69: Distribution of 90% upper limit obtained for each pseudo-experiment, for a given fixed spectral index, i.e. $\Gamma=3.5$. Sensitivity is extracted taking the median upper limit (marked by the red dashed line).

In Table 5 the sensitivities calculated for the different data sets have been reported, as well as more general combinations, for a subset of tested spectral indices. The combination of different detector configurations is performed by multiplying the respective posterior probabilities.

Sensitivities						
Γ	ARCA6	ARCA8	ARCA6+8	ARCA19	ARCA21	ARCA6+8+19+21
2.2	$7.3 \cdot 10^{-5}$	$3.6 \cdot 10^{-5}$	$2.8 \cdot 10^{-5}$	$4.1 \cdot 10^{-5}$	$3.0 \cdot 10^{-5}$	$1.4 \cdot 10^{-5}$
2.3	$2.2 \cdot 10^{-4}$	$1.1 \cdot 10^{-4}$	$8.3 \cdot 10^{-5}$	$1.2 \cdot 10^{-4}$	$8.9 \cdot 10^{-5}$	$4.2 \cdot 10^{-5}$
2.4	$5.7 \cdot 10^{-4}$	$3.2 \cdot 10^{-4}$	$2.4 \cdot 10^{-4}$	$3.6 \cdot 10^{-4}$	$2.6 \cdot 10^{-4}$	$1.2 \cdot 10^{-4}$
2.5	$1.6 \cdot 10^{-3}$	$8.8 \cdot 10^{-4}$	$7.0 \cdot 10^{-4}$	$9.7 \cdot 10^{-4}$	$7.2 \cdot 10^{-4}$	$3.5 \cdot 10^{-4}$
2.6	$4.2 \cdot 10^{-3}$	$2.4 \cdot 10^{-3}$	$1.9 \cdot 10^{-3}$	$2.6 \cdot 10^{-3}$	$1.89 \cdot 10^{-3}$	$9.8 \cdot 10^{-4}$
2.7	$1.1 \cdot 10^{-2}$	$6.3 \cdot 10^{-3}$	$4.9 \cdot 10^{-3}$	$6.9 \cdot 10^{-3}$	$4.85 \cdot 10^{-3}$	$2.5 \cdot 10^{-3}$

Table 5: Sensitivities for KM₃NeT/ARCA 6, 8, 6+8, 19, 21 and the full combination. Reported in units of $\text{GeV}^{-1} \text{cm}^{-2} \text{s}^{-1} \text{sr}^{-1}$ at a reference energy $E_0=1$ GeV.

The energy range validity for the sensitivities shown above is considered by calculating the 5% and 95% quantiles for the weighted signal energy distribution. The results are reported in Table 6.

Energy quantiles - $\log_{10}(E)$ [GeV]								
Γ	ARCA6		ARCA8		ARCA19		ARCA21	
	5%	95%	5%	95%	5%	95%	5%	95%
2.2	3.16	6.30	3.26	6.36	3.27	6.21	3.25	6.18
2.3	2.99	6.04	3.11	6.10	3.13	6.21	3.11	5.94
2.4	2.84	5.81	2.97	5.88	2.99	5.97	2.98	5.73
2.5	2.71	5.59	2.83	5.67	2.87	5.56	2.86	5.54
2.6	2.59	5.40	2.70	5.48	2.76	5.39	2.75	5.36
2.7	2.49	5.22	2.59	5.30	2.66	5.22	2.65	5.20

Table 6: 5% and 95% quantiles for the different detector geometries as a function of the tested spectral index Γ .

In the left panel of Figure 70, a graphical representation of the sensitivity is given, for a fixed spectral index $\Gamma=2.4$. Another commonly used representation to express, with a unique line, all the different sensitivities, calculated for various spectral indices, is the so-called *butterfly plot*, like the one shown in the right panel of Figure 70.

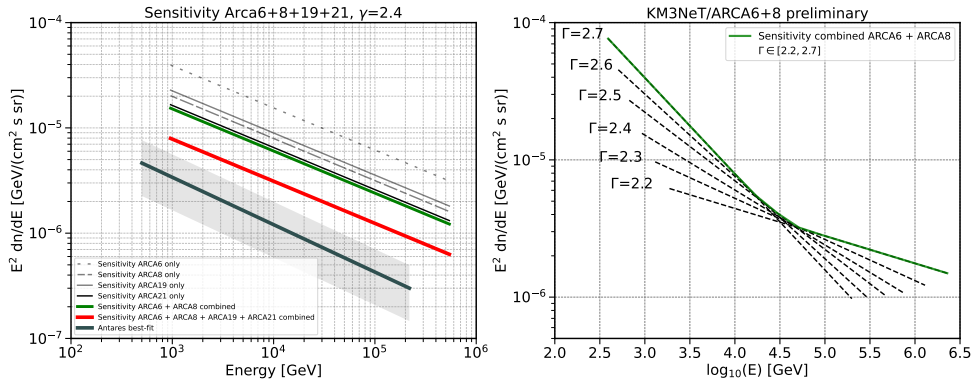


Figure 70: **Right:** sensitivity reported for the single KM3NeT/ARCA detector configurations as well as final combinations. The best-fit flux by ANTARES is also reported. **Right:** graphical explanation of the construction of the butterfly contour, summarising, within a single plot, all the different tested spectral indices.

In Figure 71, a comparison of the sensitivities obtained with KM3NeT/ARCA is reported, considering separately smaller detector configurations, i.e. KM3NeT/ARCA6+8, and the full combination. Even if the KM3NeT/ARCA19+21 data sets have a limited livetime, compared to KM3NeT/ARCA6 or 8, their contribution to overall sensitivity is significant, due to the increase in the detector effective area (roughly by a factor 3). For comparison, also the ANTARES best-fit flux with relative uncertainties is reported, as well as IceCube best-fit fluxes, obtained for the KRA_{γ}^5 and Fermi- π^0 models. Since the IceCube analysis was based on a full-sky template fitting proce-

ture, while ANTARES and KM₃NeT exploit the ON-OFF methodology, to produce a fair comparison, the ANTARES and KM₃NeT sensitivities have been integrated over the solid angle extension of the Galactic Ridge.

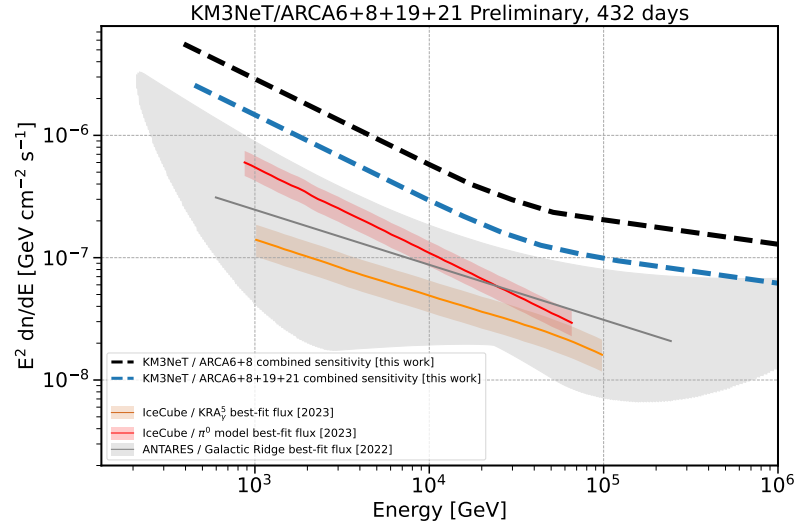


Figure 71: KM₃NeT combined sensitivity for ARCA6+8 (dark blue dashed line) and the full data set (light blue dashed line). The ANTARES and IceCube best-fit fluxes have been reported. For a fair comparison, the ANTARES and KM₃NeT limits have been integrated over the solid angle spanned by Galactic Ridge.

7.7 UNBLINDED RESULTS AND UPPER LIMITS

Once the unblinding is granted, the final energy distributions can be drawn (see Figure 72) and the total number of events in the ON region, found for each detector configuration, are reported in Table 7.

Detector	BKG from DATA	Signal-best fit Antares	ON region events
ARCA6	4.8	0.34	7
ARCA8	7.6	0.8	8
ARCA19	4.9	0.59	4
ARCA21	8.03	0.93	8

Table 7: Final numbers for the background data estimation from the OFF region, number of events found in the ON region, and expected number of signal events assuming the best-fit flux of ANTARES, specifically for each KM₃NeT detector configuration.

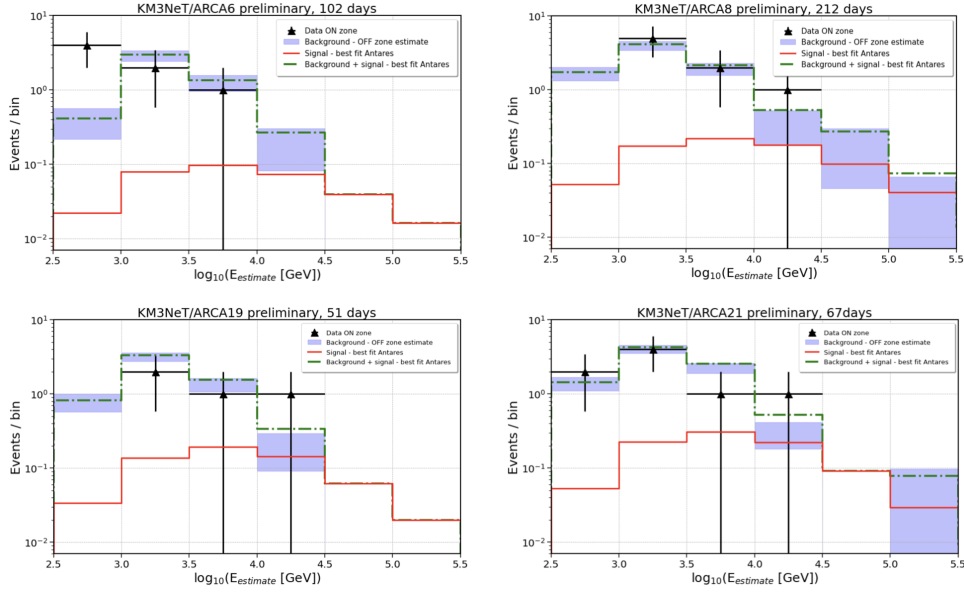


Figure 72: Final energy distributions, after unblinding, for the ON and OFF regions, for each different detector configuration.

The numbers found are compatible with the background expectation, not showing any significant excess in any of the energy bins. For this reason, exploiting the energy distribution of the ON events found after unblinding, the 90% confidence level upper limit can be calculated, and has been reported in Table 8.

90% C.L. upper limits						
Γ_ν	ARCA6	ARCA8	ARCA6+8	ARCA19	ARCA21	ARCA6+8+19+21
2.2	$8.6 \cdot 10^{-5}$	$4.5 \cdot 10^{-5}$	$3.4 \cdot 10^{-5}$	$4.9 \cdot 10^{-5}$	$3.4 \cdot 10^{-5}$	$1.9 \cdot 10^{-5}$
2.3	$2.7 \cdot 10^{-4}$	$1.3 \cdot 10^{-4}$	$1.1 \cdot 10^{-4}$	$1.5 \cdot 10^{-5}$	$1.0 \cdot 10^{-4}$	$5.8 \cdot 10^{-5}$
2.4	$8.2 \cdot 10^{-4}$	$3.9 \cdot 10^{-4}$	$3.0 \cdot 10^{-4}$	$4.1 \cdot 10^{-4}$	$2.8 \cdot 10^{-4}$	$1.7 \cdot 10^{-4}$
2.5	$2.3 \cdot 10^{-3}$	$1.1 \cdot 10^{-3}$	$9.0 \cdot 10^{-4}$	$1.1 \cdot 10^{-3}$	$7.8 \cdot 10^{-4}$	$4.8 \cdot 10^{-4}$
2.6	$6.5 \cdot 10^{-3}$	$2.9 \cdot 10^{-3}$	$2.5 \cdot 10^{-3}$	$2.8 \cdot 10^{-3}$	$2.1 \cdot 10^{-3}$	$1.3 \cdot 10^{-3}$
2.7	$1.7 \cdot 10^{-2}$	$7.4 \cdot 10^{-3}$	$6.8 \cdot 10^{-3}$	$7.1 \cdot 10^{-3}$	$5.5 \cdot 10^{-3}$	$3.5 \cdot 10^{-3}$

Table 8: 90% C.L. upper limits under a single power-law assumption for a reference energy $E_0 = 1$ GeV and with spectral indices Γ ranging from 2.2 to 2.7 for KM3NeT/ARCA6, KM3NeT/ARCA8, KM3NeT/ARCA19, KM3NeT/ARCA21 and the combined data sets. All results are expressed in units of $\text{GeV}^{-1} \text{cm}^{-2} \text{s}^{-1} \text{sr}^{-1}$ at a reference energy $E_0=1$ GeV.

A similar plot to Figure 71 has also been produced, reporting this time the upper limits found after the unblinding (see Figure 73).

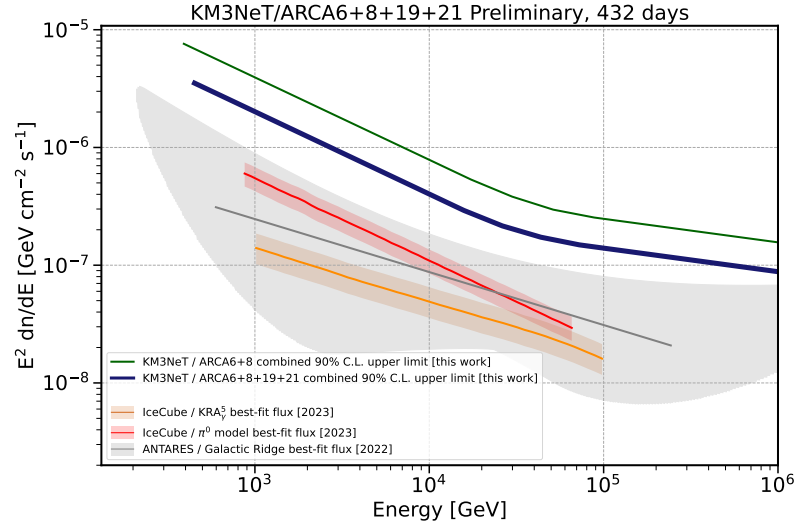


Figure 73: 90% confidence level upper limit, for the tested spectral indices, reported in Table 8 and drawn here as butterfly contour. For comparison, ANTARES and IceCube best-fit fluxes are reported. As previously done for the sensitivity plot, ANTARES and KM₃NeT limits have been integrated over the solid angle, spanned by the Galactic Ridge.

7.8 SYSTEMATIC EVALUATION

The systematic error in the signal acceptance has been evaluated by performing dedicated Monte Carlo simulations, allowing a limited number of parameters to be identified as the main contributors. To differentiate and quantify their contribution to the overall systematic error, a dedicated simulation has been performed, varying one parameter at a time. The main two parameters considered in this study were the light absorption length and the PMT quantum efficiency. Since the final upper limits are extracted from distributions derived from data, no other systematic uncertainties, possibly affecting the background simulation, have been considered. The 10% of the overall livetime of the KM₃NeT/ARCA8 data set has been used and simulated with varying starting conditions: a $\pm 10\%$ for the absorption length, in agreement with what was previously done by the ANTARES Collaboration [121] and a $\pm 5\%$ on the PMT quantum efficiency. The percentage variation with respect to the standard Monte Carlo production has been calculated and shown in Figure 74. When combining the respective variations in quadrature, an overall value of 20%, assumed constant in energy, has been adopted and used at the statistical analysis level. Taking into account the time-consuming computational cost of launching several different Monte Carlo productions, the value of 20%, calculated over the KM₃NeT/ARCA8 data set, has also been used for the other detector configurations. In other analyses of the KM₃NeT Collaboration, other uncertainties affecting atmospheric neutrino and muon flux, reported in Figure 50, have also been considered.

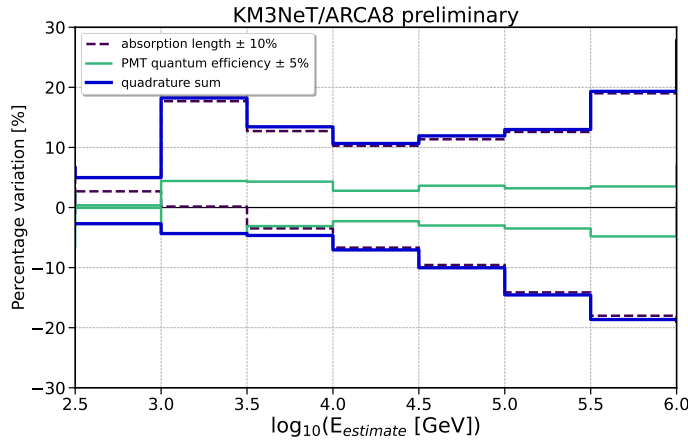


Figure 74: Percentage variation of the modified Monte Carlo simulations with respect to the standard simulation, as a function of the reconstructed energy. Each of the single contribution is visible: PMT quantum efficiency (green solid line), light absorption length (purple dashed line) and the quadrature sum of the two (blue solid line).

ENERGY RESOLUTION Another point currently under evaluation by the KM3NeT Collaboration is the energy resolution obtained on the different data samples and the impact of the parameter variations on it. In Figure 75 with the same methodology described in the previous paragraph, the percentage variation with respect to the standard Monte Carlo has been computed as a function of the true neutrino energy. The main visible effect occurred for the decreased absorption length, which produced a greater number of detected and reconstructed neutrinos with true energy below ~ 5 TeV. These events are then redistributed in different bins of reconstructed energy, generating the differences observed in Figure 74. The shift of these events among the two distributions is just due to the energy resolution of the detector. In Figure 76, an estimate of the energy resolution for ν_μ -CC events, weighted with an E^{-2} spectrum, is also reported.

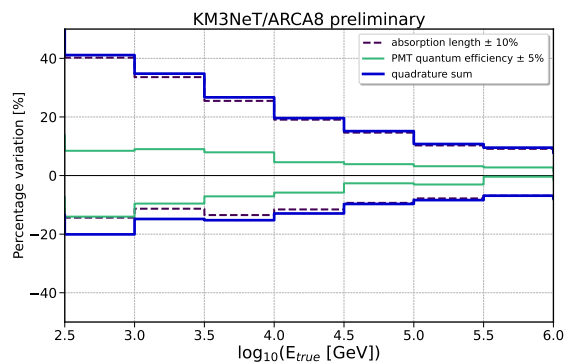


Figure 75: Percentage variation of the modified Monte Carlo simulations performed with respect to the standard simulation chain, in function of the true neutrino energy.

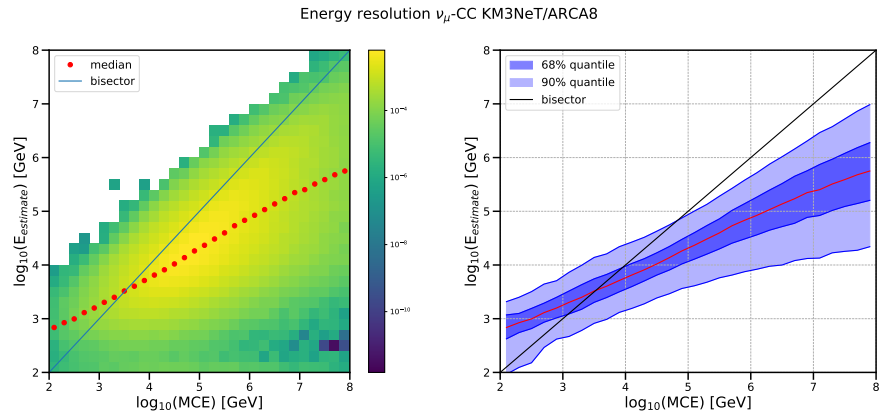


Figure 76: **Left:** 2D histogram of the Monte Carlo energy (MCE) as a function of the reconstructed energy for ν_{μ} -CC events. With the red points the weighted median distribution is marked. **Right:** median, 68% and 90% contour distribution for the energy resolution.

In the context of multi-messenger astronomy, real-time alerting systems have been developed by several experiments from CR to GW detectors, including neutrino telescopes and electromagnetic satellites and ground-based detectors, constantly exchanging information on interesting events.

The alerts sent through circulars, rapid bulletins distributed to the community worldwide, contain key information on the event: sky localisation, time of the event, angular uncertainty, and localisation map. Within this context, KM₃NeT, on the basis of the experience gathered with follow-ups conducted by the ANTARES Collaboration [122], has started to develop tools and frameworks capable of reconstructing and analysing data in real-time. The necessity to rapidly perform follow-up of external alerts arises, particularly during the occurrence of fast transient phenomena. In fact, neutrino signals have been predicted, in many scenarios, to constitute part of the prompt emission, which, if detected, would allow other observatories to point their field of view in the same direction.

8.1 FIRST KM₃NET FOLLOW-UP: PKS 0735+17

The first follow-up search, conducted by the KM₃NeT Collaboration, in which I was among the corresponding authors, was for the IceCube-211208A alert, occurred during the KM₃NeT/ARCA8 data taking period. Specifically, the IceCube Collaboration reported an event with a moderate probability of having astrophysical origin (signalness 50.3%) and a reconstructed energy of 172 TeV [124]. The source PKS 0735+17, a prominent radio and γ -ray blazar, was located just outside the 90% containment of the IceCube event. Other follow-up observations of the source found the blazar experiencing a strong flaring activity in the γ -ray [125], X-ray [126–128], optical [129, 130] and radio [131] bands. The IceCube [132] and the ANTARES Collaboration [133] searched for additional neutrino events in correlation with the source, but no further candidate events were found.

The signalness definition given by IceCube Collaboration, in order to categorise alerts, is defined as follow:

$$\frac{N_{\text{signal}}}{N_{\text{signal}} + N_{\text{bkg}}}$$

with N_{signal} and N_{bkg} respectively the number of signal and background events surviving to the selection cuts [123].

8.1.1 Time windows

The strategy adopted to follow up the alert, within the KM3NeT Collaboration, was to perform two separate searches, trying to find neutrino events in spatial and time coincidence with the source PKS 0735+17, during its flaring activity. The first focused on a time window of ± 1 day with respect to the IceCube event time (2021-12-08, 20:02:51.1 UT), and centred on the Fermi sky localisation of the PKS 0735+17 blazar: right ascension (RA) = 114.539° and declination (DEC) = 17.707° . A second similar analysis was performed following up the longer flaring period observed in γ -ray by the FERMI-LAT telescope, accounting for the whole month of December, as also shown in Figure 77.

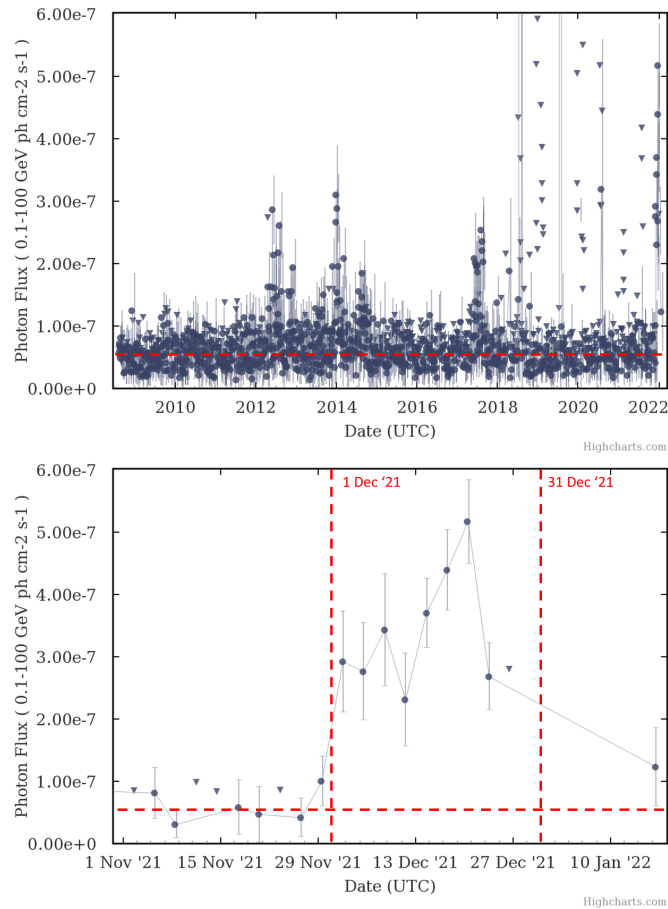


Figure 77: γ -ray flux of the blazar PKS0735+17 observed by the Fermi-LAT telescope in the period 2009 - 2022 (**left**) and around the flaring period in December 2021 (**right**). Figures taken from [134].

8.1.2 Analysis procedure: ON-OFF method

The analysis strategy adopted for the follow-up of this event is the same cut-and-count approach exposed in Chapter 7. The main change here is the definition of the ON and OFF regions. The ON region, also referred to as the Region of Interest (RoI), has been assumed to be a circular cone, centred on the source position and with a variable radius, established through an optimisation procedure. The OFF region was selected as a declination band centred on the source declination and with an amplitude of 20° . The main reason for this choice is to obtain a reliable background estimate, avoiding bias selecting events from regions in the sky with a different declination distribution. At the same time, the amplitude of the band of 20° allows enough events to be selected in order to reduce the statistical error associated with the background estimation. As in the case of the OFF region construction in Section 7.3, the right ascension of the centre of the ON region moves roughly $\sim 15^\circ/\text{hour}$, spanning the full declination band within a full day. For this reason, also in this case, the OFF region can be seen as the continuous time-shifted ON region in 24 hours. A schematic representation of the ON and OFF regions is shown in Figure 78. The background estimation can

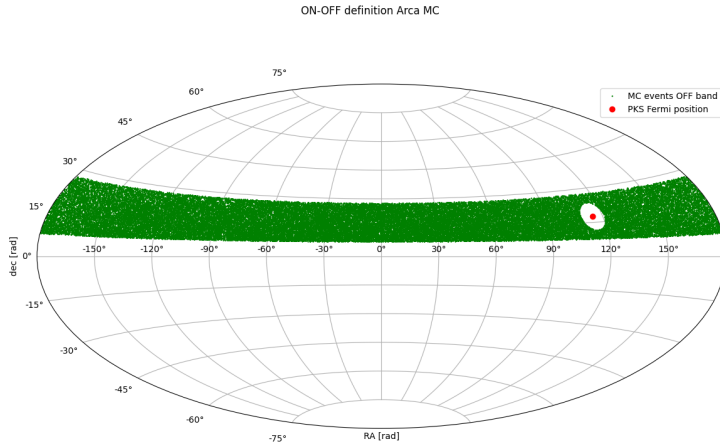


Figure 78: Schematic representation of the ON and OFF region considered in IceCube-211208A alert follow-up.

then be derived by rescaling the number of data events falling in the OFF region by a solid angle factor, defined as:

$$\frac{\Omega_{\text{ON}}}{\Omega_{\text{OFF}}} = \frac{\Omega_{\text{ON}}}{\Omega_{\text{band}} - \Omega_{\text{ON}}}, \quad (115)$$

with:

$$\Omega_{\text{ON}} = 2\pi \cdot [1 - \cos(\text{RoI radius})] \quad (116)$$

$$\Omega_{\text{band}} = 2\pi \cdot [\sin(\delta_{\text{PKS}} + 10^\circ) - \sin(\delta_{\text{PKS}} - 10^\circ)] \quad (117)$$

where δ_{PKS} is the declination of the blazar PKS 0735 + 017, determined by the FERMI-LAT detector.

8.1.3 Event selection

The event selection adopted in this search was similar to the one exposed also in Chapter 6. It is based on a series of consecutive fixed cuts on reconstruction variables, trying to get rid of the environmental and of the atmospheric muon background. Subsequently, an optimisation was performed, searching for the optimal value of the extension of the region of interest and the best cut in the reconstructed energy. As a starting point, the same preliminary, anti-noise (events with likelihood values above 50 instead of 40) and upward-going selection have been applied to the data set (see Section 6.5.3). At the moment of the alert, no Monte Carlo simulations were available for the KM3NeT/ARCA8 detector, but only those referring to the KM3NeT/ARCA6 configuration. However, to perform a rapid follow-up, the selection procedure was tested and optimised on the available simulations, incorporating a constant shifting factor, for the event normalisation, to match the KM3NeT/ARCA8 data.

MODEL DISCOVERY POTENTIAL The optimisation procedure was based on the minimisation of a metric, commonly used within the context of neutrino telescopes, called Model Discovery Potential (MDP) [135]. It is defined as follows:

$$\text{MDP} = \frac{n_\alpha(\langle n_b \rangle)}{\langle n_s \rangle}, \quad (118)$$

where n_α is the signal strength that leads to a p-value less than α in a fraction $1 - \beta$ of the hypothetical experiments, and $\langle n_b \rangle$ and $\langle n_s \rangle$ are, respectively, the number of expected background and signal events.

The MDP could be interpreted, taking into account an arbitrarily astrophysical flux (Φ_s), producing $\langle n_s \rangle$ signal events inside the detector during the livetime ΔT , as:

$$\Phi_\alpha = \Phi_s \cdot \text{MDP}, \quad (119)$$

where Φ_α is just the minimum flux leading to a discovery. The values of α and β chosen in this specific work were $\alpha = 1.35 \cdot 10^{-3}$ (for a statistically significant evidence above 3σ) and a power of $1 - \beta = 0.5$.

The optimal values found from the minimisation of the MDP, carried out in the two-dimensional parameter space radius of the RoI region and reconstructed energy, are:

$$\text{ROI radius} = 1.4^\circ \text{ and reconstructed energy} > 500 \text{ GeV.}$$

8.1.4 Results

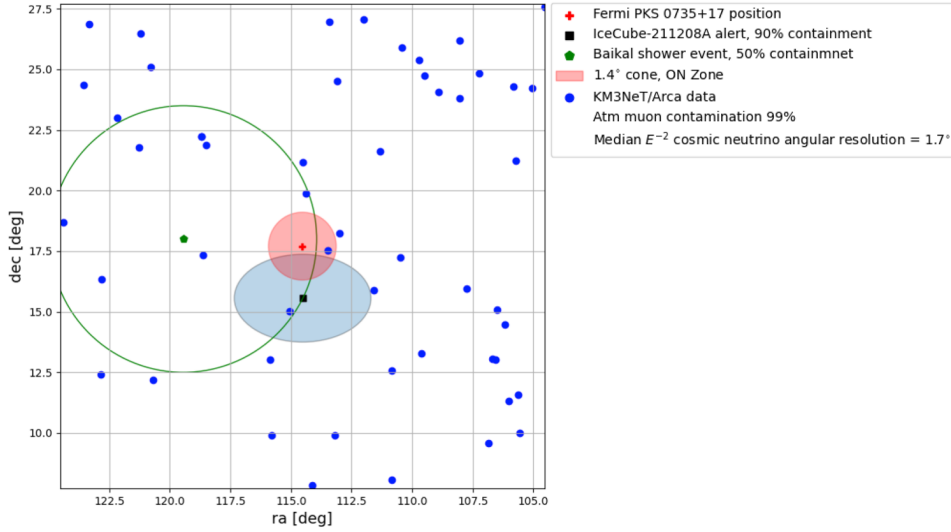


Figure 79: Sky map for the full month of December 2021, showing KM₃NeT/ARCA events falling in a cone with radius of 10°. Reported with shaded areas: the KM₃NeT ON region in red (centred on the blazar location detected by the Fermi-LAT telescope), the best-fit IceCube position, and the relative 90% containment error in blue, and the Baikal-GVD shower event with associated uncertainty in green.

In Table 9 the final unblinded results for this analysis have been reported: no events have been found in the ON region for the time window of ±1 day. For the full month time window, instead, 1 event has been found in the ON region, providing a Poisson significance of 1.06σ. For completeness, the reconstruction variables for this event are provided in Table 10.

FINAL RESULTS		
Time window	± 1 day	1 month
Signal (ON region)	0	1
OFF region band	52	736
Background (OFF region, after solid angle factor)	$(4.7 \pm 0.7) \cdot 10^{-2}$	$(6.6 \pm 0.3) \cdot 10^{-1}$
Poisson significance	—	1.06σ

Table 9: Final number of events in the ON region, once data set has been unblinded. The value "OFF region band" reported the number of events found in the full declination band, whereas the "background" refers to the estimate after the solid angle rescaling.

FINAL NEUTRINO CANDIDATE EVENT #1	
1 month time window	
DETECTION TIME	15th December 2021 08:51:31.6 UT
RECONSTRUCTED ENERGY	4.104 TeV
RIGHT ASCENSION	113.48°
DECLINATION	+17.55°
ZENITH	101.44°
AZIMUTH	211.37°
ANGULAR UNCERTAINTY β_0	0.74°
LIKELIHOOD	58.82
NUMBER_OF_HITS	42
TRACK LENGTH	241.07 m
RUN	10845
EVT.ID	32588

Table 10: Values of the main reconstructed variables for the unique neutrino candidate event found inside the ON region in the full month time window.

The results of the follow-up have been published through the first Astronomer telegram, sent by the KM3NeT Collaboration, available here [136]¹.

¹ Analysis conducted in tight collaboration with J. Palacios Gonzales: Juan.Palacios@ific.uv.es and R. Muller: rasamuller@gmail.com.

8.1.5 Other IceCube alert follow-ups

Other searches, similar to the one exposed in the previous section, have also been performed soon after, looking for possible space and time correlations of candidate neutrino events within the KM3NeT data set with IceCube alerts. The following alerts have been followed-up:

- IC-220225A [137]. Time: 2022-02-25 14:12:00.7 UT; position (J2000): RA: $34.7^\circ (+3.1^\circ / -2.6^\circ)$, DEC: $0.00^\circ (+1.8^\circ / -1.5^\circ)$, errors referring to the 90% point spread function containment. One γ -ray source was found within the 90% error region: the flat-spectrum radio quasar PKS 0215+015, which is known to be a radio and γ -bright AGN. PKS 0215 + 0215 has shown enhanced γ -ray activity since mid-2021;
- IC-220303A [138]. Time: 2022-03-03 18:00:07.62 UT; position (J2000) RA: $267.80^\circ (+1.50^\circ / -1.17^\circ)$, DEC: $+11.42^\circ (+0.89^\circ / -1.14^\circ)$. There were no Fermi 4FGL or 3FHL catalogue sources in the 90% uncertainty region.
- IC-220304A [139]. Time: 2022-03-04 17:44:12.21 UT; position (J2000) RA: $48.78^\circ (+7.68^\circ / -6.24^\circ)$, DEC: $4.48^\circ (+5.91^\circ / -4.96^\circ)$. The energy of the event was estimated to be 263.21 TeV. Many γ -ray sources were compatible with the 90% region;
- IC-220425A [140]. Time: 2022-04-25 02:44:57.82 UT; position (J2000) RA: $268.24^\circ (+1.98^\circ / -1.66^\circ)$, DEC: $-10.73^\circ (+1.71^\circ / -1.48^\circ)$. One γ -ray source listed in the 4FGL-DR3 Fermi-LAT catalogue was located within the 90% containment region. The source was associated with the flat-spectrum radio object TXS 1749-101;
- IC-220524A [141]. Time: 2022-05-24 07:41:32.185 UT; position (J2000) RA: $47.20^\circ (+4.21^\circ / -2.51^\circ)$, DEC: $-3.28^\circ (+0.77^\circ / -0.89^\circ)$. No Fermi 4FGL or 3FHL catalogue sources were located within the 90% uncertainty region.

The analysed ON time window, for each of the alerts listed above, was the "standard" ± 1 day with respect to the alert time. Furthermore, an optimisation procedure was conducted separately for each of them. After unblinding, no events have been found in the ON region for any of the alerts analysed.

8.2 GRB221009A FOLLOW-UP

During October 9th 2022, at 14:10:17 UT, the Swift-BAT telescope detected a transient event catalogued as *Swift J1913.1+1946*, with a position in equatorial coordinates $RA = 288.263^\circ$ and $DEC = +19.803^\circ$ [142]. Then Fermi-GBM sent an alert pointing out a triggered event at time 13:16:59.0 UT (since now referred to as T_0) at the location $RA = 290.4^\circ$ and $DEC = +22.3^\circ$, with 1-degree statistical uncertainty, consistent with the Swift-BAT localisation [143]. The event represents one of the brightest GRBs ever detected by Fermi-GBM. Soon after, the LHAASO Collaboration reported the detection of events in coincidence with GRB221009A with energies greater than 500 GeV and up to 18 TeV, within 2000 s after T_0 [144]. This was the first detection of photons above 10 TeV in association with a GRB. The Fermi-LAT telescope also observed the event in a time window T_0+200s and T_0+800s , detecting the highest energy photon 240 seconds after the Fermi-GBM time, with an estimated energy of 99.3 GeV [145]. Tentative redshift determination from the afterglow observation derived a value of $z = 0.151$. In a follow-up analysis of the Carpet-2 data [146], at the Baksan Neutrino Observatory, a photon shower event was detected, consistent with the position of GRB221009A, with an estimated energy of 251 TeV, detected 4536 s after the Fermi-GBM trigger time.

High-energy photons lose energy through the creation of electron-positron pairs in interaction with the EBL, as described in Section 1.3.2. A 250 TeV photon cannot reach Earth from a source located at redshift $z=0.151$ (~ 638 Mpc), as also shown in Figure 14. A possible explanation of the Baksan observation, not invoking new physics beyond the Standard Model, could be, given the declination of the source near the Galactic plane, a coincidence detection of a photon originated inside our Galaxy. A further search for neutrino emission was performed by the IceCube Collaboration, without any significant detection. Unfortunately, ANTARES was no longer taking data at that time, and no results were promptly reported by the Baikal-GVD telescope. Given the importance of this event, a fast analysis was performed with the data collected by the KM3NeT detectors.

8.2.1 KM3NeT follow-up

The same ON-OFF strategy described before has also been used for the follow-up of the event GRB221009A. The selected time window for this search, often referred to in the text as *ON time window*, regards a transient phenomenon. For this reason, it is considerably shorter with respect to previous follow-ups and has been chosen as an interval of the form: $[T_0-50$ s, T_0+5000 s]. Although the window is longer than 90% time containment of the flaring light curve detected by Fermi and Swift, it was conservatively decided to extend it in order to account for the event measured by the Carpet-2 detector. Within the entire duration of the ON time window, the source was located in the downgoing sky for the KM3NeT detectors.

In fact, the zenith of the source, specifically for the KM₃NeT/ARCA telescope, at time $T_0 - 50$ s was 50.8° and at the time $T_0 + 5000$ s was 34.2° . As already specified in this thesis, the downgoing sky is dominated by atmospheric muon background, which makes neutrino selection quite challenging. However, considering the limited extension of the ON time window and the importance of the event, a follow-up analysis was performed. The KM₃NeT/ARCA detector, at the time of the event, comprised 21 active detection units. Unfortunately, no Monte Carlo was available, therefore, a fast search was performed directly on the data. A first inspection of the event

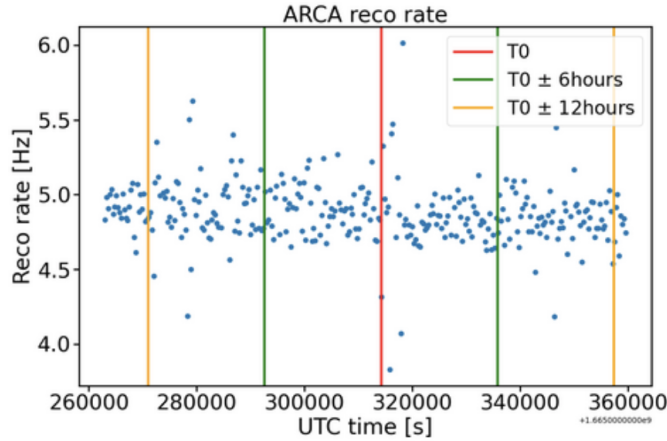


Figure 80: Reconstructed event rate in KM₃NeT/ARCA₂₁ (dominated by the atmospheric muons) as function of UTC time, in time bins of 5 minutes. The T_0 (red), $T_0 \pm 6$ hours (green), and $T_0 \pm 12$ hours (yellow) are also reported with vertical lines.

rates in the data collected in ± 12 hours with respect to T_0 , available in Figure 80, suggested stable data acquisition and good quality of the data acquired by the KM₃NeT/ARCA detector.

Furthermore, the ON region was selected as a circular cone around the source location, with a fixed radius of 2° . This value was chosen considering a rough estimate for the median angular resolution of neutrino events detected with the KM₃NeT/ARCA₂₁ telescope. Since the time window selected for the search was not an entire multiple of a day, the background estimation has not been performed in equatorial or Galactic coordinates. In fact, considering a time interval shorter than a day, the source spans only a subset of the right ascension range, with respect to what occurs for other follow-ups, making the background estimation no more reliable. For this reason, the search was performed in local coordinates, always taking advantage of the concept of band, in order to reduce the statistical error associated with the background estimation, but now defined as zenith bands, following the schematic procedure also reported in Figure 81. Additionally, considering the limited extension of the ON time window, the background estimate was derived considering larger time windows around T_0 , referred often in the text as *OFF time window*. Specifically for this event, the following windows have been selected: $[T_0 - 50 \text{ s} - 1.5 \text{ h}, T_0 - 50 \text{ s}]$ and $[T_0 + 5000$

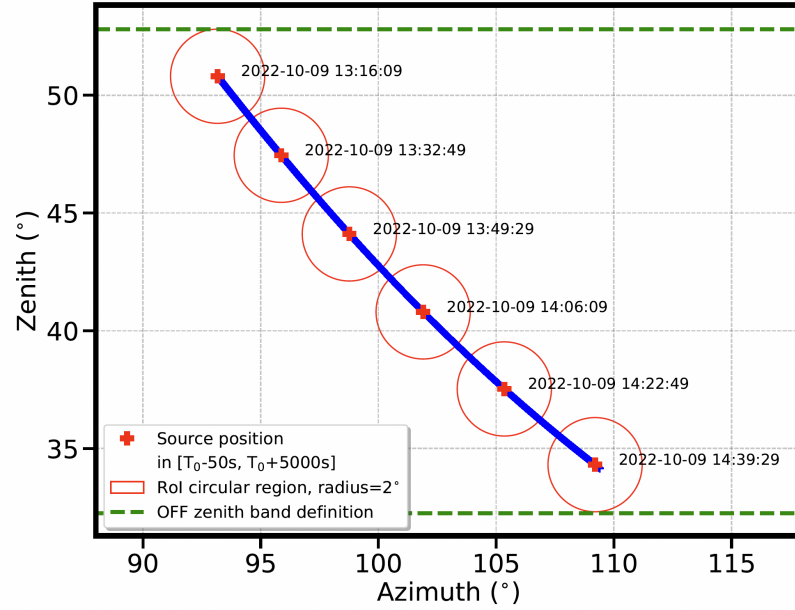


Figure 81: ON and OFF region definition for the GRB2201009A follow-up taking into account the movement of the source in local coordinates (blue points) in the time interval $[T_0 - 50 \text{ s}, T_0 + 5000 \text{ s}]$. OFF zenith band defined as the maximum and minimum zenith values reached by the region of interest in the ON time window (green dashed lines).

$s, T_0 + 5000 \text{ s} + 1.5 \text{ h}]$, accounting for a total livetime of 3 hours. The number of events found in the zenith band, in the OFF time window, should then be rescaled by a solid angle and a livetime ratio factor, following the form:

$$N_{\text{bkg}} = N_{\text{OFF}} \cdot \frac{\Omega_{\text{ON}}}{\Omega_{\text{OFF}}} \cdot \frac{T_{\text{ON}}}{T_{\text{OFF}}}, \quad (120)$$

with Ω_i the solid angle spanned by the ON and OFF regions (see Equation 117) and T_i the livetime considered for the ON and OFF time windows respectively.

8.2.2 Event selection

The event selection adopted for this follow-up, which does not rely on any Monte Carlo simulation and involves the downgoing sky, is based on simple assumptions looking at the data distributions. The starting point is the usual preliminary selection level (see Section 6.5.3). Additionally, other simple cuts on reconstruction variables have been adopted, with the main goal of deriving a background expectation below 0.1 events. When inspecting the energy distribution, as shown in the left panel of Figure 82, a double-peaked structure is visible. The first peak, around hundreds of GeV, is mainly due to single atmospheric muons traversing the detector. Instead, the second broader peak, in between 1 and 10 TeV, should be mainly due to muon bundles traversing the detector. In fact, bundles are reconstructed

as a single atmospheric muon with energy equal to the sum of the energies of all the muons in the bundle. For this reason, a cut has been set, selecting events with reconstructed energy larger than 1 TeV, to exclude single atmospheric muons. The second cut on the likelihood has been tuned to reach the background of 0.1 expected events, without any specific requirement on the resulting signal efficiency or muon contamination (for a detailed definition, see Section 7.4.3). Nevertheless, atmospheric muon events that survive to the energy cut are dominated by muon bundles. These are expected to be reconstructed with lower likelihood values with respect to neutrino-induced track-like events (corresponding to actually one muon). In fact, the likelihood function is constructed assuming, as hypothesis, a single track for the fit. For these reasons, events with a likelihood value greater than 155 were selected.

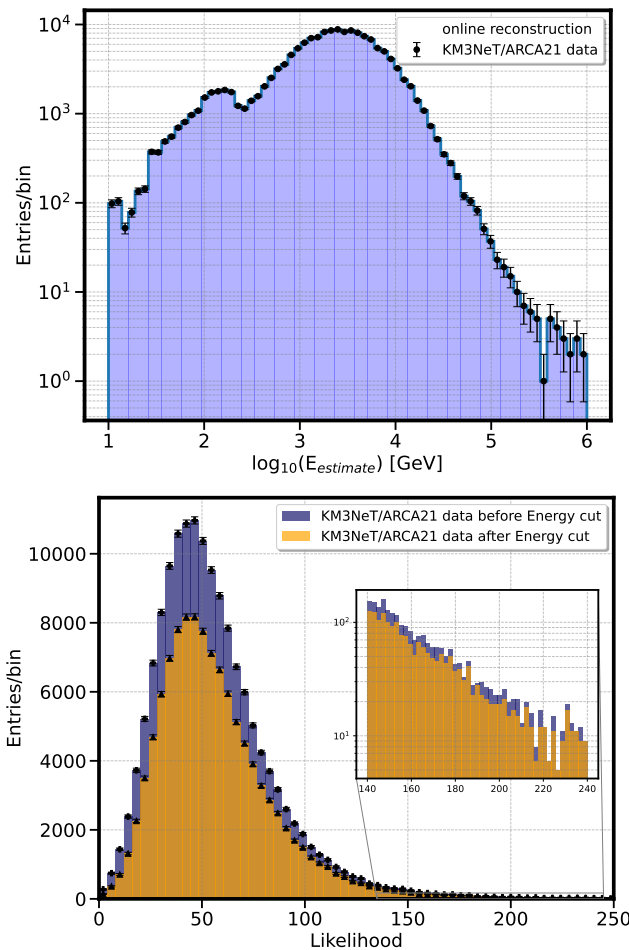


Figure 82: **Top:** reconstructed energy distribution of the KM₃NeT /ARCA₂₁ data, showing the double peak distribution, also described in the text. **Bottom:** reconstructed likelihood distribution for the KM₃NeT/ARCA₂₁ data set considered in the follow-up, highlighting the distribution before (blue) and after(orange) the cut in energy introduced.

In summary, the selection adopted for the follow-up of the event is:

$$\text{likelihood} > 155, \text{reconstructed energy} > 1 \text{ TeV and RoI radius}=2^\circ.$$

The number of events found in the OFF zenith band, within the OFF time window, is 452. When taking into account the solid angle ($\sim 2.5 \cdot 10^{-3}$) and the livetime (5050 s / 10800 s ~ 0.47) rescaling factors, the expected background derived is:

$$(84 \pm 9) \cdot 10^{-3}.$$

After unblinding, no events have been found in the ON region, and a sky map showing a 15° cone around the source localisation is available in Figure 83.

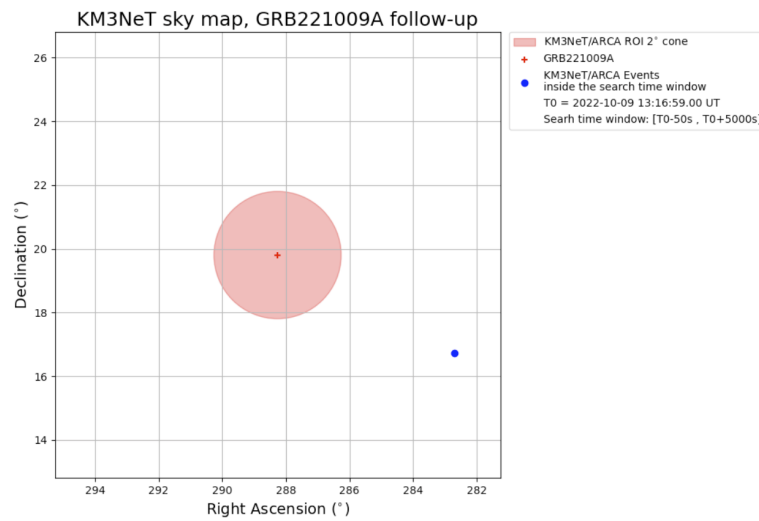


Figure 83: Sky map showing a circular region of 15° centred on the FERMI localisation for the GRB221009A. Highlighted the region of interest (red shaded circle) and possible events found in KM3NeT/ARCA data set (blue dot).

Additional searches have been performed with KM3NeT/ORCA data and combining the two KM3NeT detectors for a low energy search, centred in the MeV-low GeV range. Even in this case no statistically significant excess has been found.

The results of all these searches, conducted within the KM3NeT Collaboration, have been summarised and sent to the outside community through the GCN circular, available here [147], just three days after the event.

The Collaboration also produced more refined analyses in the subsequent months, exploiting ad hoc Monte Carlo simulations and the most up-to-date version for calibrations, whose results are available here [148]. Even in this case, no events in the ON region have been found, and upper limits have been derived ².

² Analysis conducted in tight collaboration with J. Palacios Gonzales: Juan.Palacios@ific.uv.es and A. Zegarelli : Angela.Zegarelli@roma1.infn.it.

8.3 TOWARDS AN AUTOMATIC ANALYSIS PIPELINE

The follow-ups reported in the previous sections were among the first to be ever performed within the KM₃NeT Collaboration. Although manually triggered and with some limitations, for example, the occasional lack of Monte Carlo simulations and/or calibrations, they allowed us to gain invaluable experience and expertise regarding detector capabilities, generating a deeper understanding of the data sets and of the different analysis methodologies. All acquired know-how has then been implemented into a series of programmes and tools capable of performing automatically follow-ups for specific events and integrated into the real-time framework developed by the Collaboration.

The new fully automated procedure starts already from the online data acquisition stages and terminates realising the results of a correlation analysis (the part in which I was mainly involved in). To achieve all this, many intermediate steps are performed.

8.3.1 *Online data reconstruction*

One of the main goals of the real-time framework is to automatically reconstruct and make the data available shortly after data taking. For this reason, the stream of data, coming from the detector, is continuously mirrored to a series of clients, namely C++ applications, running on dedicated servers. This procedure is also intended to avoid overloading or perturbing the data acquisition system and related services. The processing strategy follows a partial edge-computing model, where the major requirements in terms of CPU load are for the real-time event reconstruction (both tracks or showers) algorithms, directly running in the shore station computer centres. The number of clients and the resources assigned to this duty have been, and are constantly tuned on the basis of the incoming event rate from the detector and on the basis of the available hardware resources. The performance of this step is constantly monitored, reaching a median processing time, for the entire chain, from data acquisition to reconstruction, on the order of less than 5 seconds. Also, a large set of monitoring tools have been set up to store and keep under control interesting metrics, reflecting the correct functioning of the online apparatus and the status of the resource usage. Furthermore, the static calibration system has been used up to now, assuming nominal positions for the active elements of the detector. There are plans, however, by the Collaboration, to filter the acoustic data stream in real time, therefore, deriving a precise determination of the string position as a function of time, in order to apply the system of dynamic calibrations (see Section 4.9) even in real-time data processing. Once reconstructed, the events are first tagged with some quality factors and then sent to a common platform, currently hosted at the KM₃NeT/ORCA shore station, where the data flow coming from the two KM₃NeT detectors is merged. Data is stored in a centralised database and are ready to be accessed and analysed by pro-

grammes and tools. The database is constantly filled, allowing the various analysis pipelines to run and retrieve, in real time, events from both detectors.

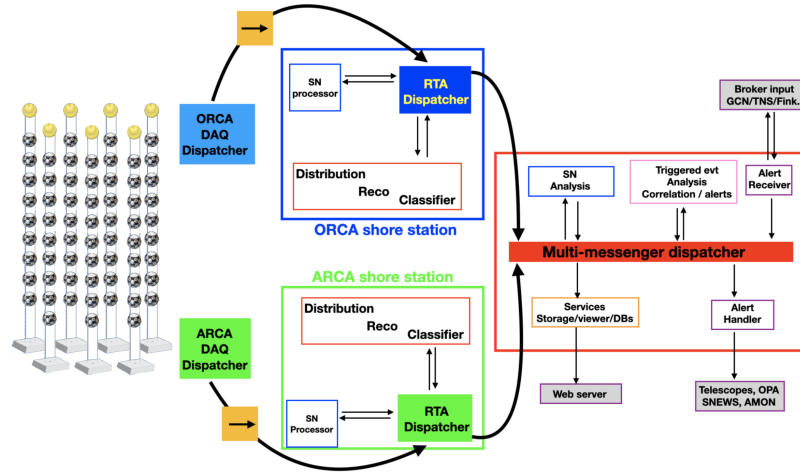


Figure 84: Schematic representation of the real-time framework developed within the KM3NeT Collaboration. Figure taken from [149]

8.3.2 External trigger receiver

Another pool of programmes and software has been built by the Collaboration to receive and filter the alerts sent by other experiments. Each notice received through, i.e. the GCN stream, or other specific brokers, is parsed, and the main information on the event automatically extracted. Then, each external alert is tagged as "Selected" or "Excluded" on the basis of specific criteria, such as the visibility of the best-fit localisation at the time of the alert, the probability for the event to originate from terrestrial noise or by BBH merger, and other criteria tuned on the specific nature of the astrophysical object. In the first case, once an alert is "Selected", then the due analysis pipeline is triggered. In addition, more notices could be sent by external experiments focused on a single specific event, each time containing more refined information.

The alerts currently received and analysed belong to mainly five categories: gamma-ray bursts, transient events, gravitational waves, neutrinos, and Core Collapse SuperNovae (CCSN). These alerts are sent by other observatories such as Fermi-GBM, Fermi-LAT, Swift, INTEGRAL, IceCube, LVK (Ligo, Virgo, and Kagra) and by supernova warning systems such as SNEWS [150].

CCSN correlation and low-energy searches are based on a different approach relying on the number of photon hit multiplicity evaluated at the level of a single DOM. They will not be treated in this section. For more information, see [151].

All the other 4 main categories of alerts, instead, are currently analysed based on the ON-OFF methodology exposed above.

8.3.3 Statistics

The real-time framework is currently running and analysing data 24 hours a day. Starting from September 2022, mainly for debug reasons, automatic correlation analyses have been performed, allowing external alerts to flow into the system and trigger specific analysis pipelines. Additionally, from May 24th 2023, Ligo interferometers started the O₄ observational run, consequently sending alerts to the community. Except for a first period, from the beginning of July 2023, the system has continuously filtered and processed external GW alerts. In Figure 85, the number of alerts that flowed into the system and those automatically followed up ("Selected"), is reported, as well as the rate of alerts per day the system has to handle.

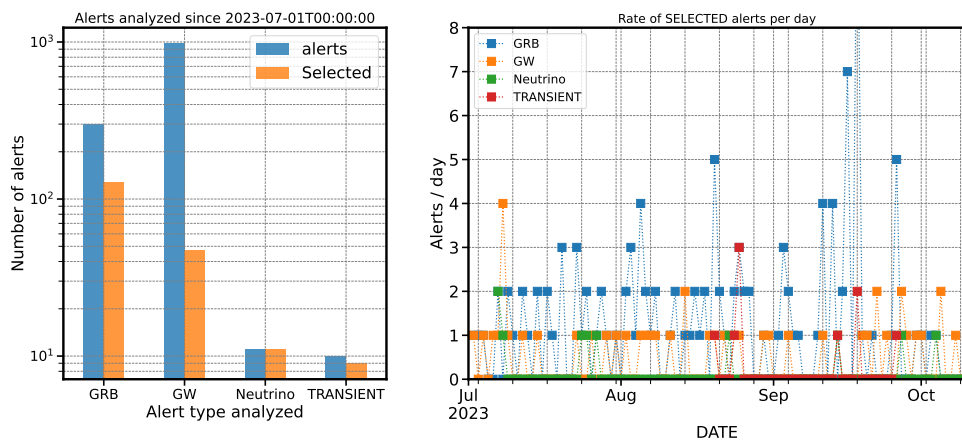


Figure 85: **Left:** bar chart showing the number of received (blue bars) and selected (orange bars) external alerts as a function of the four main categories analysed. **Right:** rate of selected alerts per day, subdivided by category. Both the plots refer to a period ranging from July 1st 2023 up to October 17th 2023.

More than 1300 alerts of all of the above categories have been received by the system from July 1st 2023 up to October 17th 2023, and around 200 were scrutinised and analysed in order to perform the due correlation analyses.

8.3.4 Automatic correlation analysis

A set of specific programmes has been built capable of triggering the processes that implement the correlation analysis, retrieving data, and managing the final result, which can, in principle, be reported to the external community. All these tools are centralised and communicate with each other through a common dispatcher. Specifically, when an external alert is received, a message is sent through the dispatcher properly parsed into a pre-defined json format. Then, one of the programmes continuously listens to the dispatcher, extracts the main information from the alert, and triggers

A dispatcher client connects processes according to a many (m) to many (n) m : n protocol over Ethernet. The dispatcher is capable of multiplexing the distribution of the same information to multiple destinations, according to the due tag subscription.

the specific pipeline built for each alert category. The pipeline can be easily configured through external configuration files, in which it is possible to specify all the parameters needed to perform the correlation search, i.e. the duration of the ON and OFF time windows, the selection cuts to apply to the data, and many others.

For example, in correlation searches of neutrino or transient alerts, the following ON time windows have been chosen:

- first iteration [$T_0 - 1$ hour, $T_0 + 1$ hour];
- second iteration [$T_0 - 24$ hours, $T_0 + 24$ hours];

The neutrino pipeline therefore waits respectively for 1 and 24 hours, in order to have all the required data processed and stored in the database, before launching the iteration. For GW alerts instead, the two iterations, corresponding to two different ON time windows that are actually used, are: [$T_0 - 500$ s, $T_0 + 500$ s] and [$T_0 - 500$ s, $T_0 + 6$ hours].

Regardless of the nature of the alert, each iteration performs a set of common tasks listed in the following:

- it accesses and retrieves from a database the most refined information concerning the analysed alert. Since multiple circulars could be sent by an experiment regarding a specific alert, even after couple of hours, each iteration performs this step;
- definition of the ON region, based on the type of follow-up performed. Specifically, a circular cone around the best-fit localisation is assumed for GRBs, neutrino, and transient follow-ups, while the specific sky map, containing the 90% sky localisation probability of the gravitational wave, is exploited. The radius of the circular region is assumed to be the maximum between 2° (the estimated median angular resolution of the KM3NeT/ARCA detector) and the error radius associated with the alert position, provided directly by the external experiment. Instead, for GW alerts, the map is always enlarged by a fixed amount of 2° , as shown in Figure 86;
- definition of one or multiple bands in local coordinates for the background estimation, similarly to what has been done for the follow-up of GRB221009A event;
- retrieval of events for a specific detector (KM3NeT/ARCA or ORCA) from the centralised database, containing all the reconstructed events in real time. If the OFF time window is longer than the ON time window, then the data collected days or weeks before the alert time is retrieved. For gravitational wave events, the OFF time window covers the previous 2 weeks before the alert time, while for other searches it extends only a week before;

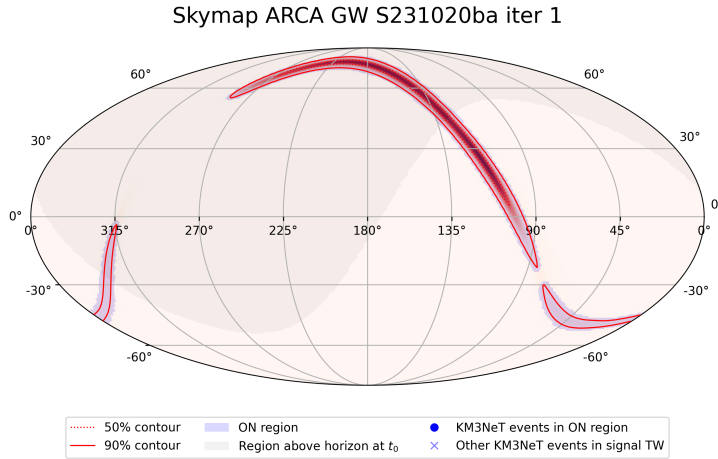


Figure 86: Map in equatorial coordinates showing the 90% sky localisation probability for a specific GW event. This contour, sent through GCN notice, is then enlarged by the due angular extension, in order to take into account the angular resolution of the KM₃NeT detectors.

- check for the quality of the data collected, computing the event rate over the full livetime, considering both the ON and OFF time windows (like in Figure 80) and selecting only those runs showing a similar rate with respect to those included in the ON time window;
- accurately compute the livetime for the ON and OFF time windows, in order to derive the due rescaling factor;
- if specified in the configuration file, perform an optimisation based only on data. Further details are available in Section 8.3.5;
- derivation of the background expectation, rescaling the number of events found in the OFF region bands by the solid angle and the livetime factors, following Equation 120;
- count the number of events falling in the ON region;
- compare the number found at the previous point to the expected background, evaluating also the associated Poisson p-value and, if pre-computed acceptances are available, also upper limits;
- production of plots for cross-checking the results and also sky maps for external reporting, such as the ones shown in Figure 87;
- sending the results back to the central dispatcher, where another specific application shows them in a clear and intelligible way into a dedicated web page.

The acceptance is computed considering the ratio: $\frac{n_s}{\Phi_0}$, with n_s the expected number of signal events according to an astrophysical flux with normalisation Φ_0 .

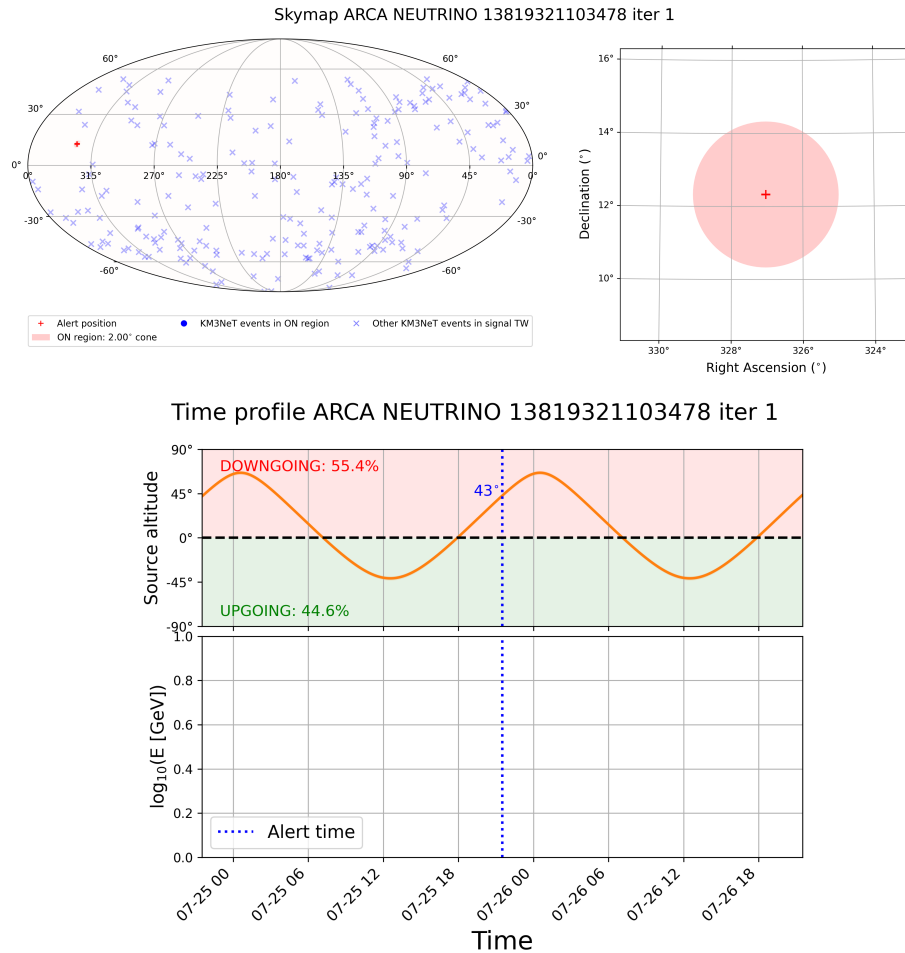


Figure 87: **Top:** sky map automatically produced by the analysis pipeline. Left, full-sky distribution of the selected events for background estimation in the Mollweide projection. Right, a zoom around the ON region. **Bottom:** visibility curve for the alert localisation. Displayed also the percentage of time spent below (upgoing sky) and above (downgoing sky) the horizon. In the same plot the bottom panel displays also the energy of events found in the ON region as a function of time.

8.3.5 Optimisation

One of the main tasks in order to maintain the system operational and capable of producing interesting physics results, even during a construction and expanding phase, like the one currently experienced by KM3NeT detectors, is to constantly update the event selection. Furthermore, considering the high variability of the characteristics of the alerts analysed, for example, spanning, with their sky localisation, from a few to hundreds of squared degrees, another critical point is to find, for each alert, the optimal selection. For this reason, a dynamical optimisation procedure has been adopted, allowing to be performed rapidly, in order not to delay the sending of the results, and relying only on data. The starting point for event selection is always a series of fixed cuts, applied to reconstruction variables, similar to the

one already reported in Section 6.5.3 in order to reduce environmental and atmospheric muon background. This also offers the advantage of reducing the overall number of events retrieved from the database. Subsequently, the optimisation is performed, specifically tuned to the characteristic of each alert. The metric chosen to be optimised is a threshold value for the background estimate: this, in fact, is computed directly from the data, without the need for any Monte Carlo simulation. A value lower than the $2.7 \cdot 10^{-3}$ is required, corresponding to the criteria $1 \text{ event} - 3\sigma$: if an event is found in the ON region, with the expected background below this threshold value, then the Poisson p-value associated with the observation is above the 3σ level. The optimisation is therefore performed scanning a set of consecutive cuts on a pre-defined variable, i.e. likelihood for the KM₃NeT/ARCA detector, or other machine learning score, until the point in which the number of background events reaches the defined threshold. The choice of the variable on which carry out the optimisation has been the object of careful evaluations by the Collaboration. It was derived mainly by looking at the variables capable of guaranteeing the highest signal efficiency once the background threshold is reached. Another factor, which is monitored, is the number of background events falling in the OFF region band, directly related to the statistical error associated with the background estimation.

GENERAL REMARKS The KM₃NeT real-time framework has been in operation for more than a year and is efficiently reconstructing data, flowing from both detectors. The overall system has been extensively tested, showing good stability under various external conditions.

Furthermore, the general idea at the base of the development of the tools and packages responsible for automatic correlation analyses is to provide a robust and user-friendly framework in which every user can deploy his own analysis, performing a specific follow-up study. Moreover, two people from the Collaboration are constantly on shift for one week at a time, monitoring the correct functioning of all the apparatus and reporting, on dedicated channels, if interesting results are obtained.

Up to now, no follow-up results with this automatic pipeline have been sent outside to other experiments through circulars. However, by the end of 2023 an automatic report to the external community is planned.

CONCLUSIONS

The emerging paradigm of multi-messenger astronomy is poised to revolutionise our understanding of astrophysical events. The synergy between different observatories and instruments, such as neutrino telescopes like KM₃NeT, gravitational wave detectors, and electromagnetic observatories, has the potential to unlock a deeper insight into the Universe's most violent and energetic events.

The work of this thesis attempts to go through an examination of recent discoveries in neutrino astronomy, trying to highlight the invaluable contribution that this field of research could bring in the study of astrophysical sources. In this context, KM₃NeT, with its field of view and unique design, will provide a novel perspective on astrophysical phenomena, ranging from core-collapse supernovae to the most energetic sources.

The recent observation of neutrino emissions from the centre of our Galaxy, as reported by the IceCube Collaboration and also hinted by the ANTARES Collaboration, marks a significant breakthrough that demonstrates the possibility of studying the properties of our Galaxy through neutrinos.

Specifically, this thesis focuses on an analysis seeking to detect a diffuse neutrino flux originating from the Galactic Ridge region, defined here in Galactic coordinates as $|b| < 2^\circ$ and $|l| < 30^\circ$, exploiting the first data collected by the KM₃NeT/ARCA detector, in various configuration geometries, for a total livetime of 432 days.

Unfortunately, the analysis presented in this study did not reveal any significant excess compared to the expected background estimates. Additionally, the upper limits placed by this work are not yet competitive with the results reported by the ANTARES and IceCube Collaboration, obtained with the respective data sets, both of which account for more than 10 years of livetime. However, the fast growth planned for the KM₃NeT detectors in the near future and its position in the Northern hemisphere will allow, in a couple of years, complementing those observations and to further constrain the neutrino emission from the centre of our Galaxy. Currently, the KM₃NeT/ARCA detector comprises 28 active detection units, for an effective area that is more than three times higher than that of ARCA6/8. Furthermore, only the first period of the KM₃NeT/ARCA₂₁ data set has been included in this analysis, but another 6 months of data, gathered with this configuration geometry, are currently under analysis.

This research showcases the evolving and expanding capabilities of the KM₃NeT neutrino observatory. The ongoing data analysis and the increasing sensitivity of this detector hold great promise for further discoveries and deeper insights into the energetic processes taking place within the Milky Way.

However, in this period of rapid development for the KM₃NeT detector, significant results can be obtained by detecting neutrino events in conjunction with rapid transient phenomena or in correlation with the observations of other experiments. In this type of search, in fact, there is no need to rely on a large livetime data set to produce stringent limits and constrains. The KM₃NeT Collaboration has thus begun a broader effort to create a framework for real-time data reconstruction and processing, as well as automated correlation analysis. Some of the results for correlation analyses, coincident with external alerts, such as IceCube-211208A and GRB221009A, have already been shared with the external community, and details have been reported in the last chapter of this thesis. In the near future, the system will be able to automatically manage a larger number of correlation analyses, allowing KM₃NeT to contribute significantly in this kind of search.

BIBLIOGRAPHY

- [1] W. Pauli. “The idea of the neutrino.” In: *Physics Today* 31.9 (1978), p. 23. DOI: <https://doi.org/10.1063/1.2995181>. URL: <https://physicstoday.scitation.org/doi/10.1063/1.2995181>.
- [2] C. L. Cowan et al. “Detection of the Free Neutrino: a Confirmation.” In: *Science* 124.3212 (1956), pp. 103–104. ISSN: 0036-8075. DOI: [10.1126/science.124.3212.103](https://doi.org/10.1126/science.124.3212.103). eprint: <https://science.sciencemag.org/content/124/3212/103.full.pdf>. URL: <https://science.sciencemag.org/content/124/3212/103>.
- [3] G. Danby et al. “Observation of High-Energy Neutrino Reactions and the Existence of Two Kinds of Neutrinos.” In: *Phys. Rev. Lett.* 9 (1 July 1962), pp. 36–44. DOI: [10.1103/PhysRevLett.9.36](https://doi.org/10.1103/PhysRevLett.9.36). URL: <https://link.aps.org/doi/10.1103/PhysRevLett.9.36>.
- [4] K. Kodama et al. “Observation of tau neutrino interactions.” In: *Phys. Lett. B* 504 (2001), pp. 218–224. DOI: [10.1016/S0370-2693\(01\)00307-0](https://doi.org/10.1016/S0370-2693(01)00307-0). arXiv: [hep-ex/0012035](https://arxiv.org/abs/hep-ex/0012035).
- [5] S. Schael et al. “Precision electroweak measurements on the Z resonance.” In: *Phys. Rept.* 427 (2006), pp. 257–454. DOI: [10.1016/j.physrep.2005.12.006](https://doi.org/10.1016/j.physrep.2005.12.006). arXiv: [hep-ex/0509008](https://arxiv.org/abs/hep-ex/0509008).
- [6] Y. Fukuda et al. “Evidence for oscillation of atmospheric neutrinos.” In: *Phys. Rev. Lett.* 81 (1998), pp. 1562–1567. DOI: [10.1103/PhysRevLett.81.1562](https://doi.org/10.1103/PhysRevLett.81.1562). arXiv: [hep-ex/9807003](https://arxiv.org/abs/hep-ex/9807003).
- [7] C.S. Wu et al. “Experimental Test of Parity Conservation in β Decay.” In: *Phys. Rev.* 105 (1957), pp. 1413–1414. DOI: [10.1103/PhysRev.105.1413](https://doi.org/10.1103/PhysRev.105.1413).
- [8] L.H. Ryder. *QUANTUM FIELD THEORY*. Cambridge University Press, June 1996. ISBN: 978-0-521-47814-4, 978-1-139-63239-3, 978-0-521-23764-2.
- [9] C.P. Burgess and G.D. Moore. *The standard model: A primer*. Cambridge University Press, Dec. 2006. ISBN: 978-0-511-25485-7, 978-1-107-40426-7, 978-0-521-86036-9.
- [10] J. A. Formaggio and G. P. Zeller. “From eV to EeV: Neutrino Cross Sections Across Energy Scales.” In: *Rev. Mod. Phys.* 84 (2012), pp. 1307–1341. DOI: [10.1103/RevModPhys.84.1307](https://doi.org/10.1103/RevModPhys.84.1307). arXiv: [1305.7513 \[hep-ex\]](https://arxiv.org/abs/1305.7513).
- [11] Daniel Ivan Scully. “Neutrino Induced Coherent Pion Production.” PhD thesis. Warwick U., 2013.

- [12] Henso Abreu et al. "Detecting and Studying High-Energy Collider Neutrinos with FASER at the LHC." In: *Eur. Phys. J. C* 80.1 (2020), p. 61. DOI: [10.1140/epjc/s10052-020-7631-5](https://doi.org/10.1140/epjc/s10052-020-7631-5). arXiv: [1908.02310](https://arxiv.org/abs/1908.02310) [hep-ex].
- [13] Victor Branco Valera, Mauricio Bustamante, and Christian Glaser. "The ultra-high-energy neutrino-nucleon cross section: measurement forecasts for an era of cosmic EeV-neutrino discovery." In: *JHEP* 06 (2022), p. 105. DOI: [10.1007/JHEP06\(2022\)105](https://doi.org/10.1007/JHEP06(2022)105). arXiv: [2204.04237](https://arxiv.org/abs/2204.04237) [hep-ph].
- [14] Raj Gandhi et al. "Neutrino interactions at ultrahigh energies." In: *Phys. Rev. D* 58 (9 Sept. 1998), p. 093009. DOI: [10.1103/PhysRevD.58.093009](https://doi.org/10.1103/PhysRevD.58.093009). URL: <https://link.aps.org/doi/10.1103/PhysRevD.58.093009>.
- [15] Sheldon L. Glashow. "Resonant Scattering of Antineutrinos." In: *Phys. Rev.* 118 (1 1960), pp. 316–317. DOI: [10.1103/PhysRev.118.316](https://doi.org/10.1103/PhysRev.118.316). URL: <https://link.aps.org/doi/10.1103/PhysRev.118.316>.
- [16] M. G. Aartsen et al. "Detection of a particle shower at the Glashow resonance with IceCube." In: *Nature* 591.7849 (2021). [Erratum: *Nature* 592, E11 (2021)], pp. 220–224. DOI: [10.1038/s41586-021-03256-1](https://doi.org/10.1038/s41586-021-03256-1). arXiv: [2110.15051](https://arxiv.org/abs/2110.15051) [hep-ex].
- [17] J. Manczak. "Sensitivity of KM₃NeT-ARCA detector to Glashow Resonance observation." In: *36th International Cosmic Ray Conference (ICRC2019)*. Vol. 36. International Cosmic Ray Conference. July 2019, 955, p. 955.
- [18] Carlo Giunti and Chung W. Kim. *Fundamentals of Neutrino Physics and Astrophysics*. Apr. 2007. ISBN: 978-0-19-850871-7.
- [19] B. Pontecorvo. "Neutrino Experiments and the Problem of Conservation of Leptonic Charge." In: *Sov. Phys. JETP* 26 (1968), pp. 984–988.
- [20] Ziro Maki, Masami Nakagawa, and Shoichi Sakata. "Remarks on the unified model of elementary particles." In: *Prog. Theor. Phys.* 28 (1962), pp. 870–880. DOI: [10.1143/PTP.28.870](https://doi.org/10.1143/PTP.28.870).
- [21] Thomas K. Gaisser, Ralph Engel, and Elisa Resconi. *Cosmic Rays and Particle Physics*. 2016. DOI: [10.1017/CB09781139192194.022](https://doi.org/10.1017/CB09781139192194.022).
- [22] M.G. Aartsen et al. "IceCube-Gen2: A Vision for the Future of Neutrino Astronomy in Antarctica." In: *arXiv:1412.5106* (Dec. 2014).
- [23] Andrea Palladino, Carlo Mascaretti, and Francesco Vissani. "The importance of observing astrophysical tau neutrinos." In: *JCAP* 08 (2018), p. 004. DOI: [10.1088/1475-7516/2018/08/004](https://doi.org/10.1088/1475-7516/2018/08/004). arXiv: [1804.04965](https://arxiv.org/abs/1804.04965) [astro-ph.HE].
- [24] Carmelo Evoli. *The Cosmic-Ray Energy Spectrum*. Dec. 2020. DOI: [10.5281/zenodo.4396125](https://doi.org/10.5281/zenodo.4396125). URL: <https://doi.org/10.5281/zenodo.4396125>.

- [25] T. Chiarusi and M. Spurio. "High-Energy Astrophysics with Neutrino Telescopes." In: *Eur. Phys. J. C* 65 (2010), pp. 649–701. DOI: [10.1140/epjc/s10052-009-1230-9](https://doi.org/10.1140/epjc/s10052-009-1230-9).
- [26] Vincent Tatischeff and Stefano Gabici. "Particle acceleration by supernova shocks and spallogenic nucleosynthesis of light elements." In: *Ann. Rev. Nucl. Part. Sci.* 68 (2018), pp. 377–404. DOI: [10.1146/annurev-nucl-101917-021151](https://doi.org/10.1146/annurev-nucl-101917-021151). arXiv: [1803.01794](https://arxiv.org/abs/1803.01794) [astro-ph.HE].
- [27] *Acceleration of cosmic-rays*. URL: <https://apc.u-paris.fr/Downloads/auger/Cours/Lectures2and3/Chapter3.pdf> (visited on 2023).
- [28] A. M. Hillas. "The Origin of Ultra-High-Energy Cosmic Rays." In: *Annual Review of Astronomy and Astrophysics* 22.1 (1984), pp. 425–444. DOI: [10.1146/annurev.aa.22.090184.002233](https://doi.org/10.1146/annurev.aa.22.090184.002233). eprint: <https://doi.org/10.1146/annurev.aa.22.090184.002233>. URL: <https://doi.org/10.1146/annurev.aa.22.090184.002233>.
- [29] Maurizio Spurio. *Probes of Multimessenger Astrophysics: Charged cosmic rays, neutrinos, γ -rays and gravitational waves*. Springer, 2018. DOI: [10.1007/978-3-319-96854-4](https://doi.org/10.1007/978-3-319-96854-4).
- [30] Zhen Cao et al. "Ultrahigh-energy photons up to 1.4 petaelectronvolts from 12 γ -ray Galactic sources." In: *Nature* 594.7861 (2021), pp. 33–36. DOI: [10.1038/s41586-021-03498-z](https://doi.org/10.1038/s41586-021-03498-z).
- [31] Zhen Cao et al. "The First LHAASO Catalog of Gamma-Ray Sources." In: (May 2023). arXiv: [2305.17030](https://arxiv.org/abs/2305.17030) [astro-ph.HE].
- [32] A. U. Abeysekara et al. "Multiple Galactic Sources with Emission Above 56 TeV Detected by HAWC." In: *Phys. Rev. Lett.* 124.2 (2020), p. 021102. DOI: [10.1103/PhysRevLett.124.021102](https://doi.org/10.1103/PhysRevLett.124.021102). arXiv: [1909.08609](https://arxiv.org/abs/1909.08609) [astro-ph.HE].
- [33] M. Ackermann et al. "Detection of the Characteristic Pion-Decay Signature in Supernova Remnants." In: *Science* 339 (2013), p. 807. DOI: [10.1126/science.1231160](https://doi.org/10.1126/science.1231160). arXiv: [1302.3307](https://arxiv.org/abs/1302.3307) [astro-ph.HE].
- [34] Damiano Caprioli. "'Espresso' Acceleration of Ultra-high-energy Cosmic Rays." In: *Astrophys. J. Lett.* 811.2 (2015), p. L38. DOI: [10.1088/2041-8205/811/2/L38](https://doi.org/10.1088/2041-8205/811/2/L38). arXiv: [1505.06739](https://arxiv.org/abs/1505.06739) [astro-ph.HE].
- [35] G.T. Zatsepin and V.A. Kuzmin. "Upper limit of the spectrum of cosmic rays." In: *JETP Lett.* 4 (1966), pp. 78–80.
- [36] Kenneth Greisen. "End to the cosmic ray spectrum?" In: *Phys. Rev. Lett.* 16 (1966), pp. 748–750. DOI: [10.1103/PhysRevLett.16.748](https://doi.org/10.1103/PhysRevLett.16.748).
- [37] Alexey Yushkov. "Mass Composition of Cosmic Rays with Energies above $10^{17.2}$ eV from the Hybrid Data of the Pierre Auger Observatory." In: *PoS ICRC2019* (2020), p. 482. DOI: [10.22323/1.358.0482](https://doi.org/10.22323/1.358.0482).

- [38] A. Aab and P. et al Abreu. "Inferences on mass composition and tests of hadronic interactions from 0.3 to 100 EeV using the water-Cherenkov detectors of the Pierre Auger Observatory." In: *Phys. Rev. D* 96 (12 Dec. 2017), p. 122003. DOI: [10.1103/PhysRevD.96.122003](https://doi.org/10.1103/PhysRevD.96.122003). URL: <https://link.aps.org/doi/10.1103/PhysRevD.96.122003>.
- [39] Anne Schukraft. "A view of prompt atmospheric neutrinos with IceCube." In: *Nucl. Phys. B Proc. Suppl.* 237-238 (2013). Ed. by Paolo Bernardini, Gianluigi Fogli, and Eligio Lisi, pp. 266–268. DOI: [10.1016/j.nuclphysbps.2013.04.105](https://doi.org/10.1016/j.nuclphysbps.2013.04.105). arXiv: [1302.0127](https://arxiv.org/abs/1302.0127) [astro-ph.HE].
- [40] Carlo Mascaretti and Francesco Vissani. "On the relevance of prompt neutrinos for the interpretation of the IceCube signals." In: *JCAP* 08 (2019), p. 004. DOI: [10.1088/1475-7516/2019/08/004](https://doi.org/10.1088/1475-7516/2019/08/004). arXiv: [1904.11938](https://arxiv.org/abs/1904.11938) [astro-ph.HE].
- [41] A. Albert et al. "Measurement of the atmospheric ν_e and ν_μ energy spectra with the ANTARES neutrino telescope." In: *Phys. Lett. B* 816 (2021), p. 136228. DOI: [10.1016/j.physletb.2021.136228](https://doi.org/10.1016/j.physletb.2021.136228). arXiv: [2101.12170](https://arxiv.org/abs/2101.12170) [hep-ex].
- [42] F. Vissani A. Palladino M. Spurio. "Neutrino Telescopes and High-Energy Cosmic Neutrinos." In: *Universe* 6.30 (2020). DOI: [10.3847/2041-8213/aa91c9](https://doi.org/10.3847/2041-8213/aa91c9).
- [43] Ofelia Pisanti. "Astrophysical neutrinos: theory." In: *J. Phys. Conf. Ser.* 1263.1 (2019). Ed. by Igor Ivanov and Yulia Kazarina, p. 012004. DOI: [10.1088/1742-6596/1263/1/012004](https://doi.org/10.1088/1742-6596/1263/1/012004). arXiv: [1906.12258](https://arxiv.org/abs/1906.12258) [astro-ph.CO].
- [44] Francis Halzen. "High-Energy Neutrinos from the Cosmos." In: *Annalen der Physik* 533.11 (2021), p. 2100309. DOI: <https://doi.org/10.1002/andp.202100309>. eprint: <https://onlinelibrary.wiley.com/doi/pdf/10.1002/andp.202100309>. URL: <https://onlinelibrary.wiley.com/doi/abs/10.1002/andp.202100309>.
- [45] Eli Waxman and John N. Bahcall. "High-energy neutrinos from astrophysical sources: An Upper bound." In: *Phys. Rev. D* 59 (1999), p. 023002. DOI: [10.1103/PhysRevD.59.023002](https://doi.org/10.1103/PhysRevD.59.023002). arXiv: [hep-ph/9807282](https://arxiv.org/abs/hep-ph/9807282).
- [46] Sara Buson et al. "Extragalactic neutrino factories." In: (May 2023). arXiv: [2305.11263](https://arxiv.org/abs/2305.11263) [astro-ph.HE].
- [47] Roberto Aloisio. "Ultra High Energy Cosmic Rays and Neutrinos." In: *Nucl. Part. Phys. Proc.* 279-281 (2016). Ed. by Gabriella Cataldi, Ivan De Mitri, and Daniele Martello, pp. 95–102. DOI: [10.1016/j.nuclphysbps.2016.10.014](https://doi.org/10.1016/j.nuclphysbps.2016.10.014). arXiv: [1603.05886](https://arxiv.org/abs/1603.05886) [astro-ph.HE].
- [48] R. Abbott et al. B. P. Abbott. "Observation of Gravitational Waves from a Binary Black Hole Merger." In: *Phys. Rev. Lett.* 116 (6 Feb. 2016), p. 061102. DOI: [10.1103/PhysRevLett.116.061102](https://doi.org/10.1103/PhysRevLett.116.061102). URL: <https://link.aps.org/doi/10.1103/PhysRevLett.116.061102>.

- [49] B. P. Abbott R. Abbott et al. “Multi-messenger Observations of a Binary Neutron Star Merger.” In: *The Astrophysical Journal* 848.2 (Oct. 2017), p. L12. DOI: [10.3847/2041-8213/aa91c9](https://doi.org/10.3847/2041-8213/aa91c9). URL: <https://doi.org/10.3847/2041-8213/aa91c9>.
- [50] A. Albert et al. “Search for High-energy Neutrinos from Binary Neutron Star Merger GW₁₇₀₈₁₇ with ANTARES, IceCube, and the Pierre Auger Observatory.” In: *The Astrophysical Journal* 850.2 (Nov. 2017), p. L35. DOI: [10.3847/2041-8213/aa9aed](https://doi.org/10.3847/2041-8213/aa9aed). URL: <https://doi.org/10.3847/2041-8213/aa9aed>.
- [51] Maxim Dvornikov. “Neutrino oscillations in gravitational waves.” In: *J. Phys. Conf. Ser.* 1435.1 (2020), p. 012005. DOI: [10.1088/1742-6596/1435/1/012005](https://doi.org/10.1088/1742-6596/1435/1/012005). arXiv: [1910.01415](https://arxiv.org/abs/1910.01415) [hep-ph].
- [52] *On high energy neutrino physics. Proceedings, 10th International Conference on High-Energy Physics (ICHEP 60): Rochester, NY, USA, 25 Aug - 1 Sep 1960*. Rochester: U. Rochester, 1960, pp. 578–581.
- [53] *The New Window into the Universe*. URL: <https://www.phys.hawaii.edu/~dumand/pict/grieder/DUMAND.htm> (visited on 2020).
- [54] S. Barwick et al. “AMANDA: South pole neutrino detector.” In: *AIP Conf. Proc.* 272 (1993). Ed. by Y. Suzuki and K. Nakamura, pp. 1250–1253. DOI: [10.1063/1.43263](https://doi.org/10.1063/1.43263).
- [55] *IceCube Explained*. URL: <https://icecube.wisc.edu/about/overview> (visited on 2020).
- [56] *Baikal-GVD home page*. URL: <https://baikalgvd.jinr.ru> (visited on 2020).
- [57] *ANTARES home page*. URL: <https://antares.in2p3.fr> (visited on 2020).
- [58] *Internal note: The probability density function of the arrival time of light*. URL: <https://common.pages.km3net.de/jpp/JPDF.PDF> (visited on 2022).
- [59] Yury Malyshkin. “Baikal-GVD neutrino telescope: Design reference 2022.” In: *Nuclear Instruments and Methods in Physics Research Section A: Accelerators, Spectrometers, Detectors and Associated Equipment* 1050 (2023), p. 168117. ISSN: 0168-9002. DOI: <https://doi.org/10.1016/j.nima.2023.168117>.
- [60] Matteo Agostini et al. “The Pacific Ocean Neutrino Experiment.” In: *Nature Astron.* 4.10 (2020), pp. 913–915. DOI: [10.1038/s41550-020-1182-4](https://doi.org/10.1038/s41550-020-1182-4). arXiv: [2005.09493](https://arxiv.org/abs/2005.09493) [astro-ph.HE].
- [61] Z. P. Ye et al. “Proposal for a neutrino telescope in South China Sea.” In: (July 2022). arXiv: [2207.04519](https://arxiv.org/abs/2207.04519) [astro-ph.HE].
- [62] M. G. Aartsen et al. “The IceCube Neutrino Observatory: Instrumentation and Online Systems.” In: *JINST* 12.03 (2017), P03012. DOI: [10.1088/1748-0221/12/03/P03012](https://doi.org/10.1088/1748-0221/12/03/P03012). arXiv: [1612.05093](https://arxiv.org/abs/1612.05093) [astro-ph.IM].

- [63] Aya Ishihara. “The IceCube Upgrade - Design and Science Goals.” In: *PoS ICRC2019* (2021), p. 1031. DOI: [10.22323/1.358.1031](https://doi.org/10.22323/1.358.1031). arXiv: [1908.09441](https://arxiv.org/abs/1908.09441) [[astro-ph.HE](#)].
- [64] M. G. Aartsen et al. “IceCube-Gen2: the window to the extreme Universe.” In: *J. Phys. G* 48.6 (2021), p. 060501. DOI: [10.1088/1361-6471/abbd48](https://doi.org/10.1088/1361-6471/abbd48). arXiv: [2008.04323](https://arxiv.org/abs/2008.04323) [[astro-ph.HE](#)].
- [65] Federica Bradascio and Thorsten Glüsenkamp. “An improved muon track reconstruction for IceCube.” In: *PoS ICRC2019* (2021), p. 846. DOI: [10.22323/1.358.0846](https://doi.org/10.22323/1.358.0846). arXiv: [1908.07961](https://arxiv.org/abs/1908.07961) [[astro-ph.IM](#)].
- [66] E. V. Bugaev et al. “Atmospheric muon flux at sea level, underground and underwater.” In: *Phys. Rev. D* 58 (1998), p. 054001. DOI: [10.1103/PhysRevD.58.054001](https://doi.org/10.1103/PhysRevD.58.054001). arXiv: [hep-ph/9803488](https://arxiv.org/abs/hep-ph/9803488).
- [67] S. Aiello et al. “Measurement of the atmospheric muon depth intensity relation with the NEMO Phase-2 tower.” In: *Astroparticle Physics* 66 (2015), pp. 1–7. ISSN: 0927-6505. DOI: <https://doi.org/10.1016/j.astropartphys.2014.12.010>. URL: <https://www.sciencedirect.com/science/article/pii/S0927650514001960>.
- [68] M. G. Aartsen et al. “Evidence for High-Energy Extraterrestrial Neutrinos at the IceCube Detector.” In: *Science* 342 (2013), p. 1242856. DOI: [10.1126/science.1242856](https://doi.org/10.1126/science.1242856). arXiv: [1311.5238](https://arxiv.org/abs/1311.5238) [[astro-ph.HE](#)].
- [69] R. Abbasi et al. “The IceCube high-energy starting event sample: Description and flux characterization with 7.5 years of data.” In: *Phys. Rev. D* 104 (2021), p. 022002. DOI: [10.1103/PhysRevD.104.022002](https://doi.org/10.1103/PhysRevD.104.022002). arXiv: [2011.03545](https://arxiv.org/abs/2011.03545) [[astro-ph.HE](#)].
- [70] R. Abbasi et al. “Improved Characterization of the Astrophysical Muon-neutrino Flux with 9.5 Years of IceCube Data.” In: *Astrophys. J.* 928.1 (2022), p. 50. DOI: [10.3847/1538-4357/ac4d29](https://doi.org/10.3847/1538-4357/ac4d29). arXiv: [2111.10299](https://arxiv.org/abs/2111.10299) [[astro-ph.HE](#)].
- [71] M. G. Aartsen et al. “Characteristics of the diffuse astrophysical electron and tau neutrino flux with six years of IceCube high energy cascade data.” In: *Phys. Rev. Lett.* 125.12 (2020), p. 121104. DOI: [10.1103/PhysRevLett.125.121104](https://doi.org/10.1103/PhysRevLett.125.121104). arXiv: [2001.09520](https://arxiv.org/abs/2001.09520) [[astro-ph.HE](#)].
- [72] Manuel Silva, Sarah Mancina, and Jesse Osborn. “Measurement of the Cosmic Neutrino Flux from the Southern Sky using 10 years of IceCube Starting Track Events.” In: *PoS ICRC2023* (2023), p. 1008. DOI: [10.22323/1.444.1008](https://doi.org/10.22323/1.444.1008). arXiv: [2308.04582](https://arxiv.org/abs/2308.04582) [[astro-ph.HE](#)].
- [73] Richard Naab, Erik Ganster, and Zelong Zhang. “Measurement of the astrophysical diffuse neutrino flux in a combined fit of IceCube’s high energy neutrino data.” In: *38th International Cosmic Ray Conference*. July 2023. arXiv: [2308.00191](https://arxiv.org/abs/2308.00191) [[astro-ph.HE](#)].
- [74] V. A. Allakhverdyan et al. “Diffuse neutrino flux measurements with the Baikal-GVD neutrino telescope.” In: *Phys. Rev. D* 107.4 (2023), p. 042005. DOI: [10.1103/PhysRevD.107.042005](https://doi.org/10.1103/PhysRevD.107.042005). arXiv: [2211.09447](https://arxiv.org/abs/2211.09447) [[astro-ph.HE](#)].

- [75] Andrea Palladino and Francesco Vissani. “Extragalactic plus Galactic model for IceCube neutrino events.” In: *Astrophys. J.* 826.2 (2016), p. 185. DOI: [10.3847/0004-637X/826/2/185](https://doi.org/10.3847/0004-637X/826/2/185). arXiv: [1601.06678](https://arxiv.org/abs/1601.06678) [astro-ph.HE].
- [76] Andrea Palladino, Maurizio Spurio, and Francesco Vissani. “On the IceCube spectral anomaly.” In: *JCAP* 12 (2016), p. 045. DOI: [10.1088/1475-7516/2016/12/045](https://doi.org/10.1088/1475-7516/2016/12/045). arXiv: [1610.07015](https://arxiv.org/abs/1610.07015) [astro-ph.HE].
- [77] R. Abbasi et al. “Evidence for neutrino emission from the nearby active galaxy NGC 1068.” In: *Science* 378.6619 (2022), pp. 538–543. DOI: [10.1126/science.abg3395](https://doi.org/10.1126/science.abg3395). arXiv: [2211.09972](https://arxiv.org/abs/2211.09972) [astro-ph.HE].
- [78] Thijs van Eeden. “Astronomy potential of KM₃NeT/ARCA230.” In: *PoS ICRC2023* (2023), p. 1075. DOI: [10.22323/1.444.1075](https://doi.org/10.22323/1.444.1075).
- [79] M. G. Aartsen et al. “Neutrino emission from the direction of the blazar TXS 0506+056 prior to the IceCube-170922A alert.” In: *Science* 361.6398 (2018), pp. 147–151. DOI: [10.1126/science.aat2890](https://doi.org/10.1126/science.aat2890). arXiv: [1807.08794](https://arxiv.org/abs/1807.08794) [astro-ph.HE].
- [80] Sjoert van Velzen et al. “Seventeen Tidal Disruption Events from the First Half of ZTF Survey Observations: Entering a New Era of Population Studies.” In: *The Astrophysical Journal* 908.1 (Feb. 2021), p. 4. DOI: [10.3847/1538-4357/abc258](https://doi.org/10.3847/1538-4357/abc258). URL: <https://dx.doi.org/10.3847/1538-4357/abc258>.
- [81] A. V. Plavin et al. “Directional Association of TeV to PeV Astrophysical Neutrinos with Radio Blazars.” In: *Astrophys. J.* 908.2 (2021), p. 157. DOI: [10.3847/1538-4357/abceb8](https://doi.org/10.3847/1538-4357/abceb8). arXiv: [2009.08914](https://arxiv.org/abs/2009.08914) [astro-ph.HE].
- [82] Julien Aublin, Giulia Illuminati, and Alexander Plavin. “ANTARES searches for neutrinos from the direction of radio-bright blazars.” In: *PoS ICRC2023* (2023), p. 1567. DOI: [10.22323/1.444.1567](https://doi.org/10.22323/1.444.1567).
- [83] M. Ageron et al. “ANTARES: The first undersea neutrino telescope.” In: *Nuclear Instruments and Methods in Physics Research Section A: Accelerators, Spectrometers, Detectors and Associated Equipment* 656.1 (2011), pp. 11–38. ISSN: 0168-9002. DOI: <https://doi.org/10.1016/j.nima.2011.06.103>. URL: <https://www.sciencedirect.com/science/article/pii/S0168900211013994>.
- [84] E Leonora and on behalf of the KM₃NeT Collaboration. “The Digital Optical Module of KM₃NeT.” In: *Journal of Physics: Conference Series* 1056.1 (July 2018), p. 012031. DOI: [10.1088/1742-6596/1056/1/012031](https://doi.org/10.1088/1742-6596/1056/1/012031). URL: <https://dx.doi.org/10.1088/1742-6596/1056/1/012031>.
- [85] S. Aiello et al. “The KM₃NeT multi-PMT optical module.” In: *Journal of Instrumentation* 17.07 (June 2022), P07038. DOI: [10.1088/1748-0221/17/07/P07038](https://doi.org/10.1088/1748-0221/17/07/P07038). URL: <https://dx.doi.org/10.1088/1748-0221/17/07/P07038>.

- [86] S. Adrian-Martinez et al. “Letter of intent for KM₃NeT 2.0.” In: *J. Phys. G* 43.8 (2016), p. 084001. DOI: [10.1088/0954-3899/43/8/084001](https://doi.org/10.1088/0954-3899/43/8/084001). arXiv: [1601.07459](https://arxiv.org/abs/1601.07459) [astro-ph.IM].
- [87] S. Aiello et al. “gSeaGen: The KM₃NeT GENIE-based code for neutrino telescopes.” In: *Computer Physics Communications* 256 (2020), p. 107477. ISSN: 0010-4655. DOI: <https://doi.org/10.1016/j.cpc.2020.107477>. URL: <https://www.sciencedirect.com/science/article/pii/S0010465520302241>.
- [88] P. Antonioli et al. “A Three-dimensional code for muon propagation through the rock: Music.” In: *Astropart. Phys.* 7 (1997), pp. 357–368. DOI: [10.1016/S0927-6505\(97\)00035-2](https://doi.org/10.1016/S0927-6505(97)00035-2). arXiv: [hep-ph/9705408](https://arxiv.org/abs/hep-ph/9705408).
- [89] J.-H. Koehne et al. “PROPOSAL: A tool for propagation of charged leptons.” In: *Computer Physics Communications* 184.9 (2013), pp. 2070–2090. ISSN: 0010-4655. DOI: <https://doi.org/10.1016/j.cpc.2013.04.001>. URL: <https://www.sciencedirect.com/science/article/pii/S0010465513001355>.
- [90] Ivone F. M. Albuquerque, Jodi Lamoureux, and George F. Smoot. “Astrophysical neutrino event rates and sensitivity for neutrino telescopes.” In: *Astrophys. J. Suppl.* 141 (2002), pp. 195–209. DOI: [10.1086/340281](https://doi.org/10.1086/340281). arXiv: [hep-ph/0109177](https://arxiv.org/abs/hep-ph/0109177).
- [91] D. Heck et al. “CORSIKA: A Monte Carlo code to simulate extensive air showers.” In: (Feb. 1998).
- [92] G. Carminati et al. “MUPAGE: a fast atmospheric MUon GENERator for neutrino telescopes based on PArametric formulas.” In: (July 2009). arXiv: [0907.5563](https://arxiv.org/abs/0907.5563) [astro-ph.IM].
- [93] Left: NASA/JPL-Caltech; right: ESA; layout: ESA/ATG medialab. *Anatomy of the Milky Way*. 2016. URL: <https://sci.esa.int/web/gaia/-/58206-anatomy-of-the-milky-way> (visited on 09/25/2023).
- [94] C Sobey et al. “Low-frequency Faraday rotation measures towards pulsars using LOFAR: probing the 3D Galactic halo magnetic field.” In: *Monthly Notices of the Royal Astronomical Society* 484.3 (Jan. 2019), pp. 3646–3664.
- [95] Glennys R. Farrar. “The Galactic Magnetic Field and Ultrahigh-Energy Cosmic Ray Deflections.” In: *Comptes Rendus Physique* 15 (2014), pp. 339–348. DOI: [10.1016/j.crhy.2014.04.002](https://doi.org/10.1016/j.crhy.2014.04.002). arXiv: [1405.3680](https://arxiv.org/abs/1405.3680) [astro-ph.HE].
- [96] Ilija Medan and B-G Andersson. “Magnetic Field Strengths and Variations in Grain Alignment in the Local Bubble Wall.” In: *The Astrophysical Journal* 873.1 (Mar. 2019), p. 87. DOI: [10.3847/1538-4357/ab063c](https://doi.org/10.3847/1538-4357/ab063c). URL: <https://doi.org/10.3847/1538-4357/ab063c>.
- [97] M. Bouyahiaoui, M. Kachelrieß, and D. V. Semikoz. “High-energy neutrinos from cosmic ray interactions in the local bubble.” In: *Phys. Rev. D* 101 (12 June 2020), p. 123023. DOI: [10.1103/PhysRevD.101.123023](https://doi.org/10.1103/PhysRevD.101.123023). URL: <https://link.aps.org/doi/10.1103/PhysRevD.101.123023>.

- [98] J. J. Balmer. “Notiz über die Spectrallinien des Wasserstoffs.” In: *Annalen der Physik* 261.5 (1885), pp. 80–87. DOI: <https://doi.org/10.1002/andp.18852610506>. eprint: <https://onlinelibrary.wiley.com/doi/pdf/10.1002/andp.18852610506>. URL: <https://onlinelibrary.wiley.com/doi/abs/10.1002/andp.18852610506>.
- [99] Roberto Aloisio and Pasquale Blasi. “Propagation of galactic cosmic rays in the presence of self-generated turbulence.” In: *Journal of Cosmology and Astroparticle Physics* 2013.07 (July 2013), p. 001. DOI: [10.1088/1475-7516/2013/07/001](https://dx.doi.org/10.1088/1475-7516/2013/07/001). URL: <https://dx.doi.org/10.1088/1475-7516/2013/07/001>.
- [100] Carmelo Evoli et al. “Cosmic-ray propagation with DRAGON2: I. numerical solver and astrophysical ingredients.” In: *JCAP* 02 (2017), p. 015. DOI: [10.1088/1475-7516/2017/02/015](https://doi.org/10.1088/1475-7516/2017/02/015). arXiv: [1607.07886](https://arxiv.org/abs/1607.07886) [astro-ph.HE].
- [101] Andrii Neronov and Dmitry V. Semikoz. “Evidence the Galactic contribution to the IceCube astrophysical neutrino flux.” In: *Astropart. Phys.* 75 (2016), pp. 60–63. DOI: [10.1016/j.astropartphys.2015.11.002](https://doi.org/10.1016/j.astropartphys.2015.11.002). arXiv: [1509.03522](https://arxiv.org/abs/1509.03522) [astro-ph.HE].
- [102] Troy A. Porter, Gudlaugur Johannesson, and Igor V. Moskalenko. “The GALPROP Cosmic-ray Propagation and Nonthermal Emissions Framework: Release v57.” In: *Astrophys. J. Supp.* 262.1 (2022), p. 30. DOI: [10.3847/1538-4365/ac80f6](https://doi.org/10.3847/1538-4365/ac80f6). arXiv: [2112.12745](https://arxiv.org/abs/2112.12745) [astro-ph.HE].
- [103] Georg Schwefer, Philipp Mertsch, and Christopher Wiebusch. “Diffuse Emission of Galactic High-energy Neutrinos from a Global Fit of Cosmic Rays.” In: *Astrophys. J.* 949.1 (2023), p. 16. DOI: [10.3847/1538-4357/acc1e2](https://doi.org/10.3847/1538-4357/acc1e2). arXiv: [2211.15607](https://arxiv.org/abs/2211.15607) [astro-ph.HE].
- [104] Pedro De La Torre Luque et al. “Gamma Rays and Neutrinos from the Galactic Plane at the PeV frontier.” In: *Journal of Physics: Conference Series* 2429.1 (Feb. 2023), p. 012036. DOI: [10.1088/1742-6596/2429/1/012036](https://doi.org/10.1088/1742-6596/2429/1/012036). URL: <https://dx.doi.org/10.1088/1742-6596/2429/1/012036>.
- [105] M. Ackermann et al. “FERMI-LAT OBSERVATIONS OF THE DIFFUSE γ -RAY EMISSION: IMPLICATIONS FOR COSMIC RAYS AND THE INTERSTELLAR MEDIUM.” In: *The Astrophysical Journal* 750.1 (Apr. 2012), p. 3. DOI: [10.1088/0004-637X/750/1/3](https://doi.org/10.1088/0004-637X/750/1/3). URL: <https://dx.doi.org/10.1088/0004-637X/750/1/3>.
- [106] Zhen Cao et al. “Measurement of ultra-high-energy diffuse gamma-ray emission of the Galactic plane from 10 TeV to 1 PeV with LHAASO-KM2A.” In: (May 2023). arXiv: [2305.05372](https://arxiv.org/abs/2305.05372) [astro-ph.HE].
- [107] M. Amenomori et al. “First Detection of sub-PeV Diffuse Gamma Rays from the Galactic Disk: Evidence for Ubiquitous Galactic Cosmic Rays beyond PeV Energies.” In: *Phys. Rev. Lett.* 126.14 (2021), p. 141101. DOI: [10.1103/PhysRevLett.126.141101](https://doi.org/10.1103/PhysRevLett.126.141101). arXiv: [2104.05181](https://arxiv.org/abs/2104.05181) [astro-ph.HE].

- [108] S. Adrian-Martinez et al. “Constraints on the neutrino emission from the Galactic Ridge with the ANTARES telescope.” In: *Phys. Lett. B* 760 (2016), pp. 143–148. DOI: [10.1016/j.physletb.2016.06.051](https://doi.org/10.1016/j.physletb.2016.06.051). arXiv: [1602.03036](https://arxiv.org/abs/1602.03036) [astro-ph.HE].
- [109] Stephen Sclafani et al. “Observation of High-Energy Neutrinos from the Galactic Plane.” In: *PoS ICRC2023* (2023), p. 1108. DOI: [10.22323/1.444.1108](https://doi.org/10.22323/1.444.1108). arXiv: [2307.14842](https://arxiv.org/abs/2307.14842) [astro-ph.HE].
- [110] Ke Fang, John S. Gallagher, and Francis Halzen. “Milky Way as a Neutrino Desert: Implications of the IceCube Galactic Diffuse Neutrino Emission.” In: (June 2023). arXiv: [2306.17275](https://arxiv.org/abs/2306.17275) [astro-ph.HE].
- [111] Morihiro Honda et al. “Calculation of atmospheric neutrino flux using the interaction model calibrated with atmospheric muon data.” In: *Phys. Rev. D* 75 (2007), p. 043006. DOI: [10.1103/PhysRevD.75.043006](https://doi.org/10.1103/PhysRevD.75.043006). arXiv: [astro-ph/0611418](https://arxiv.org/abs/astro-ph/0611418).
- [112] Thomas K. Gaisser, Todor Stanev, and Serap Tilav. “Cosmic Ray Energy Spectrum from Measurements of Air Showers.” In: *Front. Phys. (Beijing)* 8 (2013), pp. 748–758. DOI: [10.1007/s11467-013-0319-7](https://doi.org/10.1007/s11467-013-0319-7). arXiv: [1303.3565](https://arxiv.org/abs/1303.3565) [astro-ph.HE].
- [113] Rikard Enberg, Mary Hall Reno, and Ina Sarcevic. “Prompt neutrino fluxes from atmospheric charm.” In: *Phys. Rev. D* 78 (2008), p. 043005. DOI: [10.1103/PhysRevD.78.043005](https://doi.org/10.1103/PhysRevD.78.043005). arXiv: [0806.0418](https://arxiv.org/abs/0806.0418) [hep-ph].
- [114] A. Albert et al. “Hint for a TeV neutrino emission from the Galactic Ridge with ANTARES.” In: *Phys. Lett. B* 841 (2023), p. 137951. DOI: [10.1016/j.physletb.2023.137951](https://doi.org/10.1016/j.physletb.2023.137951). arXiv: [2212.11876](https://arxiv.org/abs/2212.11876) [astro-ph.HE].
- [115] *TMVA 4, toolkit for Multivariate Data Analysis with ROOT*. URL: <https://root.cern.ch/download/doc/tmva/TMVAUsersGuide.pdf> (visited on 2020).
- [116] A. Albert et al. “Joint Constraints on Galactic Diffuse Neutrino Emission from the ANTARES and IceCube Neutrino Telescopes.” In: *Astrophys. J. Lett.* 868.2 (2018), p. L20. DOI: [10.3847/2041-8213/aaecf](https://doi.org/10.3847/2041-8213/aaecf). arXiv: [1808.03531](https://arxiv.org/abs/1808.03531) [astro-ph.HE].
- [117] S. Adrian-Martinez et al. “Constraints on the neutrino emission from the Galactic Ridge with the ANTARES telescope.” In: *Phys. Lett. B* 760 (2016), pp. 143–148. DOI: [10.1016/j.physletb.2016.06.051](https://doi.org/10.1016/j.physletb.2016.06.051). arXiv: [1602.03036](https://arxiv.org/abs/1602.03036) [astro-ph.HE].
- [118] A. Neronov and D. Semikoz. “Galactic diffuse gamma-ray emission at TeV energy.” In: *Astron. Astrophys.* 633 (2020), A94. DOI: [10.1051/0004-6361/201936368](https://doi.org/10.1051/0004-6361/201936368). arXiv: [1907.06061](https://arxiv.org/abs/1907.06061) [astro-ph.HE].
- [119] S Hallmann, T Eberl, and on behalf of the KM₃NeT collaboration. “Search for neutrinos from the Fermi Bubbles with the ANTARES telescope.” In: *Journal of Physics: Conference Series* 888.1 (Sept. 2017), p. 012102. DOI: [10.1088/1742-6596/888/1/012102](https://doi.org/10.1088/1742-6596/888/1/012102). URL: <https://dx.doi.org/10.1088/1742-6596/888/1/012102>.

- [120] Gary C. Hill and Katherine Rawlins. “Unbiased cut selection for optimal upper limits in neutrino detectors: the model rejection potential technique.” In: *Astroparticle Physics* 19.3 (2003), pp. 393–402. ISSN: 0927-6505. DOI: [https://doi.org/10.1016/S0927-6505\(02\)00240-2](https://doi.org/10.1016/S0927-6505(02)00240-2). URL: <https://www.sciencedirect.com/science/article/pii/S0927650502002402>.
- [121] J.A. Aguilar et al. “Zenith distribution and flux of atmospheric muons measured with the 5-line ANTARES detector.” In: *Astroparticle Physics* 34.3 (2010), pp. 179–184. ISSN: 0927-6505. DOI: <https://doi.org/10.1016/j.astropartphys.2010.07.001>. URL: <https://www.sciencedirect.com/science/article/pii/S0927650510001246>.
- [122] D. Dornic et al. “Ten years of multi-wavelength follow-up observations of ANTARES neutrino alerts.” In: *PoS ICRC2019* (2021), p. 871. DOI: [10.22323/1.358.0871](https://doi.org/10.22323/1.358.0871).
- [123] *IceCube High-Energy Neutrino Track Alerts*. URL: https://gcn.gsfc.nasa.gov/doc/IceCube_High_Energy_Neutrino_Track_Alerts_v2.pdf (visited on 2023).
- [124] *IceCube-211208A - IceCube observation of a high-energy neutrino candidate track-like event*. URL: <https://gcn.gsfc.nasa.gov/gcn3/31191.gcn3> (visited on 2021).
- [125] *Fermi-LAT Gamma-ray Observations of IceCube-211208A*. URL: <https://www.astronomerstelegam.org/?read=15099> (visited on 2021).
- [126] *Swift-XRT observations of the blazar PKS 0735+178 in a flaring state*. URL: <https://www.astronomerstelegam.org/?read=15102> (visited on 2021).
- [127] *Swift monitoring of the BL Lac object PKS 0735+178 during a bright state*. URL: <https://www.astronomerstelegam.org/?read=15109> (visited on 2021).
- [128] *SRG/eROSITA observation of PKS 0735+17*. URL: <https://www.astronomerstelegam.org/?read=15108> (visited on 2021).
- [129] *MASTER OT J073807.40+174219.2 brightening during IceCube-211208A observations*. URL: <https://www.astronomerstelegam.org/?read=15098> (visited on 2021).
- [130] *Significant optical decay and brightening in blazar PKS 0735+17 coincident with IceCube-211208A*. URL: <https://www.astronomerstelegam.org/?read=151001> (visited on 2021).
- [131] *TELAMON, Metsahovi, Medicina, OVRO and RATAN-600 programs find a long-term radio flare in PKS0735+17 coincident with IceCube-211208A*. URL: <https://www.astronomerstelegam.org/?read=15105> (visited on 2021).
- [132] *IceCube-211208A: Upper limits from a search for additional neutrino events in IceCube*. URL: <https://gcn.gsfc.nasa.gov/gcn3/31195.gcn3> (visited on 2021).

- [133] *Search for counterpart to IceCube-211208A with ANTARES*. URL: <https://www.astronomerstelegam.org/?read=15106> (visited on 2021).
- [134] *4FGL J0738.1+1742*. URL: https://fermi.gsfc.nasa.gov/ssc/data/access/lat/LightCurveRepository/source.php?source_name=4FGL_J0738.1+1742 (visited on 2021).
- [135] GC Hill et al. "Examining the balance between optimising an analysis for best limit setting and best discovery potential." In: *Statistical Problems in Particle Physics, Astrophysics and Cosmology*. World Scientific, 2006, pp. 108–111.
- [136] *Search for neutrino counterpart to the blazar PKS0735+178 potentially associated with IceCube-211208A and Baikal-GVD-211208A with the KM₃NeT neutrino detectors*. URL: <https://www.astronomerstelegam.org/?read=15290> (visited on 2021).
- [137] *IceCube-220225A - IceCube observation of a high-energy neutrino candidate track-like event*. URL: <https://gcn.gsfc.nasa.gov/gcn3/31650.gcn3> (visited on 2022).
- [138] *IceCube-220303A - IceCube observation of a high-energy neutrino candidate track-like event*. URL: <https://gcn.gsfc.nasa.gov/gcn3/31670.gcn3> (visited on 2022).
- [139] *IceCube-220225A - IceCube observation of a high-energy neutrino candidate track-like event*. URL: <https://gcn.gsfc.nasa.gov/gcn3/31650.gcn3> (visited on 2022).
- [140] *IceCube-220425A - IceCube observation of a high-energy neutrino candidate track-like event*. URL: <https://gcn.gsfc.nasa.gov/gcn3/31944.gcn3> (visited on 2022).
- [141] *IceCube-220524A - IceCube observation of a high-energy neutrino candidate track-like event*. URL: <https://gcn.gsfc.nasa.gov/gcn3/32102.gcn3> (visited on 2022).
- [142] *Swift J1913.1+1946 a new bright hard X-ray and optical transient*. URL: <https://gcn.gsfc.nasa.gov/gcn3/32632.gcn3> (visited on 2022).
- [143] *GRB 221009A: Fermi GBM detection of an extraordinarily bright GRB*. URL: <https://gcn.gsfc.nasa.gov/gcn3/32636.gcn3> (visited on 2022).
- [144] *LHAASO observed GRB 221009A with more than 5000 VHE photons up to around 18 TeV*. URL: <https://gcn.gsfc.nasa.gov/gcn3/32677.gcn3> (visited on 2022).
- [145] *GRB 221009A or Swift J1913.1+1946: Fermi-LAT detection*. URL: <https://gcn.gsfc.nasa.gov/gcn3/32637.gcn3> (visited on 2022).
- [146] *Swift J1913.1+1946/GRB 221009A: detection of a 250-TeV photon-like air shower by Carpet-2*. URL: <https://www.astronomerstelegam.org/?read=15669> (visited on 2022).
- [147] *GRB 221009A: search for neutrinos with KM₃NeT*. URL: <https://gcn.gsfc.nasa.gov/gcn/gcn3/32741.gcn3> (visited on 2022).

- [148] J. Palacios et al. "Refined neutrino follow-up analysis of GRB221009A with KM₃NeT ARCA and ORCA detectors." In: *PoS ICRC2023* (2023), p. 1503.
- [149] Celli S. et al. "The Real-Time Analysis Platform of KM₃NeT and its first results." In: *PoS ICRC2023* (2023), p. 1125.
- [150] *SNEWS - SuperNova Early Warning System*. URL: <https://snews2.org/> (visited on 2023).
- [151] S. Aiello et al. "The KM₃NeT potential for the next core-collapse supernova observation with neutrinos." In: *Eur. Phys. J. C* 81.5 (2021), p. 445. DOI: [10.1140/epjc/s10052-021-09187-5](https://doi.org/10.1140/epjc/s10052-021-09187-5). arXiv: [2102.05977](https://arxiv.org/abs/2102.05977) [[astro-ph.HE](https://arxiv.org/archive/hep)].